UNIVERSIDAD COMPLUTENSE DE MADRID
**FACULTAD DE CIENCIAS QUÍMICAS**

**Departamento de Química Inorgánica I**


# NEW STRATEGIES FOR THE SYNTHESIS OF NANOSTRUCTURED INORGANIC FUNCTIONAL MATERIALS

**MEMORIA PARA OPTAR AL GRADO DE DOCTOR**
**PRESENTADA POR**

**Ana Querejeta Fernández**

Bajo la dirección de los doctores

José M. González Calbet
Marina Parras Vázquez
Aurea Varela Losada

**Madrid, 2011**

**ISBN: 978-84-694-6511-0** 

UNIVERSIDAD COMPLUTENSE DE MADRID
FACULTAD DE CIENCIAS QUÍMICAS
DEPARTAMENTO DE QUÍMICA INORGÁNICA I

# NEW STRATEGIES FOR THE SYNTHESIS OF NANOSTRUCTURED INORGANIC FUNCTIONAL MATERIALS

# NUEVAS ESTRATEGIAS DE SÍNTESIS DE MATERIALES FUNCIONALES INORGÁNICOS NANOESTRUCTURADOS

TESIS DOCTORAL

ANA QUEREJETA FERNÁNDEZ

MADRID, 2011

# New Strategies for the Synthesis of Nanostructured Inorganic Functional Materials

# Nuevas Estrategias de Síntesis de Materiales Funcionales Inorgánicos Nanoestructurados

Memoria presentada
para optar al grado de
Doctor en Química
con Mención Europea


Universidad Complutense de Madrid
Facultad de Ciencias Químicas
Departamento de Química Inorgánica I

Ana Querejeta Fernández

Directors/Directores: José M. González Calbet
Marina Parras Vázquez
Aurea Varela Losada

# AGRADECIMIENTOS / ACKNOWLEDGEMENTS

*"Empiezo a escribir esta sección pensando en sus particularidades. A priori parece ser la menos relacionada con los resultados científicos que se presentan, pero quizás sea la que contiene los hechos más importantes para la obtención de los mismos. Es la única parte en la que se permite la subjetividad, y las afirmaciones no necesitan referencias o datos que las apoyen, puesto que tienen un destinatario concreto al que no le hacen falta pistas para saber de qué hablo. Además, ni es evaluable ni va a sufrir corrección alguna. Es por esto la más libre; de hecho no hay ni formato ni normas que la regulen, pero los usos y costumbres indican que suele ser corta. Sin embargo, pienso que caer en este costumbrismo sería injusto para demasiada gente. Ahí va:"*

Bermejo-Álvarez

Tomo prestadas estas palabras, que susc ribo, para introducir la sección de agradecimientos de esta tesis, así com o pa ra expresar m i adm iración por su autor, excelso científico y pensador. Con frecuencia, las sentencias más acordes con nues tras tesis no se encuentran en las frases supue stamente célebres de lejanos desconocidos, sino en la gente que nos rodea, que es al fin y al cabo la que más nos influencia.

A los codirectores de esta tesis. A José Mª González Calbet, principal responsable de que decidiera em barcarme en esta tesi s d esde la s prim eras incu rsiones en su despacho para pregun tar "si se pod ía hacer una tesis de investigación po r ahí". Gracias por introducirm e desde el úl timo año de carrera en la investigación a ctual en nanociencia, por hacer que sin tiese curio sidad por el tem a y por dejarm e explorarlo durante la etapa doctoral. Por transm itirme conocim ientos de cristalografía y microscopía y por poner a m i disposición lo s m edios técnicos y hum anos para que aprendiera el m anejo instrum ental de microscopios electrónicos y técnicas difractométricas. Gracias tam bién p or la libert ad de evolución de la tesis en cuan to a proyectos se refiere. Por la financ iación (Congresos NanoSpain 2008, Braga, y NanoTech Insight 2009, Barcelona, y beca abril-junio 2010).

A Marina Parras, porque tomé la decisión de hacer esta tesis cuando supe que ibas a ser la codirectora, aunque no te conociera directamente. Gracias por tu eficiencia a la

hora de hacer la mayoría de los papeleos relacionados con mi beca. Por tus buenas conferencias docentes. Por tu confianza en mí y por la libertad de elección y desarrollo de estancias y de proyectos. Por la financiación para mi asistencia a congresos.

A Aurea Varela. Por estar amablemente pendiente de aspectos relacionados con los equipos instrumentales del laboratorio y, como codirectora, preocuparte de muchos detalles de mi tesis y de que no se me olvide ningún trámite ni papel.

A los distintos Ministerios (Ministerio de Educación y Ciencia, Ministerio de Ciencia e Innovación y Ministerio de Educación) por concederme la beca-contrato FPU y las tres estancias breves asociadas de las que he disfrutado. A la Federación de Jóvenes Investigadores / Precarios, que con su curre lograron que hoy todos tengamos derecho a paro. Al Servicio Público de Empleo Estatal, que también ha contribuido a la financiación de esta tesis.

A la gente de la Plaza Mayor, de donde procede la primera fuente de financiación de este trabajo doctoral, así como las primeras enseñanzas que recibí acerca de qué va este oficio (gracias, Luisa y familia).

A los revisores y miembros del tribunal de esta tesis. To the reviewers and committee members of this thesis. To all those great authors and papers that make me excited about this.

A otros codirectores morales de esta tesis:

A Paco del Monte (ICMM-CSIC). Gracias por abrirme las puertas de tu laboratorio, por presentarme webs y papers y demás menesteres del oficio, por iniciarme en la síntesis de nanopartículas inorgánicas, por transmitirme visiones más amplias y opiniones, por tus cruciales aportaciones a este trabajo doctoral –gran parte de los resultados que aquí se presentan no habrían sido posibles sin tus ideas y contribución a lo largo de estos años–, por decirme finalmente algún nombre y por las discusiones y razonamientos científicos. Por los cuentos y la filosofía.

A Mar García Hernández (ICMM-CSIC), que ha llevado a cabo la realización e interpretación de las medidas magnéticas de este trabajo. Gracias por enseñarme sobre

magnetismo y sobre tratamiento de datos. Por no sucumbir durante nuestro "iniciático" viaje hacia la caracterización estructural y exchange bias de nuestras caóticas muestras. Por tu coraje y empuje para que el trabajo saliera adelante. Por ese otro punto de vista más físico. Por tu aportación en la escritura de los papers.

To Nicholas Kotov (University of Michigan), for taking me in as one more in your lab. Thank you for offering me interesting work projects, for letting all the facilities in (and out) your lab completely available to me, for employing wide English, for introducing me in the proposals and collaborations, for your energy, for your example of work and dedication, and for your fundamental input in the PbS work –both in the experiments and in the process of writing the manuscript–. Thank you also for financial help (ACS 236th National Meeting, Philadelphia, PA, 2008; ACS 237th National Meeting, Salt Lake City, Utah, 2009). Last but not least, thanks for your contagious enthusiasm, for believing in people, for welcoming me so nicely even before I had arrived in my tree, for the parties/lunches/dinners and for teaching us about wines. Thanks, Nick.

To Markus Niederberger (ETH-Zürich), for the opportunity to work in your lab. For your help and kindness during my first stay abroad. For showing me your solvothermal reactions and other methods of synthesis of nanoparticles. Thank you for the talks and for sharing opinions.

Al resto de miembros del grupo de Jose, porque todos y cada uno habéis ayudado en alguna ocasión a esta individua eternamente deslocalizada que aparece y desaparece. A Laura, por tu optimismo y porque fuiste la primera en enseñarme el trabajo diario del laboratorio, rayos X y microscopios, gracias a lo cual pude empezar a trabajar. A Almudena, gracias por enseñarme sobre TEM, Rietveld, Diamond y responder siempre a todas mis cuestiones de ignorancia supina acerca de programas básicos. Por las charlas. A Luisa, gracias por enseñarme la cristalografía que he necesitado para avanzar mi trabajo, por pasarme algún programilla necesario y por tu enorme paciencia con todas mis dudas cristalográficas y de manejo de TEM, MacTempas, etc. A María, Julio, Raquel, Khalid, Jose, Ester, Susana, Irma, Aschraf y Andrea.

Al personal del Centro de Microscopía Luis Bru (UCM). A Luis Puebla y Julia, que tan amablemente me apuntan, "desapuntan" y me buscan hueco. A Adrián y Esteban, muchas gracias por vuestra profesionalidad, paciencia y por enseñarme de manera efectiva a manejar los distintos instrumentos del centro. A Juan Luis, por atender mis atascos con el TEM. A Eugenio, por enseñarme a preparar las muestras de SEM y su manejo. A Alfonso, por enseñarme el manejo del SEM-FEG.

Al personal del C.A.I. de difracción de rayos X (UCM), sección de polvo: Emilio, Julián e Ignacio. Muchas gracias por vuestra profesionalidad e inestimable ayuda.

A Emilio Morán y José Antonio Campo, director y secretario del Departamento de Química Inorgánica I (UCM), por vuestra ayuda a la hora de hacer los papeles "express" para depositar mi tesis. Al resto de compañeros del Departamento.

A José Luis García Fierro (ICP-CSIC), por las medidas de XPS. A María Vallet Regí (UCM), por dejarnos usar tu equipo "Nano Zeta Sizer" para realizar las medidas de dispersión de luz; a Eduardo Ruiz por la ayuda. A Francisco Gavilanes (UCM), Víctor Muñoz (CIB-CSIC), David de Sancho y el chico indio, por las medidas de dicroísmo circular.

A mis compañeros del grupo de Paco. Gracias, Marisa, por tu cercanía, opiniones, por la idea de la diálisis y por el Nano Letters de la manganita hidrotermal, origen de este camino. A Celia, Mateo y Gaspar. A Cochi, por estar siempre dispuesta a ayudar a todo aquel que llega al laboratorio; eres imprescindible para que empecemos a funcionar –y sigamos funcionando–; gracias por tus discusiones científicas y por hacer siempre fácil el trabajo contigo (incluso cuando "apestamos" laboratorios…). A Chus, Zaira, Mariló, Ílida, Matías, Giovanni, Inma, Marina, Daniel, Stefania, Paul, Lorena, Julián, Jose Luis, Conchi2 y Josué.

A gente del grupo de Mar. A Norber Nemes, por ser un compañero de despacho tan majo, por enseñarme a trabajar con el Origin y por explicarme cosas de cebollas antiferromagnéticas. A María Retuerto, por la lección de magnetismo resumido.

A todos los que me dejasteis "okupar" vuestras mesas, sillas y cables de red: Conchi, Paco, Marisa, y en especial a Sonia, Virginia y Fátima, porque sin vuestra generosidad no habría sido posible terminar la escritura de esta tesis ni de algún paper. Muchas gracias, Sonia, por acogerme como refugiada, por los ánimos, por los recuerdos tetuanero-manchegos que evocaste y por tu simpatía. Virginia, de verdad, muchas gracias por dejarme "okupar" tu sitio durante meses. Fátima, muchas gracias por aceptar refugiada de guerra como compañera de despacho.

A Rocío (Symio, diálisis, etc.), Lucía (becas y experiencias), etc. A Paqui (porque esas conversaciones dan sal a la vida; gracias por cuidarme y cada tarde traer alegría, además de la limpieza, a nuestra planta), a Marisa (por regañarme por verme con la bata, jeje, y recordarme lo que es un trabajo), a Primitivo (te voy a regalar una franja morada, jeje), etc. A todos aquellos con los que hablo en pasillos y autobuses, porque esas conversaciones son también parte de la tesis

A la gente de las comidas en Psicología. A Chus, por las historias de gente abollada, por tus alegres ocurrencias y concursos también abollados; a Zaira, por la iridología y por ser mi primera (y gran) profesora de lengua y cultura mejicanas; a las dos juntas, por esas conversaciones tan divertidas, surrealistas o absurdas, según se mire. A Aldo, que admira "los paisajes" que pasan; a Roberto, que cree en Punset y descree de "otro científico"; a Gustavo, tío tranquilo, algo descreído y "de campo", que ve documentales de La 2 y refuta datos con su "chismito" conectado a internet; a los tres, por vuestro "monotema" diario que, aunque pueda parecer superficial, es un análisis sociológico profundo que tanto enseña de la vida –y del cerebro masculino–. A otra asturiana, Belén, aunque no te guste –pero estudies a– Medem; por tu sonrisa, ánimo y buen humor. A Josué, aunque en ocasiones te enfades conmigo, jeje; gracias por animar las comidas y transmitir esos conocimientos del mundo; muchas gracias también por tu cariño, por esas pláticas, plá ticas, por tu entusiasmo y motivación con tu trabajo; por devolverme la visión de "normalidad". A Daniel, que insiste en que las jornadas laborales sean de 9 a 5. A Hernán, porque tienes mucho valor intentando comprender a tanta gente "experimental". A Julián, porque crees que tengo distorsionada la visión de la realidad…ah, gracias, chicos, por el paper y las divertidas discusiones sobre vida nanoparticulada extraterrestre. A José Luis, sabio conocedor de las entrañas de la Complu. Al gallego que se fue a Rusia. A Leticia, que nos dejó. A

Conchi2, aunque nuestros tiempos no se hayan solapado en este espacio, eres muy maja y bastó poco tiempo para entendernos. Aunque repita: Paul y Lorena, cultura chilena, Stefania y Giovanni, italiana, Marina, gallega, Conchi, granaína, e Inma, vallecana.

To my lab mates in ETH-Zürich: Dorota, Bettina, Inga, Igor, Gizem, and also Idalia. Thanks for the help and kindness. To Gisela Angst, for your secretary work and for providing me such a nice accommodation in Zürich.

To my Kinderspital's inhabitants, for making it a cosy home despite (or because) the occasional hostile environment. I just forget names: to the Iranian guy –Mostafa– (nice Iranian cuisine and pistachio-based dessert), to the Georgian girl –Ani– (for all the Georgian, for your mesmerizing way of telling stories in the kitchen at night and for the best definition of Madrid), to the French-German guy –Christophe–, another one regularly in the kitchen; thanks so much you two for your warmth in that unfair situation. To the Dutch and German guys, for making it a stupid American movie with popcorn or whatever TV moment so warm and pleasant (and for all the Dutch). To the Italian girl –Rosa–, for missing a "mocho". To the Turkish girl –Gizem–, also a lab mate, for missing the craziness in Zürich. To the German –Jasmin–, Swedish –Veronica– and Russian-Swedish –Sania– girls, active people and waterfall's excursion.

To my lab mates in Kotov's group: Paul (introducing yourself), Daniel (offering your help –CD!– from the very beginning), Sud (being in charge of the necessary boss role), Ana y Marek (comparación Spain-USA), Andrés (peculiares historias doctorales…), Jian (computer assistance), Christine (party leader), Tak (helpful and the best karaoke participant), Ming (always letting me take your first TEM minutes while you watched the soccer in Argentine), Jungwoo (regards to your wife), Bongsup, Ed, Ashish, Peter, Kevin, Ming, Yichun, Felipe, Soo Hwan, Meghan, Seong IL, Shimei, Huanan, Íñigo, Annarosa, Elizabeth and Matthew (I heard a lot of English because of you), Joong Bahng (yes-yes-yes-yes) and Joe (viking mugger, hehe) (memorable discussions, love&marriage). Thanks all of you for the stimulating atmosphere and the scientific training. Thank you also to Claire O'Connor, Ruby Sowards, Shelly Fellers and the rest of UM's staff for your efficient work and kindness.

To EMAL's staff (University of Michigan): Kai Sun, Haipin Sun, John Mansfield and Ying Qi, for your useful training and help with the instruments. To 3011, for teaching me so much about you during those long hours in the intimacy of our private room in darkness.

To Ann Arbor, my second home. To my first treehouse within my treehouse. To my main house, opposite the cemetery (nice neighbors…). To the "guy in the porch", my roomie, for opening always your mouth in the right moment, for letting me use your bathroom, for showing me another America. Thanks, Jeremy. Another location would have been a disaster. To other people there: Kevin (thanks for the wifi and room's switch) *et al*. and to the Russian guy's mother (the best *borsch* I have ever tried). To my kind landlords Bill and Naomi. Thanks also to the Indian girls from my other house and regards to the bugs!

A los que me crucé en los congresos y pasamos un buen rato.

A todos los lugares, deslumbrantes, que pisan nuestras botas. A todas las pelis fascinantes que perciben nuestros sentidos. A todas las historias que atraviesan nuestras vidas. To all the (dazzling) places, our boots step on. To all the fascinating movies perceived by our senses. To all those stories that pass through our lives.

No me olvido de mi primer contacto con un laboratorio de investigación: gracias Odón Arjona, por haberme dado la oportunidad de realizar una de las mejores "Asignatura Proyecto" que se pueden concebir (no exagero), aunque llegara de rebote. A José Nieto, por instruirme en el fino arte de columnas, destilaciones y demás.

A todos con los que solía comer ese año, por vuestro granito de culpa para que me quedara por allí. David (no he olvidado ni un momento tus sabios consejos), Lidia (ese activismo), Elías (quien acuñó el término "violento-con-b"), etc. Y después: Edu, Willy, Andrés, Yoli, Edu y a todos los demás quíficos, de antes y de ahora, gente acogedora donde las haya. A María Larriva, por poner el diván, por estar más atenta que yo a las renovaciones de mi beca y demás, por todas tus clases particulares durante la carrera y por todos los momentos durante y antes, fuera y dentro (como diría David), de la tesis.

A otros compañeros de carrera: Beatriz, Va nesa, Carlos, Alejandra y resto del CDP. A los buenos profesores.

Al Instituto Tetuán-Valdeacederas: a sus bue nos profesores, en especial a Beatriz Areces, María Acebo y María Jesús Peña, y co mpañeros, en especial a Susana, por tu universo. A esos años, al barrio y al espíritu de El Rojo.

A Albano, autor de la portada de esta tesis (cuando estabas liado). Gracias por todo el arte que has volcado en m i tesis, en ocasiones de carácter tan práctico; por dejarme seguir el proceso creativo a través de tu ventana al mundo de 27 pulgadas; por dejarme fastidiar –un poco– el resultado (menos mal que no caímos en la tentación de la Mahou o de las banderas de la UE, CAM; m ejor el portal de Belén); por los autónomos. A otro daño colateral: Eva. A Paqui, Pablo y Noemí (qué bien que votases por esa estrella), por estar ahí y recordármelo (fíjate tú que la tesis iba a servir para que cenara con vosotros…). Al gran 205, incluso cuando se te cae un pedal o no arrancas, porque sin ti no habría podido estar en varios sitios el mismo día, sobre todo al final de la tesis; por deslocalizarme entre la UCM y el ICMM y también por llevarnos a playas remotas e islas celtas. A Rodrigo y Marisol, por la foto del autoclave.

A mi padre (José Luis), madre y hermana (Rosas), por los embolados de autoclaves y otros proyectos locos en los que os meto, por los guisitos, por daros cuenta de qué día sale realmente mi avión…Por el hogar agradable (a ratos) para estudiar durante instituto y universidad. Por inculcarme la ilusión por explorar y el trabajo como forma de vida. Por ser de dónde vengo y estar ahí.

A Pablo, mi incompatible favorito. Por conocer gran parte de lo que rodea a esta tesis. Por conocerme. Por estar siempre ahí. Por, en ocasiones, ver y hacer por mí. *Por analizar situaciones y recargar ideales*. Por rom per moldes. Por compartir tantas aventuras. Por buscar soluciones y nunca perder el sentido del humor cuando llegamos de noche a poner la tienda, cuando nos la parte el viento o cuando no llevamos los palos. Por los tironcitos cuando subimos a las montañas. Por hacerme de rabiar y hacerme sonreír. Por ver amanecer y salir las estrellas desde nuestro refugio de almortas o campo base. Por tu arte con la sartén, por el pollo en el congelador (y los gusanos en

la nevera), por enmohecerme la toalla, por entender lo mío, por el pecado, por merodear a mi alrededor. Por existir.

*Mañana será otro día y verá la tuerta los espárragos*.

# INDEX / ÍNDICE

VII. Appendices/Anexos

# ABSTRACT / RESUMEN

# ABSTRACT

Nanoscience and nanotechnology are in the forefront of scientific research nowadays and they are expected to generate the next scientific-technical revolution. Specifically, functional materials can greatly benefit from this scientific field in areas such as energy, biomedicine, communications, *etc.* In this framework, inorganic nanoparticles (NPs) play a leading role. These can be considered fragments of bulk inorganic solids whose size lie within the nanometer scale (1 nm = $10^{-9}$ m) and exhibit new properties as compared to their bulk counterparts. Furthermore, such properties are strongly dependent on varied factors such as size, shape, defects and surface functionalization, allowing their multifold manipulation for the preparation of a new generation of stimuli-responsive materials. Besides, not only the NPs but also their self-assembly (SA) behaviour deserve much attention, since it can bring new fundamental insights and can help realize complex geometries as well as enhanced/combined properties. In this field, a better understanding of the relation between the NP's important features and properties is still needed for the realization of practical technologies.

The key for any material to exist is its preparation. Chemical synthetic pathways are cost- and time-effective and offer much flexibility for the tailoring of the features of the nanostructured materials. The synthetic strategies developed until now can be classified into solid-matrix methods, which make use of a hard matrix whose nanovoids shelter the confined crystallization of NPs, and liquid routes, which typically make use of low temperatures and either organic ligands or ions to protect the NP's surface, avoiding thus aggregation and allowing the control over their characteristics and their manipulation in different solvents. New directions in the synthetic field are focused on "all-in-one" liquids that simultaneously act as solvents and ligands at mild temperature. Ionic liquids (ILs), *i.e.* salts which are liquid at low temperature, excel in this direction; its peculiar characteristics such as high polarity, low interface tension, self-structuration, *etc.* are unique for the nucleation and stabilization of NPs. The existing synthetic routes have quite succeeded in attaining control over the size, shape and surface important attributes of NPs. However, control over complex compositions, defects and SA behaviour are still a challenge. Hence, new methods of synthesis which allow the exploration of those features are much needed.

I. Abstract

The present thesis frames within the nanochemistry discipline and targets the design of new chemical methods of synthesis of nanostructured inorganic functional materials. Specifically, focus is on new classes of low-temperature melts and highly ionic media, as-inspired in the characteristics of ILs. In regard to the features of the as-obtained products, the aim was to attain control over complex compositions, defects and SA features of ligand-free NPs. The role of such characteristics on the properties of the resulting products was evaluated.

In Chapter 1.1, the synthesis of the nano-sized ternary oxide $BaMnO_3$ was addressed. Manganites, or manganese oxides with perovskite structure, are a rich class of compounds with many varied applications, therefore the exploration of their synthesis and properties at the nanoscale is very desired. The main challenge in this case was to avoid the precipitation of separated Ba and Mn oxides as well as the formation of $BaCO_3$. Given the large number of hydrothermally synthesized micro-sized manganites, on one hand, and the potential of the hydrothermal pathway for the preparation of binary oxide NPs, on the other, such a route was evaluated for the synthesis of NPs of the ternary oxide $BaMnO_3$. The conditions for the formation of pure $BaMnO_3$ were found and a careful study of the experimental variables led to the tailoring of the as-prepared nano-sized product: nanorods formed by SA of NPs were produced for 70 % reactor filling volume, whereas more isotropic NPs were obtained for ~ 50 % filling volume; in the latter case, high KOH concentrations were found to play a crucial role in the control over the size (NPs as small as ~ 20 nm –with an interval of 8-40 nm– are obtained for a KOH concentration of 20 M). The key role played by high alkalinities under hydrothermal conditions was ascribed to the burst nucleation produced in a highly supersaturated medium in combination with the surface stabilization of the NPs via ions. Furthermore, the SA of the NPs observed at high reactor filling volumes could be attributed to the high viscosity, polarity contrasts and lubricant properties of this mixed molecular/ionic system. The magnetic characterization of the as-obtained ligand-free NPs revealed shifts of the hysteresis loops, similarly to the exchange-bias (EB) effect exhibited by ferromagnetic (FM)/antiferromagnetic (AFM) contacts at the nanoscale. This difference in respect to the AFM bulk material could be ascribed to FM contributions from uncompensated surface spins.

The extrapolation of the above route to more drastic alkaline conditions finds an example in the molten eutectic hydroxides route. The use of molten inorganic salts is a well-known traditional route for the synthesis of inorganic materials. Its adaptation for the synthesis of inorganic NPs requires either low reaction temperatures, which involves salts with low melting temperatures, or the use of organic stabilizers. A smart approach in the former direction is the selection of mixtures of salts with a eutective point in their phase diagram, for which the melting temperature of the mixture is drastically decreased as compared to those of the individual components. This is the case of NaOH/KOH mixture, whose eutectic composition has a melting temperature of 165 ºC. The corresponding melt had been previously reported to be a suitable medium for the crystallization of several binary and ternary nanooxides. Chapter 1.2 addresses failed attempts to prepare pure nano-sized alkali earth manganites and chapter 1.3 reports the successful preparation of ligand-free NiO nanooctahedra in such a solvent. Again, the high concentration of salts and ionic strength of the solvent are thought to be responsible for a burst nucleation, while the adsorption of ions to polar faces of the octahedra with rock salt structure could favour the preferential growth along the apolar vertexes of these geometries.

In the search of novel low temperature molten media for the synthesis of NPs, urea was considered on the basis of its shared attributes with alkali hydrothermal route and molten hydroxides: first, it has a low melting temperature (133 ºC); second, it provides the medium with alkaline character upon decomposition in water; third, as an organic melt (and in combination with low amounts of water) should be viscous and posses polarity contrasts and lubricant properties, which would favour the stabilization and assembly of NPs. Chapter 2 addresses the use of molten urea as a solvent for the synthesis of NPs. While mixtures of the melt and metal salts were found to not lead to the crystallization of either nickel, cobalt or manganese oxides or to their corresponding metals, their thermal treatments led to urea oligomerization, constituting thus a suitable organic matrix for the crystallization of NPs. The analysis of the route was done in chapter 2.1, which describes the synthesis of Ni/NiO NPs. Upon thermal treatment of the $Ni^{2+}$-oligomer, its self-combustion and formation of Ni/NiO NPs takes place in a two-stepped process of $Ni^{2+}$ reduction plus crystallization and subsequent inward oxidation after removal of the matrix. Control over the $Ni_{nuclei}/NiO_{shell}$ ratio was achieved by means of the urea content and calcination time: lower urea amounts and

longer calcination times led to thicker NiO shells. Three regimes were observed: C NPs, corresponding to large Ni cores and thin NiO shells, B NPs, consisting of small Ni cores –in the limit of coherence of X-ray diffraction– surrounded by thick NiO shells, and A nanostructured material, made up of porous nanosized NiO which might contain non-stoichiometry defects or tiny Ni nuclei. The stabilization of small Ni cores is a remarkable achievement as compared to previous reports on this material. Also, an interesting aspect is the structural defects, represented by a NiO component with a defective crystallinity stemming likely from both structural imperfection of the crystals quenched while being formed and tiny Ni nuclei of a few atoms. This translates into a high Ni/NiO surface and, thus, large EB effects were found, which may make this type of magnetic material interesting for diverse potential applications. Chapter 2.2 describes the synthesis of ligand-free $Co_3O_4$ (~ 20 nm) and $Mn_3O_4$ (~ 40 nm) NPs through this route.

In view of the lack of synthetic ability of melt urea, which was attributed to the low ionic strength of a mainly molecular/oligomeric medium, attempts to improve such a skill were done through the addition of ions. Specifically, it was found in the literature that the mixture of urea and choline chloride –a salt with an organic cation– has a deep eutectic point at 2:1 molar ratio and the resulting deep eutectic solvent (DES) is liquid at room temperature ($T_m$ = 12 ºC). Its properties should be similar to those of ILs; hence we tested the feasibility of the synthesis of inorganic NPs in such a solvent. In chapter 3.1 the crystallization of PbS NPs as well as to their different SA behaviours were studied. Initially, epitaxial SA of nucleated NPs (size ~ 30 nm) yielded sub-micron sized octahedral mesocrystals, in which the building units were oriented in the same crystallographic direction but still identified as a result of imperfect fusing. Further growth resulted into hierarchical hyperbranched PbS nano/micro crystals which possessed octahedral motifs at most levels of hierarchy. It is believed that dipole-dipole interactions between crystals are responsible for the SA behaviour and that the common geometries at every level of hierarchy are sculptured by the need to balance dipolar forces in pairs to avoid strongly polarized high-energy systems. Subsequently, SA modality switched to the incorporation of the remaining NPs into the body of the hyperbranched structures, resulting in six-arm faceted rods, and this was related to the decrease of polarity of the DES upon decomposition. Concomitant increase of electrostatic repulsion within the branches eventually led to the deconstruction of the

six-arm faceted rods into more isotropic particles with diameters comparables to the widths of the rods. The evaluation of the optoelectronic properties of ligand-free hierarchical branched PbS crystals could be a task of future work given the potential of this material for solar cells and related devices. Finally, in Chapter 3.2 the extension of the use of urea/choline chloride DES for the synthesis of other materials was undertaken. It reports the preparation of γ-$Fe_2O_3$ (~ 15 nm), α-$Fe_2O_3$ (~ 15 nm) and $Mn_3O_4$ (porous, rice-grain 140 nm) NPs.

Overall, the adaptation of the hydrothermal route for the preparation of ternary nano-sized oxides was successfully accomplished. Besides, two new methods of synthesis of inorganic NPs were developed. On one hand, urea-melt route presents a suitable solid matrix whose calcination leads to the crystallization and quenching of $Ni_{core}$-$NiO_{shell}$ (and other binary oxide) NPs showing non-stoichiometry defects. On the other hand, urea-choline chloride DES is a suitable fluid for the synthesis, stabilization and assembly (including irreversible deconstruction) of PbS (and binary oxides) NPs. All the synthetic pathways developed possess the feature of leading to ligand-free nanostructures, which is a remarkable attribute for many technologies. The study of these routes revealed that reaction liquids must fulfil two crucial requirements in order to allow the nucleation and stabilization of ligand-free NPs: enabling low temperatures of reaction and possessing a high polarity. The highly ionic systems studied showed important similarities between inorganic and organic compositions and it is envisioned that molecular/inorganic salt/organic salt complex mixtures will offer much potential for the study of the synthesis and SA of inorganic NPs with a combination of surface, size-, shape- and defect-dependent properties which eventually lead to practical technologies.

I. Abstract

# RESUMEN

La nanociencia y la nanotecnología están al frente de la investigación científica hoy en día y se espera que generen la próxima revolución científico-técnica. En concreto, los materiales funcionales se pueden beneficiar enormemente de este campo científico en áreas como la energía, la biomedicina, las comunicaciones, *etc.* En este marco, las nanopartículas (NPs) inorgánicas ocupan un lugar destacado. Éstas se consideran fragmentos de sólidos inorgánicos masivos con tamaños en la escala nanométrica (1 nm = $10^{-9}$ m) y exhiben nuevas propiedades en comparación con sus análogos masivos. Adicionalmente, dichas propiedades son muy dependientes de varios factores tales como el tamaño, la forma, los defectos y la *funcionalización* superficial, permitiendo su múltiple manipulación para la preparación de una nueva generación de materiales que responden a estímulos. Además, no sólo las NPs, sino su auto-ensamblado (AE) merecen mucha atención, ya que éste puede revelar nuevos principios fundamentales y puede ayudar a construir geometrías complejas así como a generar propiedades aumentadas/combinadas. En este campo, para la realización de tecnologías aún se requiere una mejor comprensión de la relación entre las características de las NPs y sus propiedades.

La clave para que un material exista es su preparación. Las rutas químicas de síntesis son eficientes en cuanto a costes y tiempo y ofrecen una gran flexibilidad para la manipulación de los rasgos de los materiales nanoestructurados. Las estrategias sintéticas desarrolladas hasta la fecha pueden clasificarse en métodos de matriz sólida, los cuales hacen uso de una matriz dura con nanohuecos que albergan la cristalización confinada de NPs, y rutas líquidas, las cuales hacen uso típicamente de bajas temperaturas y, o bien *ligandos* orgánicos, o bien iones que protegen la superficie de las NPs, evitando así su agregación y permitiendo el control de sus características y su manipulación en distintos disolventes. Las nuevas direcciones en el campo sintético están enfocadas hacia los líquidos "todo en uno" que actúen simultáneamente como disolventes y *ligandos* a temperatura suave. Los líquidos iónicos (LIs), *i.e.* sales que son líquidas a baja temperatura, destacan en esta dirección; sus características peculiares tales como alta polaridad, baja tensión superficial, auto-estructuración, *etc.* son únicas para la nucleación y estabilización de NPs. Las rutas sintéticas existentes han tenido gran éxito en el control del tamaño, la forma y la superficie de las NPs. Sin embargo, el

control de composiciones complejas, defectos y AE son todavía un reto. Por consiguiente, se necesitan nuevos métodos de síntesis que permitan la exploración de dichos rasgos.

La presente tesis se enmarca dentro de la disciplina de la nanoquímica y tiene como objetivo fundamental el diseño de nuevos métodos químicos de síntesis de materiales funcionales inorgánicos nanoestructurados. Específicamente, está enfocada hacia nuevas clases de fundidos de baja temperatura y medios altamente iónicos, inspirándose así en las características de los LIs. Respecto a los rasgos de los productos sintetizados, la meta era lograr el control de las características de composición compleja, defectos y AE de NPs sin *ligandos*. Asimismo, se evaluó el papel de dichos rasgos en las propiedades de los productos resultantes.

En el capítulo 1.1 se abordó la síntesis del óxido ternario nanoestructurado $BaMnO_3$. Las manganitas u óxidos de manganeso con estructura perovskita son una rica clase de compuestos con diversas aplicaciones, por lo que la exploración de su síntesis y propiedades en la nanoescala es muy deseada. El principal reto en este caso era evitar la precipitación de óxidos de Ba y Mn por separado, así como la formación de $BaCO_3$. Dado el gran número de manganitas con tamaños micrométricos sintetizadas hidrotermalmente, por un lado, y el potencial de la ruta hidrotermal para la preparación de NPs de óxidos binarios, por el otro, se evaluó esta ruta para la síntesis de NPs del óxido ternario $BaMnO_3$. Se encontraron las condiciones para la formación de $BaMnO_3$ puro y un estudio detallado de las variables experimentales condujo al "confeccionado" del producto nanoparticulado: para volúmenes de llenado del reactor del 70 % se formaron *nanorods* mediante AE de NPs, mientras que para volúmenes de llenado del ~ 50 % se obtuvieron NPs más *isotrópicas*; en el último caso, se encontró que una alta concentración de KOH es fundamental para el control del tamaño de partícula (se obtuvieron NPs de hasta ~ 20 nm –con un intervalo de 8-40 nm– para una concentración de KOH de 20 M). El papel clave que desempeña la alta alcalinidad bajo condiciones hidrotermales se atribuyó a la nucleación súbita producida en un medio altamente supersaturado en combinación con la estabilización superficial de las NPs por medio de iones. Además, el AE de las NPs observado a altos volúmenes de llenado podría atribuirse a la alta viscosidad, los contrastes de polaridad y las propiedades lubricantes de este sistema mixto molecular/iónico. La caracterización magnética de las NPs libres

de *ligandos* resultantes reveló desplazamientos de los ciclos de histéresis, de manera similar al efecto de *exchange-bias* (EB) exhibido por contactos ferro (FM)/antiferromagnéticos (AFM) a la nanoescala. Esta diferencia respecto al material AFM masivo podría adscribirse a contribuciones FM por parte de espines superficiales no compensados.

La extrapolación de la ruta anterior hacia condiciones más drásticas de alcalinidad encuentra representación en la ruta del fundido de eutéctico de hidróxidos. El uso de sales inorgánicas fundidas es un método bien conocido para la síntesis de materiales inorgánicos. Su adaptación para la síntesis de NPs inorgánicas requiere, o bien temperaturas suaves de reacción, lo cual implica sales con bajas temperaturas de fusión, o bien el uso de agentes estabilizadores orgánicos. Una aproximación elegante en la primera dirección es la elección de mezclas de sales con un punto eutéctico en su diagrama de fases, para el cual la temperatura de fusión de la mezcla es drásticamente menor en comparación con las de los componentes individuales. Este es el caso de la mezcla NaOH/KOH, cuya composición eutéctica tiene una temperatura de fusión de 165 ºC. El correspondiente fundido había sido utilizado previamente para la cristalización de varios nanoóxidos binarios y ternarios. El capítulo 1.2 aborda intentos fallidos de preparación de manganitas puras de metales alcalinotérreos con tamaños de partícula nanométricos, mientras que el capítulo 1.3 recoge la preparación de nanooctaedros de NiO sin *ligandos* en dicho disolvente. De nuevo, se piensa que la alta concentración de sales y la alta fuerza iónica del disolvente son responsables de la nucleación súbita, mientras que la adsorción de iones a las caras polares de los octaedros con estructura cloruro sódico podría favorecer el crecimiento preferencial a lo largo de los vértices apolares de estas geometrías.

En la búsqueda de nuevos medios fundidos de baja temperatura para la síntesis de NPs, se pensó en la urea en base a sus atributos comunes con la ruta hidrotermal alcalina y la de hidróxidos fundidos: primero, tiene una temperatura baja de fusión (133 ºC); segundo, su descomposición en presencia de agua proporciona carácter básico; tercero, como fundido orgánico (y en combinación con pequeñas cantidades de agua) debería ser viscoso y poseer contrastes de polaridad y propiedades lubricantes, lo cual favorecería la estabilización y ensamblaje de NPs. El capítulo 2 aborda el uso de la urea fundida como disolvente para la síntesis de NPs. Se encontró que, mientras que mezclas

del fundido y las sales metálicas no conducen a la cristalización ni de óxidos de níquel, cobalto, o manganeso ni de los correspondientes metales, el tratamiento térmico conduce a la oligomerización de la urea, que forma así una matriz orgánica adecuada para la cristalización de NPs. El análisis de la ruta se hizo en el capítulo 2.1, el cual describe la síntesis de NPs de Ni/NiO. Un tratamiento térmico adicional del oligómero-$Ni^{2+}$ conduce a la auto-combustión del componente orgánico y a la formación de NPs de Ni/NiO en dos pasos: reducción de $Ni^{2+}$ más cristalización y oxidación hacia dentro tras la eliminación de la matriz. Se consiguió el control del ratio $Ni_{núcleo}/NiO_{cáscara}$ por medio del contenido de urea y el tiempo de calcinación: cantidades menores de urea y tiempos de calcinación más largos condujeron a cáscaras más gruesas de NiO. Se observaron tres regímenes: NPs C, correspondientes a núcleos de Ni grandes y cáscaras de NiO finas, NPs B, formadas por núcleos de Ni pequeños –en el límite de la longitud de coherencia de la difracción de rayos X– rodeadas por cáscaras gruesas de NiO, y el material nanoestructurado A, constituido por un NiO poroso nanoestructurado que pudiera contener defectos no estequiométricos o núcleos de Ni diminutos. Un logro destacable en comparación con trabajos previos sobre este material es la estabilización de núcleos pequeños de Ni. Asimismo, un aspecto interesante son los defectos estructurales, representados por una componente de NiO con una cristalinidad defectuosa, posiblemente proveniente tanto de la imperfección estructural de los cristales "enfriados" durante su formación a alta temperatura como de núcleos diminutos de unos pocos átomos de Ni. Esto se traduce en una alta superficie Ni/NiO y, por tanto, se encontraron grandes efectos de EB, los cuales podrían hacer este tipo de materiales magnéticos interesantes para diversas aplicaciones potenciales. El capítulo 2.2 describe la síntesis de NPs sin *ligandos* de $Co_3O_4$ (~ 20 nm) y $Mn_3O_4$ (~ 40 nm) por medio de esta ruta.

En vista de la falta de habilidad sintética de la urea fundida, la cual se atribuyó a la baja fuerza iónica de un medio principalmente molecular/oligomérico, se intentó aumentar dicha capacidad mediante la adicción de iones. Específicamente, se encontró en la literatura que la mezcla de urea y cloruro de colina –una sal con un catión orgánico– presenta un punto eutéctico profundo para la relación molar 2:1 y el resultante disolvente con eutéctico profundo (DES) es líquido a temperatura ambiente ($T_f$ = 12 ºC). Sus propiedades deberían ser similares a las de los LIs; por consiguiente comprobamos la viabilidad de la síntesis de NPs inorgánicas en dicho disolvente. En el

capítulo 3.1 se estudió la cristalización de NPs de PbS así como sus diferentes comportamientos de AE. Inicialmente, el AE epitaxial de NPs (de tamaño ~ 30 nm) produjo mesocristales octaédricos de tamaño inferior a la micra, en los cuales las NPs constituyentes estaban orientadas en la misma dirección cristalográfica pero todavía se identificaban como resultado del imperfecto fusionado entre ellas. El crecimiento subsiguiente resultó en nano/micro cristales de PbS jerárquicos y super-ramificados, los cuales poseían motivos octaédricos en la mayoría de los niveles de jerarquía. Se cree que interacciones dipolo-dipolo entre cristales son las responsables del comportamiento de AE y que las geometrías comunes en cada nivel de jerarquía obedecen a la necesidad de compensar por parejas fuerzas bipolares para evitar sistemas de alta energía fuertemente polarizados. Posteriormente, la modalidad de AE cambió hacia la incorporación de las NPs restantes en el cuerpo de las estructuras super-ramificadas, lo que dio como resultado *rods* facetados de seis ramas. Este hecho se atribuyó a la disminución de polaridad del DES durante su descomposición. El aumento concomitante de la repulsión electrostática en las ramas condujo finalmente a la deconstrucción de los *rods* facetados de seis ramas en partículas más *isotrópicas* con diámetros comparables a la anchura de los *rods*. La evaluación de las propiedades optoelectrónicas de los cristales de PbS sin ligandos, jerárquicos y ramificados sería interesante dado el potencial de este material en células solares y dispositivos relacionados. Finalmente, en el capítulo 3.2 se extiende el uso del DES urea/cloruro de colina a la síntesis de otros materiales nanoparticulados: $\gamma$-$Fe_2O_3$ (~ 15 nm), $\alpha$-$Fe_2O_3$ (~ 15 nm) y $Mn_3O_4$ (poroso, con forma de grano de arroz, 140 nm).

En resumen, se consiguió adaptar la ruta hidrotermal para la preparación de nanoóxidos ternarios. Además, se desarrollaron dos nuevos métodos de síntesis de NPs inorgánicas. Por un lado, la ruta del fundido de urea presenta una nueva matriz sólida cuya calcinación conduce a la cristalización y *quenching* de NPs de, entre otros óxidos binarios, $Ni_{núcleo}$-$NiO_{cáscara}$ con defectos de no-estequiometría. Por otro lado, el DES urea-cloruro de colina es un fluido apropiado para la síntesis, estabilización y ensamblaje (incluyendo la deconstrucción irreversible) de NPs de PbS (y óxidos binarios). Todas las rutas sintéticas desarrolladas poseen la peculiaridad de conducir a nanoestructuras sin *ligandos*, lo cual es un atributo importante para muchas tecnologías. El estudio de estas rutas reveló que los líquidos de reacción deben satisfacer dos requerimientos cruciales para posibilitar la nucleación y la estabilización de NPs sin

*ligandos*: permitir el uso de bajas temperaturas de reacción y poseer una alta polaridad. Los sistemas iónicos estudiados mostraron importantes similitudes entre las composiciones inorgánicas y orgánicas y se prevé que mezclas complejas de sistemas moleculares/sales inorgánicas/sales orgánicas ofrezcan mucho potencial para el estudio de la síntesis y AE de NPs inorgánicas con una combinación de propiedades dependientes de la superficie, tamaño, forma y defectos, que finalmente conduzca a aplicaciones tecnologicas.

# INTRODUCTION / INTRODUCCIÓN

# INTRODUCTION

Nanoscience and nanotechnology are in the forefront of scientific research nowadays. This is evident by the large number of initiatives and amount of funding to promote their study all around the world, as well as by the plentiful output generated. In this sense, the number of papers published on NPs in 2009 is around 10-15 times higher than nine years before (Figure 1) and it is widely accepted that it will continue to grow in the foreseeable future. Actually, many expectations have been created towards the nanoscience and nanotechnology as the source of the next scientific-technical revolution.

This scientific field can exert an impact on society through functional materials, those materials which exhibit a certain property under a determined stimulus, performing thus intelligent and controlled actions. Nowadays, functional materials are ubiquitous, from energy, health, communications or information, and, overall, they play a leading role in the quality of life and wealth of the society. Today, the most dynamic area in the search of new functional materials is the nanoscience[1-12] due to the new and frequently unexpected (magnetic, optic, electric, optoelectronic, mechanic, thermal, catalytic, *etc.*) properties found in NPs in respect to their bulk counterparts. Moreover, such properties are dependent on many factors (such as size), so a broad set of conditions can be manipulated in order to design new materials which face the current world challenges.

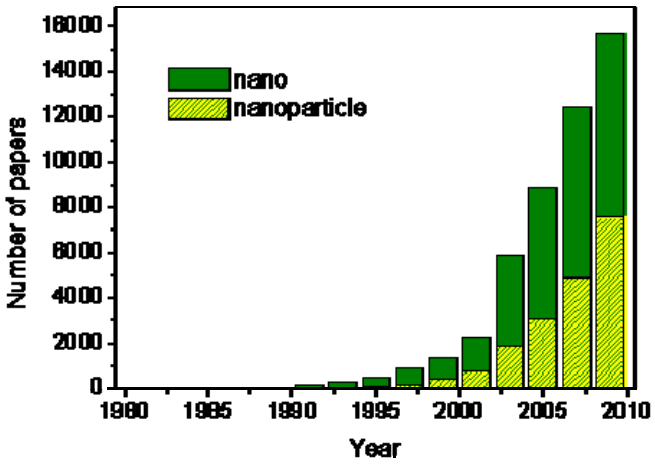


**Figure 1.** Number of papers published per year containing "nano" and "nanoparticle" terms according to Web of Science.

A popular example is microelectronics, which has demonstrated a continuous trend towards the size reduction of the devices, following Moore's observation and prediction that the number of transistors per square inch on integrated circuits doubled every 1.5 to

2 years and would do it in the near future. This has been possible due to the ability to manipulate matter in smaller dimensions, reaching the current nanometer regime,[13] and has not only translated into diminished dimensions but also into greater performance and reduced costs of a number of devices such as computers.

At the onset, the term nanoscience was defined as the synthesis, manipulation and study of objects in the nanometer scale and a tacit agreement pondered that the threshold would be structures with at least one dimension sized between 1 to 100 nm (approximately 10 to 1000 atoms; 1 nanometer is $10^{-9}$ meters); *i.e.* NPs.[13, 14] However, modern insights of the topic contend that such an arbitrary definition does not account for the multidimensionality of the phenomena.[15, 16] Thus, the definition based only on a length scale, either if the maximum is 100 or 1000 nm, is too tight and lacks complexity and precision. For instance, quantum confinement effects can be experienced at very different maximum sizes (5 nm for CdSe and 40 nm for PbSe) depending on the material; capillary forces, which are crucial for SA at the nanoscale, act along long distances; and nanovoids, ranging from zero- to three-dimensional (0D, 3D), offer countless possibilities for nanotechnology, from nanocapsules delivering drugs to sensors or to hydrogen-storage materials. What seems to be an agreement among the scientific community is the prospect that nanoscience –"the science at the nanoscale"– blurs the boundaries of classical disciplines, such as chemistry, physics, biology, engineering and medicine.

## Nanoparticles in nature and along mankind history

Nanomaterials are as natural as human beings and human beings (unconsciously) prepared and engineered nanomaterials since their ancient times in The Earth. Regarding their environmental apparition, nanoparticulate (*i.e.* matter with particle sizes between 1 and 1000 nm) materials such as carbon nanotubes appear in soot (and, then, in the atmosphere) as a result of naturally occurring and anthropogenic processes of combustion of natural resources like wood or fuels.[17] Similarly, volcanic ash and interstellar dust are matter divided at the nanometer scale (mentioned in [18]). Haze (mentioned in [18]) and silica-based minerals such as asbestos[17] are further examples. On the other hand, NPs are also encountered as building blocks within the structure of rocks

such as shale (containing octahedral NPs of iron sulfide)[18] and in minerals such as the clay group of phyllosilicates (which consist of nanosized 2D silicate sheets) and in zeolites (which posses a 3D aluminosilicate framework with periodical pores at the nano/microscale). Opals are an eye-catching example of organized colloids; they are colorful gemstones composed of monodispersed spherical silica ($SiO_2$) particles periodically packed into optical nanostructures.[19] The same type of periodic structural framework –called photonic crystal– is also responsible for the color of peacock's feathers[20] and butterflies' wings[21] due to the diffraction of phonons within the structure, composed of a chitinous protein in this case.[15] Chitin, a long-chain polymer of N-acetylglucosamine, is a common organic component of hybrid materials at the nano/microscale forming together with silica the exoskeletons of arthropods as well as the skeletons of the protozoa radiolarian and the unicellular algae diatom.[22, 23] In the latter cases, the aesthetic perforated design provides the microstructure with advanced functionality promoting the economic use of silica, lightness of a dense material and a filtration mechanism for water and nutrients. Nacre is another composite nanomaterial which is produced by some mollusks as an inner shell layer and also as pearls. Composed of 95 % of brittle calcium carbonate tablets and ~5 % of biopolymers, it is twice as hard and more than 1000 times as tough as its constituent phases, which constitute exceptional mechanical properties.[24] Eggshells are also advanced materials made up of a protein matrix aligned with nanocrystals of calcium carbonate engineered in such a way that the resulting hard structure protects the inner against external aggressions while allowing an excellent gas and water permeability for the avian embryo.[25] Regarding endoskeletons of vertebrates, bones are mainly composed of carbonated hydroxyapatite and collagen engineered at the nanoscale to move, support and protect organs and produce cells and store minerals.[26, 27] Organic nanostructures in nature also show advanced functionality, such as the high tensile strength (exceeding that of steel) and great extensibility of spider silk, stemming from a nanoconfinement effect in which the nanocrystals of protein enable a highly efficient use of hydrogen bonds.[28] Superhydrophobic lotus leaves[29] and supersticky gecko foot pads[30] are further examples of superior properties found in organic nanostructures. In the latter, the millions of aligned "hairs" in each toe are split at the end into billions of nanoscale spatula, allowing a rapid switching through van der Waals forces between the strong adhesion/friction (attached) state and zero adhesion/friction (detached) state.

On the other hand, all the biological systems present the intriguing feature of building their organic structural components, such as microtubules, microfilaments and chromatin at the nanoscale.[31] Besides, a key property of living organisms is the molecular recognition leading to self-assembly, through which nanoscale building blocks are autonomously organized into complex and functionally sophisticated structures (note for instance the high efficiency of photosynthesis in producing and storing energy, the brain of humans in storing and processing information or, in whole, the smart design of alive organisms, with ability to reproduce from the basic information storage molecule in nature, DNA). Gaining understanding of nature's pathway of producing and manufacturing nanoscale materials is very desirable for the achievement of superior functional materials.

Regarding to the production of inorganic NPs, some living systems have been shown to behave as "nanofactories".[32, 33] Thus, monodispersed NPs of different nature, from semiconductors[34-36] to (magnetic,[37] ferroelectric,[38] *etc.*) oxides and metals[39-41], are produced both intracellular and extracellularly by yeasts,[34, 36] bacteria,[35] fungus[38, 39, 41], viruses and plants[40]. Such synthetic strategies belong to a bottom-up approach, in which individual atoms/molecules are combined to build a larger-sized entity.

However, the opposite top-down strategy, *i.e.* the controlled destruction of a bulk solid sculpturing nanopatterns, also occurs in nature. The weathering of rocks is not only caused by a "geo-milling" or mechanical action performed by factors such as temperature changes, wind erosion, freezing and thawing, extraction by rain and snow melt water, but also by microbial activity. In-lab acceleration of the latter process happening slowly in nature has opened the path to the "bio-milling" pathway, such as the fungus-mediated break down of bismuth oxide chloride nanoplatelets (~150-200 nm) into < 10 nm NPs.[42, 43]

So, there is a myriad of examples of NP's formation mechanisms in nature for humans' inspiration. In this sense, although through observation and trial and error experiments, human beings developed chemical synthesis methodologies for the preparation of inorganic NPs from ancient times. One of the oldest identified examples is probably the making-up in ancient Egypt dating back from at least 1000-2000 BC, which was composed of fine powders of lead[44] and hematite (mentioned in ref. [17] )

compounds. Similarly, ~ 5 nm PbS NCs –a current nanoscience favorite– have been recently identified[45] as a common hair dyeing and wool blackening agent used from Greco-Roman times up to modern times, including Arabian reports from medieval period, Renaissance, modern chemists and the present day (mentioned in [45]). In these cases, the synthetic formula involves the mixture of lead oxide (PbO), slaked lime ($Ca(OH)_2$) and water to form a paste that is successively applied to the hair giving rise to the black color. The irreversible formation of PbS NPs, ultimately responsible for the color, is achieved through the reaction of $Pb^{2+}$ ions with the sulfur-based amino acids from the hair and the protein matrix could serve as a nanoscale reactor. The hair mechanical properties are essentially unaffected because of the extremely small size of the crystals.

Further ancient uses of nanomaterials date back to at least ~ 2000 BC in Egypt and China, when inks contained black carbon and $TiO_2$ NPs, or to ~ 500 BC, when Phoenicians already took advantage of silver NPs to treat infections due to their antibacterial properties (mentioned in ref. [17]). Damascus steel (1100-1700 AD) has been shown to contain NPs.[46]

Another illustrative example is the dyeing of glass and ceramic porcelains by colloidal solutions of gold –also a current nanoscience favorite–, which was already known in China more than a thousand years ago (mentioned in [3, 15]) and in late Greco-Roman times[47, 48] and has found wide use in stained glass and porcelain manufactories since the eighteen century. The variety of colors stems from the characteristic plasmon resonance corresponding to the different diameters (1-50 nm) of the gold NPs.

A more deliberated preparation of gold colloids dates back from 1665, when Andreas Cassius and his son prepared from gold precursors the Purple of Cassius, presumed to possess medicinal qualities –the Elixir of Life– for a time (mentioned in [49]). However, it is not until 1857 when modern colloidal chemistry is born from Michael Faraday's work[47] on the preparation of metallic colloids and the exploration of the relations between matter, on the one hand, and electrical, magnetic, and optical phenomena on the other.[49] His pioneer observations lead him to state that the color of the transparent solutions stemmed from particles that are "*very minute in their dimensions. … Known phenomena appeared to indicate that a mere variation in the size*

*of its particles gave rise to a variety of resultant colours"*. Nevertheless, a century had to pass until the term colloid was coined (by Thomas Graham, 1861).[50] Further pioneers of colloid science were Marian Smoluchowsky, Richard Zsigmondy and Wilhelm and Wolfgang Ostwald (mentioned in ref. [49]).[51-53] The latter, in 1915 entitled his immortal book on colloid chemistry "The World of Neglected Dimensions", implying that this was a science in its own right.[54]

## The rising of nanoscience

The mentioned examples illustrate that research on the nanometer scale is not new nowadays. What is new, though, is both the availability of techniques to image, characterize and manipulate systems in the nanometer scale and our understanding of atomic scale interactions. Thus, for instance, the excellence and prodigious merit of Faraday's work was probably somehow stained with a touch of disappointment due to the lack of ability to directly "see" the particles: *"The state of division of these particles must be extreme; they have not as yet been seen by any power of the microscope"*.

Thus, for some time new prophecies followed, such as the visionary talk that physicist Richard Feynman gave on 1959 at the annual meeting of the American Physical Society, entitled *"There's plenty of room at the bottom"*,[55] elegantly suggesting the idea that multitude of possibilities would arise from the science at the small scale and that in decades to come, it might be possible to arrange atoms *"the way we want"*.[56]

The invention and development of the scanning tunneling microscope (STM) in 1981 and the subsequent number of tools collectively called scanning probe microscopy (SPM) such as atomic force microscopy (AFM), together with the improvement of transmission electron microscopy (TEM), scanning electron microscopy (SEM) and analytical techniques such as mass spectrometry opened up new possibilities for the characterization, measurement and manipulation of nanostructures.[57] In parallel, the higher capacity of computers enabled the theoretical study (simulations) of the behavior

of matter at the nanoscale, which is of absolute importance for both basic understanding and predictions of unreported phenomena.

As a consequence of the previous advances and the enrichment of society, the birth of the nanoscience and nanotechnology fields took place in the eighties. Thus, quantum dot research, one of the main areas of NPs, started in 1982 with the realization[58] that the optical and electric properties of small semiconductor particles were heavily dependent on the particle size due to quantum confinement of the charge carriers in small spaces (mentioned in ref.[59], pag. 4).[60] Also, fullerenes (molecule $C_{60}$, a new form of carbon) were discovered in 1985[61] while the discovery of carbon nanotubes took place in 1991.[62] The subsequent sprouting of the field occurred in the nineties while a real triggering off was initiated around the year 2000 (Figure 1).

Nevertheless, despite that many advances are actually current and new scientific insights in the field of nanoscience emerge every day, some commercial applications of NPs have been significant for quite a long time, such as the industrial relevance of nanostructured heterogeneous catalysis[63] or the $TiO_2$ or ZnO NPs contained in sunscreens.[64-66] The spectrum of commercial applications broadens continuously and today NPs have already been incorporated into paints,[67] cosmetics,[68] foods and food-packaging,[69, 70] dentistry,[71] cleaning products,[72] anti-odor clothing,[73] *etc.*[74] Such a rapid and widespread use of NPs in consumer products faces the novel issues of toxicity for humans[75] and environmental impact,[76] which have not been properly tackled. Gaining knowledge and certainty about those aspects is a compulsory challenge for a sustainable nanoscience and nanotechnology.[77-81]

## Current trends in nanoscience

Endeavors towards the nanoscience field ultimately aim to find unprecedented phenomena that shake the pillars of our current scientific knowledge. Also, the eventual goal is to achieve technologies that exert an impact on society. In order to accomplish such *a priori* insurmountable aims, a better understanding of NPs must be achieved first. Thus, the study of matter and its phenomena at the nanoscale, or in other words, the study of nanomaterials, is based on understanding which aspects of matter at the

nanoscale determine its properties, making it different from bulk materials. Such aspects are strongly interconnected and include surface, size, shape, self-assembly and defects. Appendix A describes these general concepts of inorganic NPs comprising a multitude of convenient examples that show the state of the art of the special properties exhibited by nanomaterials. However, prior to the existence of a nanomaterial, there is the key step of its preparation. Synthesis allows the creation of unprecedented materials, possessing thus a huge potential for discovery, for realizing the unreal. A review of the chemical synthetic strategies developed up to date for the preparation of nanostructured inorganic materials can be found in Appendix B. The existing synthetic routes have quite succeeded in attaining control over the size, shape and surface important attributes of NPs. However, control over complex compositions, defects and SA behavior are still a challenge. Hence, new methods of synthesis which allow the exploration of those features are much needed.

### *The present thesis*

The main motivation of the present thesis is the development of new chemical methods for the synthesis of nanostructured functional materials, so the thesis is framed within the nanochemistry sub-discipline of nanoscience according to the definition by Cademartiri and Ozin: *"nanochemistry is a branch of chemistry dealing with the synthesis and self-assembly of building blocks with a combination of surface, size-, shape-, and defect-dependent properties, and their possible use in chemical and physical, materials science and engineering and biological and medical applications"*.[15]

The target materials present an inorganic nature and they were selected with a variety of both compositions and physical properties to show the high versatility of chemistry for the achievement of a broad spectrum of nanostructured functional materials with tailored features. Three main compounds have been prepared and thoroughly studied: $BaMnO_3$, a ternary oxide with perovskite structure, $Ni_{core}$-$NiO_{shell}$ NPs exhibiting structural disorder and EB effects and hierarchical star-like PbS microstructures formed through the NPs SA.

The first block –chapter 1– deals with the synthesis of nanooxides in highly alkali medium. In chapter 1.1 the hydrothermal synthesis of NCs of $BaMnO_3$, a ternary manganese oxide with perovskite structure ("manganites"), is described. The challenge in this case was to avoid the segregation of phases due to the differences in the rate of reaction of the two metals. Also, it faced the problem of the tendency of alkaline earth metals (Ba in this case) to form carbonates which would contaminate the target product. On the basis of numerous previous works reporting on i) the hydrothermal synthesis of NCs of binary oxides[82] and ii) the hydrothermal preparation of manganite microcrystals,[83-92] hydrothermal method was thought to potentially be a pathway for the successful synthesis of manganite NCs; since the composition appeared to be achievable one just should find the suitable conditions for the formation and stabilization of nano-sized crystals. In this sense, three works positively pointed towards that hypothesis. They dealt with the hydrothermal synthesis in alkaline medium of $Ln_{1-x}A_xMnO_3$ (Ln = La, Pr; A = Ca, Sr, Ba) NWs of 30-150 nm diameter and tens of micrometers length,[93-97] nanometer-sized cubes of 50-100 nm diameter[98] and sub-micron cubes of 100-450 nm,[99] but a clear establishment of the variables affecting the shape and size of the products lacked. In all the cases, a highly ionic medium through high KOH concentrations seemed to play a crucial role. Thus, Chapter 1.1 focuses on the thoroughly study of the variables of hydrothermal alkali method and describes the size-controlled synthesis of $BaMnO_3$ NCs. Chapters 1.2 and 1.3 tackle the synthesis of nanooxides by a related pathway, based on the use of highly ionic melted NaOH/KOH eutectic mixture.[100, 101] While unsuccessful attempts to prepare $BaMnO_3$, $SrMnO_3$ and $CaMnO_3$ NCs are described in chapter 1.2, the successful synthesis of NiO nanooctahedra is reported in chapter 1.3.

The second block –chapter 2– addresses the synthesis of nano-sized oxides and metals via a urea melted medium. Several points inspired the design of this synthetic route. First, molten salt synthesis is a classical approach for the preparation of inorganic materials.[102, 103] The advantage of such a solvent lies in its high ionic strength, which allows the homogeneous dissolution of precursors and promotes the reactivity of ions composing the precipitated product, although the typical high melting temperatures of conventional molten salts such as carbonates[104, 105] or NaCl[106-108] hamper the stabilization of NPs, so microcrystals are obtained instead. The adaptation of that type of route for the synthesis of nanostructured materials requires i) an election of salts with

low melting temperatures[109] and/or ii) the use of the suitable stabilizers. In this sense, the use of molten NaCl at 820 ºC in the presence of nonionic surfactant has improved the stabilization of NPs.[110, 111] A further step is the use of salt mixtures in its eutectic composition, whose melting point is much lower than the corresponding to the individual salts. Thus, eutectic mixtures of nitrates ($T_{melting}$ ~ 550 ºC) in combination with the suitable organic capping agents have yield the isolation of aggregation-free perovskite NPs of 20 nm of size,[112] whereas NaOH/KOH mixture in its deep eutectic composition –$T_{melting}$ = 165 ºC– has allowed the isolation of a number of ligand-free nanostructures of complex oxides.[101] Second and on the other hand, the use of urea in solution has been widely reported for the synthesis of different materials because it provides a gradual basic medium due to the release of $OH^-$ groups upon decomposition.[18, 113] However, its use as a melt ($T_{melting}$ ~ 133 ºC) is mainly restricted to the functionalization of carbon nanotubes;[114] the thermal transformation of metal oxide NPs into metal nitrides;[115] and the synthesis of metal nitride particles[116, 117] and NPs,[118, 119] metal oxynitride NPs,[120] and metal carbides.[119] No previous reports regarding the synthesis of oxides and metals by making use of a urea melt exist. On the basis of the previous experience with the synthesis of nanooxides in highly ionic NaOH/KOH eutectic solvent (chapters 1.2 and 1.3), chapter 2 addresses the evaluation of the suitability of low-temperature urea melt as a basic viscous liquid for the synthesis of nano-sized oxides and metals. Alternatively, the possibility of urea oligomerization during reaction is regarded and an evaluation of the crystallization of NPs upon matrix calcination is undertaken. Quenching of crystallization process by interrupting annealing treatment is tested as a feasible route for the preparation of $Ni_{core}$-$NiO_{shell}$ NPs with high metal/metal oxide interfacial area (chapter 2.1). Additional compositions for the as-prepared nanooxides (*e.g.* $Co_3O_4$ and $Mn_3O_4$) are tested in chapter 2.2.

The third block –chapter 3– of this thesis addresses the synthesis of nanooxides and nanosulfides in urea/choline chloride DES. On the search of novel synthetic routes in this thesis, attempts to improve the synthetic capability of urea melt medium (chapter 2) are done through the formation of DES with choline chloride. Urea/choline chloride mixture[121] in its deep eutectic composition possesses an enhanced polarity as compared with melt urea, which should favor the reactivity of species. Actually, the drastic decrease of the melting point of the mixture stems from the charge delocalization through hydrogen bonding between the halide anion of choline chloride and the

hydrogen of urea, which leads to similar features than those of ILs (high polarity, self-organization, low surface tension, *etc.*), very convenient attributes for nanochemistry. While the synthesis of NPs in "regular" ILs has been widely reported,[122] the exploration of the nano-synthetic capability of (organic) DESs is restricted to limited works published during the development of this thesis.[123] Herein, chapter 3.1 addresses the synthesis of PbS NPs in urea/choline chloride DES, as well as their SA and deconstruction processes, whereas chapter 3.2 broadens the synthetic route to iron oxides ($\gamma$-$Fe_2O_3$ and $\alpha$-$Fe_2O_3$) and manganese oxides ($Mn_3O_4$ and $Mn_2O_3$) NPs.

A colophon closing the circular line of argument throughout this thesis is the prospect that a thin (or perhaps nonexistent) boundary between (inorganic) molten salts and (organic) ILs (including DESs) is depicted.[124]

In regard to the characteristics and properties of the main materials prepared, a full characterization of $BaMnO_3$ NCs regarding their 2H hexagonal perovskite structure, size, shape (NRs and NPs), SA and their magnetic phenomenology are overtaken in chapter 1.1. $Ni_{core}$-$NiO_{shell}$ and NiO NCs are mainly characterized in terms of their core-shell nature and their defect-related peculiarities, respectively. Furthermore, their magnetic phenomenology, in particular the EB effects typical of FM/AFM junctions at the nanoscale, are studied and correlated with their structural features. This is tackled in chapter 2.1. The study of PbS NCs is focused on their cooperative behavior leading to the formation of hierarchical star-like microcrystals. Both SA and deconstruction processes are addressed in chapter 3.1.

II. Introduction

# INTRODUCCIÓN

La nanociencia y la nanotecnología están al frente de la investigación científica hoy en día. Esto queda patente en el gran número de iniciativas y cantidad de financiación destinadas a promover su estudio alrededor del mundo, así como en la gran cantidad de producción generada. En este sentido, el número de publicaciones sobre NPs producidas en 2009 es alrededor de 10-15 veces mayor que el de nueve años atrás (Figura 1) y es ampliamente aceptado que continuará creciendo en el futuro inmediato. De hecho, se han generado mucha expectación hacia la nanociencia y nanotecnología como fuentes de la próxima revolución científico-técnica.

Este campo científico puede impactar en la sociedad por medio de los materiales funcionales, los cuales exhiben ciertas propiedades bajo determinados estímulos, desempeñando así acciones inteligentes y controladas. En la actualidad los materiales funcionales son ubicuos, desde la energía, la salud, las comunicaciones o la información, y, en global, juegan un papel destacado en la calidad de vida y la riqueza de la sociedad. Hoy en día, el área más dinámica en la búsqueda de materiales funcionales es la nanociencia[1-12] debido a las propiedades (magnéticas, ópticas, eléctricas, optoelectrónicas, mecánicas, térmicas, catalíticas, *etc.*) nuevas y frecuentemente inesperadas en comparación con los correspondientes materiales masivos. Es más, tales propiedades dependen de muchos factores (tales como el tamaño), de manera que pueden manipularse un amplio rango de condiciones para el diseño de nuevos materiales que den respuesta a los retos a los que se enfrenta actualmente el mundo.

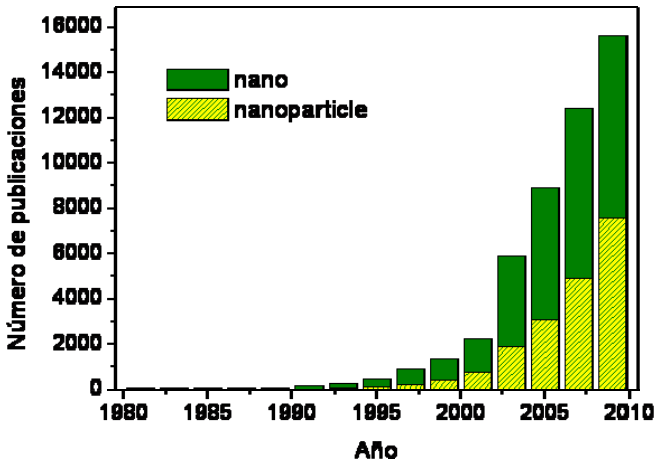


**Figura 1.** Número de publicaciones anuales que contienen los términos "nano" y "nanoparticles". Fuente: Web of Science.

Un ejemplo popular es la microelectrónica, la cual ha mostrado una tendencia continuada hacia la reducción del tamaño de sus dispositivos, siguiendo la observación y predicción de Moore de que el número de transistores por pulgada cuadrada en circuitos integrados se duplicaba cada 1.5 a 2 años y lo seguiría haciendo en el futuro cercano. Esto ha sido posible gracias a la habilidad de manipular la materia en dimensiones cada vez menores, alcanzando el actual régimen nanométrico,[13] y no sólo se ha traducido en dimensiones reducidas, sino también en un mejor funcionamiento y en menores costes de un gran número de dispositivos como los ordenadores.

Al principio, el término nanociencia se definió como la síntesis, la manipulación y el estudio de objetos en la escala nanométrica y un acuerdo tácito fijaba el umbral en estructuras con al menos una dimensión con tamaño comprendido entre 1 y 100 nm (aproximadamente 10 a 1000 átomos; 1 nanómetro es $10^{-9}$ metros); *i.e.* NPs.[13,14] Sin embargo, consideraciones más modernas sostienen que dicha definición es arbitraria y no incluye la multidimensionalidad de la fenomenología subyacente.[15,16] Así, la definición basada sólo en una longitud escalar, tanto si el máximo son 100 o 1000 nm, es demasiado rígida y carece de complejidad y precisión. Por ejemplo, el confinamiento cuántico puede darse a tamaños máximos muy variados (5 nm para el CdSe y 40 nm para el PbSe) dependiendo del material; las fuerzas capilares, las cuales son cruciales para el AE a la nanoescala, actúan a lo largo de distancias largas; y los nanohuecos, desde los cero a los tridimensionales (0D, 3D) ofrecen incontables posibilidades para la nanotecnología, desde las nanocápsulas que transportan drogas pasando por los sensores o los materiales de almacenamiento de hidrógeno. En lo que parece estar de acuerdo la comunidad científica es en la idea de que la nanociencia –"la ciencia a la nanoescala"– difumina las fronteras de las disciplinas clásicas, tales como la química, la física, la biología, la ingeniería y la medicina.

## Las nanopartículas en la naturaleza y a lo largo de la historia de la humanidad

Los nanomateriales son tan naturales como el ser humano y los seres humanos prepararon y manufacturaron nanomateriales desde tiempos inmemorables en La Tierra. Respecto a su aparición medioambiental, materiales nanoparticulados (*i.e.* materia con tamaño de partícula entre 1 y 1000 nm) tales como nanotubos de carbono aparecen en el

hollín (y, por tanto, en la atmósfera) como resultado de procesos de combustión naturales y antropogénicos de fuentes naturales como madera o combustibles fósiles.[17] Análogamente, la ceniza volcánica y el polvo interestelar son materia dividida en la escala nanométrica (mencionado en [18]). La bruma (mencionado en [18]) y minerales basados en sílice como los asbestos[17] son ejemplos adicionales. Por otro lado, las NPs también se encuentran formando parte de la estructura de rocas como la pizarra (la cual contiene NPs octaédricas de sulfuro de hierro)[18] y en minerales como el grupo de arcillas de los filosilicatos (los cuales constan de láminas de silicato 2D nanométricas) y en zeolitas (las cuales poseen un armazón aluminosilicato 3D con poros periódicos en la nano/microescala). Los ópalos son un ejemplo vistoso de coloides organizados; se trata de gemas formadas por partículas esféricas y monodispersas de sílice ($SiO_2$) ordenadas de forma periódica en nanoestructuras ópticas.[19] El mismo tipo de armazón estructural periódico –llamado cristal fotónico– es también responsable del color de las alas de pavos reales[20] y mariposas;[21] el color es debido a la difracción de los fonones dentro de la estructura, compuesta de una proteína de quitina en este caso.[15] La quitina, un polímero de cadena larga de N-acetilglucosamina, es un componente orgánico habitual de materiales híbridos a la nano/microescala y forma junto con la sílice los exoesqueletos de artrópodos, así como los esqueletos del protozoo radiolaria y la alga unicelular diatomea.[22,23] En los últimos casos, el estético diseño perforado proporciona a la microestructura una funcionalidad avanzada al hacer un uso económico de la sílice, que dota de ligereza a un material denso, y al constituir un mecanismo de filtración para el agua y los nutrientes. El nácar es otro nanomaterial compuesto y es producido por algunos moluscos en forma de concha interna y también en forma de perlas. Compuesto en un 95 % de un frágil carbonato cálcico en forma de placas y un ~5 % de biopolímeros, es el doble de duro y más de 1000 veces más resistente que sus constituyentes, lo cual redunda en unas propiedades mecánicas excepcionales.[24] La cáscara de huevo también es un material avanzado formado por una matriz proteica y nanocristales de carbonato cálcico entremezclados de tal modo que la estructura resultante es dura y protege el interior de agresiones externas a la par que permite una excelente permeabilidad de gas y agua para el desarrollo del embrión aviar.[25] Respecto a los endoesqueletos de vertebrados, los huesos están compuestos principalmente de un entramado de hidroxiapatita y colágeno en la nanoescala y sus funciones son motoras, de soporte y de protección de los órganos y de producción de células y almacenamiento de minerales.[26,27] Las nanoestructuras orgánicas presentes en la naturaleza también

muestran funcionalidades avanzadas, como por ejemplo la alta fuerza de tensión (superior a la del acero) y la gran extensibilidad de la seda de araña, propiedades provenientes de un efecto de nanoconfinamiento en el cual los cristales de proteína posibilitan un uso muy eficiente de los enlaces de hidrógeno.[28] Otros ejemplos de propiedades superiores en nanoestructuras orgánicas se encuentran en las hojas de la flor de loto, que son superhidrofóbicas,[29] y las almohadillas de las patas de lagartija, que son superadherentes.[30] En este último caso, los millones de "pelos" de cada dedo se dividen en la punta en billones de nanoespátulas, permitiendo un cambio rápido por medio de fuerzas de van der Waals entre los estados de fuerte adhesión/fricción (pegado) y de adhesión/fricción nulas (despegado).

Por otro lado, todos los sistemas biológicos presentan el rasgo fascinante de construir sus componentes estructurales orgánicos, como los microtúbulos, los microfilamentos y la cromatina, en la nanoescala.[31] Además, una propiedad clave de los organismos vivos es el reconocimiento molecular que conduce al auto-ensamblado, por medio del cual los nanoelementos constituyentes se organizan autónomamente en estructuras complejas y funcionalmente sofisticadas (veáse, por ejemplo, la alta eficiencia en la producción y almacenamiento de energía de la fotosíntesis, la capacidad del cerebro humano para almacenar y procesar información, o, en global, el diseño inteligente de los organismos vivos, con habilidad para reproducirse a partir del ADN, la macromolécula básica de almacenamiento de información). A la hora de conseguir materiales funcionales superiores, sería muy deseable el conocer más a fondo las vías que posee la naturaleza para producir y manufacturar materiales en la nanoescala.

En lo que concierne a la producción de NPs inorgánicas, algunos sistemas vivos se comportan como "nanofábricas".[32,33] De este modo, levaduras,[34,36] bacterias,[35] hongos,[38,39,41] virus y plantas[40] producen tanto intra como extracelularmente NPs monodispersas de distinta naturaleza, desde semiconductores[34-36] a óxidos (magnéticos,[37] ferroeléctricos,[38] *etc.*) y metales.[39-41] Dichas estrategias sintéticas pertenecen a la aproximación "de abajo a arriba", en la cual átomos/moléculas individuales se combinan para formar una entidad de mayor tamaño.

Sin embargo, en la naturaleza también se da la aproximación contraria, "de abajo a arriba", que consiste en la destrucción controlada de un sólido masivo esculpiendo

nanoesculturas. La erosión de las rocas no se debe exclusivamente a una "geomolienda" o acción mecánica desempeñada por cambios de temperatura, erosión del viento, congelado y descongelado, extracción por el agua de la lluvia y nieve, sino también por la actividad microbiana. Este último proceso, que ocurre lentamente en la naturaleza, se ha acelerado en el laboratorio, abriendo el camino a la "biomolienda"; por ejemplo, cierto hongo produce la ruptura de nanoplacas (~150-200 nm) de óxido de bismuto en NPs de tamaño < 10 nm.[42,43]

Por consiguiente, en la naturaleza existen una multitud de ejemplos de mecanismos de formación de NPs en los que los humanos pueden inspirarse. En este sentido, aunque por medio de la observación y de experimentos de ensayo y error, los seres humanos desarrollaron desde la antigüedad metodologías de síntesis química de NPs inorgánicas. Probablemente, uno de los ejemplos más antiguos identificados es el maquillaje en el antiguo Egipto, que data al menos del 1000-2000 a.C., y que estaba formado por polvos finos de compuestos de plomo[44] y hematina (mencionado en la ref.[17]). Asimismo, recientemente se ha identificado que NCs de PbS –actualmente un "favorito" de la nanociencia– de ~ 5 nm eran un agente corriente para el teñido del cabello y de la lana desde los tiempos Greco-romanos hasta la época actual, incluyendo reseñas árabes del período medieval, el Renacimiento, la química moderna y actual (mencionado en [45]).[45] En estos casos, la fórmula sintética consiste en la formación de una pasta a base de óxido de plomo (PbO), cal ($Ca(OH)_2$) y agua que se aplica en el pelo repetidamente dando lugar al color negro. La formación irreversible de NPs de PbS es en última instancia la responsable del color negro y se logra mediante la reacción de iones $Pb^{2+}$ con los aminoácidos sulfurados del pelo y la matriz proteica podría servir como un reactor a la nanoescala. Las propiedades mecánicas del pelo no se ven afectadas debido al pequeño tamaño de los cristales.

Algunos ejemplos adicionales del antiguo uso de los nanomateriales se remonta al menos al año ~ 2000 a.C. en Egipto y China, donde las tintas contenían negro de carbón y NPs de $TiO_2$, o al año ~ 500 a.C., cuando los fenicios ya conocían el uso antibactericida de las NPs de plata (mencionado en ref.[17]). También se ha visto que el acero de Damasco (1100-1700 d.C.) contiene NPs.[46]

Otro ejemplo ilustrativo es el teñido del vidrio y la porcelana con soluciones coloidales de oro –también otro "favorito" de la nanociencia–, lo que ya se conocía en China desde hace más de mil años (mencionado en [3, 15]) y en el período Greco-romano tardío[47, 48] y que ha encontrado amplio uso en las fábricas de teñido de vidrio y porcelana desde el siglo decimoctavo. La variedad de colores proviene de la resonancia del plasmón correspondiente a distintos diámetros (1-50 nm) de las NPs de oro.

La preparación intencionada de oro coloidal se remonta al año 1665, cuando Andreas Cassius y su hijo prepararon a partir de precursores de oro el Púrpura de Cassius, al cual se le atribuyeron cualidades medicinales –el elixir de la vida– (mencionado en [49]). Sin embargo, no es hasta 1857 cuando se produce el nacimiento de la química coloidal moderna de la mano de Michael Faraday,[47] quien trabajó en la preparación de coloides metálicos y en el estudio de las relaciones entre la materia y la fenomenología eléctrica, magnética y óptica.[49] Sus pioneras observaciones le condujeron a afirmar que el color de las disoluciones transparentes provenía de partículas que son *"muy diminutas en sus dimensiones. … La fenomenología conocida parecía indicar que una mera variación del tamaño de las partículas daba lugar a una variedad de colores resultantes"*. No obstante, tuvo que pasar un siglo hasta que el término coloide fue acuñado (por Thomas Graham, 1861).[50] Marian Smoluchowsky, Richard Zsigmondy y Wilhelm y Wolfgang Ostwald fueron subsiguientes pioneros de la ciencia coloidal (mencionado en ref. [49]).[51-53] El último, en 1915 tituló su inmortal libro sobre química coloidal "El Mundo de las Dimensiones Despreciadas", dando a entender que ésta era una ciencia en sí misma.[54]

## El nacimiento de la nanociencia

Los ejemplos citados son ilustrativos de que la investigación en la escala nanométrica no es nueva hoy en día. Lo que es nuevo, sin embargo, es tanto la disponibilidad de técnicas para visualizar, caracterizar y manipular sistemas en la escala nanométrica, así como nuestro conocimiento de las interacciones atómicas. Así, por ejemplo, la excelencia y el prodigioso mérito del trabajo de Faraday probablemente fuera acompañado con un toque de decepción debido a la falta de capacidad para "ver"

directamente las partículas: *"El estado de división de estas partículas debe de ser extremo; no se han conseguido ver con ninguna potencia de los microscopios"*.

De este modo, durante un tiempo se sucedieron nuevas profecías, como la visionaria charla que el físico Richard Feynman dio en 1959 en el encuentro anual de la *American Physical Society*, titulada *"En el fondo hay espacio de sobra"*,[55] que de forma elegante sugería la idea de que una multitud de posibilidades surgirían de la ciencia en la pequeña escala y que en las décadas siguientes sería posible ordenar los átomos *"a voluntad"*.[56]

La invención y desarrollo de la microscopía de efecto túnel (STM) en 1981 y la subsiguiente cantidad de técnicas colectivamente llamadas microscopía de sonda de barrido (SPM), tales como la microscopía de fuerza atómica (AFM), junto con la mejora de las microscopías electrónicas de transmisión (TEM) y barrido (SEM) y de las técnicas analíticas, como la espectrometría de masas, abrieron nuevas posibilidades para la caracterización, medida y manipulación de las nanoestructuras.[57] De forma paralela, la creciente capacidad computacional permitió el estudio teórico (simulaciones) del comportamiento de la materia a la nanoescala, lo cual es de absoluta importancia para su comprensión fundamental y para predecir fenómenos no observados experimentalmente.

Como consecuencia de dichos avances y del enriquecimiento de la sociedad, el nacimiento de los campos de la nanociencia y la nanotecnología tuvo lugar en los años ochenta. De este modo, la investigación en los *quantum dots*, una de las principales áreas de las NPs, surgió en el año 1982 con la observación[58] de que las propiedades ópticas y eléctricas de pequeñas partículas de semiconductores eran fuertemente dependientes del tamaño de partícula, lo que se debía al confinamiento cuántico de los portadores de carga en pequeños espacios (mencionado en ref.[59], pag.4).[60] Además, los fulerenos (la molécula $C_{60}$, una nueva forma del carbono) fueron descubiertos en el año 1985,[61] mientras que el descubrimiento de los nanotubos de carbono tuvo lugar en el año 1991.[62] El crecimiento de este campo ocurrió en los años noventa, mientras que el despegue definitivo se inició alrededor del año 2000 (Figura 1).

No obstante, a pesar de la actualidad de muchos de los avances y de que cada día emergen nuevos aspectos en el campo de la nanociencia, existen desde hace bastante tiempo significativas aplicaciones comerciales de las NPs. Baste mencionar, por ejemplo, la gran relevancia industrial de catalizadores heterogéneos nanoestructurados[63] o las NPs de $TiO_2$ o ZnO en las cremas solares.[64-66] El espectro de aplicaciones comerciales se amplía continuamente y hoy en día las NPs han sido incorporadas a las pinturas,[67] los cosméticos,[68] la comida y su empaquetado,[69,70] la odontología,[71] los productos de limpieza,[72] la ropa anti-olor,[73], *etc.*[74] El empleo tan rápido y extendido de las NPs en los productos de consumo se enfrenta a nuevos problemas de toxicidad para los humanos[75] y de impacto medioambiental,[76] los cuales no han sido abordados adecuadamente. El mayor conocimiento de dichos aspectos es un reto obligatorio para unas nanociencia y nanotecnología sostenibles.[77-81]

## Tendencias actuales en nanociencia

Todo esfuerzo hacia el campo de la nanociencia apunta hacia el descubrimiento de fenómenos sin precedente que hagan tambalear los pilares de nuestro actual conocimiento científico. Asimismo, la meta final es el la generación de nuevas tecnologías de impacto. Para lograr tales fines *a priori* insalvables, primero se debe profundizar en el conocimiento de las NPs. Así, el estudio de la materia y su fenomenología a la nanoescala, o, en otras palabras, el estudio de los nanomateriales, se basa en entender cómo y qué aspectos de la materia a la nanoescala determinan sus propiedades, diferenciándola de los materiales masivos. Tales aspectos se encuentran íntimamente interconectados e incluyen la superficie, el tamaño, la forma, el auto-ensamblado y los defectos. El anexo A describe dichos conceptos generales de las NPs inorgánicas, incluyendo una multitud de ejemplos que muestran de manera conveniente el estado del arte de las propiedades especiales que muestran los nanomateriales. Sin embargo, el paso previo y crucial para que exista un nanomaterial es su preparación. La síntesis posibilita la creación de materiales sin precedente, poseyendo así un gran potencial para el descubrimiento, para hacer real lo irreal. El anexo B resume las estrategias de síntesis químicas desarrolladas hasta la fecha para la preparación de materiales inorgánicos nanoestructurados. Las rutas sintéticas existentes han conseguido un alto control del tamaño, la forma y la superficie de las NPs. Sin embargo, el control

de composiciones complejas, defectos y AE es aún un reto. Por consiguiente, se precisan nuevos métodos de síntesis que permitan la exploración de dichas características de las NPs.

### *La presente tesis*

La principal motivación de esta tesis es el desarrollo de nuevos métodos químicos de síntesis de materiales funcionales nanoestructurados, de manera que la tesis se enmarca dentro de la sub-disciplina de la nanociencia llamada nanoquímica, que Cademartiri y Ozin definen de la siguiente manera: *"la nanoquímica es una rama de la química que se ocupa de la síntesis y auto-ensamblado de unidades elementales con una combinación de propiedades dependientes de la superficie, el tamaño, la forma y los defectos, y su posible uso en aplicaciones químicas, físicas, de la ciencia e ingeniería de materiales, biológicas y médicas".*[15]

Los materiales objeto de estudio son de naturaleza inorgánica y fueron seleccionados con composiciones y propiedades físicas variadas para mostrar la gran versatilidad de la química para la preparación de un amplio espectro de materiales funcionales nanoestructurados con características controladas. Se han preparado y estudiado a fondo tres compuestos principales: el $BaMnO_3$, un óxido ternario con estructura perovskita, NPs $Ni_{núcleo}$-$NiO_{cáscara}$ que presentan desorden estructural y EB y microestructuras de PbS con forma de estrella formadas mediante AE de NPs.

El primer bloque –capítulo 1– trata de la síntesis de nanoóxidos en medios altamente alcalinos. En el capítulo 1.1 se describe la síntesis hidrotermal de NCs de $BaMnO_3$, un óxido ternario de manganeso con estructura perovskita hexagonal tipo 2H. En este caso el reto era evitar la segregación de fases debido a diferencias de reactividad de los dos metales. Asimismo, se encaraba el problema de la gran tendencia de los metales alcalinotérreos (Ba en este caso) a formar carbonatos que contaminarían el producto deseado. En base a numerosos trabajos previos que reportaban i) la síntesis hidrotermal de NCs de óxidos binarios[82] y ii) la preparación hidrotermal de microcristales de manganita,[83-92] se pensó que el método hidrotermal podría potencialmente ser una ruta de síntesis de NCs de manganita; ya que la composición

parecía ser alcanzable, sólo se debían de encontrar las condiciones adecuadas para la formación y estabilización de cristales nanométricos. En este sentido, tres trabajos apuntaban positivamente hacia esta hipótesis. En ellos, se describía la síntesis hidrotermal en medio alcalino de $Ln_{1-x}A_xMnO_3$ (Ln = La, Pr; A = Ca, Sr, Ba) en forma de NWs (30-150 nm de diámetro y decenas micrómetros de longitud),[93-97] nanocubos de 50-100 nm[98] y sub-microcubos de 100-450 nm.[99] Sin embargo, quedaba patente que era necesario un establecimiento de las variables que afectaban a la forma y el tamaño de los productos. En todos estos casos, parecía que el medio altamente alcalino alcanzado mediante el uso de altas concentraciones de KOH jugaba un papel fundamental. Así, el capítulo 1.1 se centra en un estudio pormenorizado de las variables del método hidrotermal alcalino y describe la síntesis de NCs de $BaMnO_3$ con tamaños controlados. Los capítulos 1.2 y 1.3 abordan la síntesis de nanoóxidos por una vía relacionada, basada en el uso de un medio altamente iónico, en concreto la mezcla eutéctica NaOH/KOH:[100,101] el capítulo 1.2 describe intentos fallidos de preparar NCs de $BaMnO_3$, $SrMnO_3$ y $CaMnO_3$, y el capítulo 1.3 reporta la síntesis de nanooctaedros de NiO.

El segundo bloque –el capítulo 2– trata la síntesis de óxidos y metales nanométricos mediante un medio de urea fundida. Varios aspectos inspiraron el diseño de esta ruta sintética. En primer lugar, la síntesis en sales fundidas es una aproximación clásica para la preparación de materiales inorgánicos.[102, 103] La ventaja de este tipo de fluidos reside en su alta fuerza iónica, que permite la disolución homogénea de precursores y favorece la reactividad de los iones. Sin embargo, las altas temperaturas de fusión de las sales fundidas convencionales, tales como carbonatos[104,105] y NaCl,[106-108] impiden la estabilización de NPs, obteniéndose microcristales. La adaptación de ese tipo de rutas para la síntesis de materiales nanoestructurados requiere i) una elección de sales con bajas temperaturas de fusión[109] y/o ii) el uso de surfactantes. En este sentido, el empleo de NaCl fundido a 820 ºC en presencia de surfactantes no iónicos ha mejorado la estabilización de NPs.[110,111] Un paso más allá es el empleo de mezclas de sales en su composición eutéctica, cuyo punto de fusión es mucho menor que el de las correspondientes sales individuales. De esta forma, mezclas eutécticas de nitratos ($T_{fusión}$ ~ 550 ºC) en combinación con *ligandos* orgánicos han conducido a la obtención de NPs de perovskita no agregadas con tamaño de 20 nm,[112] mientras que la mezcla eutéctica NaOH/KOH –$T_{fusión}$ = 165 ºC– ha permitido la obtención de un gran número de

nanoóxidos de composición compleja y sin ligandos.[101] En segundo lugar y por otro lado, el empleo de urea en disolución es ampliamente conocido para la síntesis de distintos materiales ya que al descomponerse libera grupos $OH^-$, proporcionando un medio básico.[18,113] Sin embargo, su uso como fundido ($T_{fusión}$ ~ 133 ºC) se encuentra restringido a la funcionalización de nanotubos de carbono;[114] la transformación térmica de NPs de óxidos metálicos en nitruros metálicos;[115] y la síntesis de nitruros metálicos en forma de particulas[116,117] y NPs,[118,119] de NPs de oxinitruros,[120] y de carburos metálicos.[119] El fundido de urea no había sido empleado con anterioridad para la síntesis de óxidos y metales. En base a nuestra experiencia previa en la síntesis de nanoóxidos en medio eutéctico NaOH/KOH altamente alcalino (capítulos 1.2 y 1.3), el capítulo 2 evalúa la adecuación del fundido de urea de baja temperatura como medio líquido viscoso y básico para la síntesis de óxidos y metales nanoparticulados. Alternativamente, se evalúa la posibilidad de que la urea oligomerice durante la reacción y se lleva a cabo el estudio de la cristalización de NPs al calcinar la matriz. Se analiza la viabilidad de la ruta para la preparación de NPs de $Ni_{núcleo}$-$NiO_{cáscara}$ con alta área metal/óxido metálico mediante el "congelado" del proceso de cristalización al interrumpir el tratamiento de calentamiento (capítulo 2.1). Se examinan también composiciones alternativas de los nanoóxidos (*e.g.* $Co_3O_4$ y $Mn_3O_4$) (capítulo 2.2).

El tercer bloque –capítulo 3– de esta tesis trata la síntesis de nanoóxidos y nanosulfuros en un medio DES urea/cloruro de colina. En la búsqueda de nuevas rutas de síntesis, se hicieron intentos de mejorar la capacidad sintética del fundido de urea (capítulo 2) mediante la formación de un DES con cloruro de colina. La mezcla urea/cloruro de colina[121] en su composición de eutéctico profundo posee una polaridad mayor que la de la urea fundida, lo que debería favorecer la reactividad de las especies. De hecho, el gran descenso del punto de fusión de la mezcla proviene de la deslocalización de la carga a través de enlaces de hidrógeno entre el anión cloruro de la colina y los hidrógenos de la urea, lo que conduce a características similares que las de los LIs (alta polaridad, auto-organización, baja tensión superficial, *etc*.), atributos muy convenientes para la nanoquímica. Mientras que la síntesis de NPs en LIs "convencionales" ha sido ampliamente tratada,[122] el estudio de la habilidad sintética de DESs orgánicos se limita a un número reducido de trabajos publicados durante el desarrollo de esta tesis.[123] En esta tesis, el capítulo 3.1 aborda la síntesis de NPs de PbS en el DES urea/cloruro de colina, así como sus procesos de AE y deconstrucción,

mientras que el capítulo 3.2 extiende la aplicabilidad de la ruta a la síntesis de nanoóxidos de hierro ($\gamma$-$Fe_2O_3$ and $\alpha$-$Fe_2O_3$) y manganeso ($Mn_3O_4$ and $Mn_2O_3$).

Como colofón que cierra la línea argumental circular de esta tesis se vislumbra una delgada (o quizás inexistente) frontera entre las sales fundidas (inorgánicas) y los LIs (orgánicos), incluyendo los DESs.[124]

En cuanto a las características y propiedades de los principales materiales obtenidos, el capítulo 1.1 recoge una completa caracterización de los NCs de $BaMnO_3$ en cuanto a su estructura perovskita hexagonal 2H, tamaño, forma (NRs y NPs), AE y fenomenología magnética. Los NCs de $Ni_{núcleo}$-$NiO_{cáscara}$ y NiO se caracterizaron fundamentalmente en términos de su naturaleza núcleo-cáscara y peculiaridades relacionadas con los defectos, respectivamente. Además, se estudió su fenomenología magnética, en particular los efectos de EB típicos de juntas FM/AFM a la nanoescala, y se correlacionó con sus características estructurales. Esto es abordado en el capítulo 2.1. El estudio de NCs de PbS está enfocado hacia su comportamiento cooperativo, conducente a la formación de microcristales jerárquicos con forma de estrella. El capítulo 3.1 recoge los correspondientes procesos de AE y deconstrucción.

# BIBLIOGRAPHY / BIBLIOGRAFÍA


1. Liz-Marzán, L. M. and Kamat, P. V. *Nanoscale Materials*. Kluwer Academic Pusblishers: **2003**.
2. Tjong, S. C., *Nanocrystalline Materials*. Elsevier: **2006**.
3. Cao, G., *Nanostructures & Nanomaterials*. Imperial College Press: **2004**.
4. Schmid, G., *Nanoparticles*. Wiley-VCH: **2004**.
5. Rotello, V. M., *Nanoparticles: building blocks for nanotechnology* **2004.**
6. Vilarinho, P. M.; Rosenwaks, Y. and Kingon, A. (Eds.), *Scanning Probe Microscopy: Characterization, Nanofabrication and Device Application of Functional Materials*. NATO Science Series: **2002**.
7. Liz-Marzán, L. M. and Norris, D. J. (Guest Eds.), New aspects of nanocrystal research. *MRS Bulletin* **2001,** 26, (12), 981-1019.
8. Goesmann, H.; Feldmann, C., Nanoparticulate functional materials. *Angewandte Chemie - International Edition* **2010,** 49, (8), 1362-1395.
9. Stupp, S. I., Introduction: Functional nanostructures. *Chemical Reviews* **2005,** 105, (4), 1023-1024.
10. Kotov, N. A.; Stellacci, F., Frontiers in nanoparticle research: Toward greater complexity of structure and function of nanomaterials. *Advanced Materials* **2008,** 20, (22), 4221-4222.
11. Tang, Z. and Sheng, P., *Nano Science and Technology*. Taylor & Francis Inc.: **2003**.
12. Lindsay, S. M., *Introduction to Nanoscience*. Oxford University Press: **2010**.
13. Pradeep, T., *Nano: The Essentials*. Tata McGraw-Hill: **2007**.
14. Ozin, G. A., Nanochemistry: Synthesis in diminishing dimensions. *Advanced Materials* **1992,** 4, (10), 612-649.
15. Cademartiri, L. and Ozin, G.A., *Concepts of Nanochemistry*. Wiley-VCH: **2009**.
16. Tomalia, D. A., In quest of a systematic framework for unifying and defining nanoscience. *Journal of Nanoparticle Research* **2009,** 11, (6), 1251-1310.
17. Murr, L. E., Nanoparticulate materials in antiquity: The good, the bad and the ugly. *Materials Characterization* **2009,** 60, (4), 261-270.
18. Matijevic, E., Preparation and properties of uniform size colloids. *Chemistry of Materials* **1993,** 5, (4), 412-426.
19. Sanders, J. V., Colour of precious opal. *Nature* **1964,** 204, (4964), 1151-1153.
20. Heeso, N.; Seng Fatt, L.; Vinodkumar, S.; Simon, G. J. M.; Richard, O. P.; Eric, R. D.; Hui, C., How Noniridescent Colors Are Generated by Quasi-ordered Structures of Bird Feathers. *Advanced Materials* **2010,** in press.
21. Kolle, M.; Salgard-Cunha, P. M.; Scherer, M. R. J.; Huang, F.; Vukusic, P.; Mahajan, S.; Baumberg, J. J.; Steiner, U., Mimicking the colourful wing scale structure of the Papilio blumei butterfly. *Nat Nano* **2010,** 5, (7), 511-515.
22. http://www.microscopy-uk.org.uk/mag/indexmag.html?http://www.microscopy-uk.org.uk/mag/artfeb05/cbdiatoms.html.
23. http://en.wikipedia.org/wiki/Radiolaria.
24. Smith, B. L.; Schöffer, T. E.; Vlani, M.; Thompson, J. B.; Frederick, N. A.; Klndt, J.; Belcher, A.; Stuckyll, G. D.; Morse, D. E.; Hansma, P. K., Molecular mechanistic origin of the toughness of natural adhesives, fibres and composites. *Nature* **1999,** 399, (6738), 761-763.
25. Behrens, P. and Baeuerlein, E. (Eds.), *Handbook of Biomineralization* Wiley-VCH **2007**.
26. Epple, M. and Baeuerlein, E. (Eds.), *Handbook of Biomineralization*. Wiley-VCH: **2007**.
27. Currey, J. D., Mechanical properties of bone tissues with greatly differing functions. *Journal of Biomechanics* **1979,** 12, (4), 313-319.
28. Keten, S.; Xu, Z.; Ihle, B.; Buehler, M. J., Nanoconfinement controls stiffness, strength and mechanical toughness of δ-sheet crystals in silk. *Nature Materials* **2010,** 9, (4), 359-367.
29. Lei, J.; Yong, Z.; Jin, Z., A Lotus-Leaf-like Superhydrophobic Surface: A Porous Microsphere/Nanofiber Composite Film Prepared by Electrohydrodynamics13. *Angewandte Chemie International Edition* **2004,** 43, (33), 4338-4341.
30. Zhao, B.; Pesika, N.; Zeng, H.; Wei, Z.; Chen, Y.; Autumn, K.; Turner, K.; Israelachvili, J., Role of Tilted Adhesion Fibrils (Setae) in the Adhesion and Locomotion of Gecko-like Systemsâ€ *The Journal of Physical Chemistry B* **2008,** 113, (12), 3615-3621.
31. Sackler, A. M., *Nanoscience: Underlying Physical Concepts and Phenomena*. National Academy of Sciences: 2001.
32. Arya, V., Living systems: Eco-friendly nanofactories. *Digest Journal of Nanomaterials and Biostructures* **2010,** 5, (1), 9-21.

33. Narayanan, K. B.; Sakthivel, N., Biological synthesis of metal nanoparticles by microbes. *Advances in Colloid and Interface Science* **2010,** 156, (1-2), 1-13.
34. Dameron, C. T.; Reese, R. N.; Mehra, R. K.; Kortan, A. R.; Carroll, P. J.; Steigerwald, M. L.; Brus, L. E.; Winge, D. R., Biosynthesis of cadmium sulphide quantum semiconductor crystallites. *Nature* **1989,** 338, (6216), 596-597.
35. Sweeney, R. Y.; Mao, C.; Gao, X.; Burt, J. L.; Belcher, A. M.; Georgiou, G.; Iverson, B. L., Bacterial biosynthesis of cadmium sulfide nanocrystals. *Chemistry and Biology* **2004,** 11, (11), 1553-1559.
36. Kowshik, M.; Vogel, W.; Urban, J.; Kulkarni, S. K.; Paknikar, K. M., Microbial synthesis of semiconductor PbS nanocrystallites. *Advanced Materials* **2002,** 14, (11), 815-818.
37. Baeuerlein, E. E., *Handbook of biomineralization*. Wiley-VCH: **2007**.
38. Bansal, V.; Poddar, P.; Ahmad, A.; Sastry, M., Room-temperature biosynthesis of ferroelectric barium titanate nanoparticles. *Journal of the American Chemical Society* **2006,** 128, (36), 11958-11963.
39. Mukherjee, P.; Ahmad, A.; Mandal, D.; Senapati, S.; Sainkar, S. R.; Khan, M. I.; Parishcha, R.; Ajaykumar, P. V.; Alam, M.; Kumar, R.; Sastry, M., Fungus-Mediated Synthesis of Silver Nanoparticles and Their Immobilization in the Mycelial Matrix: A Novel Biological Approach to Nanoparticle Synthesis. *Nano Letters* **2001,** 1, (10), 515-519.
40. Kumar, V.; Yadav, S. K., Plant-mediated synthesis of silver and gold nanoparticles and their applications. *Journal of Chemical Technology and Biotechnology* **2009,** 84, (2), 151-157.
41. Das, S. K.; Das, A. R.; Guha, A. K., Microbial synthesis of multishaped gold nanostructures. *Small* **2010,** 6, (9), 1012-1021.
42. Mazumder, B.; Uddin, I.; Khan, S.; Ravi, V.; Selvraj, K.; Poddar, P.; Ahmad, A., Bio-milling technique for the size reduction of chemically synthesized $BiMnO_3$ nanoplates. *Journal of Materials Chemistry* **2007,** 17, (37), 3910-3914.
43. Mazumder, B.; Uddin, I.; Khan, S.; Ravi, V.; Selvraj, K.; Poddar, P.; Ahmad, A., Erratum: Bio-milling technique for the size reduction of chemically synthesized $BiMnO_3$ nanoplates (Journal of Materials Chemistry (2007) 17 (3910-3914) DOI: 10.1039/b706154d). *Journal of Materials Chemistry* **2008,** 18, (48), 5998.
44. Walter, P.; Martinetto, P.; Tsoucaris, G.; BrÃ©niaux, R.; Lefebvre, M. A.; Richard, G.; Talabot, J.; Dooryhee, E., Making make-up in Ancient Egypt. *Nature* **1999,** 397, (6719), 483-484.
45. Walter, P.; Welcomme, E.; HallÃ©got, P.; Zaluzec, N. J.; Deeb, C.; Castaing, J.; VeyssiÃ¨re, P.; BrÃ©niaux, R.; LÃ©vÃªque, J. L.; Tsoucaris, G., Early use of PbS nanotechnology for an ancient hair dyeing formula. *Nano Letters* **2006,** 6, (10), 2215-2219.
46. Reibold, M.; Pätzke, N.; Levin, A. A.; Kochmann, W.; Shakhverdova, I. P.; Paufler, P.; Meyer, D. C., Structure of several historic blades at nanoscale. *Crystal Research and Technology* **2009,** 44, (10), 1139-1146.
47. Faraday, M., *Philos. Trans. R. Soc. London* **1857,** 147, 145-181.
48. Kerssenbrock-Krosigk, D. v., Rubinglas des ausgehenden 17. und des 18. Jahrhunderts. *Verlag Philipp von Zabern, Mainz* **2001**.
49. Edwards, P. P.; Thomas, J. M., Gold in a metallic divided state - From Faraday to present-day nanoscience. *Angewandte Chemie - International Edition* **2007,** 46, (29), 5480-5486.
50. Graham, T. H., *Philos. Trans. R. Soc. London* **1861,** 151, 183-196.
51. Ostwald, W., *Z. Kolloidchem.* **1910,** 6, (183).
52. Zsigmondy, R. Z., *Kolloidchem.* **1912,** 198, 217.
53. Dörfler, H. D., *Grenzflächen und kolloid-disperse Systeme*. Springer: Berlin, **2001**.
54. Ostwald, W., *Die Welt der vernachlässigten Dimensionen* Steinkopf: Dresden, **1915**.
55. Feynman, R. P., There's plenty of room at the bottom. *California Institute of Technology Journal of Engineering and Science* **1960,** 4, (2), 23-36.
56. Junk, A.; Riess, F., From an idea to a vision: There's plenty of room at the bottom. *American Journal of Physics* **2006,** 74, (9), 825-830.
57. http://nobelprize.org/nobel_prizes/physics/laureates/1986/.
58. Note the enormous merit of Faraday's work, who envisioned the connection between the color and the size of the particles more than a century before without a direct vision of the particles, but "just" through observation and qualitatively study of the optical, electric and magnetic effect of the colloidal solutions. Moreover, Faraday's explorations (including all of his more than 460 papers) were entirely qualitative, without a single equation, due to the fact that he left primary school at 13 years old and knew no algebra. Yet, J. Clerk Maxwell said that Faraday was one of the greatest theoreticians and Einstein declared him to be responsible –together with Clerk Maxwell– for the greatest change in the intellectual framework of physics since Isaac Newton.

59. Kumar, C., *Semiconductor Nanomaterials*. Wiley-VCH: **2010**.
60. Schmid, G.; Pfeil, R.; Boese, R.; Bandermann, F.; Meyer, S.; Calis, G. H. M.; Vandervelden, W. A., $Au_{55}[P(C_6H_5)_3]_{12}Cl_6$ - a Gold Cluster of an Exceptional Size. *Chem. Ber.-Recl.* **1981,** 114, (11), 3634-3642.
61. Kroto, H. W.; Heath, J. R.; O'Brien, S. C.; Curl, R. F.; Smalley, R. E., $C_{60}$: Buckminsterfullerene. *Nature* **1985,** 318, (6042), 162-163.
62. Iijima, S., Helical microtubules of graphitic carbon. *Nature* **1991,** 354, (6348), 56-58.
63. Bell, A. T., The impact of nanoscience on heterogeneous catalysis. *Science* **2003,** 299, (5613), 1688-1691.
64. Newman, M. D.; Stotland, M.; Ellis, J. I., The safety of nanosized particles in titanium dioxide- and zinc oxide-based sunscreens. *Journal of the American Academy of Dermatology* **2009,** 61, (4), 685-692.
65. Osmond, M. J.; McCall, M. J., Zinc oxide nanoparticles in modern sunscreens: An analysis of potential exposure and hazard. *Nanotoxicology* **2010,** 4, (1), 15-41.
66. Barnard, A. S., One-to-one comparison of sunscreen efficacy, aesthetics and potential nanotoxicity. *Nature Nanotechnology* **2010,** 5, (4), 271-274.
67. http://www.tec-star.it/eng/nanoparticles-paints.asp.
68. http://www.foe.org.au/nano-tech/publications/Background%20briefing%20nanoparticles%20in%20cosmetics%20November%20%20%20%20%202009.pdf.
69. Augustin, M. A.; Sanguansri, P., Nanostructured materials in the food industry. *Advances in food and nutrition research* **2009,** 58, 183-213.
70. Sanguansri, P.; Augustin, M. A., Nanoscale materials development - a food industry perspective. *Trends in Food Science and Technology* **2006,** 17, (10), 547-556.
71. Rybachuk, A. V.; Chekman, I.S.; Nebesna, T. Y., Nanotechnology and Nanoparticles in Dentistry. *Pharmacol.Pharmaceutics* **2009,** 616.314 - 085 + 615.01.
72. Nero, M.; Tran, B. In *An investigation of natural nano-particles for cleaning*, 2007 NSTI Nanotechnology Conference and Trade Show - NSTI Nanotech 2007, Technical Proceedings, 2007; **2007**; pp 624-627.
73. Anti-odour clothing: Bringing fresh appeal to the textile and apparel market. *Textile Outlook International* **2009**, (140), 90-121.
74. Schmid, K.; Riediker, M., Use of nanoparticles in swiss industry: A targeted survey. *Environmental Science and Technology* **2008,** 42, (7), 2253-2260.
75. Hoet, P. H. M.; BrÃ¼ske-Hohlfeld, I.; Salata, O. V., Nanoparticles - Known and unknown health risks. *Journal of Nanobiotechnology* **2004,** 2.
76. Baun, A.; Hartmann, N. B.; Grieger, K.; Kusk, K. O., Ecotoxicity of engineered nanoparticles to aquatic invertebrates: A brief review and recommendations for future toxicity testing. *Ecotoxicology* **2008,** 17, (5), 387-395.
77. Handy, R. D.; Owen, R.; Valsami-Jones, E., The ecotoxicology of nanoparticles and nanomaterials: Current status, knowledge gaps, challenges, and future needs. *Ecotoxicology* **2008,** 17, (5), 315-325.
78. Auffan, M.; Rose, J.; Bottero, J. Y.; Lowry, G. V.; Jolivet, J. P.; Wiesner, M. R., Towards a definition of inorganic nanoparticles from an environmental, health and safety perspective. *Nature Nanotechnology* **2009,** 4, (10), 634-641.
79. Som, C.; Berges, M.; Chaudhry, Q.; Dusinska, M.; Fernandes, T. F.; Olsen, S. I.; Nowack, B., The importance of life cycle concepts for the development of safe nanoproducts. *Toxicology* **2010,** 269, (2-3), 160-169.
80. Barnard, A. S., Nanohazards: Knowledge is our first defence. *Nature Materials* **2006,** 5, (4), 245-248.
81. Borm, P. J. A.; Robbins, D.; Haubold, S.; Kuhlbusch, T.; Fissan, H.; Donaldson, K.; Schins, R.; Stone, V.; Kreyling, W.; Lademann, J.; Krutmann, J.; Warheit, D. B.; Oberdorster, E., The potential risks of nanomaterials: A review carried out for ECETOC. *Particle and Fibre Toxicology* **2006,** 3.
82. Mao, Y.; Park, T. J.; Zhang, F.; Zhou, H.; Wong, S. S., Environmentally friendly methodologies of nanostructure synthesis. *Small* **2007,** 3, (7), 1122-1139.
83. Christensen, A. N.; Ollivier, G., Hydrothermal and high-pressure preparation of some $BaMnO_3$ modifications and low-temperature magnetic properties of $BaMnO_3$ (2H). *Journal of Solid State Chemistry* **1972,** 4, (1), 131-137.
84. Spooren, J.; Rumplecker, A.; Millange, F.; Walton, R. I., Subcritical hydrothermal synthesis of perovskite manganites: A direct and rapid route to complex transition-metal oxides. *Chemistry of Materials* **2003,** 15, (7), 1401-1403.

85. Liu, J.; Wang, H.; Zhu, M.; Wang, B.; Yan, H., Synthesis of $La_{0.5}A_{0.5}MnO_3$ (A = Sr, Ba) by a hydrothermal method at low temperature. *Materials Research Bulletin* **2003,** 38, (5), 817-822.
86. Spooren, J.; Walton, R. I.; Millange, F., A study of the manganites $La_{0.5}M_{0.5}MnO_3$ (M = Ca, Sr, Ba) prepared by hydrothermal synthesis. *Journal of Materials Chemistry* **2005,** 15, (15), 1542-1551.
87. Spooren, J.; Walton, R. I., Hydrothermal synthesis of the perovskite manganites $Pr_{0.5}Sr_{0.5}MnO_3$ and $Nd_{0.5}Sr_{0.5}MnO_3$ and alkali-earth manganese oxides $CaMn_2O_4$, 4H-$SrMnO_3$, and 2H-$BaMnO_3$. *Journal of Solid State Chemistry* **2005,** 178, (5), 1683-1691.
88. Wang, Y.; Lu, X.; Chen, Y.; Chi, F.; Feng, S.; Liu, X., Hydrothermal synthesis of two perovskite rare-earth manganites, $HoMnO_3$ and $DyMnO_3$. *Journal of Solid State Chemistry* **2005,** 178, (4), 1317-1320.
89. Li, J. Q.; Sun, W. A.; Ao, W. Q.; Tang, J. N., Hydrothermal synthesis and Magnetocaloric effect of $La_{0.5}Ca_{0.3}Sr_{0.2}MnO_3$. *Journal of Magnetism and Magnetic Materials* **2006,** 302, (2), 463-466.
90. Chen, Y.; Yuan, H.; Li, G.; Tian, G.; Feng, S., Crystal growth and magnetic property of orthorhombic $RMnO_3$ (R=Sm-Ho) perovskites by mild hydrothermal synthesis. *Journal of Crystal Growth* **2007,** 305, (1), 242-248.
91. Chen, Y.; Yuan, H.; Tian, G.; Zhang, G.; Feng, S., Hydrothermal synthesis and magnetic properties of $RMn_2O_5$ (R=La, Pr, Nd, Tb, Bi) and $LaMn_2O_{5+\delta}$. *Journal of Solid State Chemistry* **2007,** 180, (4), 1340-1346.
92. Chen, Y.; Yuan, H.; Tian, G.; Zhang, G.; Feng, S., Mild hydrothermal synthesis and magnetic properties of the manganates $Pr_{1-x}Ca_xMnO_3$. *Journal of Solid State Chemistry* **2007,** 180, (1), 167-172.
93. Zhu, D.; Zhu, H.; Zhang, Y., Hydrothermal synthesis of $La_{0.5}Ba_{0.5}MnO_3$ nanowires. *Applied Physics Letters* **2002,** 80, (9), 1634.
94. Zhu, D.; Zhu, H.; Zhang, Y. H., Hydrothermal synthesis of single-crystal $La_{0.5}Sr_{0.5}MnO_3$nanowire under mild conditions. *Journal of Physics Condensed Matter* **2002,** 14, (27).
95. Zhu, D.; Zhu, H.; Zhang, Y., Microstructure and magnetization of single-crystal perovskite manganites nanowires prepared by hydrothermal method. *Journal of Crystal Growth* **2003,** 249, (1-2), 172-175.
96. Zhang, T.; Jin, C. G.; Qian, T.; Lu, X. L.; Bai, J. M.; Li, X. G., Hydrothermal synthesis of single-crystalline $La_{0.5}Ca_{0.5}MnO_3$ nanowires at low temperature. *Journal of Materials Chemistry* **2004,** 14, (18), 2787-2789.
97. Rao, S. S.; Anuradha, K. N.; Sarangi, S.; Bhat, S. V., Weakening of charge order and antiferromagnetic to ferromagnetic switch over in $Pr_{0.5}Ca_{0.5}MnO_3$ nanowires. *Applied Physics Letters* **2005,** 87, (18), 1-3.
98. Urban, J. J.; Ouyang, L.; Jo, M. H.; Wang, D. S.; Park, H., Synthesis of single-crystalline $La_{1-x}Ba_xMnO_3$ nanocubes with adjustable doping levels. *Nano Letters* **2004,** 4, (8), 1547-1550.
99. Chai, P.; Liu, X.; Wang, Z.; Lu, M.; Cao, X.; Meng, J., Tunable synthesis, growth mechanism, and magnetic properties of $La_{0.5}Ba_{0.5}MnO_3$. *Crystal Growth and Design* **2007,** 7, (12), 2568-2575.
100. Hu, C. G.; Liu, H.; Lao, C. S.; Zhang, L. Y.; Davidovic, D.; Wang, Z. L., Size-manipulable synthesis of single-crystalline BaMnO3 and $BaTi_{0.5}Mn_{0.5}O_3$ nanorods/nanowires. *Journal of Physical Chemistry B* **2006,** 110, (29), 14050-14054.
101. Liu, H.; Hu, C.; Wang, Z. L., Composite-hydroxide-mediated approach for the synthesis of nanostructures of complex functional-oxides. *Nano Letters* **2006,** 6, (7), 1535-1540.
102. Hayashi, Y.; Kimura, T.; Yamaguchi, T., Preparation of rod-shaped $BaTiO_3$ powder. *Journal of Materials Science* **1986,** 21, (3), 757-762.
103. Yoon, K. H.; Cho, Y. S.; Kang, D. H., Molten salt synthesis of lead-based relaxors. *Journal of Materials Science* **1998,** 33, (12), 2977-2984.
104. Kojima, T.; Nomura, K.; Miyazaki, Y.; Tanimoto, K., Synthesis of various $LaMO_3$ perovskites in molten carbonates. *Journal of the American Ceramic Society* **2006,** 89, (12), 3610-3616.
105. Hungría, T.; Algueró, M.; Castro, A., Synthesis of nanosized (1-x)$NaNbO_{3-x}SrTiO_3$ solid solution by mechanochemical activation, processing of ceramics, and phase transitions. *Chemistry of Materials* **2006,** 18, (22), 5370-5376.
106. Lubyova, Z.; Danek, V., Formation mechanism, nucleation and crystallization of $Li_2TiO_3$ from fused salts. *Ceramics - Silikaty* **1992,** 36, (1), 21-25.
107. Lubyova, Z.; Danek, V., Reaction mechanism and kinetics of $SrTiO_3$ crystal growth in molten alkali metal chlorides medium. *Ceramics - Silikaty* **1992,** 36, (4), 181-185.
108. Battisha, I. K.; Speghini, A.; Polizzi, S.; Agnoli, F.; Bettinelli, M., Molten chloride synthesis, structural characterisation and luminescence spectroscopy of ultrafine $Eu^{3+}$-doped $BaTiO_3$ and $SrTiO_3$. *Materials Letters* **2002,** 57, (1), 183-187.

109. Wang, X.; Gao, L.; Zhou, F.; Zhang, Z.; Ji, M.; Tang, C.; Shen, T.; Zheng, H., Large-scale synthesis of δ±-$LiFeO_2$ nanorods by low-temperature molten salt synthesis (MSS) method. *Journal of Crystal Growth* **2004,** 265, (1-2), 220-223.
110. Mao, Y.; Banerjee, S.; Wong, S. S., Large-Scale Synthesis of Single-Crystalline Perovskite Nanostructures. *Journal of the American Chemical Society* **2003,** 125, (51), 15718-15719.
111. Mao, Y.; Wong, S. S., Composition and shape control of crystalline $Ca_{1-x}Sr_xTiO_3$ perovskite nanoparticles. *Advanced Materials* **2005,** 17, (18), 2194-2199.
112. Tian, Y.; Chen, D.; Jiao, X., $La_{1-x}Sr_xMnO_3$ (x = 0, 0.3, 0.5, 0.7) nanoparticles nearly freestanding in water: Preparation and magnetic properties. *Chemistry of Materials* **2006,** 18, (26), 6088-6090.
113. Yang, L. X.; Zhu, Y. J.; Tong, H.; Wang, W. W., Submicrocubes and highly oriented assemblies of $MnCO_3$ synthesized by ultrasound agitation method and their thermal transformation to nanoporous $Mn_2O_3$. *Ultrasonics Sonochemistry* **2007,** 14, (2), 259-265.
114. Ford, W. E.; Jung, A.; Hirsch, A.; Graupner, R.; Scholz, F.; Yasuda, A.; Wessels, J. M., Urea-melt solubilization of single-walled carbon nanotubes. *Advanced Materials* **2006,** 18, (9), 1193-1197.
115. Buha, J.; Djerdj, I.; Antonietti, M.; Niederberger, M., Thermal transformation of metal oxide nanoparticles into nanocrystalline metal nitrides using cyanamide and urea as nitrogen source. *Chemistry of Materials* **2007,** 19, (14), 3499-3505.
116. Podsiadlo, S., Stages of the synthesis of indium nitride with the use of urea. *Thermochimica Acta* **1995,** 256, (2), 375-380.
117. Gomathi, A., Ternary metal nitrides by the urea route. *Materials Research Bulletin* **2007,** 42, (5), 870-874.
118. Gomathi, A.; Sundaresan, A.; Rao, C. N. R., Nanoparticles of superconducting γ-$Mo_2N$ and δ-MoN. *Journal of Solid State Chemistry* **2007,** 180, (1), 291-295.
119. Giordano, C.; Erpen, C.; Yao, W.; Antonietti, M., Synthesis of Mo and W carbide and nitride nanoparticles via a simple "urea glass" route. *Nano Letters* **2008,** 8, (12), 4659-4663.
120. Gomathi, A.; Reshma, S.; Rao, C. N. R., A simple urea-based route to ternary metal oxynitride nanoparticles. *Journal of Solid State Chemistry* **2009,** 182, (1), 72-76.
121. Abbott, A. P.; Capper, G.; Davies, D. L.; Rasheed, R. K.; Tambyrajah, V., Novel solvent properties of choline chloride/urea mixtures. *Chemical Communications* **2003,** 9, (1), 70-71.
122. Antonietti, M.; Kuang, D.; Smarsly, B.; Zhou, Y., Ionic liquids for the convenient synthesis of functional nanoparticles and other inorganic nanostructures. *Angewandte Chemie - International Edition* **2004,** 43, (38), 4988-4992.
123. Liao, H. G.; Jiang, Y. X.; Zhou, Z. Y.; Chen, S. P.; Sun, S. G., Shape-controlled synthesis of gold nanoparticles in deep eutectic solvents for studies of structure-functionality relationships in electrocatalysis. *Angewandte Chemie - International Edition* **2008,** 47, (47), 9100-9103.
124. Gaune-Escard, M. and Seddon, K. R., *Molten Salts and Ionic Iiquids*. Wiley: **2010**.

II. Bibliography/Bibliografía

# OBJECTIVES / OBJETIVOS

# OBJECTIVES

1. Design of new methods of chemical synthesis of nanostructured inorganic functional materials. Specifically, the focus is on development of both inorganic and organic low-temperature molten salts/molecules media suitable for the nucleation and stabilization of inorganic NCs under mild reaction conditions.
2. Characterization of the prepared NCs regarding composition, surface, size, shape, defects and SA features. Regarding the target compositions, mainly oxides and also lead sulphide –due to its unique properties and potential applications in optoelectronic devices– are addressed. A special interest is focused on the preparation of ligand-free NPs.
3. Characterization of the most relevant physical properties exhibited by the prepared materials, corresponding in a first approach to the magnetic phenomenology. Study of the relation microstructure-magnetic properties.

III. Objectives

# OBJETIVOS

1. Diseño de nuevos m étodos de síntesis quím ica de m ateriales funcionales inorgánicos nanoestructurados. Específicam ente, el objeti vo es el desarrollo de medios tanto inorgánicos com o orgáni cos basados en sales o m oléculas fundidas a baja tem peratura que sean adecuados para la nucleación y la estabilización de NCs inorgánicos bajo condiciones suaves de reacción.
2. Caracterización de los NCs preparados atendiendo a las car acterísticas de composición, superficie, tam año, for ma, defectos y AE. Respecto a las composiciones objeto de estudio, princi palmente se abordan óxidos; adem ás, se estudia el sulfuro de plom o, debido a sus propiedades únicas y potenciales aplicaciones en dispositivos optoelectrónicos. Se presta un especial inte rés a la preparación de NPs cuya superficie esté desprovista de ligandos.
3. Caracterización de las propiedad es físi cas m ás relevantes m ostradas por los materiales preparados, que corresponde n en una prim era aproxim ación a la fenomenología m agnética. Estudio de la relación m icroestructura-propiedades magnéticas.

# III. Objetivos

# CHAPTER 1

# SYNTHESIS OF NANOOXIDES IN HIGHLY ALKALI MEDIUM

Chapter 1.1. Hydrothermal Synthesis: A Suitable Route to Elaborate Nanomanganites

Chapter 1.2. Hydroxides Eutectic Route for the Preparation of Nanomanganites

Chapter 1.3. Hydroxides Eutectic Route for the Synthesis of NiO Nanooctahedra

# CHAPTER 1.1

# Hydrothermal Synthesis: A Suitable Route to Elaborate Nanomanganites

1898 *Chem. Mater.* **2009,** *21,* 1898–1905

# Hydrothermal Synthesis: A Suitable Route to Elaborate Nanomanganites

A. Querejeta,[†] A. Varela,[†] M. Parras,[†] F. del Monte,[‡] M. García-Hernández,[‡] and J. M. González-Calbet*,[†]

*Departamento de Química Inorgánica, Facultad de Químicas, Universidad Complutense, 28040-Madrid, Spain, and Instituto de Ciencia de Materiales, CSIC, Spain*

*Received January 15, 2009. Revised Manuscript Received March 5, 2009*

A tunable hydrothermal synthesis of single-crystalline $BaMnO_3$ nanoparticles is reported. The parameters governing the synthesis pathway are carefully evaluated, assessing their influence on both the morphology and size of the as-prepared products. The reactor filling volume is found to have a main influence on the particle shape (predominance of microrods for a filling volume of 70% and particles for ca 40−50 %), whereas the alkalinity is crucial for the control over the size: higher alkalinities lead to a drastic decrease in both final particle size and aspect ratio. Average minimum particle diameters of ca 20 nm are prepared using a KOH concentration of 20 M, metallic salts concentrations of 50 or 100 mM, and a filling volume of 53%. Finally, the temperature and time exert a minor influence on the final structural properties of the resulting products: 200 °C and lower (even 150°C) and times of 24 hours or less (4 hours) are suitable for nanoparticles formation. The ability to synthesize nanoscale manganites with a narrow particle size distribution has allowed the study of the correlation between the nanoparticle average diameter and magnetic properties. An exchange bias phenomenology is observed in nanosized $BaMnO_3$ as a result of ferromagnetic (FM) correlations in coexistence with a dominant antiferromagnetism. The stronger FM correlations in smaller nanoparticles lead to larger remanence and smaller exchange bias fields.

## Introduction

Hydrothermal synthesis is gaining increased interest for the preparation of nanocrystals of binary transition metal oxides given that it offers a wide range of reaction conditions (e.g., temperature, salt and mineralizer concentration, reaction time, etc.) to tailor the composition, shape, and size of the final products. Moreover, the dramatic change in density, ionic product, viscosity, and dielectric constant of water under hydrothermal conditions due to autogenous pressure and high temperature favor the solubility and mobility of species, accessing crystallization reactions that would not occur under conventional conditions.[1] Finally, the one-step and easy handling character of hydrothermal synthesis besides the low temperatures used for reaction makes this procedure a convenient method for the synthesis of not only binary but also multinary metal transition nanooxides.

In spite of its potential, the hydrothermal method has been little employed for the synthesis of nanocrystals of multinary oxides. Although numerous manganese related perovskites or manganites ($A_{1-x}A'_xMn_{1-y}M_yO_{3-\delta}$, $AMn_2O_4$, $AMn_2O_{5+\delta}$) microcrystals have been synthesized by the hydrothermal method,[2−13] nanomanganites hydrothermally prepared are restricted to $La_{1-x}Ba_xMnO_3$ ($x = 0.3$, 0.5, 0.6) nanocubes[14] and $Ln_{0.5}A_{0.5}MnO_3$ (Ln = La, Pr; A = Ca, Sr, Ba) nanowires.[15−19]

Nanomanganites are a promising system in the field of nanoscience and nanotechnology, as a result of the structural variety and outstanding properties found in their bulk counterparts. The ability of Mn to be stabilized in mixed oxidation states allows many combinations of chemical doping and anion vacancies to be adopted, leading in turn

* Corresponding author. E-mail: jgcalbet@quim.ucm.es. Fax: (34) 91 394 43 52.
[†] Universidad Complutense.
[‡] Instituto de Ciencias de Materiales, CSIC.

(1) Rabenau, A. *Angew. Chem. Int. Ed.* **1985**, *24*, 1026.
(2) Chai, P.; Liu, X.; Wang, Z.; Lu, M.; Cao, X.; Meng, J. *Cryst. Growth Des.* **2007**, *7*, 2568.
(3) Spooren, J.; Rumplecker, A.; Millange, F.; Walton, R. I. *Chem. Mater* **2003**, *15* (7), 1401.
(4) Spooren, J.; Walton, R. I.; Millange, F. *J. Mater. Chem.* **2005**, *15*, 1542.
(5) Liu, J.; Wang, H.; Zhu, M.; Wang, B.; Yan, H. *Mater. Res. Bull* **2003**, *38*, 817–822.
(6) Spooren, J.; Walton, R. I. *J. Solid State Chem.* **2005**, *178*, 1683–1691.
(7) Zhu, J.; Liu, J.; Wang, H.; Zhu, M.; Yan, H. *Cryst. Res. Technol.* **2007**, *42*, 3–241.
(8) Christensen, A. N.; Ollivier, G. *J. Solid State Chem.* **1972**, *4*, 131.
(9) Chen, Y.; Yuan, H.; Li, G.; Tian, G.; Feng, S. *J. Cryst. Growth* **2007**, *305*, 242.
(10) Wang, Y.; Lu, X.; Chen, Y.; Chi, F.; Feng, S.; Liu, X. *J. Solid State Chem.* **2005**, *178*, 1317.
(11) Li, J. Q.; Sun, W. A.; Ao, W. Q.; Tang, J. N. *J. Magn. Magn. Mater.* **2006**, *302*, 463.
(12) Chen, Y.; Yuan, H.; Tian, G.; Zhang, G.; Feng, S. *J. Solid State Chem.,* **2007**, *180*, 167.
(13) Chen, Y.; Yuan, H.; Tian, G.; Zhang, G.; Feng, S. *J Solid State Chem.* **2007**, *180*, 1340.
(14) Urban, J. J.; Ouyang, L.; Jo, M.-H.; Wang, D. S.; Park, H. *Nano Lett.* **2004**, *4* (8), 1547.
(15) Zhu, D.; Zhu, H.; Zhang, Y. *Appl. Phys. Lett.* **2002**, *80*, 1634.
(16) Zhu, D.; Zhu, H.; Zhang, Y. *J. Cryst. Growth* **2003**, *249*, 172.
(17) Zhu, D.; Zhu, H.; Zhang, Y. H. *J. Phys.: Condens. Matter* **2002**, *14*, L519.
(18) Zhang, T.; Jin, C. G.; Qian, T.; Lu, X. L.; Bai, J. M.; Li, X. G. *J. Mater. Chem.* **2004**, *14*, 2787.
(19) Rao, S. S.; Anuradha, K. N.; Sarandi, S.; Bhat, V. *App. Phys. Lett.* **2005**, *87*, 182503.

10.1021/cm9001306 CCC: $40.75 
Published on Web 04/06/2009

**Table 1. Detailed Reaction Conditions of the Hydrothermal Synthesis of $BaMnO_3$ Nanoparticles and XRD and TEM Results**

| set | entrant | %autoclav filling | [KOH] (M)[a] | [Ba](mM)[a] | *T* (°C) | time (h) | XRD particle size (101) (nm) | TEM results: morphology and range of particle size[b] (nm) |
|---|---|---|---|---|---|---|---|---|
| 1 | 1 | **70** | 20 | 100 | 200 | 2 | | nanoparticles; aggregates |
| | 2 | **70** | 20 | 100 | 200 | 24 | | nanoparticles/microparticles/ microrods |
| | 3 | **70** | 2 | 25 | 200 | 24 | | nanoparticles/microparticles/ microrods/nanoparticles' assemblies in form of microrods |
| 2 | 4 | 38 | **2** | 25 | 200 | 24 | | nanoparticles/microrods 45−750 ($\phi$)/150−10000 (L) |
| | 5 | 38 | **2** | 50 | 200 | 24 | | nanoparticles/microrods 25−350($\phi$)/ 90−10000 (L) |
| | 6 | 38 | **2** | 75 | 200 | 24 | | nanoparticles/microparticles/ microrods |
| | 7 | 38 | **2** | 100 | 200 | 24 | | nanoparticles/microparticles/ microrods |
| 3 | 8 | 42 | 8 | **50** | 200 | 24 | | nanoparticles (8−150) nanorods:15−200($\phi$)/80−1000 (L) |
| | 9 | 48 | 14 | **50** | 200 | 24 | 30.2 | nanoparticles (10−55) |
| | 10 | 53 | 20 | **50** | 200 | 24 | 24.9 | nanoparticles (8−40) |
| | 11 | 58 | 26 | **50** | 200 | 24 | 30.8 | nanoparticles (12−139) |
| 4 | 12 | 53 | **20** | 75 | 200 | 24 | 22.2 | nanoparticles (11−44) |
| | 13 | 53 | **20** | 100 | 200 | 24 | 21.9 | nanoparticles (12−41)/microcrystals |
| 5 | 14 | 53 | 20 | 100 | 200 | **4** | 19.9 | nanoparticles (6−37) |
| 6 | 15 | 53 | 20 | 50 | **150** | 24 | 20.0 | nanoparticles (10−32)/microcrystals |

[a] Concentrations listed in the table do not correspond to the final solution because high KOH concentrations provide a significant increase in volume. [b] Size interval containing 90% particles.

to structures with different dimensionality[20] and to interplay among spin, charge, and orbital degrees of freedom.[21−24] Thus, diverse and interesting properties are found in this rich variety of oxides: colossal magnetoresistance in $La_{1-x}A'_xMnO_3$ ($A'$ = alkali earth),[24−28] high permittivity in $BaMn_{0.5}Ti_{0.5}O_3$,[29] multiferroic behaviour and large nonlinear optical response in $BiMnO_3$,[30−33] giant magneto-elastic coupling in multiferroic hexagonal manganites,[34] etc.

We consider that, to date and from a synthetic point of view, neither the variables affecting the shape and size of the products nor their relative relevance have been clearly established in the limited number of works reporting on the hydrothermal synthesis of nanomanganites. Herein, we report a tunable hydrothermal synthesis of single-crystalline nanoparticles of $BaMnO_3$. The optimization of parameters governing this synthesis procedure has allowed to the preparation of monodispersed nanoparticles with minimum sizes in the range of 10−40 nm. The correlation between the nanoparticle average size and magnetic properties is discussed.

## Experimental Section

$KMnO_4$ (Aldrich, 99+%), $MnCl_2 \cdot 4H_2O$ (Aldrich, 99.99%), $BaCl_2$ (Aldrich, 99.9 %), and KOH (Merck, pellets, 85 %) were used as-received without further purification. The hydrothermal treatment was performed in a Teflon-lined, aluminium autoclave with a volume of ca. 107 mL. Solutions of each starting material were prepared by dissolving the required amounts of $Ba^{2+}$, $Mn^{2+}$, and $MnO_4^-$ salts and KOH (Table 1) in a total volume of 40 mL (sets 2, 3, 4, 5, 6), 50 mL (entrants 1, 2 of set 1) or 66 mL (entrant 3 of set 1) of deionized water. Note that in set #1 a constant filling volume of 70% is achieved for different KOH concentrations by using distinct water amounts. The $Ba^{2+}$:$Mn_{Total}$ molar ratio was 1:1, according to the nominal composition. The initial mole ratio of the manganese salts was 6 $Mn^{2+}$:4 $MnO_4^-$ in order to obtain the desired average manganese oxidation state of 4+ in the reaction mixture. The $Mn^{2+}$ and $Ba^{2+}$ solutions were mixed into the Teflon vessel and stirred using a magnetic bar. KOH was added to the resulting homogeneous solution, either as a water solution for samples of low KOH concentration or as pellets for samples of high KOH concentration. Finally, the $MnO_4^-$ solution was added to the solution containing $Mn^{2+}$ and $Ba^{2+}$ salts and KOH. Right after $MnO_4^-$ addition, precipitation of insoluble $Mn^{4+}$-containing dark-brown oxides can be observed. Because of the appearance of this precipitate, removal of the magnetic bar is recommended before $MnO_4^-$ addition. The Teflon vessel was then placed in a closed autoclave and thermally treated at 200 °C and different reaction times. The detailed reaction conditions and corresponding brief results are summarized in Table 1. After reaction completion, the solution was cooled to room temperature and the resulting green/brown suspensions were centrifugated in order to separate the precipitate from the mother liquid. Excess of alkali impurities were removed by dialysis and the final powder was dried at 50−80 °C overnight.

(20) Mitchell, R. H. *Perovskites Modern and Ancient*; Almaz Press Inc.: Thunder Bay, ON, Canada, 2002.
(21) Millis, A. J. *Nature (London)* **1998**, *392*, 147.
(22) Moreo, A.; Yunoki, S.; Dagotto, E. *Science* **1999**, *283*, 2034.
(23) Tokura, Y.; Nagaosa, N. *Science* **2000**, *288*, 462.
(24) Salamon, M. B.; Jaime, M. *Rev. Mod. Phys.* **2001**, *73*, 583.
(25) Jin, S.; Tiefel, T. H.; McCormack, M.; Fastnacht, R. A.; Ramesh, R.; Chen, L. H. *Science* **1994**, *264*, 413.
(26) Von Helmolt, R.; Wecker, J.; Holzapfel, B.; Schultz, L.; Samwer, K. *Phys. Rev. Lett.* **1993**, *71*, 2331.
(27) Renner, C.; Aeppli, G.; Kim, B.-G.; Soh, Y.-A.; Cheong, S.-W. *Nature (London)* **2002**, *416*, 518.
(28) Loudon, J. C.; Mathur, N. D.; Midgley, P. A. *Nature (London)* **2002**, *420*, 797.
(29) Keith, G. M.; Kirk, C. A.; Sarma, K.; Alford, N. M.; Cussen, E. J.; Rosseinsky, M. J.; Sinclair, D. C. *Chem. Mater.* **2004**, *16*, 2007.
(30) Hill, N. A.; Rabe, K. M. *Phys. Rev. B* **1999**, *59*, 8759.
(31) Moreira dos Santos, A.; Cheetham, A. K.; Atou, T.; Syono, Y.; Yamaguchi, Y.; Ohoyama, K.; Chiba, H.; Rao, C. N. R. *Phys. Rev. B* **2002**, *66*, 064425.
(32) Kimura, T.; Kawamoto, S.; Yamada, I.; Azuma, M.; Takano, M.; Tokura, Y. *Phys. Rev. B* **2003**, *67*, 180401.
(33) Sharan, A.; Lettieri, J.; Jia, Y.; Tian, W.; Pan, X.; Schlom, D. G.; Gopalan, V. *Phys. Rev. B* **2004**, *69*, 214109.
(34) Lee, S.; Pirogov, A.; Kang, M.; Jang, K.-H.; Yonemura, M.; Kamiyama, T.; Cheong, S.-W.; Gozzo, F.; Shin, N.; Kimura, H.; Noda, Y.; Park, J.-G. *Nature (London)* **2008**, *451*, 805.

Powder X-ray diffraction (XRD) patterns were measured using a Siemens D5000 diffractometer with Cu Kα radiation ($\lambda = 1.5418$ Å). Particle size distributions of the powders were measured using dynamic light scattering (DLS) experiments performed using a Malvern instrument, Nano ZS-ZEN3600 fitted with a 630 nm red laser. Samples for DLS measurements were prepared by ultrasonication of the solid (∼0.5 mg) in a 0.1 wt % solution of sodium bis(2-ethylhexyl) sulphosuccinate (AOT) in distilled water (∼5 mL).

Transmission electron microscopy (TEM) was performed on a JEOL JEM-2000 FX electron microscope whereas high-resolution transmission electron microscopy (HRTEM) characterization was carried out using a JEOL300FEG microscope. Chemical composition of the nanocrystals was determined by energy-dispersive X-ray analysis (EDX) in an AN10000 analyzer adapted to both microscopes. Samples for TEM and HRTEM were prepared by adding 1−2 drops of an *n*-butanol suspension onto a copper grid covered by an amorphous carbon film.

Magnetization measurements on fresh samples were obtained by SQUID magnetometry using a Quantum Design magnetometer equipped with a 5 Tesla superconducting coil. The temperature range explored is (2−400 K).

## Results and Discussion

As previously mentioned, the aim of this work is to optimize the parameters determining the achievement of nanomanagnites under hydrothermal conditions. Since the seminal work published in 1972 by Christensen and co-workers,[8] there has been a single paper reporting on the hydrothermal synthesis of tablet-shaped $BaMnO_3$ crystallites with lengths ranging from ∼0.5 to 2 μm.[6] The experimental conditions used in this case (i.e., a combination of both high KOH and metallic salts concentrations with barium and manganese concentrations of ∼222 mM and KOH concentration of ∼40 M) failed in the achievement of nanometer-sized particles, most likely because (i) reactants were not soluble enough for creating a homogeneous medium at supersaturation and/or (ii) first nuclei tend to aggregate and sinter.

The experimental conditions for the synthesis of $La_{1-x}Ba_xMnO_3$ nanoparticles with different doping levels have been the most widely explored. A close inspection of these works allows two synthetic conditions to be distinguished for the achievement of (i) nanowires of 30−150 nm diameter and tens of micrometers length for [KOH] = 10 M and [metallic salts concentrations] = 284 mM,[15] and (ii) nanometer-sized cubes of 50−100 nm diameter for [KOH] = 12 M and [metallic salts concentrations] = 100 mM.[14] These close reaction conditions make it quite difficult to establish any correspondence between morphology and concentrations. Actually, both concentrations were also slightly lower than those described above for the synthesis of $BaMnO_3$, where microparticles (rather than nanoparticles or nanowires were obtained). More recently, Chai et al[2] have observed that the increase on the KOH concentration from 6 up to 14 M leads to a drastic decrease of the final particle size of $La_{0.5}Ba_{0.5}MnO_3$; e.g., for KOH 14 M, microcubes of 100−450 nm are obtained, whereas for 10 M, the particle size increases up to 0.5−2 μm; finally, for [KOH] = 6 M, flowerlike particles of 5−15 μm diameter are obtained.

On the basis of the above mentioned results, we consider it highly desirable to study the influence of the experimental conditions used to carry out the hydrothermal synthesis on the morphology (e.g. micro/nanoparticles or nanowires) of the resulting manganites. A careful inspection to those works reporting on nanoparticles and nanowires revealed that the most significant difference among them was the reactor filling volume (e.g., ∼70 % for $La_{0.5}Ba_{0.5}MnO_3$ nanowires[12] and ∼33 % for nanocubes[14]). Thus, we first aimed to reproduce the synthetic conditions described by Zhu and co-workers (in terms of reactor filling volume) for preparation of $BaMnO_3$ nanowires within a certain range of KOH and metal salts concentrations (see Table 1, set 1). The temperature of the reactions was fixed at 200 °C (autoclave filling around 70%), whereas the influence of the reaction time in the final products was also evaluated. All the obtained samples exhibit the XRD patterns corresponding to the 2H-structure of $BaMnO_3$, as shown in Figure 1. The symmetry and calculated lattice parameters are consistent with the bulk values ($a$ = 5.6990 Å, $c$ = 4.8170 Å, $P6_3/mmc$).[35]

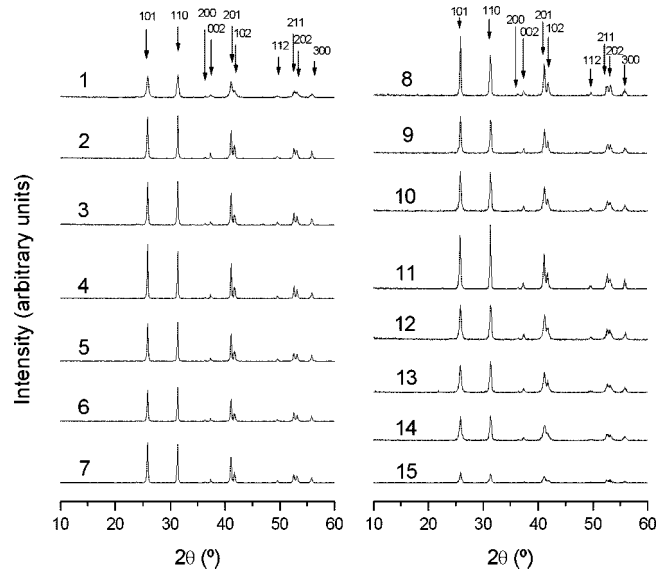


**Figure 1.** XRD patterns corresponding to all samples depicted in Table 1. All of them are monophasic and can be assigned to the $BaMnO_3$ unit cell.

The cationic composition, determined at the nanoscale level by EDX after analyzing around 30−40 crystallites, reveals a stoichiometric 1.0:1.0 ratio for Ba:Mn within experimental errors, in good agreement with the nominal composition.

TEM micrographs (Figure 2) show that in all cases, the morphology of the resulting $BaMnO_3$ is somewhat heterogeneous, ranging from microparticles to microrods, no matter the reaction time or KOH metal salt concentrations. Regardless of the unsuccessful achievement either of $BaMnO_3$ nanoparticles or nanorods in any of these samples, the $BaMnO_3$ synthesized using the lowest KOH and metallic salts concentrations provide quite interesting information with regards to the formation mechanism of microrods: self-assembly of acicular $BaMnO_3$ nanoparticles. Such assembly is shown in the TEM image of the sample 4 (Figure 3a). The corresponding electron diffraction pattern (Fig. 3b) reveals the monocrystalline character of this assembly.

(35) Chamberland, B. L.; Sleight, A. W.; Weiher, J. F. *J. Solid State Chem.* **1970**, *1*, 506.

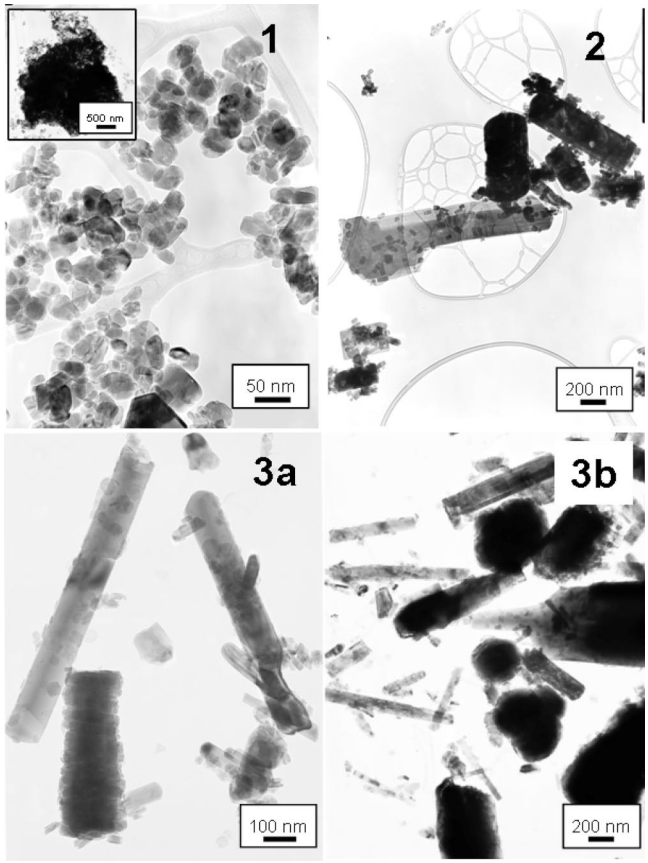


**Figure 2.** TEM micrographs of $BaMnO_3$ samples 1, 2 and 3. These samples correspond to a constant autoclave filling of 70%. The formation of nano/microrods by self-assembly of nanoparticles seems to be favored under this condition.

Actually, all the observed maxima can be indexed on the basis of the hexagonal unit cell of the 2H-$BaMnO_3$ along the [100] zone axis. This result indicates that all the nanoparticles are oriented along the same direction, corroborating that the observed assembly is an intermediate in the microrod formation.

The presence of small nanoparticles as intermediates of the large microrods is also encouraging for the achievement of isolated nanoparticles; one should just determine the synthethic conditions to avoid aggregation. As mentioned above, the particle shape seems to be mostly related to the reactor filling volume. So to determine the influence of this variable, our next sets of samples were prepared from solutions filling ca. 40% of reactor volume. In the first set of samples (set #2), KOH concentration was fixed at 2 M, and metallic salts concentration ranged from 25 to 100 mM. For concentrations of 25 and 50 mM, mixed microrods and nanoparticles with broad particle size distributions were obtained. In both cases, the nanoparticles size ranged from 25 to above 100 nm, whereas rods were slightly smaller for a metallic salt concentration of 50 mM (25−350 nm diameter and 90−1000 nm length) than for that of 25 mM (45−750 nm diameter and 150−1000 nm length). Besides, it is worth noting that further aggregation tendency is observed for the 50 mM sample. Further increase in concentration (e.g., 75 and 100 mM) leads to very inhomogeneous samples with predominance of aggregated particles (of undefined shape)

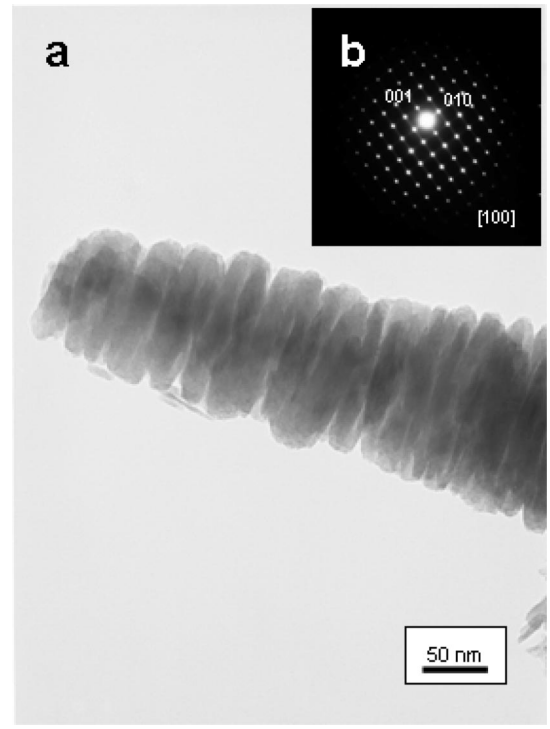


**Figure 3.** (a) TEM micrograph of self-assembled acicular $BaMnO_3$ nanoparticles into a microrod. (b) Corresponding SAED pattern, showing the monocrystalline character of the assembly. Such formations are characteristic of sample 3 (Table 1).

at the micrometer scale and some wide rods (200 nm diameter). Representative TEM images are shown in Figure 4.

The above results seem to indicate that aggregation of primary particles tends to be favored in a solution rich in metallic salts and low ionic strength. Because a KOH concentration of 2 M failed in avoiding aggregation (in form of both large particles and microwires) and hence to obtain uniform nanoparticles, in our next set of samples (set #3), the metallic salts concentration was fixed at 50 mM and the filling volume was kept close to 50%, whereas the KOH concentration varies from 2 to 26 M. First, the increase in the KOH concentration from 2 M (sample 5) to 8 M (sample 8) results in partial disappearance of aggregates and in a decreasing of the particle size, though rods and particles remain in coexistence (Figure 5, sample 8). Further KOH increase (14 and 20 M) gives rise to isolated nanoparticles (Figure 5, samples 9, 10). The high-resolution TEM image (Figure 6a) and the Fourier Transformation pattern (Figure 6b) of the resulting $BaMnO_3$ nanoparticles show a single crystalline nature, corresponding to the 2H structural type. The micrograph was taken along the 010 zone axis; in this zone, the structure is viewed parallel to the columns of Ba−O close-packed rows and the stacking sequence of the layers is revealed directly. By considering that Ba atoms are projected as brighter dots, the experimental contrast is associated with a (hh) layered sequence. A calculated image with the ideal atomic positions corresponding to a 2H polytype (see inset in Figure 6a) fits well with the experimental image for $\Delta t = 5$ nm, $\Delta f = -500$ nm.

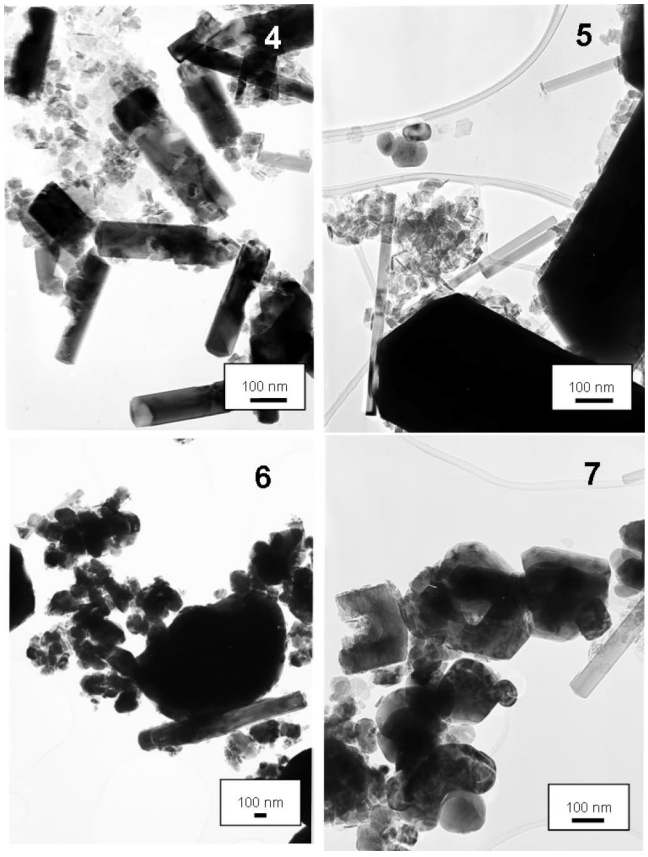


**Figure 4.** TEM micrographs of $BaMnO_3$ samples 4, 5, 6, and 7 of Table 1, corresponding to a fixed KOH concentration of 2 M, fixed autoclave filling ca. 40%, and metallic salts concentration of 25 (4), 50 (5), 75 (6), and 100 mM (7).

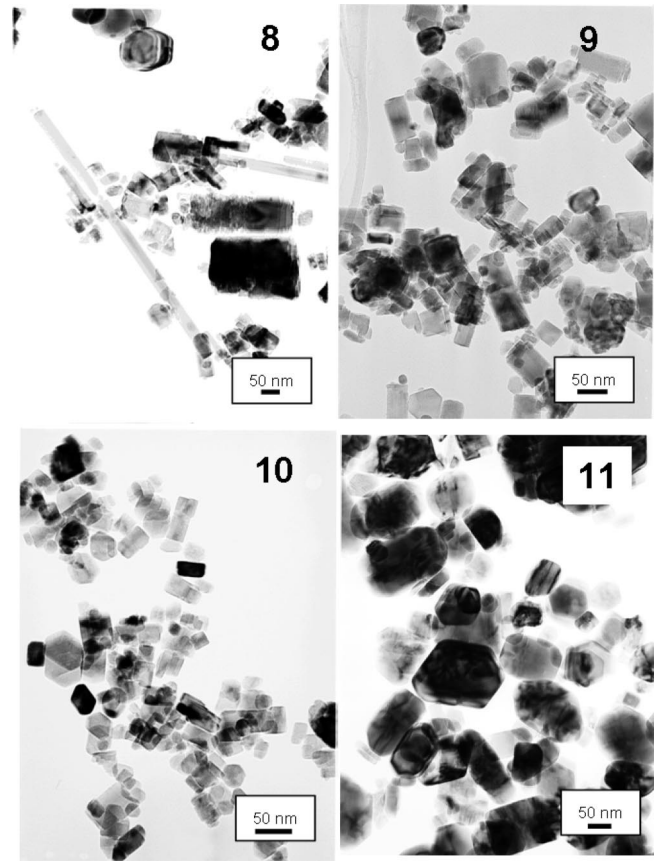


**Figure 5.** TEM micrographs of $BaMnO_3$ samples 8, 9, 10, and 11 (see Table 1), corresponding to a fixed metallic salts concentration of 50 mM, filling volume of ca. 50 %, and KOH concentrations of 8 (8), 14 (9), 20 (10), and 26 M (11). Note that the increase in KOH concentration from 8 to 20 M leads to a decrease in both particle size and aspect ratio of the resulting nanoparticles.

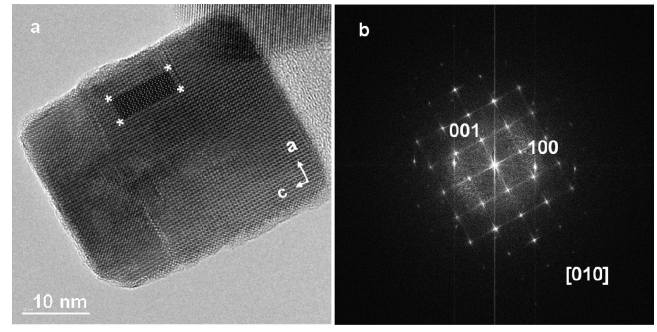


**Figure 6.** (a) HRTEM image of a ca. 30 nm × 37 nm $BaMnO_3$ nanoparticle along the 010 zone axis corresponding to sample 10 of Table 1. Simulated image is shown in the inset. (b) Corresponding Fourier transformation pattern.

Further insights about synthesized $BaMnO_3$ nanoparticles (e.g., mean particle size, particle size distribution) were provided by dynamic light scattering measurements (DLS). Figure 7 depicts a narrow particle size distribution with mean particle size centred at 37 nm for sample 13, a value slightly larger than that average value estimated by TEM (e.g., ∼26 nm). Such discrepancy can be ascribed to the eventually larger hydrodynamic volume of AOT coated nanoparticles (remind AOT was used for nanoparticle resuspension, see experimental). Besides, sizes determined by TEM images were based on the minimal dimension of the nanoparticles, while the size detected by dynamic light scattering measurements is related with the diameter of the corresponding hydrodynamic sphere. Note that $BaMnO_3$ nanoparticles exhibit certain acicular form in each of the synthesized samples. Interestingly, DLS measurements allowed discarding the presence of large aggregates and microcrystals in each of the selected samples, in good concordance with TEM micrographs.

An overall analysis of the above results reveals the different relevance of studied parameters on the final $BaMnO_3$ particle size. From these, the KOH concentration appears as the most significant one in the achievement of isolated nanoparticles of $BaMnO_3$. On one hand, KOH favors the homogenous dissolution of metallic salts thanks to the high ionic strength of the solution, whereas on the other, it helps for inhibition of uncontrolled growth of first nucleus by aggregation processes. Note that two typical growth mechanisms, ion-to-ion attachment[36,37] and self-assembly of nanocrystals,[38] are both hampered; the former because of the lack of remaining $Ba^{2+}$ and $Mn^{4+}$ cations in solution and the latter because of electrostatic repulsion of nanoparticles ($OH^-$-surface-charged at high pH levels). The third most typical growth mechanism (e.g., Ostwald-like ripening pro-

(36) Cushing, B. L.; Kolesnichenko, V. L.; O'Connor, J. *Chem. Rev.* **2004**, *104*, 3893–3946.
(37) Park, J.; Joo, J.; Kwon, S. G.; Jang, Y.; Hyeon, T. *Angew. Chem., Int. Ed.* **2007**, *46*, 4630–4660.
(38) Niederberger, M.; Cölfen, H. *Phys. Chem. Chem. Phys.* **2006**, *8*, 3271–3287.

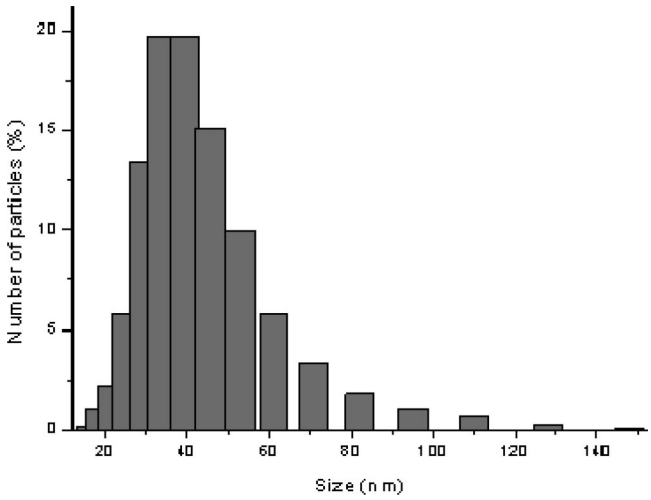


**Figure 7.** Particle size distribution of sample 13 measured by dynamic light scattering (DLS). The size distribution is centred at 37 nm.

cess[39]) also seems to be disfavored, most likely because of the poor solubility of smallest crystallites in such an alkaline solution. Actually, the use of 14−20 M KOH concentrations allowed for the achievement of $BaMnO_3$ nanoparticles even for metallic salts concentrations of 75−100 mM (Figure 8, samples 12, 13), opposite the large aggregates found for KOH 2 M (Figure 4, samples 6, 7). Nonetheless, metallic salt concentrations ranging from 75 to 100 mM (set 4 in Table 1; Figure 8, samples 12, 13) kept exhibiting a strong tendency to aggregate even for KOH 20 M, so that the achievement of single nanoparticles required of shorter reaction times (4 h; set 5 in Table 1; Figure 8, sample 14). It should also be noted that decreasing particle size was accompanied by decreasing aspect ratio of the final particles (compare samples 8 and 10, Figure 5). This tendency has also been reported for hydrothermally synthesized $La(OH)_3$ nanorods.[40] Finally, at KOH concentrations of 26 M (sample 11), the above-mentioned trend changes and microparticles of average size of 59 nm are obtained. It is worth stressing that KOH may also play an additional role in the synthesis of $BaMnO_3$ because of the formation of an intermediate, a birnessite-type phase $K_{0.5}MnO_2 \cdot nH_2O$ having the desired Mn oxidation state in between the $[MnO_4]^{4-}$ and $Mn^{2+}$ precursors, by coproportionation reaction between $[MnO_4]^{4-}$ and $Mn^{2+}$.[4]

The achievement of $BaMnO_3$ nanoparticles of ca. 26−37 nm by hydrothermal synthesis is remarkable. Not only because $BaMnO_3$ nanoparticles have not been reported up to now but, even more, because the smallest nanomanganites reported to date (also by hydrothermal synthesis)[14]in other manganese-related systems, e.g., $La_{0.5}Ba_{0.5}MnO_3$, were larger (ca. 50−100 nm) and the particle size distribution broader. Furthermore, Urban et al[14] used a higher temperature than we did (300 versus 200 °C), but it is worth noting that increased temperatures might be required given the different composition of the nanomanganites ($La_{0.5}Ba_{0.5}MnO_3$ and $BaMnO_3$). Nonetheless, the use of lower temperatures is of tremendous interest for practical applications, making the synthesis more affordable in terms of energy and equipment (note that temperatures below 240 °C allow for the use of reactors having Teflon inner containers). Given the relevance of this issue, we further explored the suitability of hydrothermal synthesis at even lower temperatures (e.g., 150 °C, set #6, and sample 15 in Figure 8). TEM micrographs and XRD revealed that this low temperature was high enough for the preparation of single $BaMnO_3$ nanoparticles of ca. 20 nm.

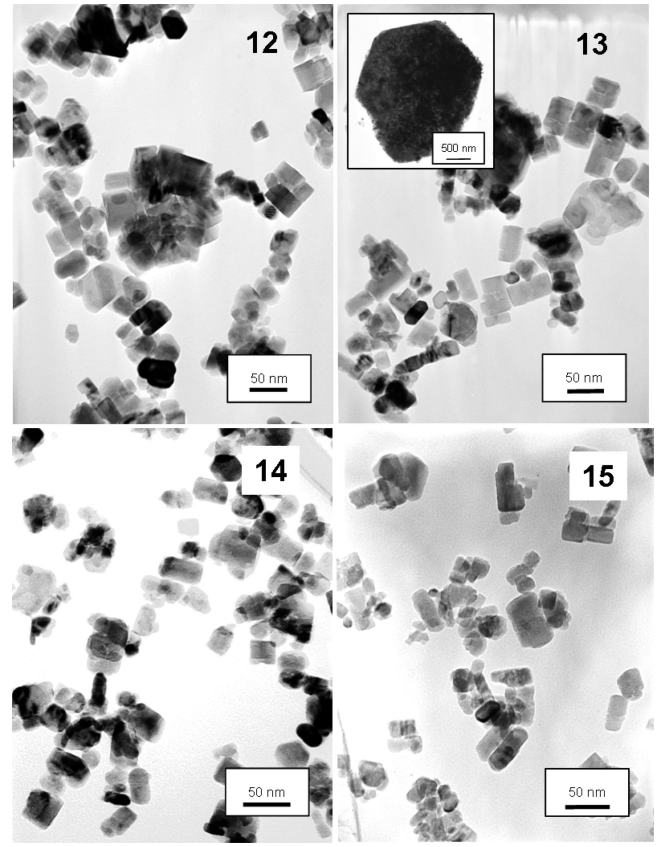


**Figure 8.** TEM micrographs of $BaMnO_3$ samples 12, 13, 14 and 15 of Table 1, corresponding to a fixed KOH concentration of 20 M. Comparison of images 12 and 13 show the small influence of metallic salts concentration. Aggregation and microcrystals favored at those metallic salts concentrations can be avoided by using shorter reaction times: (12), 24 h. and (14), 4 h. Temperatures as low as 150 °C are suitable for the synthesis of $BaMnO_3$ nanocrystals (sample 15).

To study the influence of the particle size in the magnetic properties, we performed a full characterization of 2H-$BaMnO_3$ using squid-magnetometer techniques. We recorded zero-field-cooled and field-cooled (ZFC-FC) scans, as well as 5 K isotherms under several conditions, in searching for an exchange bias phenomenology so specific of antiferromagnetic materials in intimate contact with ferromagnetic layers/patches.[41] This is to be expected if surface magnetism plays an important role, as is the case in nanoparticles composed by a core magnetically different from the outer layers or, alternatively, if there exists a number of uncompensated spins on a *n*-sublattice model in which the reduced coordination of surface spins leads to fundamental changes in the magnetic order throughout the particle.[42]

(39) Boistelle, R.; Astier, J. P. *J, Cryst. Growth* **1988**, *90*, 14–30.
(40) Wang, X.; Li, Y. *Angew. Chem., Int. Ed.* **2002**, *41* (24), 4790–4793.
(41) Nogués, J.; Sort, J.; Langlais, V.; Skumryev, V.; Suriñach, S.; Muñoz, J. S.; Baró, M. D. *Phys. Rep.* **2005**, *422*, 65–117.

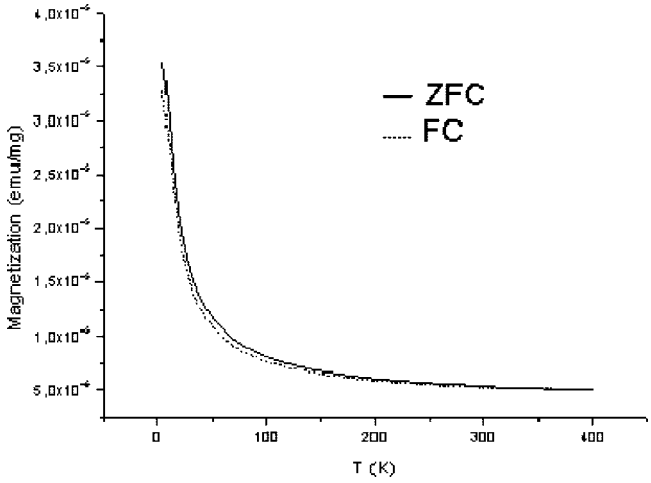


**Figure 9.** Representative plot (sample 10) of a ZFC-FC run of the magnetization versus temperature, as measured under 1000 Oe cooling and measuring field.

From magnetometry and neutron diffractions data, it has been reported that the bulk behaviour of 2H-$BaMnO_3$ exhibits the basic characteristics of an antiferromagnet, although no obvious antiferromagnetic peak is spotted in the temperature dependence of the magnetization.[8]

Figure 9 shows a representative (sample 10) plot of a ZFC-FC run of the magnetization versus temperature, as measured under 1000 Oe cooling and measuring field. The absence of singularities as well as a modest irreversibility is the most remarkable feature. As already mentioned, the ocurrence of an antiferromagnetic transition has been reported for bulk $BaMnO_3$. However, the nature of the AF ordering has been strongly debated. Although Christensen and Ollivier[8] proposed a collinear AFM model to fit their neutron diffraction (ND) data, Cussen and Battle,[43] from higher-resolution ND patterns, demonstrate the existence of canting. This canting in the *xy* plane would be a consequence of the triangular lattice formed by the Mn cations. Also, there is no consensus about the Néel temperature of the transition. Christensen and Ollivier locate the transition bellow 2.4 K, whereas the Cussen and Battle measurements render $T_N = 59$ K. The latter authors take the high $T_N$ as a strong point against the 1D character of the AF of 2H-oxides bellow room temperature, suggesting that the intrachain magnetic interactions cannot be considered negligible as compared to the intrachain interactions. However, the proposed 3D ordering below 59 K does not translate into a maximum in the *M* vs. *T* data, contrary to what it is expected for a long-ranged three-dimensional AF ordering. Christensen and Ollivier put forward the existence of a partial AFM order below 150 K and conjecture that a 1D AFM could be at the origin of their observations. Discrepancies between both groups could possibly be ascribed to the very different systhesis methods followed.[8,43] Our data in Figure 9 are more in accordance with those reported by Christensen and Ollivier because no hint of an AFM transition can be seen in the *M* vs. *T* plot, down to the lowest temperature explored (2 K).

From our data, the existence of some kind of ferromagnetic correlations is established in Figure 10, where representative hysteresis cycles measured at $T = 2$ K recorded after a 1000 Oe cooling and after a 20 kOe are depicted.

Two distinct characteristics are already apparent: although saturation is not reached, the cycle opens up rendering non-zero remanence and coercive field. Also a clear exchange bias (displacement of the center (0,0) of the hysteresis cicle when cooling the system under an applied external field), pointing out that the Néel transition has already taken place at this temperature. Both facts points toward the coexistence of FM correlations in addition to the dominant antiferromagnetism. From considerations about the role of uncompensated spins in the nanoparticle surface, it is plausible to think that our observations are a direct consequence of the downsizing of particles[44] and that our synthesis pathway has rendered an assembly of particles with dominant AFM correlations and some kind of FM interactions. Whether the FM fraction is located at the surface or it does exist throughout the nanoparticle is unknown but the interaction between the AFM and FM fractions is clearly assessed by the observed exchange bias effects.

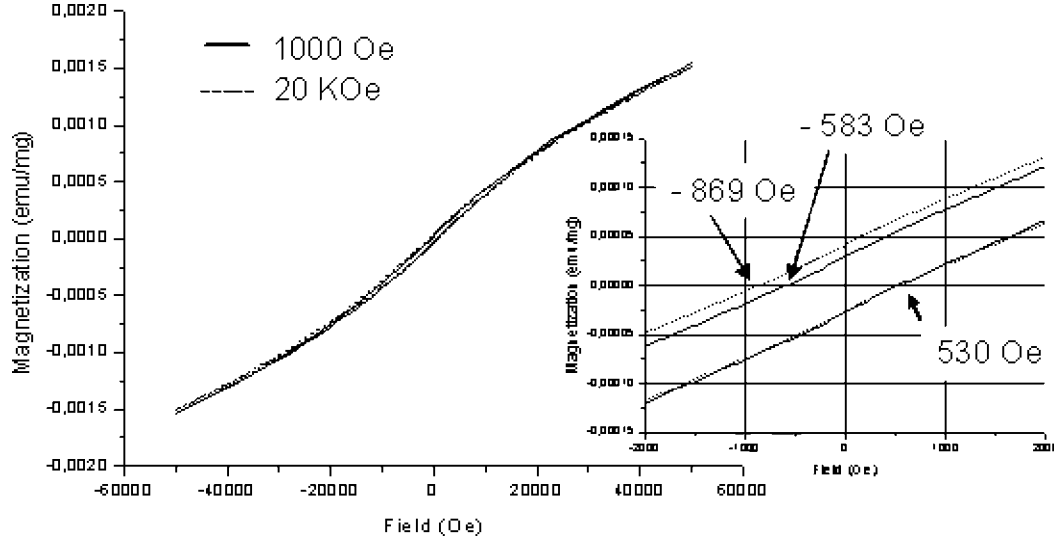


**Figure 10.** Representative hysteresis cycles (sample 14) measured at $T = 2$ K, recorded after a 1000 Oe and after a 20 kOe field cooling protocol. Inset: close up of the central region.

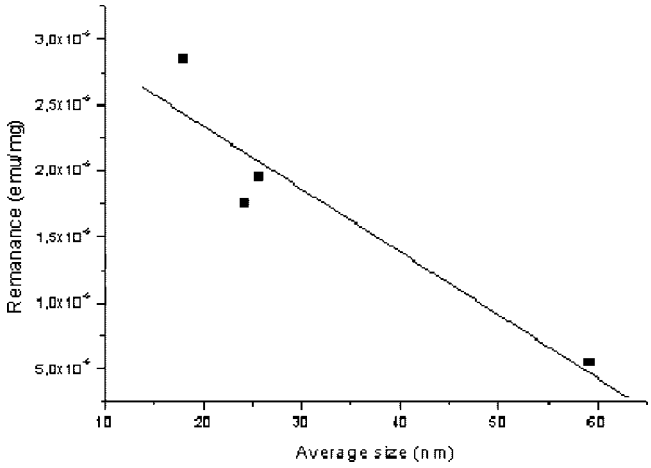


**Figure 11.** Remanence (emu/mg) vs average diameter (nm). The straight line should be interpreted only as a guide for the eye.

Although the distribution of particle size is not monodisperse in our samples, it is possible to extract some information on the average diameter dependence of the remanence, as it is shown in Figure 11. As the particle size decreases the remanence increases, pointing out that a stronger and larger ferromagnetic fraction develops. This is consistent with the fact that the smallest nanoparticle shows larger surface/volume ratios: smaller particles must contain a larger number of uncompensated spins in one of the sublattices of the antiferromagnet, enabling stronger FM correlations. The same behavior is observed from the measured magnetization at the highest measured field (50 KOe) (not shown).

An inverse trend is observed in the variation of the exchange bias field, $H_{eb}$, with the average size of the particles, as measured at 2 K after a 2 T field cooling. Small particles exhibit smaller $H_{eb}$ than the large particles (160 Oe and 363 Oe for 18-sample 14-and 59 nm-sample 11-average diameters, respectively). This is consistent with a weakening of the AFM interactions and enhancement of the FM interactions when the particle size decreases. As the diameter is reduced, AFM interactions become less efficient to induce exchange bias effects at a given temperature, as a result of a lower blocking temperature or a lower anysotropy.

## Conclusions

In this work, we have performed a careful study of the features governing 2H $BaMnO_3$ nanocrystals synthesis and stabilization under hydrothermal conditions. Thus, high KOH concentration has been found to be crucial for the synthesis of nanoparticles by both promoting fast precipitation of first nuclei and charging their surface ($OH^-$ anions attachment) that ultimately impedes nanoparticles aggregation. Meanwhile, metallic salt concentrations have a minor influence on final particle size and their increase (within the studied range) exhibited a certain tendency to favor aggregation and sintering effects. In any case, such a tendency can be hampered by using shorter reaction times. In regards to the reaction temperature, the study has demonstrated that temperatures of 200 °C and below (even 150 °C) are enough for nanoparticle formation, with minor differences on final particle size distribution. In particular, nanoparticle diameters have been finely tuned within the range ∼18−59 nm depending on the reaction parameters, while preserving narrow size distributions in every case. The good control on the particle size distribution within the nanometer scale has also allowed for the achievement of preliminary investigations of the size-dependent evolution of the magnetic phenomena in this family of compounds.

We consider that the decrease in the synthesis temperature to 150 °C, besides the good particle size control even for high precursor concentrations, opens the path for the consolidation of hydrothermal synthesis as a suitable route to prepare not-agglomerated, surface-free 2H $BaMnO_3$ nanocrystals and, eventually, of other types of mixed manganese oxide nanocrystals (e.g., $La_xBa_{1-x}MnO_3$).

**Acknowledgment.** Financial support through research Projects MAT2007-61954 (Ministerio de Ciencia e Innovación (MCINN), Spain) and PR34/07-15855 (Santander-Universidad Complutense, Spain) are acknowledged. A.Q. thanks the MCINN for financial support through a postgraduate grant.

CM9001306

(42) Kodama, R. H.; Berkowitz, A. E. *Phys. Rev. Lett.* **1999**, *59*, 6321.
(43) Cussen, E. J.; Battle, P. D. *Chem. Mater.* **2000**, *12*, 831.
(44) Néel, L. In *Low Temperature Physics*; De witt, C., Dreyfus, B., De Gennes, P. D., Eds.; Gordon and Beach: New York, 1962; p 213.

# CHAPTER 1.2

# Hydroxides Eutectic Route for the Preparation of Nanomanganites

In this chapter, the use of highly alkali media is extended to molten alkali salts in the absence of aqueous solvent. The strategy followed to obtain a fluid phase at mild temperature was the utilization of a mixture of alkali salts in its eutectic composition. As in the previous chapter, manganites were the target materials. Failed experiments for the preparation of pure $BaMnO_3$, $SrCO_3$ and $CaCO_3$ NPs are reported herein.

# Hydroxides Eutectic Route for the Preparation of Nanomanganites

## 1. Introduction

Perovskites are one of the families of oxides which have attracted most attention from the material science community.[1] The general formula unit is $ABO_3$, where A is a large cation, *e.g.* K, Sr, Ba, La, and B is a smaller one, *e.g.* Ti, Mn, Co, Ni, and they present a great compositional flexibility (around 90% of the metal elements form oxides with perovskite structure and also carbides, nitrides, halides and hydrides crystallize in this structural type). It is not surprising, then, the structural diversity exhibited by perovskites, from cubic (tri-dimensionals, 3D), to laminars (2D) and hexagonals (1D). As a consequence, a variety of interesting properties are found in perovskites, such as superconductivity; ferro-, piro- and piezoelectricity and colossal magnetoresistance.

Perovskite structure can be described in terms of a close-packed arrangement of $AO_3$ layers with B cations occupying octahedral sites. The stacking sequence of the $AO_3$ layers can be cubic (ABC), leading to the 3C-polytype; hexagonal (ABAB), leading to the 2H-polytype; or a combination of both, leading to numerous polytypes. In the 3C-polytype all $BO_6$ octahedra share corners (*i.e.* $SrTiO_3$), whereas the 2H-polytype is characterized by infinite strings of face-sharing $BO_6$ octahedra parallel to the c-axis, (*i.e.* $BaNiO_3$) (Figure 1). Hexagonal polytypes show both corner- and face-sharing octahedra; *e.g.* 4H-poltype presents a 1:1 apex:face sharing. Because 2H-type perovskites are less common than 3C-type ones due to unfavourable electrostatic cation repulsion associated with shorter B-B- distance in the former, hexagonal polytypes and their structure/properties correlations remain partially unexplored.[2]

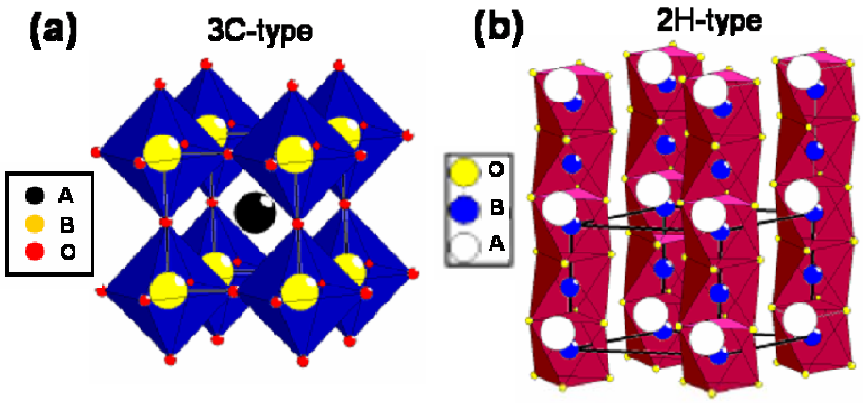


**Figure 1**. Representations of the ideal cubic or 3C-polytype **(a)** and ideal hexagonal or 2H-polytype **(b)** of the perovskite structure. Reproduction of ref. [2].

Manganese-based perovskites, commonly known as manganites, have attracted a great deal of interest due to their structural and phenomenological wealth. The ability of Mn to be stabilized in many oxidation states ($2^+$, $3^+$, $4^+$, $5^+$, $6^+$, $7^+$) allows many combinations of chemical doping and anion vacancies, leading to a multitude of multinary oxides which can show an interplay among spin, charge, and orbital degrees of freedom.[3-6] Thus, interesting properties are found in bulk manganites: colossal magnetoresistance ($La_{1-x}A'_xMnO_3$)[7], high permittivity ($BaMn_{0.5}Ti_{0.5}O_3$)[8] and giant magneto-elastic coupling in multiferroic hexagonal manganites.[9] The structure/properties exploration of hexagonal manganites particularly in their nanocrystalline forms urges the design of methods of preparation of nanomanganites.

Classical molten salt synthesis is especially suitable for the achievement of multinary oxides such as bulk manganites.[10-16] Its adaptation for the preparation of the nanostructured counterparts requires adopting the fundamental strategies for the achievement of nanoparticles (NPs): low temperatures of reaction and/or the use of suitable surface protection, either electrostatic or steric. In this sense, the use of a non-ionic surfactant in molten NaCl at 820 ºC has been reported to allow the preparation of single-crystalline $BaTiO_3$ (nanowires of diameter ~ 50-80 nm) and $SrTiO_3$ (nanocubes of edge length ~ 80 nm) perovskites, although the high temperature resulted in aggregation of the particles.[17, 18] Decreasing of the melting temperature of the salts, and subsequently of the reaction temperature, can be achieved by the use of salt mixtures in its eutectic composition, whose melting point is much lower than the corresponding to the individual salts. In this sense, Hu *et al.* reported the preparation of $BaMnO_3$ nanorods (tailored width –30-100 nm– and length –100-1000 nm–), $BaMnO_3$ NPs (diameter 50 nm) and $BaTi_{0.5}Mn_{0.5}O_3$ elliptical nanorods (20-50 nm width and 100-500 nm length) through the use of molten NaOH/KOH eutectic mixture.[19, 20] While the melting points of NaOH and KOH are 323 and 360 ºC, respectively, the eutectic composition at molar ratio NaOH/KOH = 51.5/48.5 presents a melting point at 165 ºC (Figure 2), allowing a low-temperature reaction and the achievement of NPs even without the addition of organic capping agents. On the basis of such report and our experience on the synthesis of $BaMnO_3$ NPs in high alkali medium under hydrothermal conditions[21] (chapter 1.1), we considered highly desirable to study the parameters of the hydroxide eutectic route and their correlation with the hydrothermal pathway in the elaboration of 2H $BaMnO_3$ [22] NPs. Additionally, we aimed to synthesize through the

hydroxide route other nanosized manganites: $SrMnO_3$, which adopts a 4H polytype in the bulk,[23] and $CaMnO_3$, whose bulk adopts a distorted cubic perovskite structure.[24]

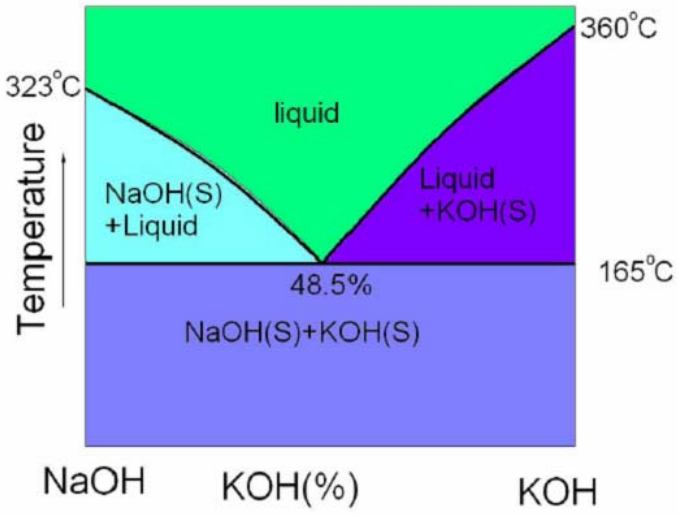


**Figure 2.** Schematic phase diagram of the KOH/NaOH mixture (reproduction of reference [20]).

## 2. Experimental Section

KOH (Merck, pellets > 85 %), NaOH (Fluka, ≥ 98 %), $BaCl_2$ (Aldrich, 99.9%), $SrCl_2{\cdot}6H_2O$ (Merck, > 99%), $Sr(NO_3)_2$ (Merck, > 99%), $CaCl_2{\cdot}2H_2O$ (Aldrich, >99%), $Ca(NO_3)_2{\cdot}\ 4H_2O$ (Sigma-Aldrich, >99%), $MnO_2$ (Aldrich, 99.999 %), $MnCl_2{\cdot}4H_2O$ (Aldrich, 99.99 %) and $KMnO_4$ (Aldrich, 99%) were used as-received. A Teflon vessel equipped with a Teflon cap was loaded with 20 g of the hydroxide mixture KOH/NaOH in its eutectic composition (molar ratio NaOH/KOH = 51.5/48.5), followed by the addition of 0.5 mmol of alkaline earth salt and 0.5 mmol of $MnO_2$. Alternatively, $MnO_2$ was replaced by a mixture of $MnCl_2{\cdot}4H_2O$:$KMnO_4$ in the 6:4 molar ratio suitable for a final oxidation state $Mn^{4+}$ in the manganite product. The closed Teflon vessel was introduced in an oven, which was preheated at 170-200 ºC. Reaction times comprehended between 20 and 216 h. After cooling down to room temperature, the solid product was dissolved with deionized water, repeatedly washed and centrifuged and further purified by dialysis. The final brown powder was dried in a furnace at temperatures between 35 and 90 ºC.

For the reaction performed under a nitrogen atmosphere, the Teflon vessel was covered with a septum in which two needles were injected: a stainless steal needle for

the exit of gas and a Teflon needle submerged into the reaction mixture accounting for the gas entrance. After flowing nitrogen for ~ 2 h 30 min, the vessel was heated in an oil bath. Nitrogen flow was kept during the whole reaction. Once the reaction had finished, the product was recovered and purified as described above.

Characterization of the powders was realized by means of powder X-ray diffraction (XRD), transmission electron microscopy (TEM) and energy-dispersive X-ray analysis (EDX).

## 3. Results and discussion

### 3.1. Synthesis of $BaMnO_3$ nanoparticles

We first attempted to reproduce the experimental procedure reported by Hu *et al.*,[19] *i.e.* we performed the reaction with $BaCl_2$ and $MnO_2$ precursors at different times and reaction temperatures, as summarized in Table 1, # 1-4. In all the cases, either $BaCO_3$ (witherite, JCPDS 00-005-0378) or mixtures of $BaCO_3$ and $BaMnO_3$ (JCPDS 01-071-1595) were obtained as the reaction products, as detected by XRD (Table 1, Figure 3).

**Table 1.** Reaction conditions of the hydroxide eutectic route for the preparation of $BaMnO_3$ NPs and XRD results of the as-prepared products.

| Experi-ment # | Ba reactant | Mn reactant | T (ºC) | t (hours) | Atmos-phere | Product (XRD) |
|---|---|---|---|---|---|---|
| 1 | $BaCl_2$ | $MnO_2$ | 170 | 20 | air | $BaCO_3$ + $BaMnO_3$ |
| 2 | $BaCl_2$ | $MnO_2$ | 170 | 98 | air | $BaMnO_3$ + $BaCO_3$ |
| 3 | $BaCl_2$ | $MnO_2$ | 170 | 216 | air | $BaCO_3$ |
| 4 | $BaCl_2$ | $MnO_2$ | 200 | 72 | air | $BaMnO_3$ + $BaCO_3$ |
| 5 | $BaCl_2$ | $MnO_2$ | 180 | 72 | nitrogen | $BaMnO_3$ + $BaCO_3$ |
| 6 | $BaCl_2$ | $KMnO_4$/ $MnCl_2 \cdot 4H_2O$ | 170 | 88.5 | air | $BaCO_3$ + $BaMnO_3$ |

It is worth commenting on the morphology of the as-obtained products and we will show the results corresponding to the sample treated at 170 ºC during 98 h – experiment 2 of Table 1– (Figure 4). Three different morphologies are clearly distinguished:

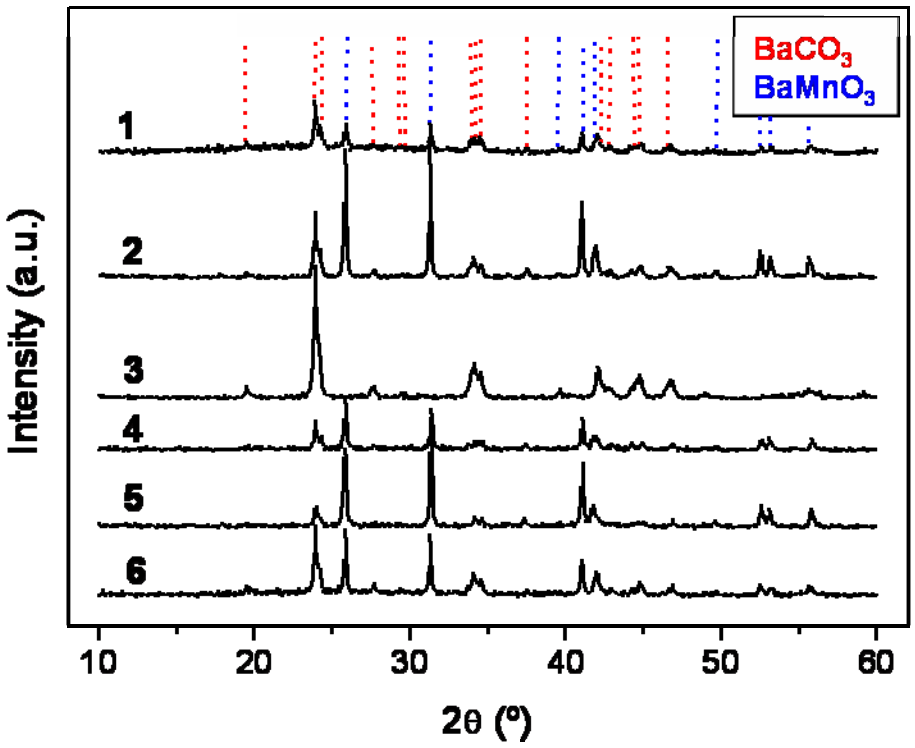


**Figure 3.** XRD patterns corresponding to all the samples described in Table 1.

- Crystals type 1: Nanorods of highly dispersed sizes and aspect ratios: diameters of ~ 50-300 nm and lengths of ~ 400-1800 nm. The corresponding cationic composition determined by EDX is Ba:Mn = 1:1 within experimental error, suggesting a $BaMnO_3$ phase.
- Crystals type 2: Micro-crystals (size > 1000 nm) whose cationic composition Ba:Mn is 9:1. These crystals are suggested to correspond to the $BaCO_3$ phase detected by XRD as the main product.
- Chapter type 3: aggregated NPs (~5 nm) whose cationic composition Ba:Mn is < 1. Such particles could be made of amorphous manganese oxides which would not be detectable by XRD and would compensate the preponderance of Ba relative to Mn in the two previous types of crystals (note that the reaction mixture was prepared with a 1:1 Ba:Mn ratio).

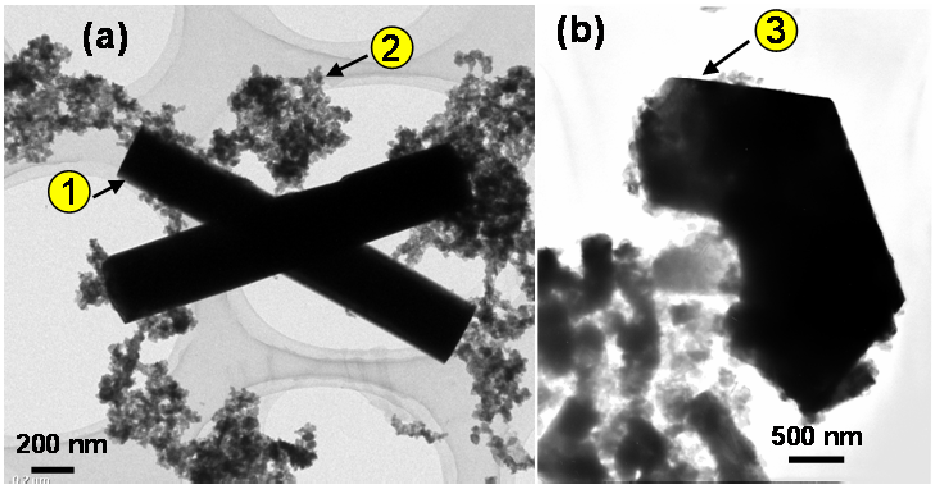


**Figure 4.** (a) and (b) TEM images of sample # 2 of Table 1. Three types of crystals (marked as 1, 2 and 3) with different morphology and cationic composition can be recognized.

It is worth mentioning the radical change of color presented by the waters during the subsequent washing steps: turquoise blue and fuchsia for the first and latter washings, respectively (Figure 5). While turquoise blue could stem from the formation of $K_2MnO_4$ as a stable product in alkali medium,[25] fuchsia coloration of the final waters is representative of $KMnO_4$, which is stable upon neutral pH. Interestingly, the presence of such compounds with peculiar colorings evidences the removal of manganese in the washing steps and is in good accordance with the Ba:Mn > 1 ratio associated to the two main reaction products detected by XRD, *i.e.* $BaCO_3$ and $BMnO_3$.

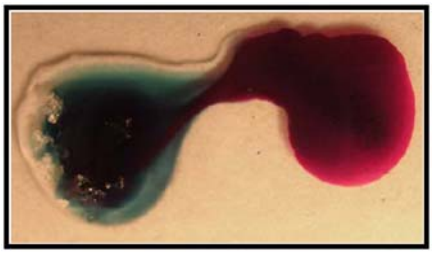

**Figure 5.** Colors of the washing waters: first (left) and last (right) washings, possibly associated to $K_2MnO_4$ and $KMnO_4$ species, respectively.

The crystallization of $BaCO_3$ is associated with the uptake of atmospheric $CO_2$. As it is well-known, alkali solutions show a strong tendency to uptake the $CO_2$ from the air and fix it as carbonate groups ($CO_3^{2-}$) due to the displacement of the dissociating equilibrium of carbonic acid ($H_2CO_3$) according to the principle of L'Châtelier:

$$H_2O + CO_2 \rightleftharpoons H_2CO_3 \qquad [1]$$

$$H_2CO_3 \rightleftharpoons H^+ + HCO_3^- \rightleftharpoons \begin{matrix} 2\ H^+ \\ 2\ OH^- \end{matrix} + CO_3^{2-} \rightarrow 2\ H_2O \qquad [2]$$

If alkaline earth elements are present in solution, the crystallization of the corresponding alkaline earth carbonate is very prone to take place.

In order to avoid the formation of undesired $BaCO_3$, several trials were attempted. First, the reaction was performed under a nitrogen atmosphere (experiment # 5, Table 1). XRD characterization of the product reveals the formation of both $BaMnO_3$ and $BaCO_3$ phases, although the amount of carbonate relative to manganite is minimized in respect to the rest of experiments (Figure 3). Since the removal of $CO_2$ should be assured with the nitrogen atmosphere, the presence of $BaCO_3$ could be associated with formation of $CO_3^{2-}$ groups in the small amounts of water adsorbed in the highly hygroscopic NaOH and KOH starting salts. Regardless of the impure product, it is worth inspecting the morphology of the as-prepared manganite crystals. Figure 6 NPs evidences the coexistence of NPs (~5 nm) and highly size-dispersed rods, which are assigned to a $BaMnO_3$ phase on the basis of EDX 1:1 Ba:Mn ratio. Interestingly, imperfectly fused NPs seem to be building up the rods, suggesting a self-assembly-mediated growth of the anisotropic structures, as previously reported for the hydrothermal synthesis of $BaMnO_3$ nanostructures in high alkali medium (chapter 1.1).[21]

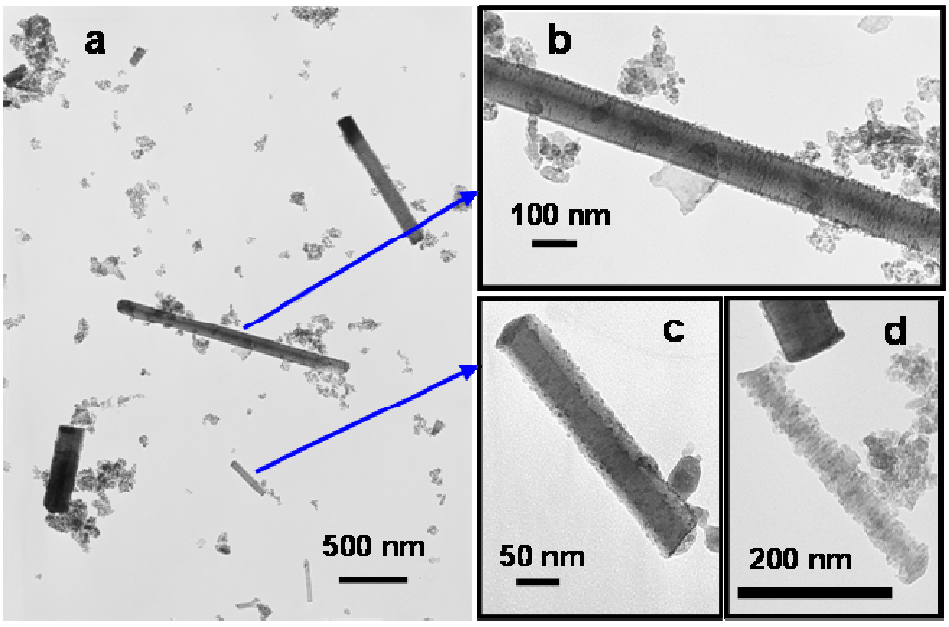


**Figure 6.** (a) TEM image corresponding to sample # 5 of Table 1 showing NPs and nanorods with a 1:1 Ba:Mn composition. (b) and (c) Magnification of the nanorods indicated in (a), showing an imperfect fusing of self-assembled NPs. (d) nanorod formed by self-assembled NPs.

A Further attempt to prevent contamination of the desired product with $BaCO_3$ included the substitution of $MnO_2$ reactant by the $MnCl_2{\cdot}4H_2O/KMnO_4$ mixture successfully employed in the hydrothermal synthesis in alkali medium of $BaMnO_3$ NPs (chapter 1.1), although such a trial also failed in the achievement of pure $BaMnO_3$ (experiment # 6, Table 1). Finally, another attempt to purify the $BaMnO_3$ from the $BaCO_3$ + $BaMnO_3$ mixtures obtained in previous experiments consisted in the selective dissolution of $BaCO_3$ phase at acid pH, although such a procedure did not lead to the desired target either.

### 3.1. Synthesis of $SrMnO_3$ nanoparticles

Since the different trials of synthesizing $BaMnO_3$ NPs in hydroxide eutectic mixture were not successful, we attempted to prepare $SrMnO_3$ by the same route. Table 2 collects the list of experiments performed and Figure 7 (a) shows the XRD patterns of the as-prepared products.

**Table 2.** Reaction conditions of the hydroxide eutectic route for the preparation of $SrMnO_3$ and $SrCO_3$ NPs and XRD results of the as-prepared products.

| Experiment # | Sr reactant | Mn reactant | T (ºC) | t (hours) | Atmosphere | Product (XRD) |
|---|---|---|---|---|---|---|
| 7 | $SrCl_2{\cdot}6H_2O$ | $MnO_2$ | 170 | 96 | air | $SrCO_3$ |
| 8 | $SrCl_2{\cdot}6H_2O$ | $MnO_2$ | 170 | 192 | air | $SrCO_3$ |
| 9 | $Sr(NO_3)_2$ | $MnO_2$ | 170 | 96 | air | $SrCO_3$ |
| 10 | $Sr(NO_3)_2$ | -- | 170 | 89 | air | $SrCO_3$ |
| 11 | $Sr(NO_3)_2$ | -- | 200 | 24 | air | $SrCO_3$ |

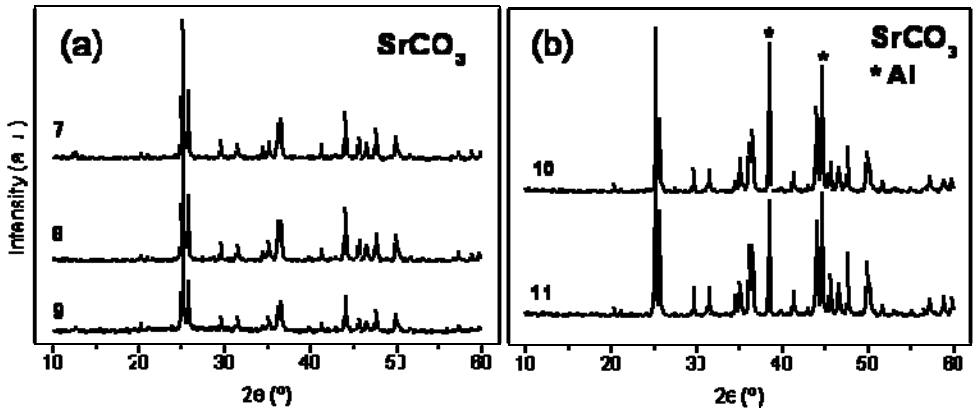


**Figure 7.** XRD patterns corresponding to all the samples described in Table 2. All of them are monophasic and can be assigned to $SrCO_3$, whiterite. Highlighted Al peaks are due to the holder.

Either $SrCl_2 \cdot 6H_2O$ and $Sr(NO_3)_2$ strontium reactants led to the formation of $SrCO_3$ (strontianite, JCPDS 01-084-1778) as the only product of reaction both at 170 ºC for 96 and 192 h for the former reactant and at the same temperature during 96 h for the latter (experiments # 7, 8 and 9, respectively). The results are in agreement with the lower solubility product of $SrCO_3$ ($K_{sp} = 5.60 \times 10^{-10}$) as compared to $BaCO_3$ ($K_{sp} = 2.58 \times 10^{-9}$) and also seem to suggest a lower precipitation capacity of $SrMnO_3$ as compared to $BaMnO_3$ within the hydroxides mixture. In order to investigate the presence of manganese in the as-obtained strontium carbonate (note that no manganese-containing compound was detected by XRD), sample # 7 was thermally treated at 950 ºC for 1 h. Figure 8 shows the XRD pattern of the annealed sample, which fits well with strontium manganese oxide $Sr_7(Mn_4O_{15})$ (JCPDS 01-081-0966). Thus, the presence of amorphous manganese compounds together with the crystalline $SrCO_3$ phase is demonstrated. Nevertheless, the ratio Sr:Mn >1 in the resulting oxide indicates the incomplete incorporation of manganese in the final powder, which is in agreement with the dissolution of manganate anions during washing steps, as evidenced by the color of the washing waters in a similar fashion to those described above for the $BaMnO_3$ experiments.

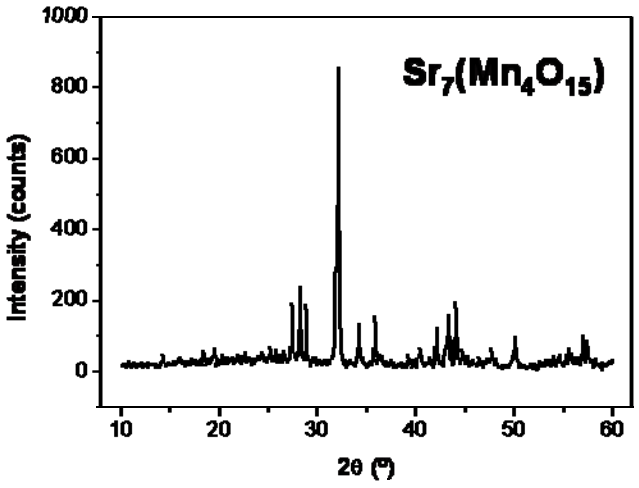


**Figure8.** XRD pattern corresponding to the sample obtained after annealing the sample # 7 (Table 2) at 950 ºC during 1 h. The monophasic pattern can be assigned to $Sr_7(Mn_4O_{15})$.

TEM characterization of sample # 7 (Figure 9, (a)) reveals quite inhomogeneous morphologies of the $SrCO_3$ particles, ranging from aggregates of NPs of < 20 nm to

rods of diameter ~ 350-1000 nm and length ~ 1000-4000 nm as well as large (micrometer-scale) aggregates of particles.

The presence of rods was encouraging for the achievement of monodisperse pure $SrCO_3$, so we performed the synthesis protocol without the addition of Mn reactant in an attempt to obtain pure $SrCO_3$ with anisotropic morphologies (experiments # 10 and 11 of Table 2). XRD characterization (Figure 7 (b)) reveals the formation of pure $SrCO_3$ for samples 10 and 11. TEM images of corresponding samples (Figure 9, (b) and (c)) shows shape-less, ~ isotropic NPs of size ≤ 1000 nm (sample 10) and ≥ 500 nm (sample 11). The results evidence the lack of tendency of $SrCO_3$ to precipitate as regular anisotropic structures in the absence of manganese reactant.

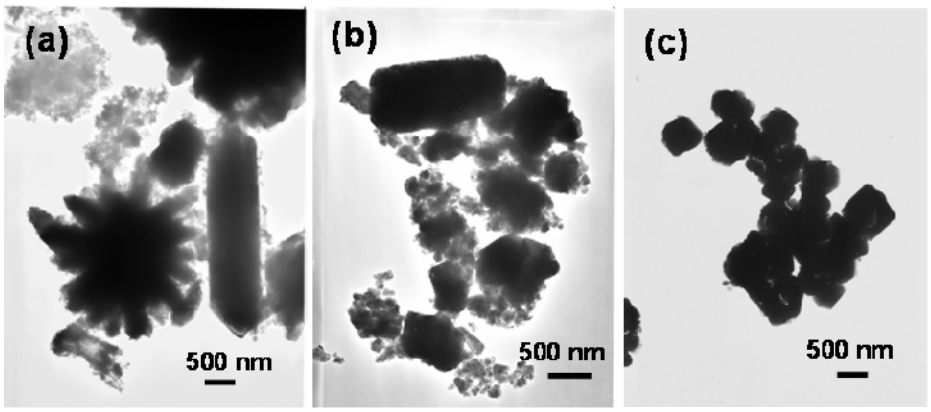


**Figure 9.** (a), (b), (c) TEM images of samples # 7, 10 and 11, respectively, of Table 2.

### 3.1. Synthesis of $CaMnO_3$ nanoparticles

Since the synthesis of manganites by hydroxides eutectic route faced the persistent problem of carbonate precipitation, we attempted to prepare $CaMnO_3$ NPs given the larger solubility product of $CaCO_3$ ($K_{sp} = 4.96 \times 10^{-9}$) as compared to $BaCO_3$ and $SrCO_3$ ($K_{sp} = 2.58 \times 10^{-9}$ and $K_{sp} = 5.60 \times 10^{-9}$, respectively). Table 3 summarizes the list of experiments and Figure10 shows the XRD patterns of the as-prepared products.

XRD results reveals that the reaction of $CaCl_2 \cdot 2H_2O$ and $MnO_2$ at 170 ºC during different reaction times (experiments # 12-14) lead to amorphous powders, while the experiment # 15, performed with variations of the hydroxide eutectic method (adding 3 ml of water to the mixture of salts and performing the reaction in a Teflon-lined

autoclave), led to pure $CaCO_3$ (calcite, JCPDS 00-005-0586). The results indicate that neither $CaCO_3$ nor $CaMnO_3$ precipitate in the hydroxide eutectic synthetic mixture under the conditions explored.

**Table 3.** Reaction conditions of the hydroxide eutectic route for the preparation of $CaMnO_3$ NPs and XRD results of the as-prepared products.

| Experiment # | Sr reactant | Mn reactant | T (ºC) | t (hours) | Atmosphere | Product (XRD) |
|---|---|---|---|---|---|---|
| 12 | $CaCl_2 \cdot 2H_2O$ | $MnO_2$ | 170 | 36 | air | No crystalline (undetermined reflexions at 12.3º, 25º) |
| 13 | $CaCl_2 \cdot 2H_2O$ | $MnO_2$ | 170 | 88.5 | air | No crystalline |
| 14 | $CaCl_2 \cdot 2H_2O$ | $MnO_2$ | 170 | 192 | air | No crystalline |
| * 15 (autoclave) | $Ca(NO_3)_2 \cdot 4H_2O$ | $MnO_2$ | 170 | 88 | * | $CaCO_3$ + (undetermined reflexions at 12.3º, 25º) |

*Experiment # 15 was performed with slight modifications in respect to typical hydroxide eutectic method: 3 ml of water were added to the reaction mixture and the reaction was performed in a Teflon-lined autoclave.

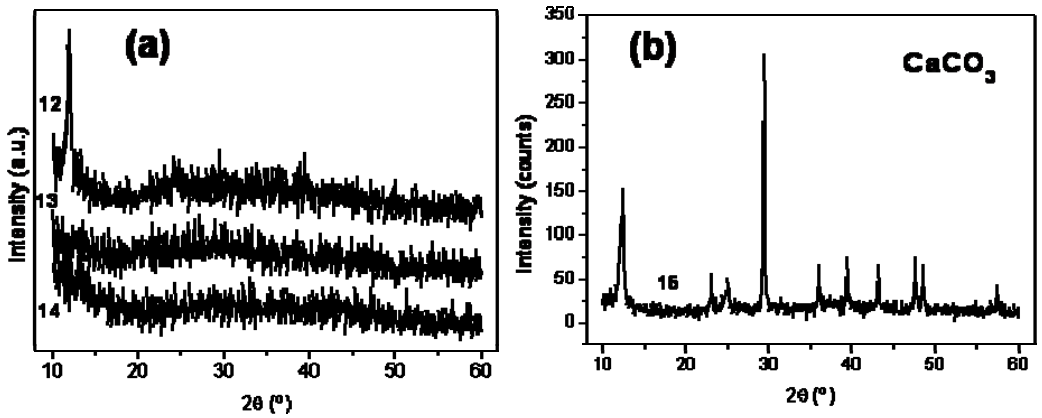


**Figure 10.** (a) and (b) XRD patterns corresponding to all the samples described in Table 3. Peaks at 12.3 and 25 º for sample # 12 are undetermined reflexions. XRD pattern corresponding to sample # 15 can be assigned to $CaCO_3$, calcite.

## 4. Conclusions

We did not succeed in the reproduction of the results obtained by Hu *et al.*[19] neither in terms of composition or shape and size of the as-prepared particles; mixtures of $BaCO_3$ and $BaMnO_3$ were always obtained as reaction products and the shape and

size of the $BaMnO_3$ NPs were highly dispersed. Attempts to eliminate $BaCO_3$ microcrystals both before and after reaction were unsuccessful, although the content of carbonate in the product was decreased by performing the reaction under a nitrogen atmosphere. The extension of the method to $SrMnO_3$ and $CaMnO_3$ manganites did not lead to the formation of the desired products, either. Actually, $BaMnO_3$ formation was allowed through such a synthetic route, while both $SrMnO_3$ and $CaMnO_3$ precipitation did not take place. Carbonate crystallization was the main problem for obtaining pure $BaMnO_3$ NPs and the tendency to carbonate precipitation within the hydroxide eutectic mixture seemed to be $SrCO_3$ > $BaCO_3$ > $CaCO_3$, which is in consonance with the solubility products tabulated for aqueous medium.

## References


1. Mitchell, R. H., *Perovskites Modern and Ancient*. Ed. Almaz Press Inc., Canada, 2002.
2. Miranda Pérez, L. Perovskitas hexagonales: una cantera fascinante de óxidos funcionales. Universidad Complutense de Madrid, Madrid, 2010.
3. Millis, A. J., Lattice effects in magnetoresistive manganese perovskites. *Nature* **1998,** 392, (6672), 147-150.
4. Moreo, A.; Yunoki, S.; Dagotto, E., Phase separation scenario for manganese oxides and related materials. *Science* **1999,** 283, (5410), 2034-2040.
5. Tokura, Y.; Nagaosa, N., Orbital physics in transition-metal oxides. *Science* **2000,** 288, (5465), 462-468.
6. Salamon, M. B.; Jaime, M., The physics of manganites: Structure and transport. *Reviews of Modern Physics* **2001,** 73, (3), 583-628.
7. Von Helmolt, R.; Wecker, J.; Holzapfel, B.; Schultz, L.; Samwer, K., Giant negative magnetoresistance in perovskitelike $La_{2/3}Ba_{1/3}MnO_x$ ferromagnetic films. *Physical Review Letters* **1993,** 71, (14), 2331-2333.
8. Keith, G. M.; Kirk, C. A.; Sarma, K.; Alford, N. M.; Cussen, E. J.; Rosseinsky, M. J.; Sinclair, D. C., Synthesis, crystal structure, and characterization of $Ba(Ti_{0.5}Mn_{0.5})O_3$: A high permittivity 12R-type hexagonal perovskite. *Chemistry of Materials* **2004,** 16, (10), 2007-2015.
9. Lee, S.; Pirogov, A.; Kang, M. S.; Jang, K. H.; Yonemura, M.; Kamiyama, T.; Cheong, S. W.; Gozzo, F.; Shin, N.; Kimura, H.; Noda, Y.; Park, J. G., Giant magneto-elastic coupling in multiferroic hexagonal manganites. *Nature* **2008,** 451, (7180), 805-U4.
10. Hayashi, Y.; Kimura, T.; Yamaguchi, T., Preparation of rod-shaped $BaTiO_3$ powder. *Journal of Materials Science* **1986,** 21, (3), 757-762.
11. Yoon, K. H.; Cho, Y. S.; Kang, D. H., Molten salt synthesis of lead-based relaxors. *Journal of Materials Science* **1998,** 33, (12), 2977-2984.
12. Kojima, T.; Nomura, K.; Miyazaki, Y.; Tanimoto, K., Synthesis of various $LaMO_3$ perovskites in molten carbonates. *Journal of the American Ceramic Society* **2006,** 89, (12), 3610-3616.
13. Hungría, T.; Algueró, M.; Castro, A., Synthesis of nanosized $(1-x)NaNbO_{3-x}SrTiO_3$ solid solution by mechanochemical activation, processing of ceramics, and phase transitions. *Chemistry of Materials* **2006,** 18, (22), 5370-5376.
14. Lubyova, Z.; Danek, V., Formation mechanism, nucleation and crystallization of $Li_2TiO_3$ from fused salts. *Ceramics - Silikaty* **1992,** 36, (1), 21-25.
15. Lubyova, Z.; Danek, V., Reaction mechanism and kinetics of $SrTiO_3$ crystal growth in molten alkali metal chlorides medium. *Ceramics - Silikaty* **1992,** 36, (4), 181-185.
16. Battisha, I. K.; Speghini, A.; Polizzi, S.; Agnoli, F.; Bettinelli, M., Molten chloride synthesis, structural characterisation and luminescence spectroscopy of ultrafine $Eu^{3+}$-doped $BaTiO_3$ and $SrTiO_3$. *Materials Letters* **2002,** 57, (1), 183-187.
17. Mao, Y.; Banerjee, S.; Wong, S. S., Large-Scale Synthesis of Single-Crystalline Perovskite Nanostructures. *Journal of the American Chemical Society* **2003,** 125, (51), 15718-15719.

18. Mao, Y.; Wong, S. S., Composition and shape control of crystalline $Ca_{1-x}Sr_xTiO_3$ perovskite nanoparticles. *Advanced Materials* **2005,** 17, (18), 2194-2199.
19. Hu, C. G.; Liu, H.; Lao, C. S.; Zhang, L. Y.; Davidovic, D.; Wang, Z. L., Size-manipulable synthesis of single-crystalline $BaMnO_3$ and $BaTi_{0.5}Mn_{0.5}O_3$ nanorods/nanowires. *Journal of Physical Chemistry B* **2006,** 110, (29), 14050-14054.
20. Liu, H.; Hu, C.; Wang, Z. L., Composite-hydroxide-mediated approach for the synthesis of nanostructures of complex functional-oxides. *Nano Letters* **2006,** 6, (7), 1535-1540.
21. Querejeta, A.; Varela, A.; Parras, M.; Del Monte, F.; García-Hernández, M.; González-Calbet, J. M., Hydrothermal synthesis: A suitable route to elaborate nanomanganites. *Chemistry of Materials* **2009,** 21, (9), 1898-1905.
22. Cussen, E. J.; Battle, P. D., Crystal and magnetic structures of 2H $BaMnO_3$. *Chemistry of Materials* **2000,** 12, (3), 831-838.
23. Battle, P. D.; Gibb, T. C.; Jones, C. W., The structural and magnetic properties of $SrMnO_3$: A reinvestigation. *Journal of Solid State Chemistry* **1988,** 74, (1), 60-66.
24. Poeppelmeier, K. R.; Leonowicz, M. E.; Scanlon, J. C.; Longo, J. M.; Yelon, W. B., Structure determination of $CaMnO_3$ and $CaMnO_{2.5}$ by X-ray and neutron methods. *Journal of Solid State Chemistry* **1982,** 45, (1), 71-79.
25. Ferguson, R. H.; Lerch, W.; Day, J. E., Permanganate decomposition in alkaline media. *Contribution from the Chemical Laboratory of The Ohio State University* **1931,** 53, 126-137.
26. It is worth noting that a total of ten experiences were performed with small variations of the experimental setup aiming to optimize the nitrogen atmosphere efficiency, but none of them resulted in the elimination of carbonate.

IV. Chapter 1.2

# CHAPTER 1.3

# Hydroxides Eutectic Route for the Synthesis of NiO Nanooctahedra

The hydroxides eutectic route previously described is studied herein for the synthesis of binary compositions. Specifically, rock-salt NiO nanocrystals with octahedral shapes were successfully prepared. An assessment of the role of the highly ionic medium in the formation and stabilization of such morphologies is reported. Further work is still needed to better understand the suitability of such a medium as a shape-directing agent of binary nanocrystals with rock-salt structure. Also, the properties of the unusual octahedral geometries of NiO nanoparticles remain still unexplored.

.

# Hydroxides Eutectic Route for the Synthesis of NiO Nanooctahedra

## 1. Introduction

Control over the shape of nanocrystals (NCs) is one of the arenas of nanoscience which has attracted most attention[1] due to the shape-dependent properties of NCs. Apart from crystalline structures with low symmetry lattice, which exhibit an intrinsic tendency towards anisotropic growth fashions, control over the shape of symmetric crystalline materials, such as rock-salt structures, can be attained through the use of capping agents, which are selectively adsorbed to different crystal faces leading to their distinct growth rates. In particular, cubic rock salt crystals of binary compounds can have non-polar and polar faces opening the path to their selective stabilization by means of charged moieties.

Highly ionic reaction media such as molten salts[2,3] or ionic liquids[4,5] are a current focus of attention for the synthesis of NCs.[6] Their peculiar properties such as low surface tension and high polarity are key factors for the formation and stabilization of NCs. A recent contribution in this field is the synthesis of complex oxides nanostructures in NaOH/KOH eutectic mixture.[7] However, since the seminal paper reporting on this general method of synthesis, the flexibility of the route has been mainly demonstrated in terms of complex composition and structure of the products; the potential of the hydroxide eutectic mixture for the synthesis of binary metal oxides is restricted to $Fe_3O_4$, whose structure is spinel.[7] Furthermore, the role of such a highly ionic medium in the shape of the resulting NCs has not been explored.

Herein we extend the applicability of the hydroxide general route to the preparation of nano-sized NiO, a binary oxide with cubic structure and a multitude of applications[8-10], particularly aiming to study the influence of the highly ionic medium in the morphology of the resulting NCs.

## 2. Experimental Section

KOH (Merck, pellets > 85 %), NaOH (Fluka, ≥ 98 %) and $Ni(NO_3)_2 \cdot 6H_2O$ (Fluka, 98.5 %) were used as-received. Amounts of 20 g of hydroxides mixture in its eutectic composition (molar ratio NaOH/KOH = 51.5/48.5) and 1 mmol (0.2908 g) of nickel salt were loaded into a Teflon vessel, which was closed and put into an oven preheated at 200 ºC. After 29 h of reaction, the mixture had a black color, so indicative of the crystallization of NiO. Once cooled down to room temperature, the product was isolated by dissolving the hydroxides with deionized water and repeated cycles of washing and centrifuging. The final black powder was dried in a furnace at 70 ºC.

Characterization of the powder was realized by means of powder X-ray diffraction (XRD) and transmission electron microscopy (TEM).

## 3. Results and Discussion

Powder XRD characterization reveals the presence of NiO (JCPDS 00-47-1049) as the only crystalline product of reaction (Figure 1). Crystal size calculated from XRD data by the Scherrer method for the most intense (200) peak is 43 nm. An inspection to the morphology of the NiO NCs was done by TEM (Figure 2), which shows the presence of octahedral, square and rhomboidal morphologies, all of them in good agreement with the two-dimensional (2D) projection so typical of TEM for octahedral morphologies. Actually, for the square 2D projections, the darker contrast in the centre corresponds to the largest crystal thickness associated to the largest apex-to-apex dimension, while the contrast becomes lighter towards the edges, where the crystal thickness is minimal. Apart from the octahedra, whose diameter associated to the square projection ranges from ~ 100 to 265 nm, some NPs of ~ 10-30 nm of size are also found.

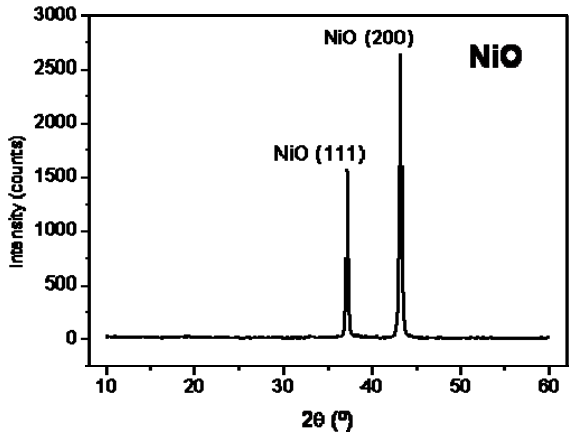


**Figure 1.** XRD pattern of the as-prepared powder, corresponding to monophasic NiO.

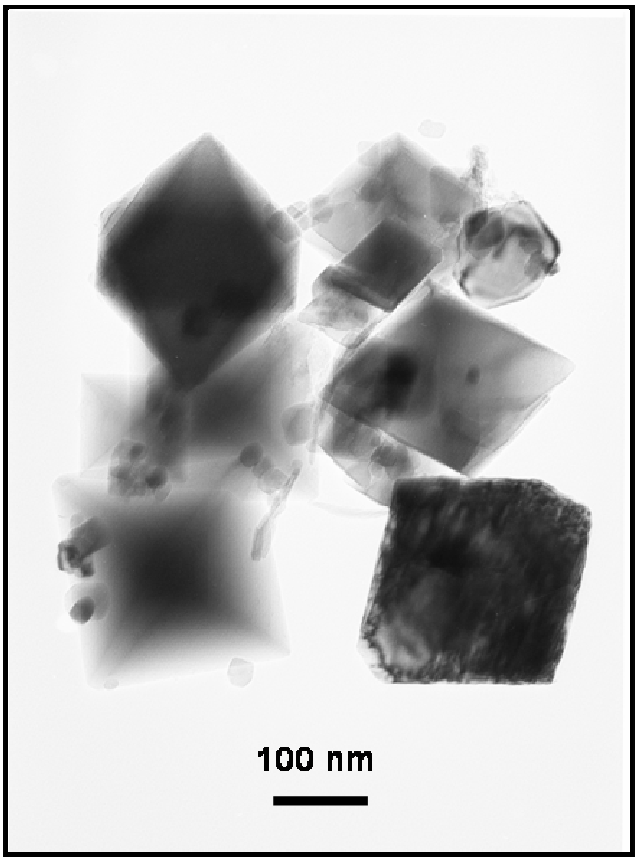


**Figure 2.** TEM image of the as-prepared NiO NCs. Octahedral morphologies are clearly observed.

The mechanism of crystallization of NiO is probably associated to the initial formation of $Ni(OH)_2$-type molecules through the electrostatic interaction of $Ni^{2+}$ cations from the reactant and $OH^-$ groups from the hydroxide reaction medium (Eq. 1), followed by condensation reactions of $Ni(OH)_2$ molecules forming Ni-O-Ni bonds (Eq. 2) which extend building a sol of NiO clusters through the melted hydroxides medium (Eq. 3). Low surface tension so typical of ionic media would prompt a burst supersaturation, leading to a moderately narrow particle size distribution, while the eventual stabilization of the NiO NCs should be associated to the electrostatic repulsion among them due to ion-surface-adsorption.

$$Ni^{2+} + 2\ OH^- \rightarrow Ni(OH)_2 \quad [1]$$

$$Ni(OH)_2 + Ni(OH)_2 \rightarrow HO\text{-}Ni\text{-}O\text{-}Ni\text{-}OH + H_2O \quad [2]$$

$$n\ HO\text{-}Ni\text{-}O\text{-}Ni\text{-}OH \rightarrow (NiO)_{2n}\ (s) \quad [3]$$

Regarding to the growth fashion, it is well-known that semiconductors with cubic symmetry and rock-salt structure nucleate with tetradecahedron or truncated octahedron shapes and the final particle morphology is associated to the relative growth rate between the six {100} faces and the eight {111} faces.[11,12] The faster growth of {111} faces results in their elimination and subsequent formation of cubes with six faces, while if the {100} faces grow faster, the resulting morphology is an eight-faced octahedra. That mechanism is also valid for the growth of other binary compounds with rock-salt structure, such as NiO. In this type of crystals, {100} faces contain the same number of cations and anions, so they are basically non-polar, while the {111} faces contain either cations or anions and, due to the difference of electronegativity between them, present a polar character. Such polar {111} faces are thus susceptible of adsorbing ionic species of opposite charge and that is very prone to occur in the melted hydroxide mixture. That is the key for the shape-controlled growth of NiO NCs in the melted hydroxide mixture: the eight {111} faces would be stabilized by electrostatic interaction with ions from the melted salts, resulting in their lower growth velocity in respect to {100} faces, which would be more naked due to their non-polar character and would be allowed to growth faster resulting in their eventual elimination and the formation of octahedral shapes with eight ion-stabilized {111} faces.

## 4. Conclusions

Octahedra NiO NCs of sizes ~100-265 nm have been prepared through the hydroxides eutectic route. An assessment of the role of the highly ionic medium in the formation and stabilization of octahedral morphologies is reported. Further work is still needed to proof the suitability of such a medium as a shape-directing agent of binary NCs with rock-salt structure.

## References

1. Jun, Y. W.; Lee, J. H.; Choi, J. S.; Cheon, J., Symmetry-controlled colloidal nanocrystals: Nonhydrolytic chemical synthesis and shape determining parameters. *Journal of Physical Chemistry B* **2005,** 109, (31), 14795-14806.
2. Hayashi, Y.; Kimura, T.; Yamaguchi, T., Preparation of rod-shaped $BaTiO_3$ powder. *Journal of Materials Science* **1986,** 21, (3), 757-762.
3. Mao, Y.; Banerjee, S.; Wong, S. S., Large-Scale Synthesis of Single-Crystalline Perovskite Nanostructures. *Journal of the American Chemical Society* **2003,** 125, (51), 15718-15719.
4. Antonietti, M.; Kuang, D.; Smarsly, B.; Zhou, Y., Ionic liquids for the convenient synthesis of functional nanoparticles and other inorganic nanostructures. *Angewandte Chemie - International Edition* **2004,** 43, (38), 4988-4992.

5. Morris, R. E., Ionothermal synthesis - Ionic liquids as functional solvents in the preparation of crystalline materials. *Chemical Communications* **2009**, (21), 2990-2998.
6. Gaune-Escard, M. a. S., K. R., *Molten Salts and Ionic Iiquids*. Wiley: 2010.
7. Liu, H.; Hu, C.; Wang, Z. L., Composite-hydroxide-mediated approach for the synthesis of nanostructures of complex functional-oxides. *Nano Letters* **2006,** 6, (7), 1535-1540.
8. Poizot, P.; Laruelle, S.; Grugeon, S.; Dupont, L.; Tarascon, J. M., Nano-sized transition-metal oxides as negative-electrode materials for lithium-ion batteries. *Nature* **2000,** 407, (6803), 496-499.
9. Park, J.; Kang, E.; Son, S.; Park, H.; Lee, M.; Kim, J.; Kim, K.; Noh, H. J.; Park, J. H.; Bae, C.; Park, J. G.; Hyeon, T., Monodisperse Nanoparticles of Ni and NiO: Synthesis, Characterization, Self-Assembled Superlattices, and Catalytic Applications in the Suzuki Coupling Reaction. *Advanced Materials* **2005,** 17, (4), 429-434.
10. Caruge, J.-M.; Halpert, J. E.; Bulovič, V.; Bawendi, M. G., NiO as an Inorganic Hole-Transporting Layer in Quantum-Dot Light-Emitting Devices. *Nano Letters* **2006,** 6, (12), 2991-2994.
11. Wang, Z. L., Transmission electron microscopy of shape-controlled nanocrystals and their assemblies. *Journal of Physical Chemistry B* **2000,** 104, (6), 1153-1175.
12. Cho, K. S.; Talapin, D. V.; Gaschler, W.; Murray, C. B., Designing PbSe nanowires and nanorings through oriented attachment of nanoparticles. *Journal of the American Chemical Society* **2005,** 127, (19), 7140-7147.

IV. Chapter 1.3

# CHAPTER 2

# SYNTHESIS OF NANOOXIDES VIA UREA-MELT ROUTE

CHAPTER 2.1

# Urea-Melt Assisted Synthesis of Ni/NiO Nanoparticles Exhibiting Structural Disorder and Exchange Bias

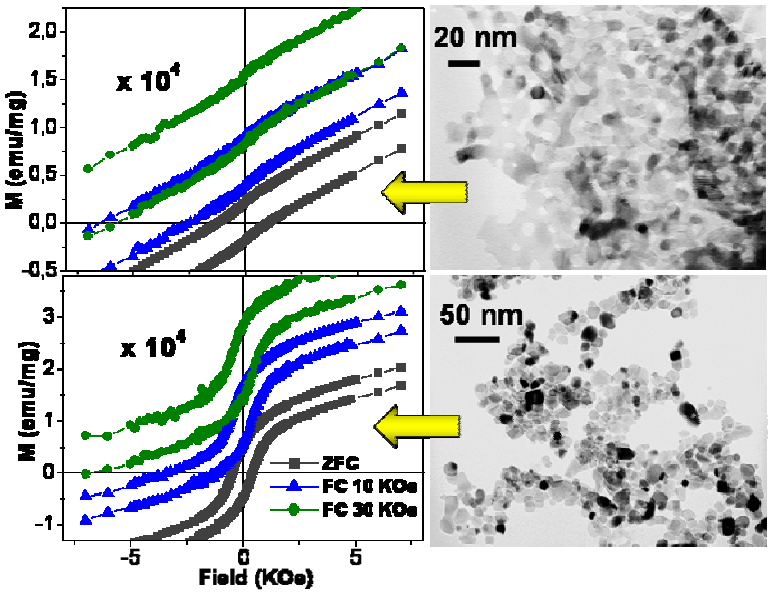

CHEMISTRY OF MATERIALS
Article

*Chem. Mater.* **2010,** *22,* 6529–6541 6529
DOI:10.1021/cm1017823

# Urea-Melt Assisted Synthesis of Ni/NiO Nanoparticles Exhibiting Structural Disorder and Exchange Bias

Ana Querejeta-Fernández,[†] Marina Parras,[†] Aurea Varela,[†] Francisco del Monte,[‡] Mar García-Hernández,[‡] and José M. González-Calbet*,[†]

[†]*Departamento de Química Inorgánica I, Facultad de Ciencias Químicas, Universidad Complutense de Madrid, 28040 Madrid, Spain, and* [‡]*Instituto de Ciencia de Materiales de Madrid, CSIC, Campus de Cantoblanco, 28049 Madrid, Spain*

*Received June 25, 2010. Revised Manuscript Received November 18, 2010*

An easy, inexpensive urea-melt assisted route was designed for the synthesis of ~10 nm-sized Ni/NiO nanoparticles (NPs). The method consists of the thermal decomposition of a urea-melted medium containing a $Ni^{2+}$-salt and involves the olygomerization and self-combustion of the organic matrix and the formation of the Ni/NiO NPs within it in a two stepped process of $Ni^{2+}$ reduction yielding Ni crystallization and subsequent inward oxidation. Control over the microstructural features of the NPs within three typical regimes was accomplished by means of the initial urea quantity. Type A samples (0.2 g urea/0.2908 g nickel nitrate) consists of NiO nanostructures which might contain dispersed Ni nuclei of a few atoms; B NPs (2 g urea/0.2908 g nickel nitrate) are made of proper small Ni cores, in the limit of the coherence length of XRD, surrounded by thick NiO shells, while C (20 g urea/0.2908 g nickel nitrate) NPs correspond to relative big Ni cores and thin NiO shells. Further control over the thickness of the NiO shell was achieved within each regime by means of the calcination time of the organic matrix, painting a whole palette of $Ni_{core}-NiO_{shell}$ NPs. Magnetic characterization revealed large (for A and B) and common (C) shifts of the hysteresis loops, which were ascribed to the high disorder of the (A, B and C) NPs obtained by quenching as well as to exchange bias (EB) effects (B and C). A thorough characterization of the reaction pathway is reported.

## 1. Introduction

The synthesis of ferromagnetic (FM) metals, such as Ni, Co, and Fe, at the nanoscale has been a subject of intense research because of their interesting magnetic properties.[1] Particularly, exchange bias (EB) phenomenology has attracted increasing attention as an effective means of overcoming the superparamagnetic limit typical of FM nanoparticles (NPs),[2,3] encountering thus promising applications in the fields of ultrahigh-density magnetic recording media,[4] spintronic devices[5] and medicine.[6] EB is manifested in systems where an antiferromagnetic (AFM) layer enhances the magnetic anisotropy of a nanosized FM component, preventing the ferromagnetic moments from fluctuating (superparamagnetism) because of thermal energy and such a sketch can be easily realized in metallic NPs surrounded by a metal oxide surface layer, that is, a core−shell structure. $Ni_{core}-NiO_{shell}$ NPs are especially promising in this field since, first, the Néel temperature of bulk NiO, 520 K, makes it suitable for generating EB at room temperature,[7] oppositely to CoO ($T_N$ = 290 K[7]), and second, the relative difficult oxidation of metallic Ni NPs in comparison with Fe and Co NPs,[8] which spontaneously oxidize to a considerable extent upon exposure to air.[9,10] Furthermore, Ni/NiO NPs have been shown to find applications as anode materials for rechargeable batteries, ethanol fuel cells, and electrochemical capacitors,[11] as catalysts in organic reactions,[12] as hole-transport layer in LEDs[13] and have been used for magnetic separation of histidine-tagged proteins.[14]

*To whom correspondence should be addressed. E-mail: jgcalbet@quim.ucm.es.

(1) Kodama, R. H. *J. Magn. Magn. Mater.* **1999**, *200*, 359–372.
(2) Skumryev, V.; Stoyanov, S.; Zhang, Y.; Hadjipanayis, G.; Givord, D.; Nogués, J. *Nature* **2003**, *423*, 850–853.
(3) Iglesias, O.; Labarta, A.; Batlle, X. *J. Nanosci. Nanotechnol.* **2008**, *8*, 2761–2780.
(4) Martín, J. I.; Nogués, J.; Liu, K.; Vicent, J. L.; Schuller, I. K. *J. Magn. Magn. Mater.* **2003**, *256*, 449–501.
(5) Prinz, G. A. *Science* **1998**, *282*, 1660–1663.
(6) Häfeli, U., Schütt, W., Teller, J., Zborowski, M., Eds. *Scientific and Clinical Applications of Magnetic Materials*; Plenum: New York, 1997.
(7) Nogués, J.; Schuller, I. K. *J. Magn. Magn. Mater.* **1999**, *192*(2), 203–232.
(8) The reduction potentials of $Ni^{2+}$ ($E^0$ = −0.257 V), $Co^{2+}$ ($E^0$ = −0.28 V), and $Fe^{2+}$ ($E^0$ = −0.447 V) indicate the following oxidation capability of the metallic elements: $Fe^0 > Co^0 > Ni^0$
(9) Peng, S.; Wang, C.; Xie, J.; Sun, S. *J. Am. Chem. Soc.* **2006**, *128*, 10676–10677.
(10) Tracy, J. B.; Weiss, D. N.; Dinega, D. P.; Bawendi, M. G. *Phys. Rev. B* **2005**, *72*, 1–8.
(11) Poizot, P.; Laruelle, S.; Grugeon, S.; Dupont, L.; Tarascon, J. M. *Nature* **2000**, *407*, 496–499.
(12) Park, J.; Kang, E.; Son, S. U.; Park, H. M.; Lee, M. K.; Kim, J.; Kim, K. W.; Noh, H. J.; Park, J. H.; Bae, C. J.; Park, J. G.; Hyeon, T. *Adv. Mater.* **2005**, *17*, 429–434.
(13) Caruge, J. M.; Halpert, J. E.; Bulović, V.; Bawendi, M. G. *Nano Lett.* **2006**, *6*, 2991–2994.


Published on Web 12/06/2010

The magnetic properties of Ni/NiO NPs are thoroughly determined by the textural and microstructural features of both components, as well as the interface (quantity, roughness, ...) between them. Such attributes are especially critical in nanosized crystals and are profoundly determined by the synthetic route employed. Thus, the design of processes for the preparation of Ni/NiO NPs, which allow for the control over those features, is of paramount interest.

Ni/NiO core−shell NPs have been previously obtained by both physical and chemical routes. Among the former, magnetron-plasma-based cluster beam deposition,[15] evaporation,[16] pulsed laser ablation,[17] arch-discharge,[18] and e-beam lithography[19] techniques offer highly crystalline and monodisperse particles with an outer thin (1−2 nm) oxide shell. On the other hand, chemical strategies offer a wider range of conditions to tailor the features of the resulting Ni/NiO NPs, and can be classified into two main blocks: (a) liquid phase routes and (b) calcination of organic matrices. The former is based either on (i) decomposition of a metal−organic precursor in an organic solvent[12,20−26] or (ii) chemical reduction of metal salts in aqueous or organic media.[27−29] While remarkable advances of such liquid phase routes are the preparation of colloidal monodisperse and size-controllable metallic nickel NPs and nanorods, stabilizers protecting the surface and used for such requirements generally hamper the formation of a robust, thick AFM NiO shell, although NiO NPs have also been reported.[12,23] Typical calcination methods,[30−33] besides making it difficult the control over size, size distribution, and aggregation,[30,33] are found to lead to either NiO NPs[33] or encapsulated-Ni NPs.[31] Between the two limit cases, that is, Ni and NiO NPs, a rich range of Ni/NiO composites, including $Ni_{core}-NiO_{shell}$ NPs, deserves additional attention because of both the close conversion between these two components at the nanoscale and to their promising magnetic phenomenology.

Despite the considerable amount of papers reporting on the synthesis of $Ni_{core}-NiO_{shell}$ NPs, both the control over NiO thickness, especially in the case of tiny Ni cores, and the clear establishment of the influence of the microstructural features on the magnetic phenomenology remain a challenge. In this sense, Li et al.[30] reported on the preparation of $Ni_{core}-NiO_{shell}$ NPs with three different thicknesses of the shell as a function of the calcination temperature of a glycerol matrix, although no structural or magnetic characterization were performed. Also, Roy et al.[27,34] reported the progressive transformation of Ni into NiO NPs by annealing at different temperatures the powders prepared by borohydride reduction method in aqueous solution and they proposed a metastable oxygen-stabilized tetragonal structure for Ni NPs. On the other hand, regarding the preparation of ligand-stabilized Ni−NiO colloids, Johnston-Peck et al.[25] obtained two shell thicknesses (2−3 nm maximum) in size-controlled NPs in the range of 8−24 nm, although the amorphous structure of the shells led to the absence of EB, while Winnischofer et al. stressed the important relevance of highly disordered atomic structures on the magnetic behavior of Ni/NiO NPs.[24,35] This issue was also addressed by Del Bianco et al.[36] in Ni/NiO systems produced by ball milling and hydrogen reduction, where a disordered NiO component embodied small Ni-enriched regions. Finally, in this sense, NiO NPs prepared by calcining a gel have been reported to exhibit large coercivities and loop shifts, which are similar effects to those associated with exchange coupled FM/AFM materials. However, because of the lack of detection of crystalline Ni phase, the authors related the anomalous magnetic behavior to a magnetic order different from that found in the bulk material, as assessed by numerical modeling.[32,37]

On the other hand, the use of urea either in aqueous or organic solvents has been widely reported for the synthesis of oxides, nitrides, and carbonates[38−41] However, its use as a viscous melted reaction media is more restricted, including the functionalization of carbon nanotubes at low temperature,[42] the thermal transformation of metal


(14) Lee, I. S.; Lee, N.; Park, J.; Kim, B. H.; Yi, Y. W.; Kim, T.; Kim, T. K.; Lee, I. H.; Paik, S. R.; Hyeon, T. *J. Am. Chem. Soc.* **2006**, *128*, 10658–10659.
(15) Zhou, Y. Z.; Chen, J. S.; Tay, B. K.; Hu, J. F.; Chow, G. M.; Liu, T.; Yang, P. *Appl. Phys. Lett.* **2007**, *90*, 043111.
(16) Löffler, J. F.; Meier, J. P.; Doudin, B.; Ansermet, J.-P.; Wagner, W. *Phys. Rev. B* **1998**, *57*, 2915.
(17) Sakiyama, K.; Koga, K.; Seto, T.; Hirasawa, M.; Orii, T. *J. Phys. Chem. B* **2004**, *108*, 523–529.
(18) Sun, X. C.; Dong, X. L. *Mater. Res. Bull.* **2002**, *37*, 991–1004.
(19) Fraune, M.; Rüdiger, U.; Güntherodt, G.; Cardoso, S.; Freitas, P. *Appl. Phys. Lett.* **2000**, *77*, 3815–3817.
(20) Cordente, N.; Respaud, M.; Senocq, F.; Casanove, M. J.; Amiens, C.; Chaudret, B. *Nano Lett.* **2001**, *1*, 565–568.
(21) Han, M.; Liu, Q.; He, J.; Song, Y.; Xu, Z.; Zhu, J. *Adv. Mater.* **2007**, *19*, 1096–1100.
(22) Leng, Y.; Li, Y.; Li, X.; Takahashi, S. *J. Phys. Chem. C* **2007**, *111*, 6630–6633.
(23) Jana, N. R.; Chen, Y.; Peng, X. *Chem. Mater.* **2004**, *16*, 3931–3935.
(24) Winnischofer, H.; Rocha, T. C. R.; Nunes, W. C.; Socolovsky, L. M.; Knobel, M.; Zanchet, D. *ACS Nano* **2008**, *2*, 1313–1319.
(25) Johnston-Peck, A. C.; Wang, J.; Tracy, J. B. *ACS Nano* **2009**, *3*, 1077–1084.
(26) Jeon, Y. T.; Moon, J. Y.; Lee, G. H.; Park, J.; Chang, Y. *J. Phys. Chem. B* **2006**, *110*, 1187–1191.
(27) Roy, A.; Srinivas, V.; Ram, S.; De Toro, J. A.; Mizutani, U. *Phys. Rev. B* **2005**, *71*, 184443.
(28) Grzelczak, M.; Pérez-Juste, J.; Rodríguez-González, B.; Spasova, M.; Barsukov, I.; Farle, M.; Liz-Marzán, L. M. *Chem. Mater.* **2008**, *20*, 5399–5405.
(29) Wu, S. H.; Chen, D. H. *Chem. Lett.* **2004**, *33*, 406–407.
(30) Li, Y.; Cai, M.; Rogers, J.; Xu, Y.; Shen, W. *Mater. Lett.* **2006**, *60*, 750–753.
(31) Koltypin, Y.; Gedanken, A. *Chem. Mater.* **1999**, *11*, 1331–1335.
(32) Makhlouf, S. A.; Parker, F. T.; Spada, F. E.; Berkowitz, A. E. *J. Appl. Phys.* **1997**, *81*, 5561–5563.
(33) Li, Q.; Wang, L. S.; Hu, B. Y.; Yang, C.; Zhou, L.; Zhang, L. *Mater. Lett.* **2007**, *61*, 1615–1618.
(34) Roy, A.; Srinivas, V.; Ram, S.; De Toro, J. A.; Riveiro, J. M. *J. Appl. Phys.* **2004**, *96*, 6782–6788.
(35) Nunes, W. C.; De Biasi, E.; Meneses, C. T.; Knobel, M.; Winnischofer, H.; Rocha, T. C. R.; Zanchet, D. *Appl. Phys. Lett.* **2008**, *92*, 183113.
(36) Del Bianco, L.; Boscherini, F.; Fiorini, A. L.; Tamisari, M.; Spizzo, F.; Antisari, M. V.; Piscopiello, E. *Phys. Rev. B* **2008**, *77*, 094408.
(37) Kodama, R. H.; Makhlouf, S. A.; Berkowitz, A. E. *Phys. Rev. Lett.* **1997**, *79*, 1393–1396.
(38) Sardar, K.; Dan, M.; Schwenzer, B.; Rao, C. N. R. *J. Mater. Chem.* **2005**, *15*, 2175–2177.
(39) Qiu, Y.; Gao, L. *J. Am. Ceram. Soc.* **2004**, *87*, 352–357.
(40) Qiu, Y.; Gao, L. *Chem. Lett.* **2003**, *32*, 774–775.
(41) Matijević, E. *Chem. Mater.* **1993**, *5*, 412–426.
(42) Ford, W. E.; Jung, A.; Hirsch, A.; Graupner, R.; Scholz, F.; Yasuda, A.; Wessels, J. M. *Adv. Mater.* **2006**, *18*, 1193–1197.

oxide NPs into nanocrystalline metal nitrides at high temperature,[43] and the synthesis of metal nitride particles[44] and NPs[45] and ternary metal oxynitride NPs.[46] It has also been used in a similar fashion as a source of nitrogen and carbon in concentrated ethanol solutions for the synthesis of metal nitrides and metal carbides NPs.[47]

Herein, we report a simple, inexpensive route for the synthesis of Ni/NiO NPs (~10 nm) with peculiar structural and magnetic properties. Interestingly, thick AFM shells and tiny FM cores are accessible. As far as we know, this is the first report of the synthesis of metal and metal oxide NPs by making use of urea as both reactant and reaction media. The magnetic behavior of the NPs has been evaluated and the coercivities and loop shifts of the three different types of prepared materials have been correlated with their proposed structures.

## 2. Experimental Section

Nickel nitrate hexahydrate ($Ni(NO_3)_2 \cdot 6H_2O$) (98.5%) and urea (99%) (Fluka) were used as received. First, Teflon vessels equipped with a Teflon cap were loaded with 1 mmol of $Ni(NO_3)_2 \cdot 6H_2O$ (0.2908 g) and four different amounts of urea (0.2 g sample A, 2 g samples B, 12 and 20 g sample C[48]). The vessels were closed with the cap and placed into an oven at 150 °C for either 2 or 16 h. It is noteworthy to note that urea does not melt if the vessels are left open. The homogeneous green liquids were cooled down at room temperature. Stirring of the products with a spatula before completely cooled is necessary to further handle them, especially in the high urea content experiments, which solidify as a hard block if not broken into smaller pieces before completely solids. Portions of the resulting green to blue oligomers were placed into porcelain crucibles, whose size was chosen to ensure a similar ratio (load's height/crucible's height), around a third, for series B and C samples. However, series A was always loaded as a thin layer because of the lower amount of matter in this case. Crucibles were put into a furnace and heated with a constant rate of 2 °C/min until 400 °C, kept at 400 °C during typical times of 2 h and cooled down within the furnace. Dark-gray powders were obtained. All the thermal treatments were performed within a fume hood.

Thermogravimetric and differential thermal analysis (TGA-DTA) of urea was measured under air on a Seiko Exstar 6300 instrument. Powder X-ray diffraction (XRD) of the as-prepared powders was carried out using a Siemens D5000 diffractometer with Cu Kα radiation ($\lambda$ = 1.5418 Å). Quantitative analysis of the relative content of Ni and NiO phases was made by means of the reference intensity ratio (RIR) method[49] in the XRD patterns making use of the X'Pert High Score Plus v2.2d Panalytical BV software. Selected area electron diffraction (SAED) and transmission electron microscopy (TEM) was performed on a JEOL JEM-2000 FX electron microscope whereas high-resolution transmission electron microscopy (HRTEM) was carried out in a JEOL300FEG microscope. Scanning electron microscopy (SEM) was performed on a JSM-6330F FEG scanning electron microscope working at 20 kV. Surface composition of the NPs was studied by X-ray photoelectron spectroscopy (XPS) in a VG Escalab 200 R equipment. The textural properties of the samples were measured by $N_2$ sorption using a gas adsorption analyzer Micromeritics ASAP 2010 V.5 02. The presence of organic traces in the Ni/NiO powders was assessed by elemental analysis in a Perkin-Elmer, Series II 2400 Elemental Analyzer. Magnetization measurements at 2−325 K were obtained by SQUID magnetometry using a Quantum Design magnetometer equipped with a 5 T superconducting coil.

## 3. Results and Discussion

**Compositional and Structural Characterization.** Figure 1 collects XRD and TEM images of the three types (A, B, C) of NPs. XRD patterns can be assigned to rock salt NiO (JCPDS 00-47-1049) for A and B samples, whereas both rock salt NiO and fcc Ni (JCPDS 01−089−7128) phases are observed in C sample.[50] The relative mass ratio of both phases in sample C was determined from the XRD pattern making use of the RIR method: 74% of NiO and 26% of Ni. The low magnification TEM images illustrate the overview of the three samples. Sample A displays nanocrystals of around 10 nm (15.0 nm calculated from XRD by Scherrer method from the (111) peak) frequently highly interconnected into a continuous thin network. Voids between nanocrystals can also be observed as a result of incomplete sintering. In overall, sample A could resemble a porous matrix. It is worth noting that sporadic bigger ( > 50 nm) crystals resulting from the sintering of the NPs from such a porous network are observed (see also the Supporting Information, Figure S1A). A slightly different morphology is shown for samples B and C, which display around 12 (16.1 nm by Scherrer) and 9 nm (15.0 nm by Scherrer), respectively, loosely aggregated NPs. As regards the connection among the NPs, it is worth mentioning that some flat sheets made up of NPs are found in B, although the network is not as continuous as in A, whereas even less continuous sheets of NPs are present in C (Supporting Information, Figure S1B and C, respectively). SAED patterns of the three samples (Supporting Information, Figure S2) reveal a random orientation among crystalline NPs (ring patterns) and show the presence of interplanar distances corresponding to rock salt NiO in A and B samples and both rock salt NiO and fcc Ni in C samples, in agreement with XRD data.

It is worth noting that different XRD-based Ni/NiO ratios were obtained for different batches (eight experiences per series, Table 1). For samples A, 100% NiO was always obtained, while samples B do show small Ni peaks in some cases and such a phase ranges from 0 to 7%. Samples C always show large Ni peaks.

(43) Buha, J.; Djerdj, I.; Antonietti, M.; Niederberger, M. *Chem. Mater.* **2007**, *19*, 3499–3505.
(44) Podsiadlo, S. *Thermochim. Acta* **1995**, *256*, 367–380.
(45) Gomathi, A.; Sundaresan, A.; Rao, C. N. R. *J. Solid State Chem.* **2007**, *180*, 291–295.
(46) Gomathi, A.; Reshma, S.; Rao, C. N. R. *J. Solid State Chem.* **2009**, *182*, 72–76.
(47) Giordano, C.; Erpen, C.; Yao, W.; Antonietti, M. *Nano Lett.* **2008**, *8*, 4659–4663.
(48) Since both 12 and 20 g urea samples display similar features, they are included in the C series.
(49) Chung, F. H. *J. Appl. Crystallogr.* **1975**, *8*, 17–19.

(50) It is worth mentioning that although the most frequent Ni structure is cubic, fcc; hexagonal, hcp; [2f,26] and highly disordered[24] Ni structures have been also found in NPs, while also amorphous[25] and $NiO_2$[28] structures have been proposed for the NiO shells apart from the typical cubic rock salt one.

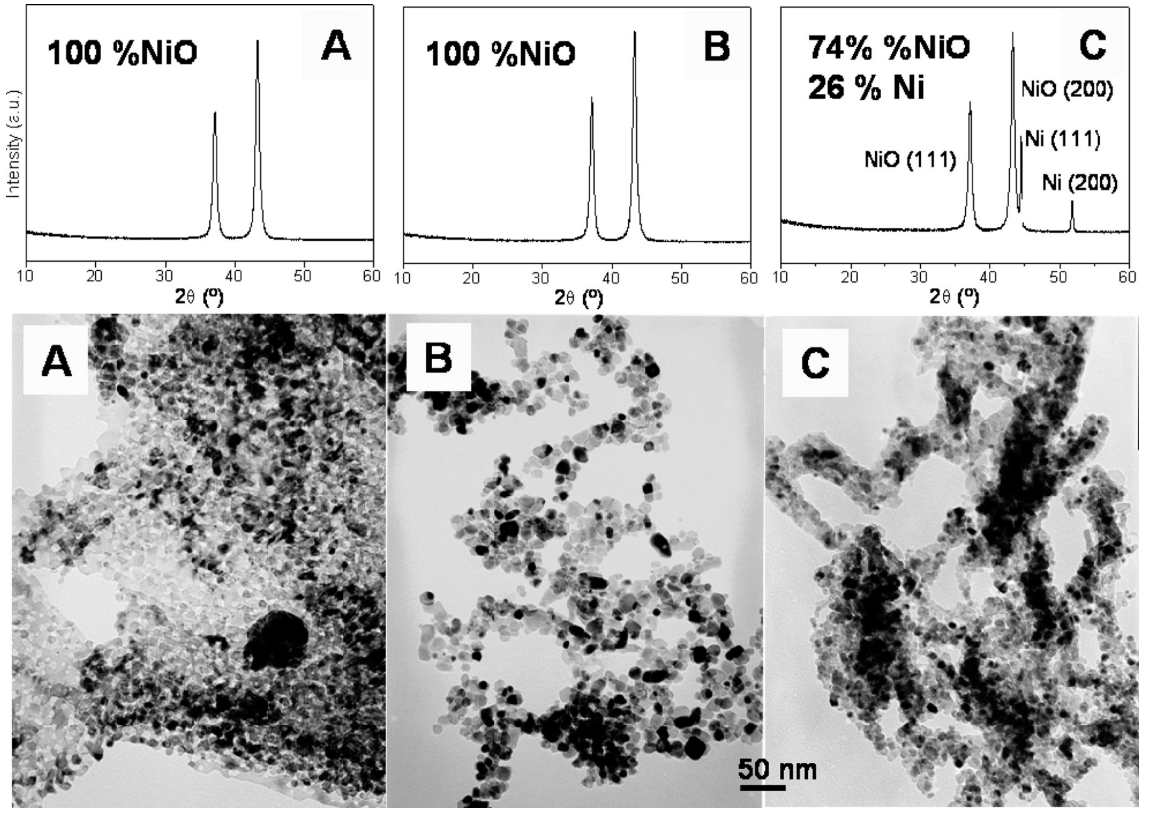


**Figure 1.** XRD patterns and TEM images of representative members of A (0.2 g urea), B (2 g urea), and C series (20 g urea) of as-prepared NPs. The samples were prepared by [150 °C, 16 h + 400 °C, 2 h] protocol.

**Table 1. Average and Range NiO Percentage Calculated by RIR Method from the XRD Patterns for the Different Experiments Performed in Series A, B, and C NPs**

| | % NiO |
|---|---|
| A (0.2 g urea) | 100 [100] |
| B (2 g urea) | 98 [93−100] |
| C (12 g urea) | 58 [48−74] |
| C (20 g urea) | 54 [40−76] |

The surface composition of A, B, and C NPs was evaluated by XPS, which reveals the presence of nickel oxide and nickel-hydroxyl bonds up to a maximum distance of 3 nm from the surface. In the Ni $2p_{3/2}$ region, a peak at a binding energy of 854.4 eV is ascribed to $Ni^{2+}$ species (Supporting Information, Figure S3a).[51,52] Complementary O 1s spectrum shows two peaks at ∼529.4 and 531.0 eV, which correspond to Ni−O−Ni and Ni−OH bonds, respectively (Supporting Information, Figure S3b).[52] Table 2 summarizes the ratios of both superficial components for the three samples. Since neither nickel hydroxide nor oxyhydroxide was detected by XRD or SAED, it is suggested that hydroxyl groups are randomly distributed as an amorphous outermost layer, in good agreement with earlier reports.[28] The lack of a peak at 852.6 eV in the Ni $2p_{3/2}$ region is a clear evidence of the absence of metallic nickel on the NPs' surface.[51] As the XRD data evidence the presence of metallic nickel in B and C samples, such a phase must exist in an inner core of the NPs at a depth not detectable by the penetration (up to 3 nm) of XPS. This demonstrates the existence of a NiO shell and the location of the Ni phase within the inner part of B and C NPs. Although the nature of such a metallic phase, either a continuous core (i.e., core−shell NPs) or discontinuous Ni/NiO core (i.e., nanocomposite) cannot be determined by this technique, the presence of crystalline Ni domains, whose size is smaller for B NPs as compared to C NPs, seems to indicate a core−shell nature for B and C NPs.

Complementary HRTEM characterization (Supporting Information, Figure S4) of the three types of samples confirms a NiO rock salt structure for all the NPs examined, which in the case of B and C samples further supports the existence of Ni as inner nuclei instead of separated Ni and NiO NPs. An apparent single crystalline nature of the particles is observed, as opposite to some polycrystalline NPs previously reported.[24,25,28] In the latter cases, the crystalline domains within a particle corresponded to the large metallic nickel cores. However, in our case, no metal fcc Ni cores could be directly observed in any case. In the case of C-26%-Ni sample, this is probably because of the relative smaller crystal size of the inner metal phase as compared to previous reports. However, HRTEM characterization of C-60%-Ni sample reveals a visible core−shell nature (Figure 2), illustrated by a shell of about 1.5−3.5 nm and an apparent amorphous core, which could be the result of the misalignment of both crystalline

(51) Grosvenor, A. P.; Biesinger, M. C.; Smart, R. S. C.; McIntyre, N. S. *Surf. Sci.* **2006**, *600*, 1771–1779.
(52) Biesinger, M. C.; Payne, B. P.; Lau, L. W. M.; Gerson, A.; Smart, R. S. C. *Surf. Interface Anal.* **2009**, *41*, 324–332.

**Table 2. XPS Data Corresponding to A, B-100%-NiO, and C-40%-NiO Samples Prepared by [150 °C, 16 h + 400 °C, 2 h] Protocol[a]**

| Sample | Ni $2p_{3/2}$ BE (eV) | O 1s BE (eV) (Int.) | species (oxygen bonds) |
|---|---|---|---|
| A (0.2 g urea) | 854.4 | 529.5 (63) + 531.0 (37) | 85% Ni−O−Ni + 24% Ni−OH |
| B (2 g urea) | 854.4 | 529.4 (69) + 531.0 (31) | 83% Ni−O−Ni + 18% Ni−OH |
| C (20 g urea) | 854.4 | 529.4 (64) + 530.9 (36) | 83% Ni−O−Ni + 23% Ni−OH |

[a] The calculated percentage of nickel oxide and nickel hydroxide species is included.

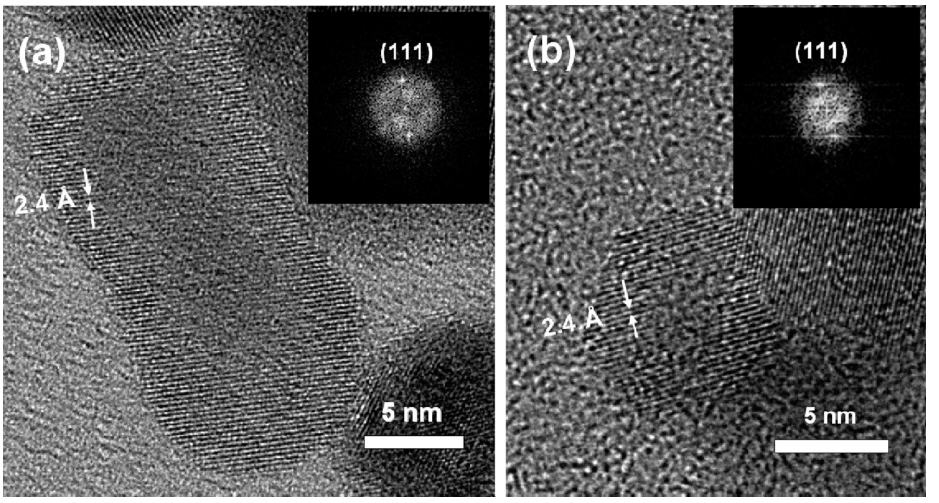


**Figure 2.** HRTEM images of $Ni_{core}-NiO_{shell}$ NPs corresponding to the C sample with 40% of NiO and 60% of Ni, prepared by [150 °C, 16 h + 400 °C, 2 h] protocol.

$Ni_{core}$ and $NiO_{shell}$ structures under the electron beam, in accordance with previous works reporting medium-thin NiO shells.[15] Nevertheless, such a core was not observed in the whole population of the particles, suggesting inhomogeneous volumes of the cores.

Further understanding of the different materials prepared can be achieved through a global inspection to the synthetic method. Crystallization of the metal nickel particles takes place at high temperature (400 °C) within a reducing organic decomposing matrix, (its self-combustion involves its oxidation, so it reduces the $Ni^{2+}$ cations), which prevents NPs from hard aggregation and sintering and oxidation. After almost complete removal of the organics, the nickel NPs are exposed to the air, so diffusion of oxygen can take place from the surface inward. Such a dynamic oxidation process can be frozen by cooling down to room temperature, which might prevent the atoms from rearranging into a perfect NiO crystal and would likely lead to quenched Ni/NiO nanocomposites with a NiO shell characterized by high atomic disorder. In other words, unstable Ni NPs at 400 °C would suffer a spontaneous oxidation and subsequent unstable $Ni_{inner}-NiO_{shell}$ NPs at 400 °C could be quenched, leading to metastable (inert at room temperature) $NiO_{shell}-$Ni/NiO NPs; thus, the quenching process would freeze two metastable features: the defective crystallinity of a nanocrystal undergoing a dynamic process of oxygen diffusion and the thickness of the resulting NiO shell. In this sense, given that A, B and C samples were prepared under the same calcination conditions from different starting quantities of urea, the greater amount of organics in C requires of larger self-combustion times. Therefore, for equal calcinations times, series C metallic nickel NPs do not accomplish fully oxidation. This is the reason why the process in samples C does render larger Ni cores as compared to samples B. It is anticipated that samples A might also contain Ni nuclei, although the small crystal size, below the length coherence of XRD, would not be detectable by the diffraction experiment. Both the reaction mechanism and the magnetic characterization below are compatible with the presence of small metallic nickel nuclei in A samples. The metallic Ni phase (A < B < C) would be a consequence of the extension of the oxidative process from the surface inward suffered by the nickel NPs after removal of the organic matrix. In addition, it is reasonable to infer that Ni cores in samples C, besides their larger size as compared to A and B, present a broader particle size distribution, that is, small metallic Ni particles achieve almost complete oxidation for a certain calcination time, while this is not the case for intermediate and large size NPs. Besides, the thicker the passivating $NiO_{shell}$, the more hampered the advance of the oxidation would be, which would lead to $Ni_{nuclei}$ size distributions in the sense A < B < C. On the other hand, since A samples are devoid of the organic matrix for longer times, as compared to B and C, a higher level of aggregation of the NPs is found, leading to some porous networks of aggregated NPs, which eventually form microcrystals because of sintering (Supporting Information, Figure S1; note also some sintering of the NPs along the same crystallographic direction in the corresponding HRTEM image in Supporting Information, Figure S4).

Therefore, control over external NiO thickness can be achieved depending on the amount of starting urea: the higher the urea content, the larger the $Ni_{core}$ due to a shorter oxidative process. Similarly, it is easy to deduce that additional control over the thickness of the oxide shell can be accomplished by means of the calcination time, as detailed in the description of the reaction mechanism: longer calcinations times allow more penetrating oxidative processes.

Control over the relative Ni/NiO content is thus achieved for three regimes, A, B, C, which possess characteristic magnetic behavior stemming from typical levels of oxidation and microstructural features. Note, however, that the quenching nature of the synthesis makes it very sensitive to small differences in both heating and cooling rates, which could lead to the observed differences in the Ni/NiO ratio among different batches within a series (Table 1). In this sense, the larger differences among batches for C as compared to A and B samples reflect that C NPs are more sensitive to heating/cooling rates because the oxidation is easier at the outlayers of the NPs. It is worth mentioning that the same crucibles and quantities of $Ni^{2+}$-containing oligomer were used in all the experiments of a series, minimizing thus surface effects during combustion. Indeed, 100% NiO was obtained when very thin layers of oligomer were calcined, even for the highest urea content, pointing out toward a sacrificial oligomer outer layer in the crucible in good contact with an oxidizing air atmosphere which leads only to NiO NPs.

**Magnetic Characterization.** Further insights regarding the nature of the NPs were accomplished by magnetic measurements. All the samples were measured using a Quantum Designed SQUID magnetometer equipped with a 50 KOe coil. To avoid uncontrolled reduction of the samples at high temperatures in the He atmosphere of the instrument, magnetization versus temperature runs were limited to the temperature range 2−325 K using ZFC-FC protocols with $H = 50$ KOe as cooling field and $H = 50$ Oe as the measuring field. Data corresponding to representative samples of series A−B−C are given in Figure 3. As expected, the blocking temperature given by the maxima of the ZFC measurements increases as the Ni content and the size of the Ni-nucleus or Ni-core increases. Also, the size distributions, related to the widths of the ZFC peaks, broaden from A to C, in good agreement with the structural features previously described. Note that ZFC−FC runs for all series exhibit large irreversibilities even at the highest temperature explored, which suggests that magnetic frustration and disorder not only are present but dominates the magnetic properties, this being particularly true for systems type A and B.

Hysteresis cycles at 2 K were systematically measured after zero field, 10, and 30 KOe cooling runs along the temperature interval 300−2 K. Figure 4 plots the magnetic field dependence of magnetization as measured in ZFC, 10 and 30 KOe FC runs, for three representative members of series A, B, and C. Three different magnetic behavior are exhibited by samples of the series A, B and C. Samples of series A are dominated by the magnetic

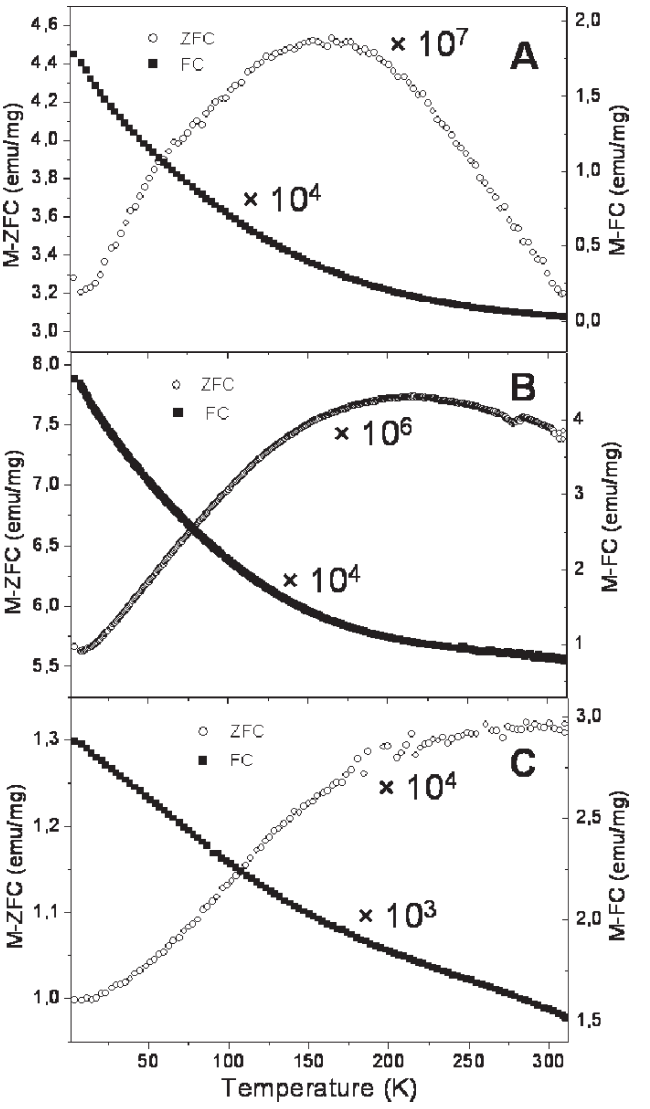


**Figure 3.** Plots of ZFC−FC runs of the magnetization versus temperature, as measured under 50 KOe cooling and 50 Oe measuring fields, for 100% NiO (A), 97% NiO (B), and 74% NiO (C) Ni/NiO NPs prepared by [150 °C, 16 h + 400 °C, 2 h] protocol.

response of a quite disordered AFM predominant component with small FM contributions evidenced by a small narrowing of the cycles around $H = 0$. Two possible hypotheses can be considered to explain the anomalous FM contributions in the AFM NiO matrix. On one hand, given the fact that no evidence for Ni nuclei is provided by other techniques, the neat magnetic moment observed could be ascribed to the existence of quite a number of unbalanced spins located at the surface and antiphase boundaries in the NiO AFM matrix, as it has been reported for NiO NPs.[32,37,53] However, since oxidation occurs from the outlayer toward the center of the particle and there is evidence for metallic Ni cores inside particles B and C, an alternative plausible interpretation is the existence of very tiny Ni nuclei inside the NiO matrix that would render short ranged FM correlations, as previously

(53) Feygenson, M.; Kou, A.; Kreno, L. E.; Tiano, A. L.; Patete, J. M.; Zhang, F.; Kim, M. S.; Solovyov, V.; Wong, S. S.; Aronson, M. C. *Phys. Rev. B* **2010**, *81*, 014420.

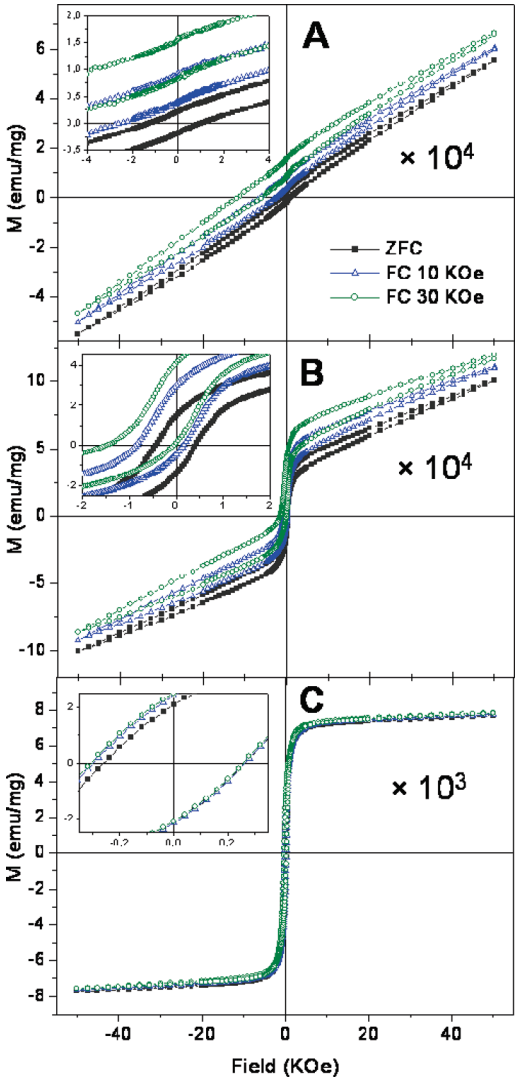


**Figure 4.** Hysteresis cycles measured at $T = 2$ K, recorded after a zero field, 10 and 30 KOe cooling protocols along the temperature interval 300−2 K for 100% NiO (A), 97% NiO (B) and 74% NiO (C) Ni/NiO NPs prepared by [150 °C, 16 h + 400 °C, 2 h] protocol. Insets show greater detail of the same measurements.

evaluated for Co/CoO NPs[10] and bilayers.[3,54] Both hypotheses would translate into large levels of magnetic disorder of the AFM matrix and would account for the irreversibility observed at the highest fields explored. Thus, within the magnetic description, we will refer to samples A as a disordered AFM NiO matrix, regardless of the proposed origins of the FM contribution, surface unbalanced spins plus antiphase boundaries or tiny Ni nuclei. Samples B show two neat contributions, one corresponding to FM Ni cores, whose size is just above the limit of the spatial coherence required to be detected by X-ray diffraction, and that of a thick NiO shell with large levels of magnetic disorder that translate into large irreversibility of the AFM component. Samples C cycles compel to what it is expected for well conformed FM Ni cores with the extra ingredient of a thin layer of AFM NiO, responsible for the slope observed at high fields. Figure 5 depicts the proposed models for A, B and C samples.

The analysis of the FM component has been done for samples with well-defined FM contribution, that is for series B and C. Although values for $H_c$, $M_s$, $M_{ex}$, and $H_{ex}$ (defined below) have been extracted for series A, as an orthodox FM contribution is absent, these values refer to the disordered AFM contribution. Consequently, they cannot be compared to the values measured for series B and C, for which a well conformed FM core exists. The saturation values of the magnetization have been determined by extrapolation to $H = 0$ Oe of the slope assigned to the AFM contribution, with $M_{sat}$ being the value corresponding to the intersection of such a slope with the M axis. As can be seen in Figure 6, $M_{sat}$ and the remanent magnetization increase almost linearly with Ni content. The observed small deviation from linearity can be probably ascribed to the existence of disorder at interfaces. Also, the coercive field $H_c$ decreases with Ni content (Figure 7 a) and, therefore, with increasing the FM particle size, compatible with the existence of various FM domains

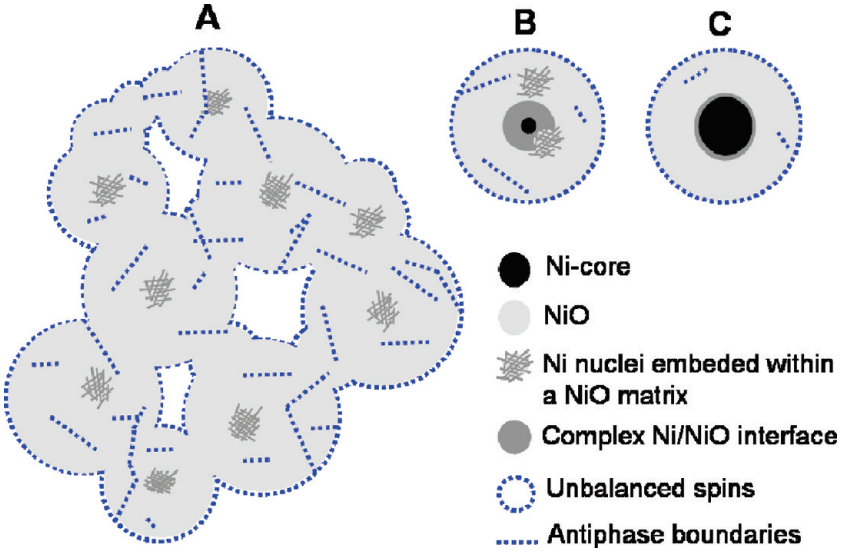


**Figure 5.** Proposed models of A, B, and C samples, contemplating all the possible contributions to the magnetic phenomenology.

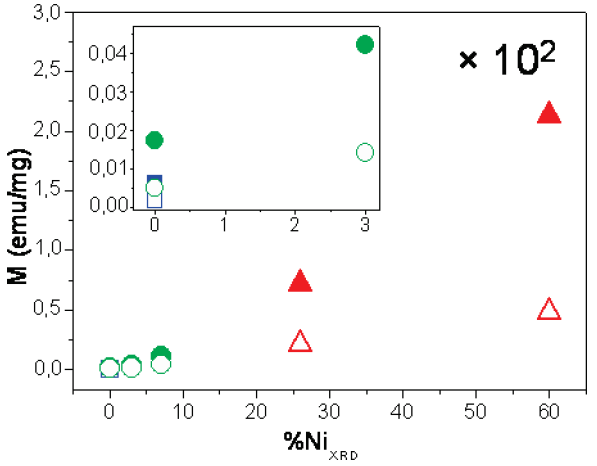


**Figure 6.** Magnetizations of saturation (solid symbols) and remanence (open symbols) vs "crystallographic" percentage of Ni phase for A (blue squares), B (green circles), and C (red triangles) members of Ni/NiO NPs prepared by [150 °C, 16 h + 400 °C, 2 h] protocol. Inset shows greater detail of the left zone of the same graph.

within the Ni cores[55,56] or a larger density of defects for series B than C. However, the smallness of the Ni cores makes the existence of multidomain clusters unlikely and the observed behavior is probably more related to the different defect density as the oxidation progresses during the synthesis. Also, it should again be kept in mind that the very high values shown by samples A cannot be compared to those of series B and C since they do not refer to well-defined FM entities.

Exchange bias (EB) is present in systems where a ferromagnet shares an interface with a larger magnetic anisotropy antiferromagnet, so the latter can pin the orientation of the FM component bellow the Néel temperature. Given the large number of interfaces intimately connecting FM Ni and AFM NiO in our samples EB effects are expected. Figure 4 shows large offsets for the ZFC and FC hysteresis loops of samples type A and B, while samples C are less affected by the cooling field. The effect is strongly enhanced for samples A and B where a large vertical shift (along M axis) is observed, pointing out toward the existence of a spin-glass like system corresponding to a highly disordered AFM NiO NP containing a large number of antiphase boundaries and surface unbalanced spins or, alternatively, some FM Ni nuclei. This is quite opposite to what it is observed in series C for which a more conventional, although small, horizontal shift (along axis H) exists, indicating that disorder in this series is comparatively less important.

To quantitatively assess the magnitude of the observed shifts, we have redefined a new coordinate system with origin at the center of each measured FC cycle. Hysteresis cycles keep the expected symmetry properties in the new coordinate system. Vertical and horizontal shifts

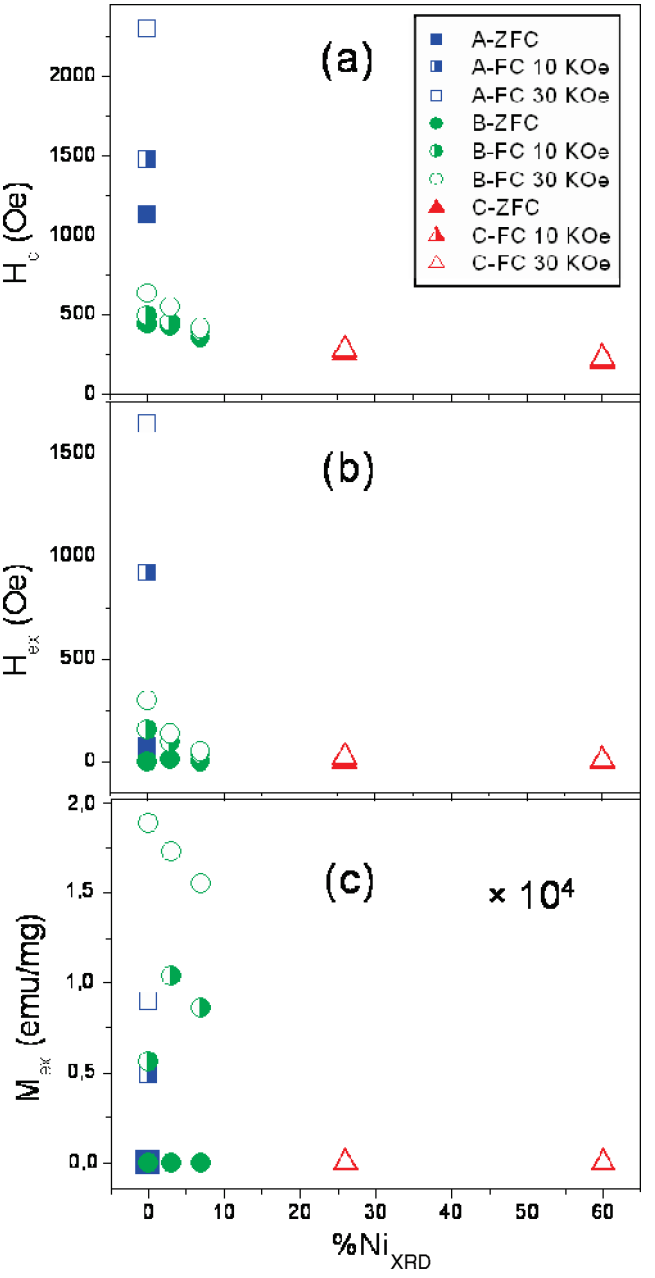


**Figure 7.** $Ni_{XRD}$ mass percentage dependence of (a) coercive field ($H_c$), (b) $H_{ex}$, and (c) $M_{ex}$, for zero field, 10, and 30 KOe protocols at 2 K.

**Table 3. $H_c$, $H_{ex}$, and $M_{ex}$ Values for 30 KOe Protocols Corresponding to the Samples within Each Series A, B, and C**

| | $H_c$ (Oe) | $H_{ex}$ (Oe) | $M_{ex}$ (emu/mg) |
|---|---|---|---|
| A (sample 100% NiO) | 2298 | 1646 | $9.0 \times 10^{-5}$ |
| B (sample 100% NiO) | 635 | 298 | $1.89 \times 10^{-4}$ |
| C (sample 74% NiO) | 281 | 24 | 0 |

($M_{ex}$ and $H_{ex}$, respectively) are then given by the displacements of the new axis relative to the old coordinate system. $M_{sat}$ and $H_c$ are then directly read in the new coordinate system. Table 3 collects the calculated values of $H_c$, $H_{ex}$, and $M_{ex}$ for the samples within each series A, B, and C.

As shown in Figure 7 b, the horizontal shift, given by $H_{ex}$, decreases as the Ni core size increases. The small bias

(54) Papusoi, C.; Hauch, J.; Fecioru-Morariu, M.; Guntherodt, G. *J. Appl. Phys.* **2006**, *99*, 123902.
(55) Cullity, B. D.; Graham, C. D. *Introduction to Magnetic Materials*; 1st ed.; John Wiley & Sons, Inc.: Hoboken, New Jersey, 1972; p 387.
(56) Leslie-Pelecky, D. L.; Rieke, R. D. *Chem. Mater.* **1996**, *8*, 1770–1783.

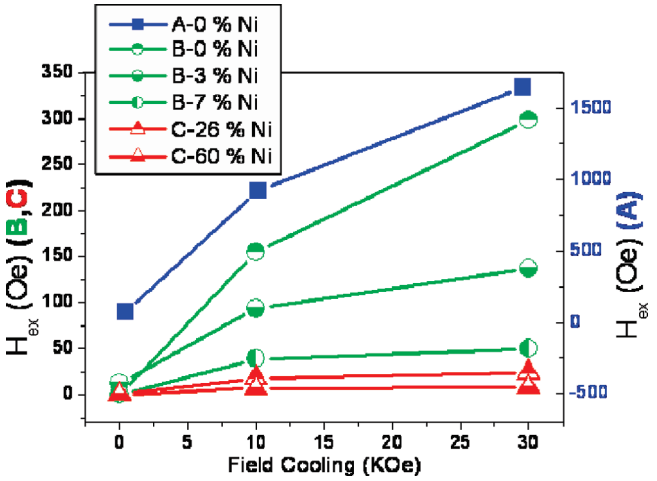


**Figure 8.** $H_{ex}$ dependence of the cooling field for different members of A, B, and C series of samples.

field in samples C can be understood in terms of a less robust AFM of the thinner NiO shell when compared to that of series B.[57] $H_{ex}$ for series A diverges, consistently with the already mentioned lack of a proper FM core and its glassy features. Hence, the hysteresis offset in series A cannot be explained in terms of an exchange anisotropy, but it is rather the result of the strong disorder and magnetic frustration in the systems. Here, metallic Ni, if at all present, is mainly as tiny clusters and crystal defects that contribute to the high disorder of the AFM NiO matrix and promote the observed spin glass-like behavior. Another precursor of the glassy contribution is the markedly different morphology of samples A, packed with nanovoids that seem to be absent in samples of series B and C.

The vertical displacement of the field cooled cycles, given by $M_{ex}$, is large for samples of series B (Figure 7c) and does not occur for samples C. This is compatible with the existence of interfaces affected by some level of disorder between proper FM cores (only present in samples B and C) and the AFM matrix, being this interfacial contribution much more obvious for sample B since the number of interfaces is larger that in series C. Also a better conformation of the FM cores in series C contributes to better structured interfaces that are less affected by disorder.

As expected, for a particular sample, $H_{ex}$ increases with the applied cooling field (Figure 8). The values for series A are much larger and separated from the trend observed in series B and C, the reason being that the component rendering these values in series A is not an orthodox FM contribution but it rather corresponds to the analysis of a disordered AFM matrix. Consequently, loop shift cannot be explained in terms of EB effects for A NPs. Notice that the cooling field dependence of $H_{ex}$ for series B and C does not follow a linear behavior, which again puts forward the important role of interfaces. Also, the observed increase of the FC coercivity as the cooling field is increased can be understood in such frustrated and disordered systems in terms of the coercive force necessary to bring the thermoremanent magnetization to zero and, therefore, it increases with the cooling field.

To determine the magnetic behavior at room temperature, the hysteresis cycle at 300 K for the B-0% Ni sample was measured (Supporting Information, Figure S5). $H_{ex}$ and $M_{ex}$ are 0, as expected, and $H_c$ is of the same order of magnitude than the ZFC cycle at 2 K.

Overall, on the basis of the compositional characterization and magnetic behavior discussed, we suggest the following crystalline and structural features for the three samples (see Figure 5). Series A consists of a nanostructured NiO matrix that might contain inner Ni nuclei of a reduced number of atoms. The most relevant feature is the high disorder, leading to the large irreversibilities observed. The presence of tiny Ni nuclei could be compatible with the FM contributions to the magnetic properties, although unbalanced spins in the AFM matrix would render the same phenomenology including (i) the small narrowing of the cycles around $H = 0$ and (ii) large vertical shifts in the magnetic hysteresis effects. Further insights regarding the presence of tiny Ni nuclei are discussed below on the basis of performing the reaction with four different quantities of urea and three calcination times for each urea quantity, which allows one to deduce the time-line vision of the oxidative process. The absence of an orthodox Ni core in A samples is supported by (a) the absence of the corresponding peaks in XRD patterns and (b) the absence of a proper FM hysteresis cycle. Regarding to series B, NPs are made up of a proper metallic nickel core, whose size is around the limit of the length coherence for XRD, surrounded by a thick and atomically disordered AFM shell. An O-deficient NiO intermediate zone between the core and shell is plausible to be present. The Ni/NiO interface and, in turn, the disorder, is lower than for A and larger than for C samples. EB effects are encountered in B and C samples. Samples C correspond to well conformed FM Ni cores, with a broader size distribution than the corresponding to B samples, in an ordered frontier with a thin layer of AFM NiO, which leads to conventional EB effects and smaller shifts in the measured loops.

**Mechanism of Reaction.** Further comprehension of the route is reported in this section. We followed the course of the reaction by a combination of TGA-DTA measurements of urea (Supporting Information, Figure S6) and XRD analysis at different stages of the synthetic process (Supporting Information, Figures S7 and S8). Note that both Supporting Information Figures S7 and S8 collect the whole net of experiments build from four different starting quantities of urea, horizontal direction, and different temperatures and times of calcination, vertical direction, being the difference between both figures the first step of heating at 150 °C in the oven: 2 h for the former and 16 h for the latter. Supporting Information Figure S6 shows that after urea melts (melting point 133 °C[42]), its decomposition and oligomerization take place from

(57) Nogués, J.; Sort, J.; Langlais, V.; Skumryev, V.; Suriñach, S.; Muñoz, J. S.; Baró, M. D. *Phys. Rep.* **2005**, *422*, 65–117.

~140 °C up to ~170 °C in an endothermic process according to eqs 1−3:[44]

$$NH_2CONH_2 \rightarrow NH_4^+NCO^- \rightarrow NH_3 + HNCO \text{ (isocyanic acid)} \quad (1)$$

$$NH_2CONH_2 \rightarrow H_2O + H_2CN_2 \text{ (cyanamide)} \quad (2)$$

$$NH_2CONH_2 + HNCO \rightarrow H_2NCONHCON_2H \text{ (biuret)} \quad (3)$$

Additional decomposition of urea takes place in the presence of water (note the hydration water of the nickel salt) according to the eqs 4 and 5.

$$NH_3 + H_2O \rightarrow NH_4^+OH^-; NH_4^+OH^- + H_2NCONH_2 \rightarrow 3NH_3 + CO_2 \quad (4)$$

$$HNCO + H_2O \rightarrow CO_2 + NH_3 \quad (5)$$

Thus, during the first step of thermal treatment at 150 °C in the oven, the homogeneous $Ni^{2+}$-solution (as evidenced by the green color of the liquid) contains mostly melted urea (JCPDS 01-072-0118) at 2 h (Supporting Information, Figure S7, first row) and urea and biuret (JCPDS 00-011-0732) if further decomposition and oligomerization are allowed at longer times, 16 h (Supporting Information, Figure S8, first row). Such compounds are predominant at higher urea/Ni ratios, while for low ratios urea is not allowed to oligomerize as pure biuret, so a different crystalline pattern is obtained at 2 h. Such intermediate evolves to ammonium nitrate (JCPDS 01-070-1443) at 16 h of thermal treatment. Pictures of the oligomers obtained at 2 and 16 h of thermal treatment are collected in Figure 9.

According to TGA-DTA, further thermal treatment from 170 to ~240 °C allows a second and third end othermic processes to take place (Supporting Information, Figure S6), which matches well with the reported formation of triurea (eq 6) and dicyandiamide around 210 °C (eq 7).[44]

$$H_2NCONHCON_2H + HNCO \rightarrow H_2NCONHCONHCONH_2 \text{ (triuret)} \quad (6)$$

$$2H_2CN_2 \rightarrow H_4C_2N_4 \text{ (dicyandiamide)} \quad (7)$$

Next, between ~240 and ~300 °C a stable compound is obtained (as evidenced by a small plateau in TGA-DTA, Supporting Information, Figure S6). Such a stable compound is detected upon a second stage of calcination of the $Ni^{2+}$-oligomer in a furnace at 300 °C and is indexed as cyanuric acid (JCPDS 00-023-1637) (Supporting Information, Figure S7, second row, and Figure S8, second row), which is an aromatically stabilized, cyclic trimer ($(HNCO)_3$) of isocyanic acid. Note that two extra reflections of low-medium intensity appear at 10.7 and 27.9° ($2\theta$), which are attributed to ammelide ($C_3H_4N_4O_2$) (JCPDS 00-031-1527), also produced in the decomposition of biuret but a slower rate than cyanuric acid. Actually, if higher calcination temperatures, that is, 360 °C (Supporting Information, Figure S7, third row), are used, only reflections of ammelide are observed in the XRD pattern. Although other compounds such as ammeline, melamine and melame have been reported to form in small quantities upon decomposition of urea,[44] no corresponding peaks have been observed in our case.

If the $Ni^{2+}$-oligomer obtained in the first step of our route is treated at 400 °C, above the decomposition temperature of aromatically stabilized cyanuric acid ($T_{\text{maximun rate of decomposition}}$ = 400 °C) and ammelide ($T_{mrd}$ = 420 °C),[44] complete self-combustion of the crystalline organic matrix takes place releasing $H_2$[44] and leading to the reduction of $Ni^{2+}$ cations to Ni. Loosely aggregated metal nickel NPs are thus allowed to crystallize at high temperature protected by the matrix, which is amorphous after 1 h of thermal treatment for the sample with the highest urea content (Supporting Information, Figure S7, fourth row, fourth column) and is completely removed after 2 h at 400 °C (Supporting Information, Figure S7, fifth row, fourth column), resulting in an outer oxidation of the Ni NPs. The NiO shell protecting the metal cores spreads via oxygen diffusion from the outside toward the center of the particles at longer combustion times, as evidenced by the facts that (i) global size of the particles remains approximately unchanged (results not shown) and (ii) NiO/Ni ratio increases as the time of calcination at 400 °C increases up to 4 h (Supporting Information, Figure S7, sixth row, fourth column). In addition, the NiO core can be manipulated in another way: the lower the urea content, the faster the self-combustion takes place, the higher NiO/Ni ratio. Thus, NiO NPs are formed even at 300 °C for the lowest urea content (Supporting Information, Figure S7, second row, first column). All in all, a whole palette of grades of oxidation, that is, $Ni_{nuclei}-NiO_{shell}$ NPs, is accessible by means of the manipulation of the urea content and calcination time, as shown in Supporting Information, Figure S7. Figure 9 summarizes the synthetic route.

Last, we will discuss the influence of the homogenization time of the Ni salt into the urea melted media at 150 °C (compare Supporting Information, Figures S7 and S8, first rows. Also, pictures of the resulting oligomers are shown in Figure 9). Obviously, longer times allow the formation of more biuret and triuret from urea, biuret and cyanic acid (eq 3 and 6), and the resulting consumption of cyanic acid translates into its minor availability to form aromatically stabilized cyanuric acid and ammelide, which are formed less efficiently and can be removed more efficiently at 400 °C. As a result, remaining organic elements in the powders are significantly lower for longer treatments of the melted media at 150 °C, as evidenced by elemental analysis measurements (Supporting Information, Table S1). Therefore, we chose the samples treated at 150 °C during 16 h for the magnetic characterization, given the absence of diamagnetic contribution. Last, elemental analysis results (Supporting Information, Table S1)

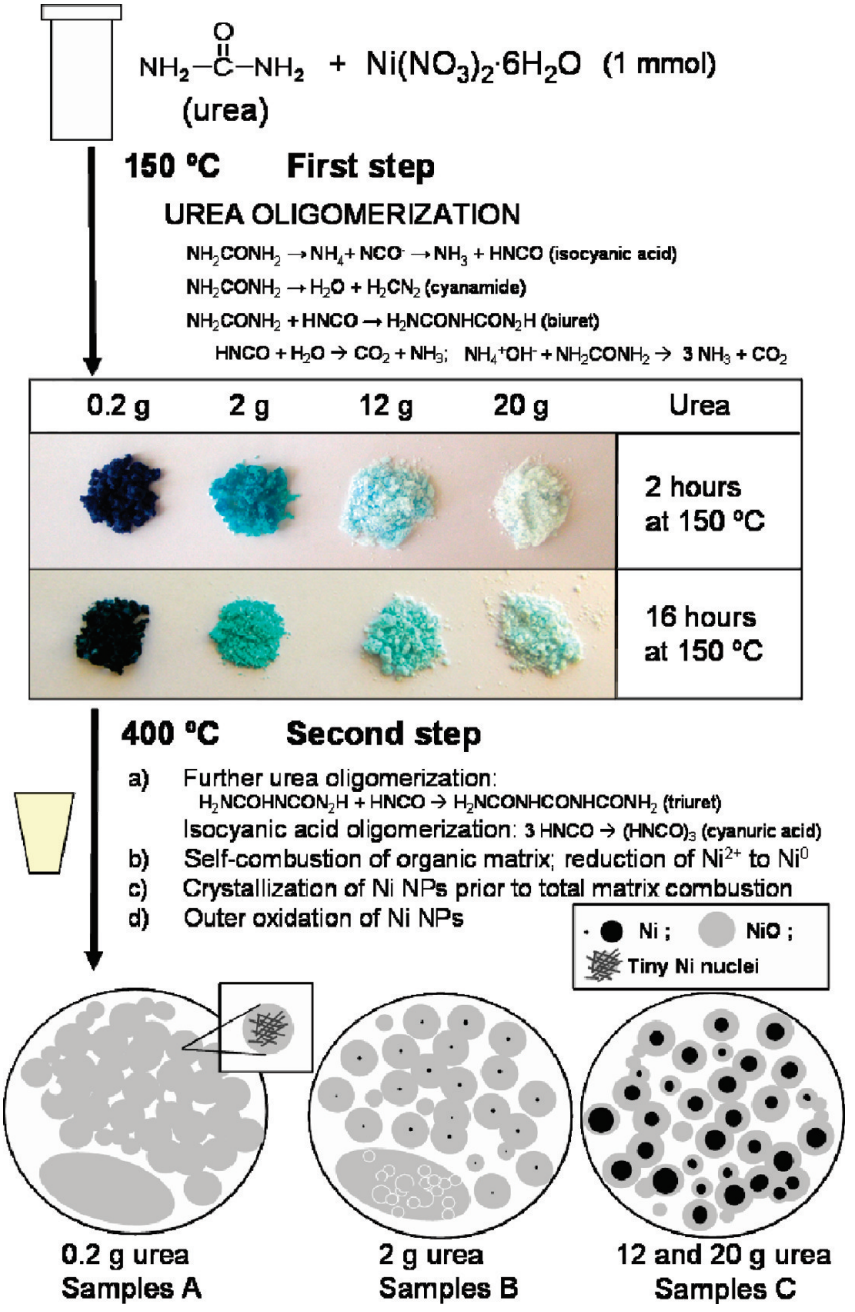


**Figure 9.** Summary of the synthesis procedure and formation mechanism of A, B, and C Ni/NiO nanostructures. Pictures of the blue to green oligomers obtained after thermal treatment at 150 °C for two different times (2 and 16 h) are shown. On the bottom, the proposed microstructural models for the nanostructures.

verified that, for equal previous thermal treatments at 150 °C, longer calcination times lead to lower amount of organic traces due to a more efficient combustion.

**Control over the Ni/NiO Ratio, Oxidation Process, and Nonstoichiometry.** It is important to emphasize that the NiO/Ni mass ratios calculated in this paper refer to the crystallographic components able to be detected by the XRD experiment. In this sense, there is evidence that B-0%-Ni NPs, whose XRD pattern does not show a Ni peak, contain a small $Ni_{core}$ since they exhibit the same magnetic regime than B-3%-Ni NPs batch displaying proper FM contributions (Supporting Information, Figure S9b and c shows the XRD patterns of B-3%-Ni and B-7%-Ni NPs, respectively). Hence, XRD may not be a valid way to detect tiny crystals, which would be ignored by the technique. In our case, both A and some B samples present XRD-based-100%-NiO and consequently an alternative assessment of the presence of tiny $Ni_{nuclei/cores}$ is desired. While magnetic characterization of B samples is quite compelling regarding the presence of $Ni_{cores}$, magnetic effects displayed by A samples cannot unambiguously be attributed to tiny Ni nuclei, and thus, further insights are desired.

Attempts to better understand the formation of the NPs were done by XRD-evaluation of the products obtained for four different urea quantities and three calcination times for each urea quantity (Supporting Information, Figure S7). Here, XRD is a useful technique for relative

rather than absolute values; i.e. for comparing products and extracting trends. First, for equal calcination times, as it has already been noted, the NiO/Ni ratio is higher for lower urea amounts (e.g., for 2 h of calcination, 100, 98, and 67% NiO is obtained for 0.2, 2, and 20 g urea, respectively) because of the faster self-combustion of the matrix and, thus, longer oxidation processes of the metallic NPs. Second, let us fix now the urea amount. In the 20 g urea experiments (forth column), the organic matrix is not removed at 1 h of calcination and no Ni/NiO is detected (fourth row), while for 2 h the content of NiO is 33% and for 4 h is 57% NiO (fifth and sixth rows). Such an increase of NiO phase at the cost of the decrease of Ni phase at longer times must be caused by the oxidation of the metal phase and given that the NPs at 2 h have a core−shell nature, as extracted from the combination of XRD, large Ni peaks, and XPS, with no Ni at the surface, the oxidative process should take place from the surface inward. If one performs the same experiment with lower urea content, the same mechanism should be expected. Thus, for 2 g urea (second column), 85% NiO is obtained at 1 h of calcination (fourth row) and longer calcination times lead to the increase of oxide at the cost of the decrease of the metallic phase: 98% NiO and 100% NiO are obtained at 2 (fifth row) and 4 h (sixth row), respectively. (Supporting Information, Figure S9a shows greater magnification of the 98% NiO XRD pattern extracted from Figure S7, the purpose being to remark the incipient, almost not detectable Ni peaks). Keeping this trend in mind, it seems feasible that a situation can be achieved in which the outer oxidation of the metallic Ni NPs is so deep that the remaining Ni nuclei are too small to be detected by XRD. Certainly, that situation should be achievable in a continuous oxidation of a metal phase; reaching it is just a matter of finding the accurate experimental conditions, represented by urea content and calcination time, to stop the oxidation process at the accurate point. Actually, that must be the case of B-0%-Ni NPs; slight differences in the heating/cooling rates among batches lead to 0, 3 or 7% Ni for B samples. In the case of A samples, we speculate with the possibility that tiny Ni nuclei remained free of oxidation. Such Ni nuclei or crystal defects would account, at least to some extent, for the unorthodox FM component manifested in the magnetic phenomenology. Experimentally, no detection of Ni phase could be done for 0.2 g urea (first column) at any calcination time (1, 2, 4 h; forth, fifth, sixth rows) and even at lower calcination temperatures (300, 360 °C; second, third rows). Consequently, the "Ni defects" of samples A are a speculation and, analogously, the intermediate zone between the $Ni_{core}$ and $NiO_{shell}$ in B samples is speculated to be a disordered, O-deficient NiO. More interestingly, it is claimed that XRD, which "detects" order, may not be a suitable technique for assessing the purity of NiO NCs, above all if prepared by organic matrix calcination routes characterized by both reduction and oxidation steps, since "disorder" stemming from unoxidized Ni atoms could remain. Therefore, previous interpretations relative to the magnetic anomalies of NiO NPs[32,37,53] might need to be revised and the hypothesis of Ni tiny nuclei might need to be taken into account in this field.

The hypothesis proposed herein relative to nonstoichiometry is in consonance with previous studies in the Co/CoO system, for which an intentional oxidation of native colloidal Co NPs allowed the detection of three different oxidation extents exhibiting magnetic anomalies, which were attributed to clusters of a few unoxidized Co atoms within a CoO phase.[10] Other experimental and simulation results in bilayers further reinforce this sketch.[3,54] Furthermore, this situation should be more prone to occur in the Ni/NiO than in the Co/CoO system given the more difficult oxidation of the former metal.[8]

Finally, it is worth remarking the differences between our process and other deliberated oxidations of Ni NPs at elevated temperatures.[58,59] In the latter reports, hollow NiO NPs are produced as a result of the nanoscale Kirkendall effect resulting from a much faster outward diffusion of nickel than the inward diffusion of oxygen. The enhanced mobility of nickel ions in such cases may be favored by the grain boundaries in the polycrystalline native Ni NPs. This might be opposite to our monocrystalline primitive Ni NPs, which would likely account for a preferential oxygen diffusion leading to solid NiO NPs.

We hope that the observations reported herein stimulate further endeavors toward the rich Ni/NiO nanostructured system from experimental, characterization and theoretical perspectives. The ability to control the microstructural features of the Ni/NiO NPs should eventually open the path to materials benefiting from the enhanced thermal stability of a small FM component embedded within an air-stable NiO component susceptible of functionalization and, thus, of manufacturing for a wide range of potential applications.[4−6,11−14]

## 4. Conclusions

In summary, an easy, inexpensive urea-melt assisted synthetic route has been designed for the synthesis of Ni/NiO NPs. It is believed that the synthetic method reported here can be extended to other metallic or oxide NPs. Herein, microstructural features of the as-prepared NPs can be controlled for three typical regimes (A, B, C) as a function of the starting urea quantity: the lower the urea amount, the thicker the $NiO_{shell}$. Additionally, extra control over the fraction of $NiO_{shell}$ within each regime was achieved by means of the calcination time: longer calcinations lead to deeper oxidations. On the other hand, organic matter in the resulting products was found to minimize at 16 h of previous thermal treatment at 150 °C of $Ni^{2+}$ salt and urea, allowing for a magnetic characterization without diamagnetic contribution. While XPS demonstrates the presence of a $NiO_{shell}$ in A, B, and C samples, the existence of $Ni_{cores}$ in samples B and C is strongly supported by XRD, as well as the observed

(58) Nakamura, R.; Lee, J. G.; Mori, H.; Nakajima, H. *Philos. Mag.* **2008**, *88*, 257–264.
(59) Railsback, J. G.; Johnston-Peck, A. C.; Wang, J.; Tracy, J. B. *ACS Nano* **2010**, *4*, 1913–1920.

magnetic properties (and also HRTEM for C samples). The formation mechanism additionally points out toward the presence of $Ni_{cores}$ in those B samples whose XRD patterns do not show a Ni peak. In the case of samples A, where no Ni at all is detected either by XRD and HRTEM, both the formation mechanism and the magnetic properties are compatible with tiny Ni nuclei, although there is no evidence of such entities. This work puts forward the important role of disorder and quality of the interfaces between FM and AFM components in the global magnetic phenomenology. The defective crystallinity of the NPs reported here is because of a 2-fold reason: (a) inclusions of a metallic phase within a metallic oxide phase, which leads to a large FM/AFM interface rich in defects, and (b) the quenching of the nanocrystals undergoing oxygen diffusion. The observed magnetic behavior, in particular the large loop shifts observed for B NPs, is remarkably different compared it with previous reports on Ni/NiO NPs,[21,22,24,25,36] whereas the large loop shifts exhibited by A nanostructures resemble those displayed by previous reports on NiO NPs and interpreted on the basis of surface or antiphase boundaries effects.[32,37,53]

**Acknowledgment.** Financial support from MICINN projects CSD2009-00013, MAT2007-61954, MAT2008-06517-C02-01, and MAT2009-10214 is greatly appreciated. A.Q.-F. acknowledges MEC for financial support through a FPU PhD fellowship. The authors thank Dr. J. García Fierro for collecting and discussing the XPS spectra, Dr. E. Matesanz and Dr. J. Velázquez (Centro de Difracción de Rayos X UCM) for technical assistance and for their help with the RIR method, and Dr. A. Gómez Herrero and Dr. E. Urones Garrote (Centro de Microscopía Electrónica Luis Bru UCM) for their help with the acquisition of the HRTEM and SEM images.

**Supporting Information Available:** TEM, HRTEM, and SEM images, SAED and XRD patterns, XPS spectra, hysteresis cycle, nitrogen physisorption isotherms results, elemental analysis results and TG-DTA curve of urea, and description of textural properties. This material is available free of charge via the Internet at http://pubs.acs.org.

IV. Chapter 2.1

# Supporting Information

## Urea-Melt Assisted Synthesis of Ni/NiO Nanoparticles Exhibiting Structural Disorder and Exchange Bias

Ana Querejeta-Fernández,[†] Marina Parras,[†] Aurea Varela,[†] Francisco del Monte,[‡] Mar García-Hernández[‡] and José M. González-Calbet[*,†]

[†]*Departamento de Química Inorgánica I, Facultad de Ciencias Químicas, Universidad Complutense de Madrid, 28040 Madrid, Spain, and* [‡]*Instituto de Ciencia de Materiales de Madrid, CSIC, Campus de Cantoblanco, 28049 Madrid, Spain*

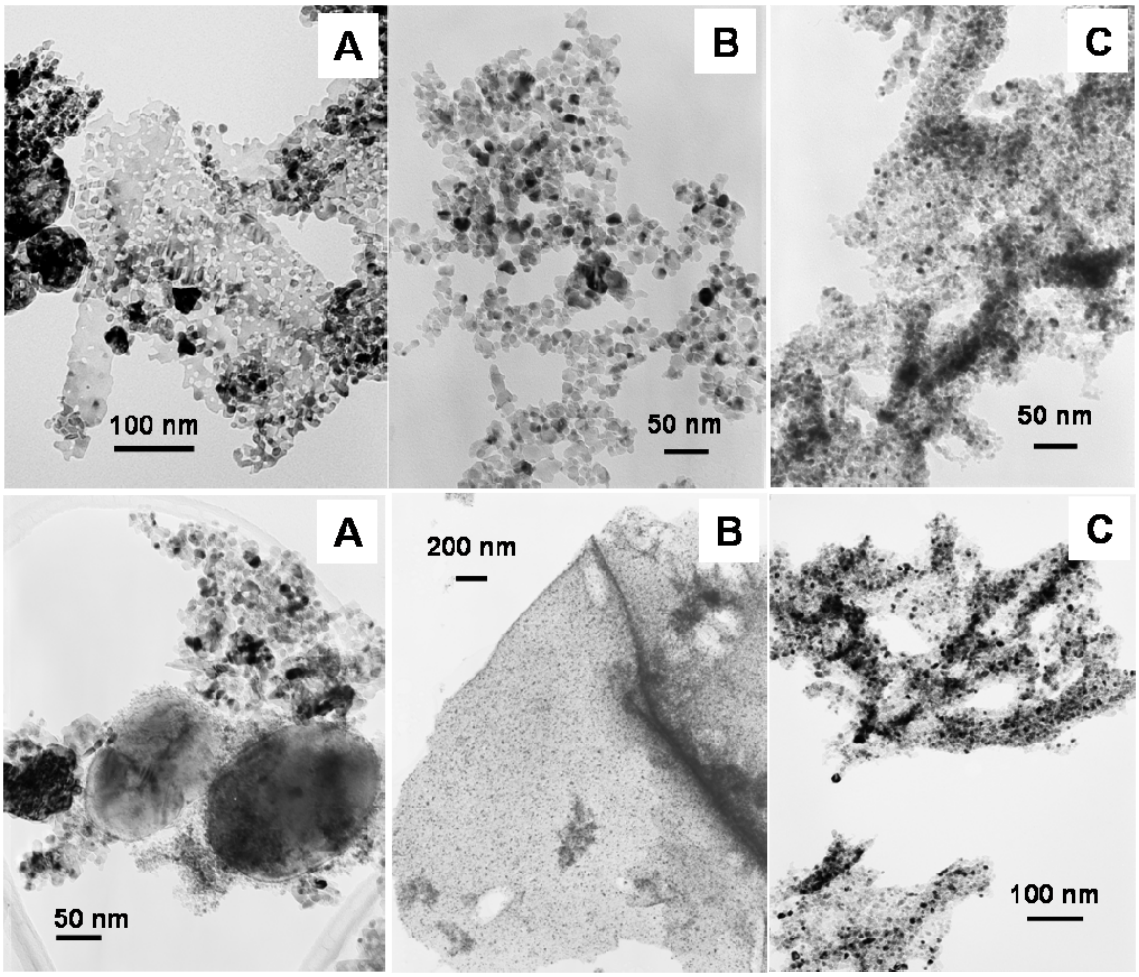

**Figure S1**. TEM images of representative members of A, B and C samples prepared by [150 ºC, 16 h + 400 ºC, 2 h] protocol. Note the typical tendency of aggregation fashion in each series: in A, a continuous thin network with pores which eventually lead to microcrystals because of sintering; plane sheets made of individual NPs in B and a thicker, although with large voids, agglomerations of individual NPs in C.

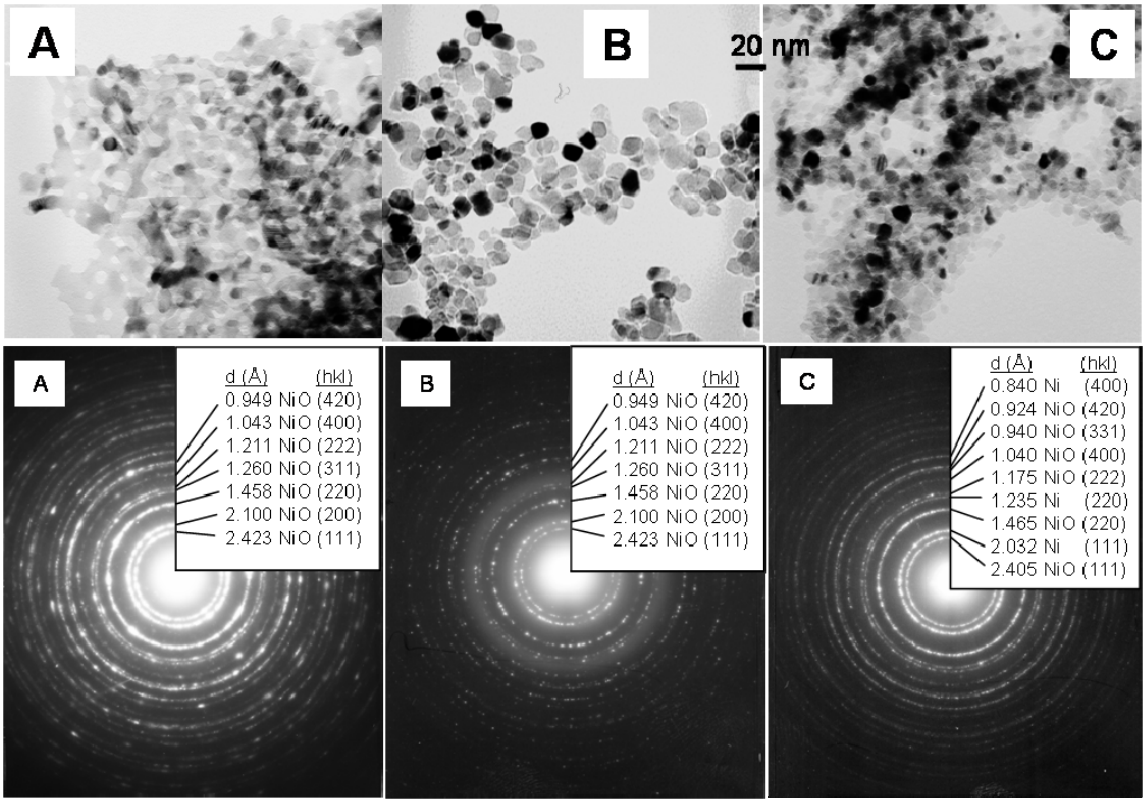


**Figure S2.** TEM images and SAED patterns of A, B and C samples prepared by [150 ºC, 16 h + 400 ºC, 2 h] protocol.

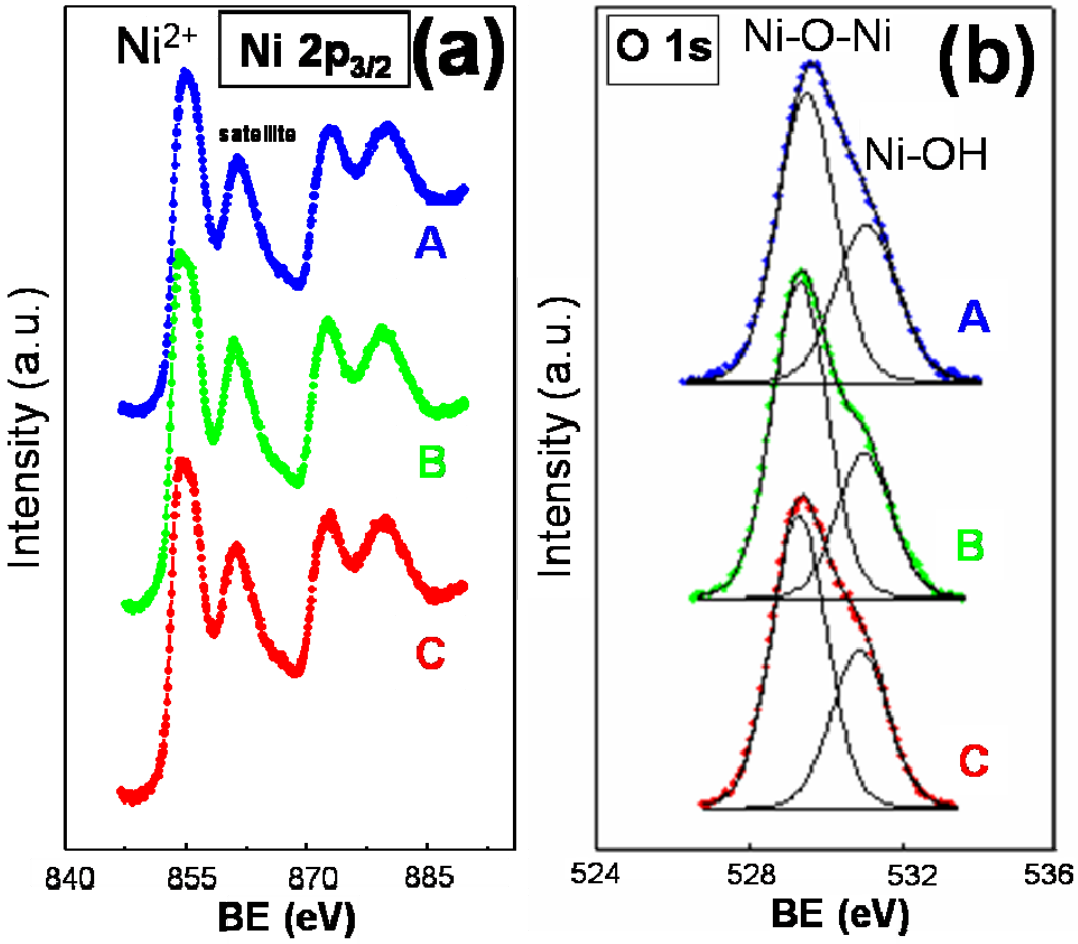


**Figure S3**. XPS spectra of (a) Ni $2p_{3/2}$ and (b) O 1s regions of A, B-100%-NiO and C-40%-NiO samples prepared by [150 ºC, 16 h+ 4 00 ºC, 2 h] protocol. "Satellite" stands for satellite peak.

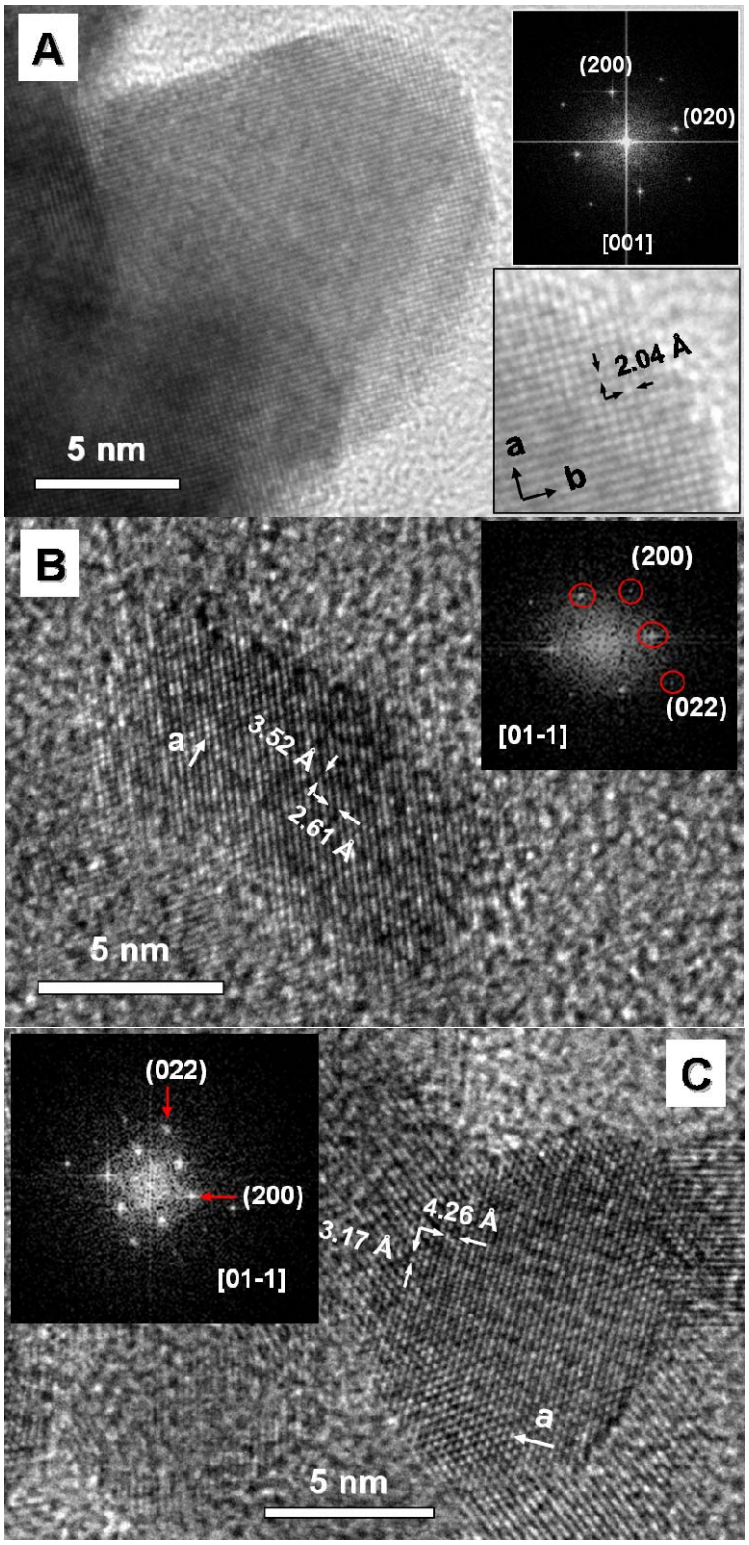


**Figure S4.** HRTEM images of A-100 %-NiO (A), B-100 %-NiO (B) and C-74 %-NiO (C). The samples were prepared by [150 ºC, 16 h + 400 ºC, 2 h] protocol. Corresponding FFT are shown at the inset.

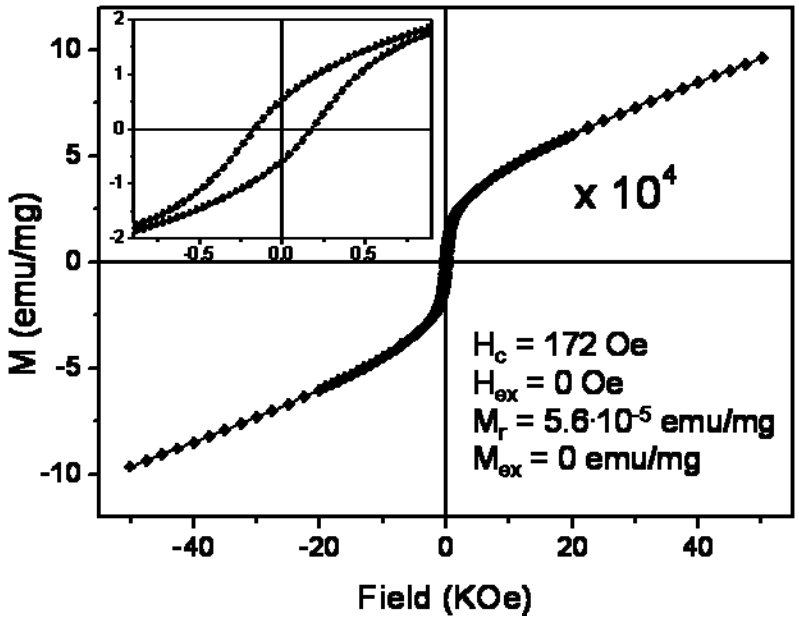


**Figure S5.** Hysteresis cycle measured at 300 K for B-0% Ni sample prepared by [150 ºC, 16 h + 400 ºC, 2h] protocol. Corresponding $H_c$, $H_{ex}$, remanence ($M_r$) values are indicated. Inset shows greater detail of the central part of the cycle.

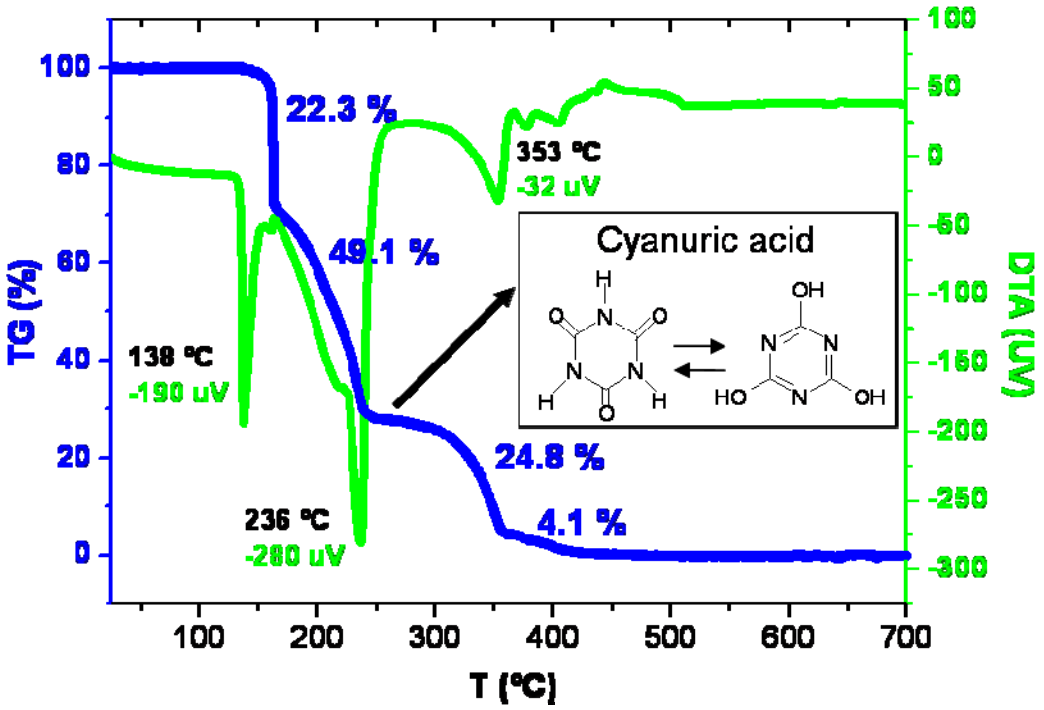


**Figure S6** . TG-DTA curve of urea. The system was kept at ~160 ºC for 20 min. Consequently, the more abrupt slope of the TG curve at that temperature as compared with the following slope is only due to the constant temperature at that point. Note that although the whole TG curve serves to characterize the course of the reaction, the temperatures are only a rough indication of the process because of the kinetics dependence of the decomposition of the products; i.e. the decomposition processes occur in a broad range of temperatures so the TG experiment is not accurately comparable to the reaction in the furnace, where the heating rate is different and gradients of temperature exist.

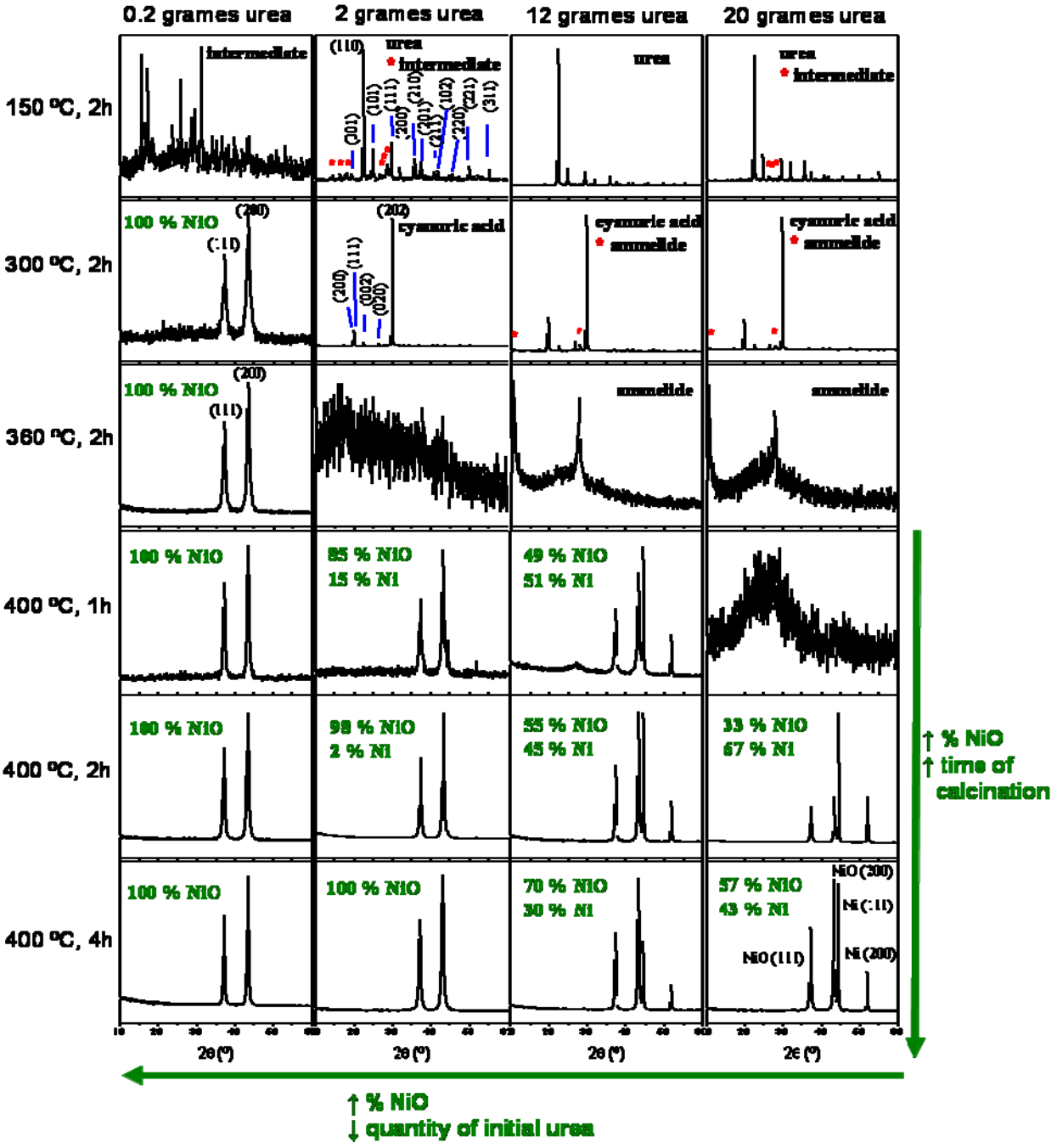


**Figure S7**. XRD patterns of the net of products obtained from different starting urea amounts (horizontal direction) and different calcination temperatures and times (vertical direction) for the oligomers obtained (first row) after 2 h of thermal treatment at 150 ºC of the urea and nickel nitrate mixture.

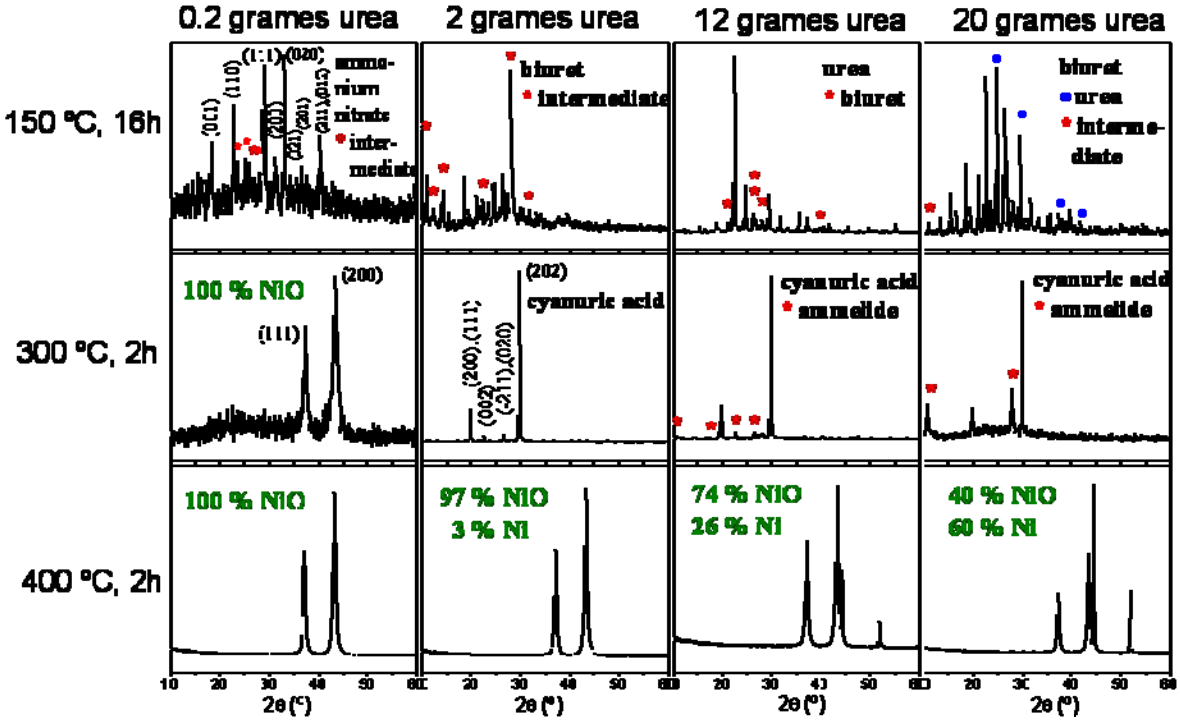


**Figure S8.** XRD patterns of the products obtained from different starting urea amounts (horizontal direction) and different calcination temperatures (vertical direction, second and third rows) for the oligomers obtained (first row) after 16 h of thermal treatment at 150 ºC of the urea and nickel nitrate mixture.

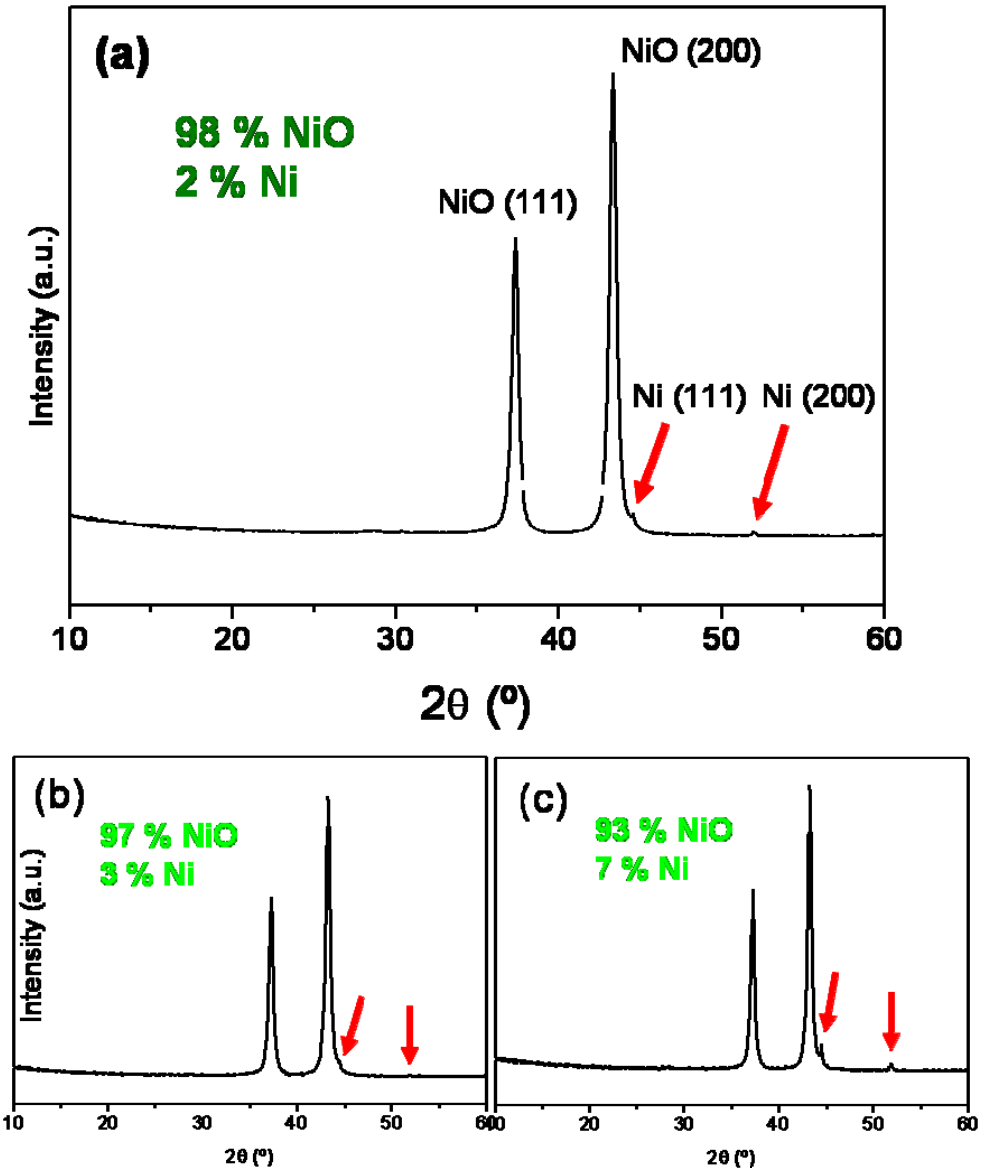


**Figure S9.** XRD patterns showing incipient Ni peaks. All of them correspond to samples prepared from 2 g urea under the following thermal treatments: a) [150 ºC, 2 h + 400 ºC, 2 h] protocol (it is the higher magnification of the pattern shown in Figure S7 fifth row, second column); (b) and (c) [150 ºC, 16 h + 400 ºC, 2 h] protocol (these are the samples whose phase % results are collected in Table 1); (b) is the higher magnification of the pattern shown in Figure S8 third row, second column.

**Table S1.** Elemental analysis results corresponding to samples treated during 2 and 16 h at 150 ºC and calcined under the same (400 ºC, 2 h) and different (400 ºC, 4 h) conditions.

| | **2 h at 150 ºC / calcined 400 ºC, 2 h** | | | **16 h at 150 ºC / calcined 400 ºC, 2h** | | |
|---|---|---|---|---|---|---|
| | **C** | **H** | **N** | **C** | **H** | **N** |
| **0.2 g urea** | 0.9 | 0.1 | 0.0 | 0.2 | 0.0 | 0.1 |
| **2 g urea** | 1.9 | 0.2 | 0.0 | 0.2 | 0.0 | 0.1 |
| **20 g urea** | 1.6 | 0.1 | 0.2 | 0.3 | 0.0 | 0.3 |
| | **2 h at 150 ºC / calcined 400 ºC, 4h** | | | | | |
| | **C** | **H** | **N** | | | |
| **2 g urea** | 0.6 | 0.1 | 0.0 | | | |
| **20 g urea** | 0.4 | 0.0 | 0.0 | | | |

---

**Textural properties**

Characterization by SEM and nitrogen adsorption-desorption measurements was performed in an attempt to characterize the textural properties of A, B and C samples. SEM (Figure S10) images mainly show fine clusters with holes and voids, remanent of the organic matrix and gases released upon its decomposition, while the $N_2$ sorption measurements (Figure S11 and Table S2) reveal a low superficial area in all the cases, as corresponds to loosely aggregated crystalline NPs. However, a clear trend of this parameter in the sense A>B>C exists. The higher superficial area in A as compared to B and C confirms the mentioned A resemblance to a porous matrix. The lower density of the packing of NPs in B and C leads to a minor presence of pores, resulting in a lower adsorption of $N_2$.

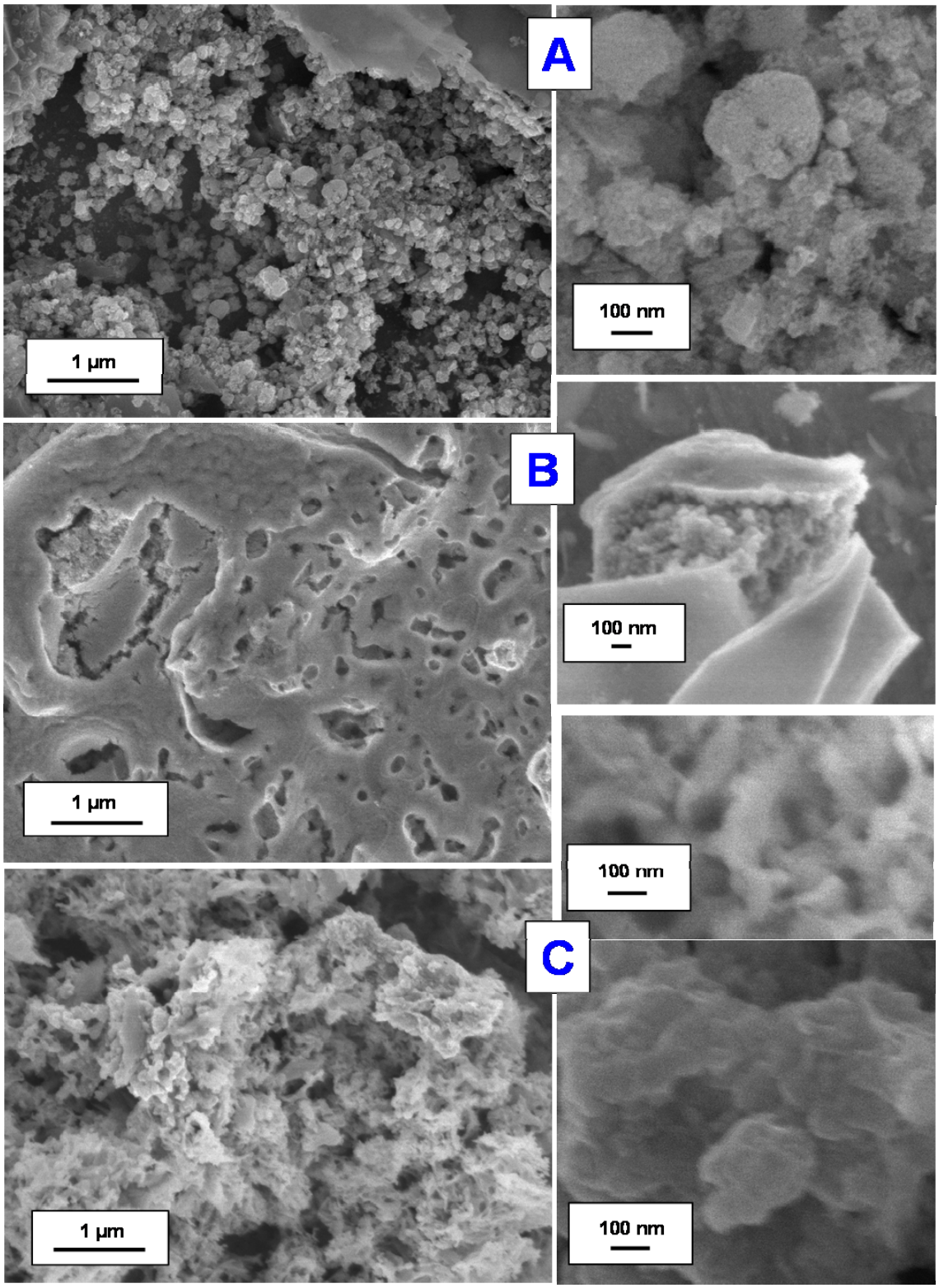


**Figure S10**. SEM images of three members of A, B and C samples: 100 % NiO (A), 100 % NiO (B) and 74 % NiO (C), prepared by [150 ºC, 16 h + 400 ºC, 2 h] protocol at low and high magnification. The samples were prepared by adding drops of an ethanol suspension in a cylindrical brass stub and letting it dry and were imaged as-prepared.

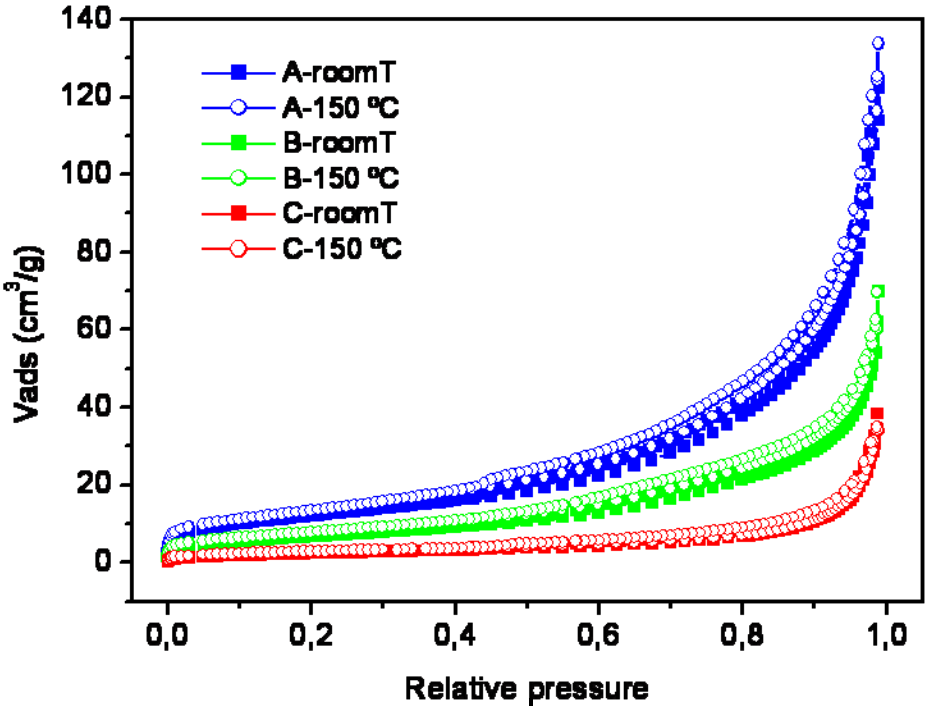


**Figure S11**. $N_2$ adsorption-desorption isotherms for samples A, B and C degasified both at room temperature and 150 ºC. For each series –A, B and C–, samples were prepared by mixing different batches of the same series. Degasification at 150 ºC did not modify the relative NiO/Ni ratio of the samples.

**Table S2**. Specific Surface Area ($m^2 g^{-1}$) of the samples A, B and C obtained after degasifying both at room temperature and 150 ºC.

| | **BET surface area ($m^2/g$)** |
|---|---|
| **A-roomT** | 44 |
| **A-150 ºC** | 49 |
| **B-roomT** | 25 |
| **B-150 ºC** | 29 |
| **C-roomT** | 9 |
| **C-150 ºC** | 10 |

# CHAPTER 2.2

## Urea-Melt Assisted Synthesis of Binary Oxides of Transition Metals

In view of the successful synthesis of Ni/NiO nanostructures via the urea-melt route, the suitability of the method for the synthesis of other compositions was studied. Thus, this chapter reports the generality of such pathway for the preparation of binary nanooxides. Pure $Co_3O_4$ (~ 20 nm) and $Mn_3O_4$ (~ 20-60 nm) nanoparticles and mixtures of nanoparticulated $\gamma$-$Fe_2O_3$ and $\alpha$-$Fe_2O_3$ were obtained. However, the method failed in the achievement of the ternary compounds barium and strontium manganites. Also, although pure $SrCO_3$ was obtained, particle size did not lay in the nanometer scale. Further work is still needed to better understand the route and optimize it in terms of purity of the products as well as particle size and aggregation. Also, its extension to other compounds remains unexplored.

.

# Urea-Melt Assisted Synthesis of Binary Oxides of Transition Metals

## 1. Introduction

In view of the successful synthesis of NiO and $Ni_{core}$-$NiO_{shell}$ nanostructures via urea-melt route (Chapter 2.1) we checked the suitability of the method for the synthesis of other nanooxides. Attempts to prepare nanosized binary metallic oxides as well as manganites and carbonates were done. As-prepared products were characterized by means of X-Ray diffraction (XRD) and transmission electron microscopy (TEM).

## 2. Experimental Section

Cobalt nitrate hexahydrate **(**$Co(NO_3)_2 \cdot 6H_2O$) (Merck), manganese nitrate tetrahydrate ($Mn(NO_3)_2 \cdot 4H_2O$) (≥ 97.0 %, Sigma-Aldrich), iron (III) chloride ($FeCl_3$) (≥ 98 %, Sigma-Aldrich), iron (II) chloride tetrahydrate ($FeCl_2 \cdot 4H_2O$) (Merck), iron (III) nitrate nonahydrate ($Fe(NO_3)_2 9H_2O$) (99.99%, Aldrich), iron (II) sulfate heptahydrate ($FeSO_4 \cdot 7H_2O$) (Merck), barium chloride ($BaCl_2$) (99.9%, Aldrich), manganese (II) chloride tetrahydrate ($MnCl_2 \cdot 4H_2O$) (99.99%, Aldrich), potassium permanganate ($KMnO_4$) (99+%, Aldrich), strontium (II) nitrate ($Sr(NO_3)_2$) (Merck) were used as received. A Teflon vessel equipped with a Teflon cap was loaded with urea (amounts detailed in Table 1) and 1 mmol of metallic salt.[1] The closed vessel was put into an oven at 150 ºC for 16 h (except indicated otherwise in Table 1). After cooling down to room temperature, a portion of the resultant oligomer was placed into a porcelain crucible. Calcinations were then performed within a furnace with constant heating rates of 2 ºC/min and cooling downs within the furnace. Calcination temperatures are detailed in Table 1.

Characterization of the as-prepared powders was done by X-Ray diffraction (XRD) and transmission electron microscopy (TEM).

## 3. Results and discussion

Table 1 collects all the experiments performed.

**Table 1.** Detailed reaction conditions of the urea-melt syntheses and XRD results.

| # | Salt (1 mmol) | Urea g | $T_{calc.}$ (ºC) | $t_{calc.}$ (h) | XRD results (Scherrer size, nm) |
|---|---|---|---|---|---|
| **Co** | | | | | |
| 1 | $Co(NO_3)_2 \cdot 6H_2O$ | 2 | 500 | 2 | $Co_3O_4$ (37) |
| 2 | " | 5 | 500 | 2 | $Co_3O_4$ (34) |
| 3 | " | 5 | 400 | 2 | $Co_3O_4$ (20) |
| 4 | " | 10 | 400 | 2 | $Co_3O_4$ (20) |
| **Mn** | | | | | |
| 5 | $Mn(NO_3)_2 \cdot 4H_2O$ | 5 | 400 | 2 | $Mn_2O_3$ (26) + $Mn_3O_4$ (28) |
| 6 | " | 10 | 400 | 2 | $Mn_2O_3$ (35) + $Mn_3O_4$ (35) |
| 7 | $Mn(NO_3)_2 \cdot 4H_2O$ + $H_2O$ (5 ml) | 5 | 400 | 2 | $Mn_3O_4$ (26) |
| **Fe** | | | | | |
| 8 | $FeCl_3$ + $FeCl_2 \cdot 4H_2O$ | 33.3 | 380 | 1 | γ-$Fe_2O_3$ (37) + α-$Fe_2O_3$ (26) |
| 9 | " | 33.3 | 600 | 1 | α-$Fe_2O_3$ (45) + α-$Fe_2O_3$ (45) |
| 10 | $Fe(NO_3)_2 \cdot 9H_2O$ + $FeSO_4 \cdot 7H_2O$ | 11.1 | 400 | 2 | γ-$Fe_2O_3$ (20) + α-$Fe_2O_3$ (26) |
| **Manganites** | | | | | |
| 11* | $BaCl_2$ + $KMnO_4$ + $MnCl_2 \cdot 4H_2O$ + $H_2O$ (2 ml) | 20 | 400 | 3.5 | $BaCO_3$ |
| | | | 750▲ | 6 | $BaCO_3$ + $Ba_3MnO_8$ + $Ba_{6.3}(Mn_{24}O_{48})$ |
| 12* | $Sr(NO_3)_2$ + $KMnO_4$ + $MnCl_2 \cdot 4H_2O$ | 40 | 400 | 43 | $SrCO_3$ |
| **Sr** | | | | | |
| 13* | $Sr(NO_3)_2$ | 40 | 400 | 43 | $SrCO_3$ |

* A different first step of thermal treatment: 170 ºC, 3 days (#11), 200 ºC, 1 day (#12 and 13).

▲Calcination was performed on the product obtained after calcination at 400 ºC (row above).

### 3.1. $Co^{2+}$ salt

Experiments under different conditions were performed (# 1-4, Table 1). Urea amounts of 2, 5 and 10 g and calcination temperatures of 500 and 400 ºC were employed. XRD characterization revealed that pure $Co_3O_4$ (JCPDS 00-042-1467) was obtained in all the cases. Figure 1 shows a representative XRD pattern. The different conditions employed make it difficult to compare the results. However, two groups of crystal sizes calculated from XRD data by Scherrer method are distinguished: 37 and 34 nm for samples # 1 and 2, respectively, and 20 nm for samples # 3 and 4. Such a difference may be due to the calcination temperature (500 and 400 ºC, respectively): higher temperatures of calcination may lead to higher crystal size. TEM images (Figure

2) reveal NCs of size ~ 20, ~ 40, ~20 and ~20 nm for samples #1, 2, 3 and 4, respectively, in reasonable accordance with XRD crystal size, although with some discrepancies regarding sample #1. Comparison of samples # 1 and 2, performed under the same conditions except for the urea amount (2 and 5 g, respectively), seems to indicate a higher NP aggregation level for lower urea amounts (Figure 2). This could be due to the fact that, under the same calcination conditions, the self-combustion of the organic matrix is completed faster the lower the urea amount, prompting the NPs free of organics to agglomerate.

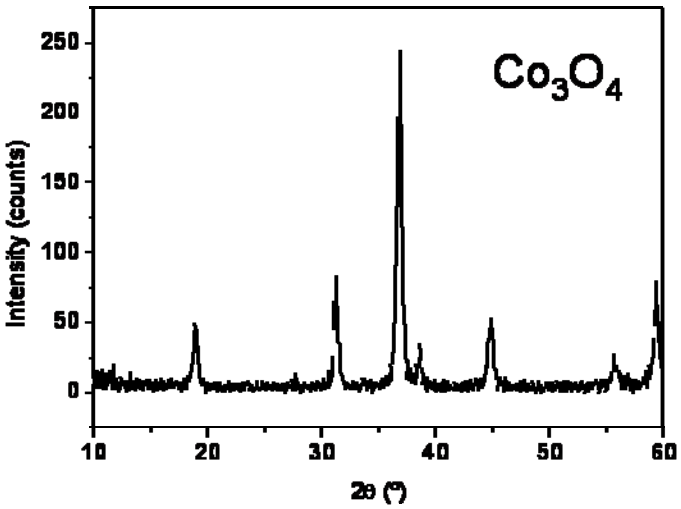


**Figure 1.** XRD pattern corresponding to # 3 of Table 1. All of the peaks can be assigned to $Co_3O_4$.

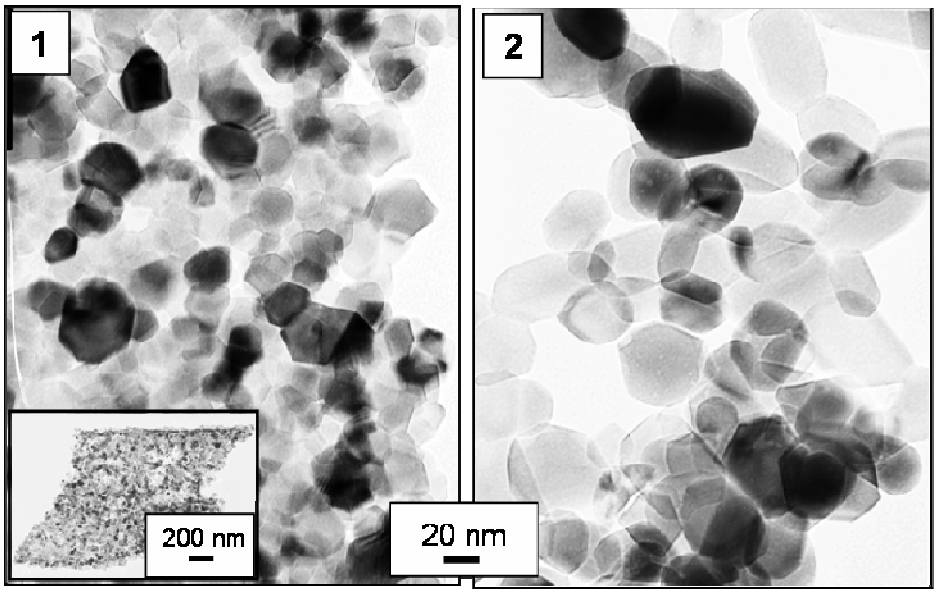


**Figure 2.** TEM images of samples # 1 and 2 of Table 1.

### 3.2. $Mn^{2+}$ salt

Reactions performed with 5 and 10 g of urea (# 5 and 6, respectively, of Table 1) led to a biphasic product consisting of $Mn_2O_3$ (bixbyite, JCPDS 00-041-1442) and $Mn_3O_4$ (hausmannite, JCPDS 01-089-4837), as detected by XRD (Figure 3, (5)). Scherrer crystal size was similar for both phases within a sample (26 and 28 nm, respectively, for sample # 5 and 35 and 35 nm for sample # 6). TEM images (Figure 4, (5), (6)) show NPs of size ~ 20 nm and some larger particles of size ~ 200 nm probably formed through the aggregation and sintering of NPs once the organic matrix had been removed. Formation of a single phase was achieved by adding water (see Table 1, # 7) to the reaction mixture, as can be seen in the corresponding XRD pattern (Figure 3, (7)). Scherrer crystal size is 26 nm. TEM characterization (Figure 4, (7)) revealed NPs with a size range ~ 20-60 nm.

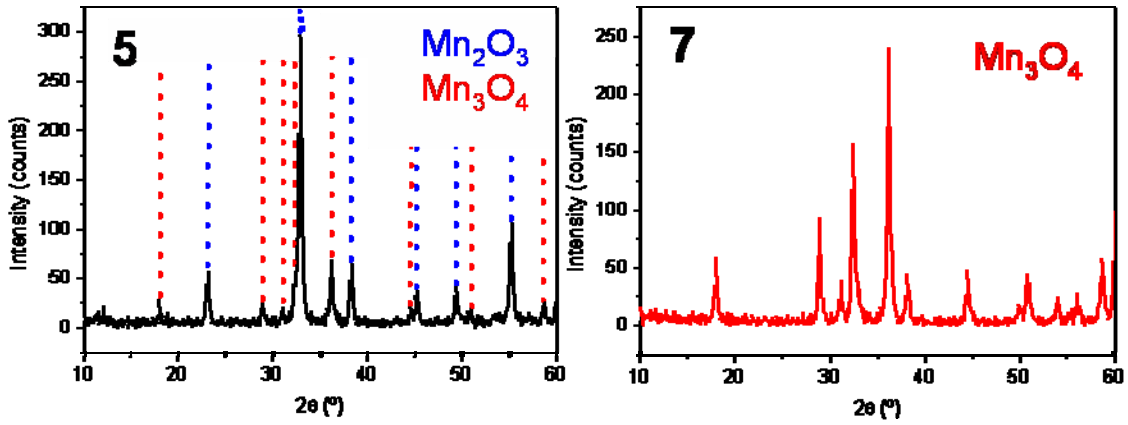


**Figure 3.** XRD patterns corresponding to samples # 5 and #7 of Table 1. Pattern #5 is biphasic and can be assigned $Mn_2O_3$ (bixbyte) and $Mn_3O_4$ (hausmannite). Pattern # 7 can be assigned to $Mn_3O_4$.

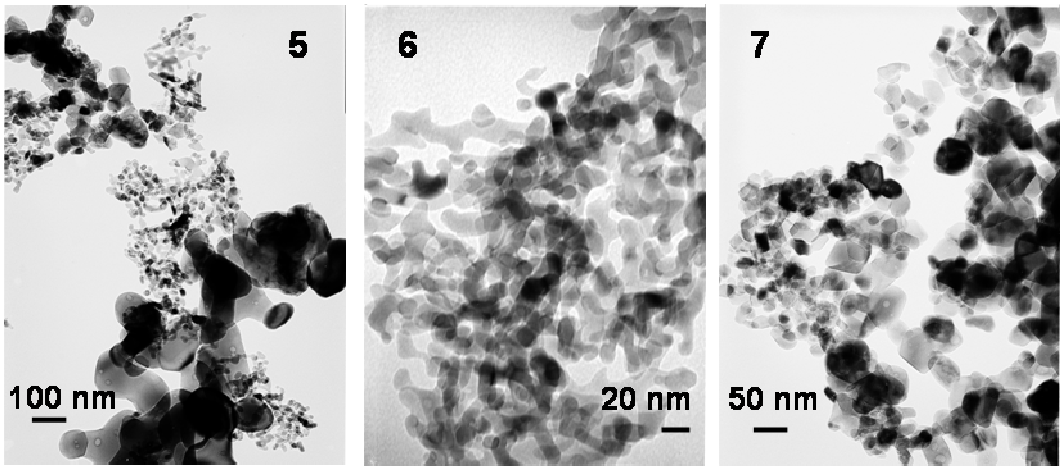


**Figure 4.** TEM images of samples # 5, 6 and 7 of Table 1.

### 3.3. $Fe^{3+}/Fe^{2+}$ salts

Starting mixtures of $Fe^{3+}$ and $Fe^{2+}$ chlorides were employed in an attempt to synthesize $Fe_3O_4$ (magnetite). The mole ratio of the salts was 0.6:0.3, respectively, according to the oxidation state of iron in the target product. All of the experiments (# 8-10 of Table 1) led to mixtures of $\alpha$-$Fe_2O_3$ (hematite, 00-039-1346) and $\gamma$-$Fe_2O_3$ (maghemite, 00-039-1346), as revealed by XRD (Figure 5). Calcination at 380 ºC (# 8, Table 1) led to a preponderance of maghemite over hematite, while the hematite was the predominant product for calcination at 600 ºC (# 9, Table 1) for equal rest of conditions. The transformation of maghemite (which is ferromagnetic and has a dark brown color) to hematite (which is diamagnetic and has a red color) at longer times indicates the progressive oxidation of $Fe^{3+}$ to $Fe^{2+}$ under the oxidative atmosphere within the oven once the organic matrix has been removed. TEM image of sample # 8 (maghemite + hematite) (Figure 6) shows the coexistence of two well-distinguished groups of crystal sizes –15 and 120 nm–, which could correspond to the two distinct phases crystallized. Last, a further experiment was performed in which the iron chloride precursors were substituted by a mixture of iron (III) nitrate and iron (II) sulphate. Calcination at 400 ºC during 2 h led to a mixture of maghemite and hematite (Figure 5, (10)).

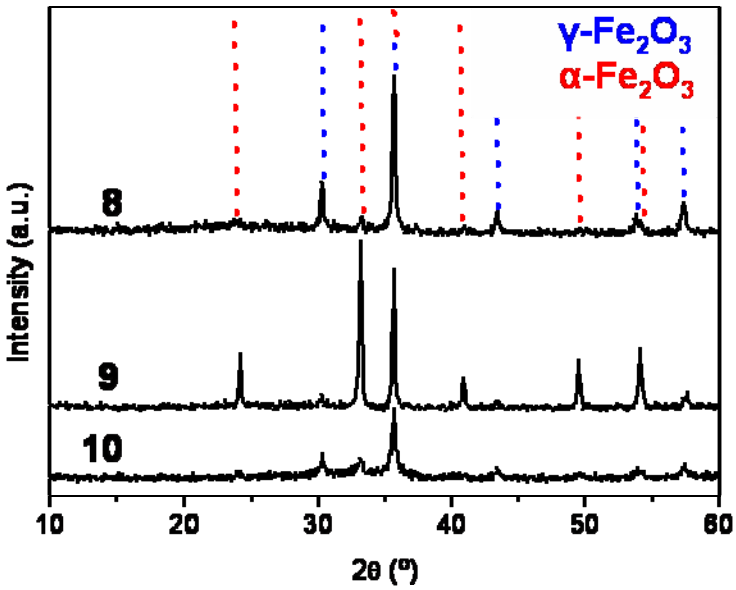


**Figure 5.** XRD patterns of samples # 8, 9 and 10 of Table 1. All of them are biphasic and can be assigned to $\gamma$-$Fe_2O_3$ and $\alpha$-$Fe_2O_3$.

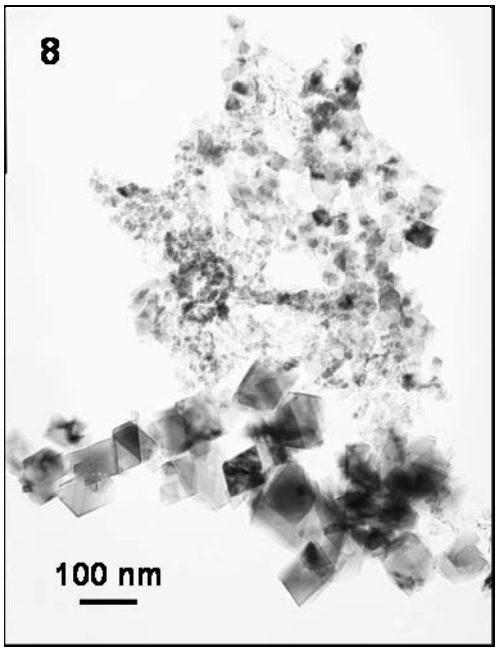


**Figure 6.** TEM image corresponding to sample # 8 of Table 1.

### 3.4. "Manganites" experiments

Multinary oxides, in particular manganites, were also tested as target products to be prepared through the urea-melt assisted route. Experiment # 11 attempted to prepare $BaMnO_3$ according to the reaction conditions detailed in Table 1. For calcination temperatures of 400 ºC during 3.5 h, $BaCO_3$ (witherite, JCPDS 00-005-0378) was obtained as the only product of reaction, as-detected by XRD (Figure 7, (11)). Note that the formation of carbonate can take place in the presence of water according to the following reactions:

$NH_2CONH_2$ (urea) → $NH_4^+ NCO^-$ → $NH_3$ + HNCO (isocyanic acid) [1]

$NH_3 + H_2O \rightarrow NH_4^+OH^-$ ; $NH_4^+OH^- + H_2NCONH_2 \rightarrow 3\ NH_3 + CO_2$ [2]

$HNCO + H_2O \rightarrow CO_2 + NH_3$ [3]

$H_2O + CO_2 \rightleftharpoons H_2CO_3$ (carbonic acid) [4]

$H_2CO_3 \rightleftharpoons H^+ + HCO_3 \rightleftharpoons 2\ H^+ + CO_3^{2-}$ (carbonate) [5]

$2\ OH^- \rightarrow 2\ H_2O$

Apart from the thermal decomposition of urea (Eq. 1) generating ammonia and isocyanic acid, further decomposition can take place in the presence of water according to Eq. 2 and 3, which produces ammonia ($NH_3$) and carbon dioxide ($CO_2$). In the presence of water, $CO_2$ forms carbonic acid ($H_2CO_3$) (Eq. 4), whose dissociation equilibrium can be displaced towards the formation of carbonate in the basic medium generated by aqueous ammonia (Eq. 5). Thus, in the presence of alkali earth cations such as $Ba^{2+}$, which show a strong tendency to form carbonate crystals, precipitation of the corresponding carbonates takes place.

Returning to experiment # 11, the lack of detection of manganese compounds could be due to manganese adsorption in the crystalline $BaCO_3$ product. To test this hypothesis, calcination of such a product was conducted at 750 ºC during 6 h and XRD characterization of the resulting product (Figure 7, "(11) + cal. 750 ºC, 6h") revealed the formation of ternary oxides of barium and manganese such as $Ba_3MnO_8$ and $Ba_{6.3}(Mn_{24}O_{48})$ (JCPDS 01-089-6599 and 01-088-0564, respectively) in addition to $BaCO_3$, confirming the presence of manganese cations or amorphous manganese oxides in the crystalline $BaCO_3$. Thus, the tendency of $BaCO_3$ to crystallize hampered the

formation of $BaMnO_3$ at the ideal temperature (~ 400 ºC) of self-combustion of the organic matrix and ternary barium manganese oxides different from stoichiometric barium manganite were obtained by solid state reactions at higher temperature (750 ºC).

Since the preparation of $BaMnO_3$ failed we tried to prepare $SrMnO_3$ (# 12, Table 1). However, XRD characterization (Figure 7, (12)) revealed the formation of $SrCO_3$ as the only crystalline product of reaction.

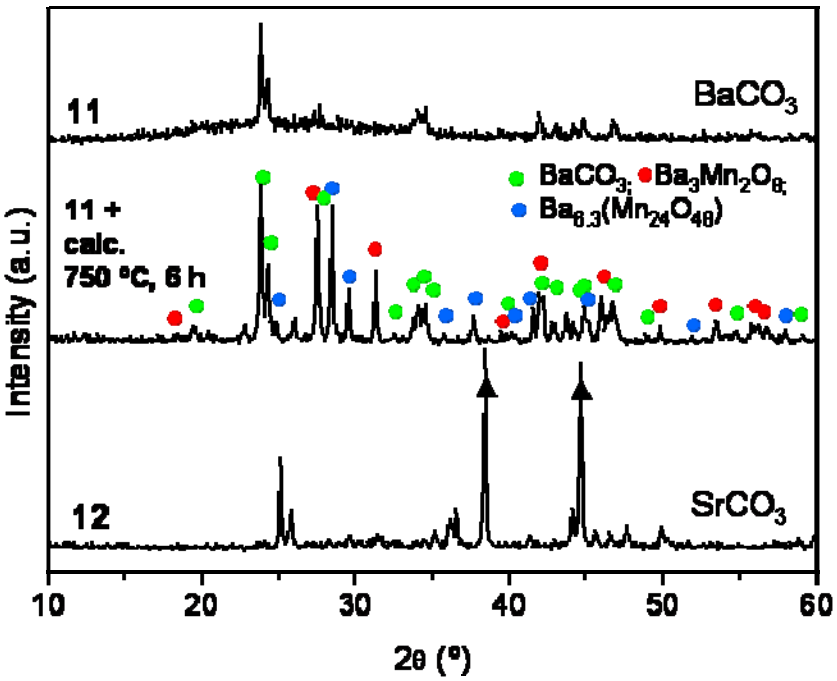


**Figure 7**. XRD patterns of samples # 11 and 12 of Table 1. ▲ Symbols mark peaks corresponding to aluminium from the holder.

### 3.5. $Sr^{2+}$

Last, when strontium nitrate was used as the only metallic precursor salt and for the conditions detailed in Table 1, # 13, strontium carbonate (strontianite, JCPDS 01-084-1778) was obtained as manifested by the corresponding XRD pattern (Figure 8).

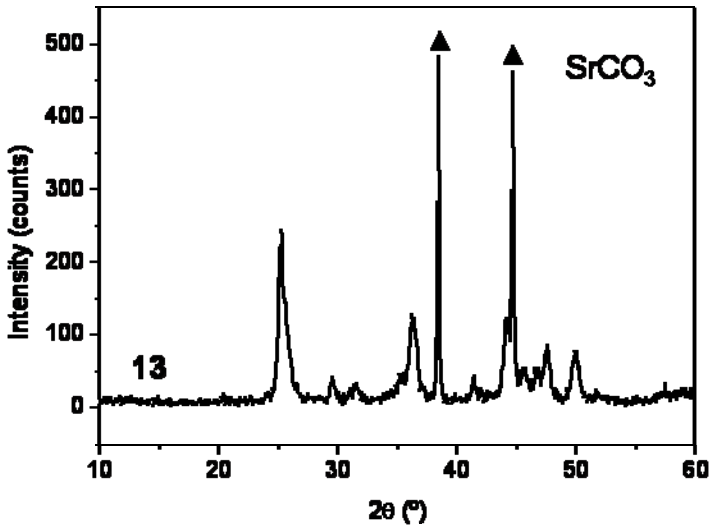


**Figure 8.** XRD pattern of sample # 13 of Table 1. All the peaks can be assigned to $SrCO_3$. ▲ Symbols mark peaks corresponding to aluminium from the holder.

## 4. Conclusions

The urea-melt assisted route has been shown to be a successful pathway for the preparation of $Co_3O_4$ NPs of size ~ 20 nm. Although in the case of manganese, mixtures of $Mn_2O_3$ and $Mn_3O_4$ were obtained through the "standard" experimental procedure, formation of $Mn_3O_4$ NPs (size range ~ 20-60 nm) as single product of reaction could be achieved by adding water to the reaction mixture. In the case of iron, mixtures of γ-$Fe_2O_3$ (maghemite) and α-$Fe_2O_3$ (hematite) NPs were always obtained and it was observed that the increase of calcination temperature led to the oxidation of maghemite to hematite. In spite of the successful synthesis of binary oxides, the method failed in the achievement of the ternary compounds barium and strontium manganites due to both the formation of carbonate groups in the presence of water and to the strong tendency of alkali earth metals to precipitate as carbonates. In this sense, carbonate formation could be avoided by performing the reaction in the absence of water. On the other hand, the method may be suitable for the preparation of carbonate NPs; while the formation of pure $SrCO_3$ has been carried out, the isolation of NPs might require performing the reaction under the suitable calcination temperatures and times. Overall, it has been demonstrated that the urea-melt assisted synthesis can be a general pathway

for the preparation of binary nanooxides. Further work is still needed to better understand the route and optimize it thus in terms of purity of the products as well as particle size and NPs' aggregation. Also, its extension to other compounds remains unexplored.

**References and Footnotes:**

1. An alternative pathway to prepare the urea-metallic salt mixture was employed. It aimed to remove the water of hydration of the salts as well as to mix the components at the molecular level prior to thermal treatment. In order to achieve that purpose, the urea and the metallic salt were separately dissolved in water (2 ml per 1 g of urea and 5 ml per 1 mmol of metallic salt). After mixing both solutions, the solvent was eliminated at 40 ºC and low pressure by using a rotavapor. The resultant dry solid was then loaded into a Teflon vessel. The rest of the experiment was identical than for the other mixing pathway. No differences among both routes were observed in the resulting products.

# CHAPTER 3

# SYNTHESIS OF NANOPARTICLES IN UREA/CHOLINE CHLORIDE DEEP EUTECTIC SOLVENT

# CHAPTER 3.1

## Assembly and Deconstruction of Hierarchical PbS Nano/Micro Crystals and Vectorial Balance of Dipolar Branches

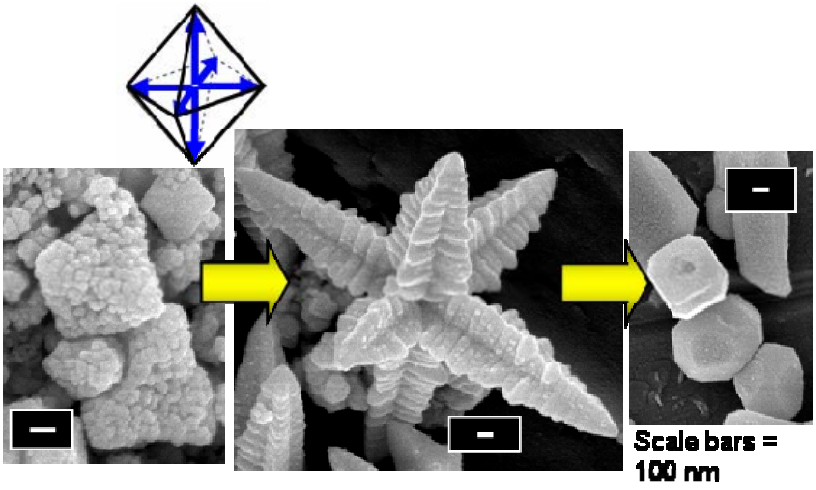


.

# Assembly and Deconstruction of Hierarchical PbS Nano/Micro Crystals and Vectorial Balance of Dipolar Branches

Ana Querejeta-Fernández,[#‡] Paul A. Podsiadlo,[§] Hengxi Yang,[⊥] Yunlong Zhou,[#] Peter F. Green,[¶] Francisco del Monte,[&] Aurea Varela,[‡] Marina Parras,[‡] Jose M. González-Calbet[‡] and Nicholas A. Kotov[#¶†*]

[#]Chemical Engineering Department, University of Michigan, Ann Arbor, MI, 48109, USA; [‡]Departamento de Química Inorgánica I, Facultad de Ciencias Químicas, Universidad Complutense de Madrid, 28040 Madrid, Spain; [§]Center for Nanoscale Materials, Argonne National Laboratory, Argonne, IL 60439, USA; [⊥]Physics Department, University of Michigan, Ann Arbor, MI 48109, USA; [&]Instituto de Ciencia de Materiales de Madrid, CSIC, Campus de Cantoblanco, 28049 Madrid, Spain; [¶]Material Science and Engineering Department, University of Michigan, Ann Arbor MI, 48109, USA; [†]Biomedical Engineering Department, University of Michigan, Ann Arbor MI, 48109, USA

**ABSTRACT:** The assembly behavior of nanoparticles (NPs) is of significant interest for a number of technologies that can exploit the nano/micro levels of organization and quantized properties of nanomaterials. Much effort is still needed to gain better understanding of different modalities of self-organization behavior including reversible and irreversible deconstruction as well as basic patterns of NP superstructures. Herein, the assembly properties of PbS particles and characteristic stages in urea/choline chloride deep eutectic solvent (DES) are analyzed. Initially, epitaxial self-assembly (SA) of nucleated PbS NPs yields octahedral mesocrystals. Subsequently they grow into highly complex hierarchical hyperbranched PbS nano/micro crystals. Dipole-dipole interactions provide a simple key for understanding of the topology of the self-assembled superstructures and its subsequent evolution. The geometry of the assembled systems and the dominant octahedral motifs at virtually all levels of hierarchy are determined by the need to balance dipolar forces in space and by the general tendency of the nanoparticle SA systems to avoid strongly polarized high-energy configurations. At all stages of particle assembly the vectorial sum of the dipole moments directed along major Cartesian axes tends to be zero. As the polarity of the medium decreases upon urea decomposition, SA pattern also switches to the incorporation of the remaining NPs between the nanobranches of the six-arm rods. Concomitant increase of electrostatic repulsion within the branches leads to deconstruction of the six-arm faceted rods. The hierarchical branched PbS crystals in DES present a promising model system for fundamental studies of nanoscale organization and understanding the synthetic methods of control for specific nano/microscale morphologies.

## INTRODUCTION

Assembly behavior of nanoparticles (NPs) is the area of great interest for basic science and can potentially revolutionize many technologies.[1-5] Self-assembly (SA) of NPs can potentially realize complex systems with novel nanoscale geometries using simple and elegant synthetic methods. It can also bridge nanoscale materials with a variety of unique characteristics and well established microscale technologies for the great benefit of both.

Self-organization takes place for NPs for many materials.[4-7] Particularly diverse behavior and resulting geometries were observed for the SA of semiconductor NPs. Their superstructures include straight nanowires,[8-10] zigzag NWs,[10] branched NWs,[10] nanorings,[10] nanochains,[11] nanocheck- and *X*-marks,[12] nanosheets[13] and even twisted ribbons.[14]

Attaining control over complex and intricate topologies requires much better understanding of the forces acting among NPs during the SA reactions. While we steadily are advancing toward greater clarity for pair-wise interactions of NPs and their effect on topology of the SA systems, understanding of motifs of NP organization involving large numbers of NPs is still in its infancy. Accumulation of different attractive and repulsive

interactions as superstructures are being formed and their interplay with crystallization patterns and ion exchange are still difficult to rationalize. Additionally, a great deal of interest has been paid to attractive forces between NPs, however, the stimuli inducing repulsions and resulting in deconstruction or modification of the self-assembled structures have been scarcely addressed.[11, 14] Deconstruction processes are to be considered for technological perspectives, since the instability of semiconductor assemblies can both limit and enrich their applications.

In this framework, lead sulphide (PbS) represents a promising candidate for future studies of NP self-organization. The first steps toward the preparation of intricate geometries of PbS nano-, submicro-, and microcrystals have been already made.[15-29] SA processes between individual NPs were found to take place even when a traditional ion-to-ion attachment was believed to be responsible for the products.[4, 5] It would be highly desirable to advance the knowledge of SA processes for PbS further, in part, because of the great relevance of PbS to photovoltaic solar cells.[30, 31] Considering the issues related to charge carrier generation,[32-36] and the spectrum of exciton energies,[37] on one hand, and charge transport,[38-40] on the other hand, it will be important to combine both nano- and (sub)micro levels of structural organization represented by hierarchical hyperbranched structures. Incidentally, such topology would be quite convenient for solar energy harvesting as well as other optoelectronic applications of PbS. Although some hyperbranched PbS structures were produced,[15-24] their synthesis involved long-chain molecules as structure-directing agents. The coats from long-chain organic surfactants on NPs suppress the charge-transfer process at the interface much needed for solar cells and other devices.[41, 42] The realization of PbS hyperbranched morphology via SA approach without surfactants would be quite advantageous. However, this also requires the knowledge of many fundamental aspects of self-organization and principles governing the topological motifs in the resultant assemblies.
Here we report the formation and progressive changes of assembly motifs of PbS NPs in a deep eutectic solvent (DES)[43] based on urea/choline chloride system, which represent a very different medium in respect to SA process compared to organic and aqueous solvents considered before.[2-7] It was found that the growth of complex superstructures occurs here by assembly of individual small NPs obtained in the process of initial nucleation rather than by ion-by-ion growth. The absence of surfactants for PbS in DES facilitate their epitaxial attachment leading to the self-organization into three-dimensional (3D) nano/microcrystals. Their topology is determined by the need to achieve electrostatic balance between different dipolar moments (DMs) of many PbS NPs attached in the SA process with epitaxial preferences.[10] Many distinct stages of the assembly and deconstruction of the SA structures have been observed. One of the important intermediate stages is the formation of the hierarchical branched superstructures with basic octahedral motif. Equality of branches directed in opposite directions to each other at many different levels of hierarchy indicates the universality of principle of net zero vectorial sum of DM of the branches which allow the system to avoid strongly polarized high-energy state. Subsequently the hyperbranched superstructures transform into six-arm faceted rods as a result of the change in the assembly fashion due to chemical reactions in the medium and gradual reduction of DES polarity. Finally, the rods are deconstructed into smaller particles of several hundred nm in diameter due to the repulsive interactions, while still following the tendency to equilibrate oppositely directed DMs.

## EXPERIMENTAL

Lead (IV) acetate (95 %, Sigma), thioacetamide (99 %, ACS reagent), urea (ultra, Sigma) and choline chloride (≥ 97 %, Fluka) were used as received. DES was prepared by mixing the components urea and choline chloride in the molar ratio 2:1, as corresponds to the eutectic point, and heating to 80 ºC in a furnace until a homogeneous, viscous liquid was formed. The synthesis was performed as follows. Deionized water (6 ml) was added to DES

(30 ml at 37 ºC, 35.70 g) under stirring in a round bottom flask of 100 ml. After heating to 80 ºC under stirring, 12 ml of the solvent were used to dissolve the thioacetamide (12 mmol, 0.9134 g) and the rest of the liquid was employed as a solvent for the lead (IV) acetate (12 mmol, 5.3206 g). Both precursor solutions were kept under stirring in an oil bath at 80 ºC until transparent. Upon hot injection at 80 ºC of the colourless thioacetamide solution into the yellowish lead (IV) acetate one, the mixture turned opaque, dark brown. Then the flask was connected to a condenser and the temperature was increased until 140 ºC in 14 min. The solution turned black quickly (< 5 min) after the hot injection. Aliquots from the same batch were collected at different reaction times. After cooling down, the resulting products were purified by dissolution in water followed by dialysis, centrifugation and drying in a furnace at temperature ≤ 80 ºC.

Selected area electron diffraction (SAED) and transmission electron microscopy (TEM) at both low and high resolution (HRTEM) modes were performed in JEOL 3011 and JEOL 3000 FEG microscopes. Scanning electron microscopy (SEM) was performed on a JSM-6330F FEG microscope working at 20 kV. X-ray diffraction (XRD) of the powders was carried out using a Rigaku Rotating Anode X-Ray Diffractometer with Cu Kα radiation (λ = 1.5418 Å).

Decomposition of the DES/water solvent was evaluated by means of dielectric spectroscopy and $^{1}$H NMR. Dielectric spectroscopy measurements were carried out using a broadband dielectric spectrometer (Novocontrol Technologies GmbH) in the frequency range from 1 Hz to 4 MHz. In order to avoid the time-dependent fluctuations typical of the measurements performed at 25 ºC, the samples were cooled down (in *ca.* 30 min) to -70 ºC. The multiple measurements done at that temperature coincided well. $^{1}$H NMR spectra (500 MHz) were recorded using a Bruker spectrometer DRX-500, placing the non-diluted samples in capillary tubes and using chloroform ($CHCl_3$) as external reference.

## RESULTS

***Hierarchical PbS nano/micro crystals in DES***. DESs[43] with short chains can be a uniquely convenient medium for assembly of NPs because they combine the properties of both organic and inorganic solvents. DESs also provide quite unusual electrostatic conditions and intermolecular interactions for solutes altering in many instances reaction pathways.[44-46] Most commonly DES are mixtures of quaternary ammonium salts (like choline chloride) and hydrogen-bond donors (like urea) in proportion corresponding to the eutective point, where the charge delocalization between the halide anion and the hydrogen-donor organic moiety via hydrogen bonds leads to a drastic decrease of the melting point of the mixture. DESs share many properties with ionic liquids (ILs), such as high polarity and supramolecular self-organization.[44-46] The special features of the former such as biodegradability and simple synthesis have advantages from the technological perspective.

Up to now the use of DESs as a synthetic medium has been taken advantage mainly of hybrid organic/inorganic composites,[45, 47] while the list of nanostructured inorganic materials in DES is limited to low-density semiconductor frameworks[48]and gold sub-micron stars.[49] Although ILs, in general, and DESs, in particular, seem to facilitate the formation of unusual topologies based on low dimensional solids, their suitability for SA processes of NPs is still enigmatic.

The synthesis of PbS NPs in choline chloride/urea DES resulted in nano/micro scale assemblies, that can be described as three-dimensional (3D) hyperbranched PbS–microstars with multiple levels of hierarchy (Figure 1a-e). They were obtained 30 minutes after mixing the $Pb^{2+}$ and $S^{2-}$ precursors. Additional products of the reaction at this point were small agglomerates of NPs and single-branched dendritic (sub)-microarms. Each “star” consists of six main microbranches (whose width and length are sub-micron and micron-sized, respectively) pointing to the six vertices (six equivalent <100> directions) of an imaginary octahedron; four of them are in the same plane, while the other two point up and down that

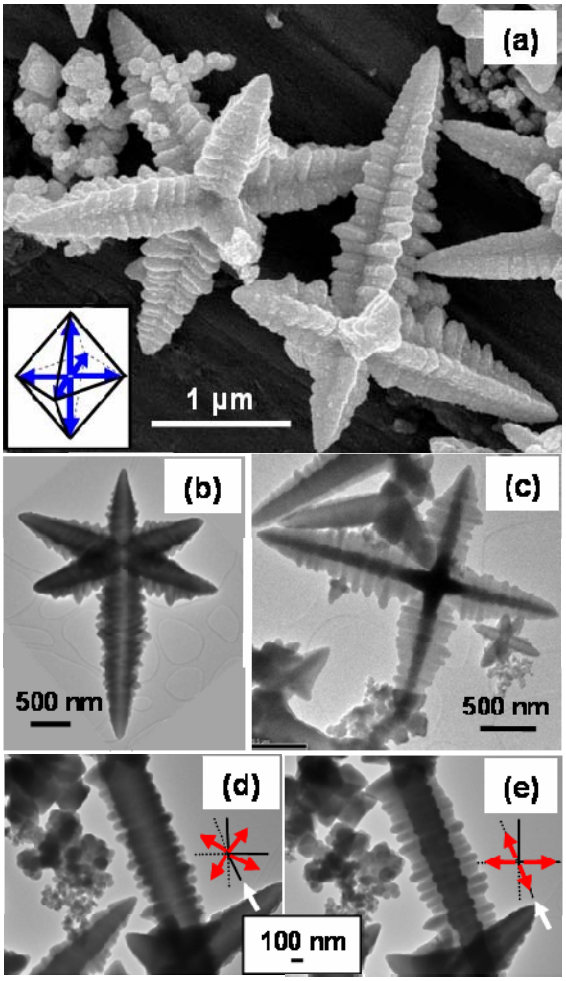


**Figure 1.** Hierarchical hyperbranched PbS crystals obtained at 30 min of reaction. (a) SEM image of microstars. Inset shows the octahedral motif displayed at every level of hierarchy. (b, c) TEM images of two microstars along two perspectives; (d, e) TEM images of a same single-arm dendritic crystal along two perspectives.

plane, resulting in angles of 90º between each pair of adjacent branches. In the TEM image corresponding to a two-dimensional (2D) [001] projection of the octahedral star (Figure 1c), the darker contrast in the centre corresponds to the two branches perpendicular to the plane containing four branches. In turn, each main branch contains four perpendicular lines of secondary nanobranches or nanorods (NRs). Each NR has a diameter of ~50-150 nm. In the TEM projection shown in Figure 1c, the darker contrast within each microbranch corresponds to the larger thickness stemming from two additional lines of parallel NRs at each side of the plane, picturing a repeated octahedral symmetry within each main branch. Note that the octahedral symmetry in this case is partially maintained thanks to a reduced crystal thickness in between adjacent NRs (Figure 2a, e, f, Fig. 1 a-e). Furthermore, each NR seems to possess four perpendicular prominent facets, which is more evident in the larger ones (Figure 1a).

It is worth noting that although the size of the NRs is larger than the Bohr radius (18 nm),[50] quantum confinement can exist in constituent NPs, the tips and/or in incipient faces of the NRs. The junction region of four orthogonal lines of NRs is relatively thin, as evidenced by a clear contrast from the adequate perspective (*i.e.* the orientations shown in Figure 1b and d), and could correspond to the diameter of a single NR. Similar junction is observed between the six main branches (Figure 1b). The high atomic quality of the interface as observed in these structures is beneficial for minimization of scattering of both electrons and holes at the grain boundaries.[51]

PbS microstars have been previously seen both with[15-24] and without[25] capping agents/surfactants. Related morphologies such as single-arm and four-arm dendrite[19, 20, 24] and eight-arm dendrite[17, 21-23] have also been reported, which seems to indicate a general trend for PbS. In contrast to the well established control of the geometry in colloidal 1D and 2D assemblies of nanocrystals,[52, 53] the mechanisms of formation of hierarchical 3D microcrystals are unclear.

High resolution TEM and SAED (Figure 2) reveal the single-crystalline nature of the 3D microstars and confirms the elongation of the branches along the six equivalent <100> crystallographic directions, as well as the <100> directions of each secondary branch or NR. Five levels of hierarchy can be identified, which is unique by itself: the rock-salt cubic structure of galena, in which each cation is surrounded by six anions and *vice versa*, picturing octahedra; the truncated octahedral shape of the nanoscale building blocks;[10, 28, 53] the incipient octahedron within each NR; the octahedral symmetry among nanobranches and, last, the octahedrons among the microbranches. Self-similar hierarchical organization points to the similarities of forces resulting in it at different scales and specifically to electrostatic

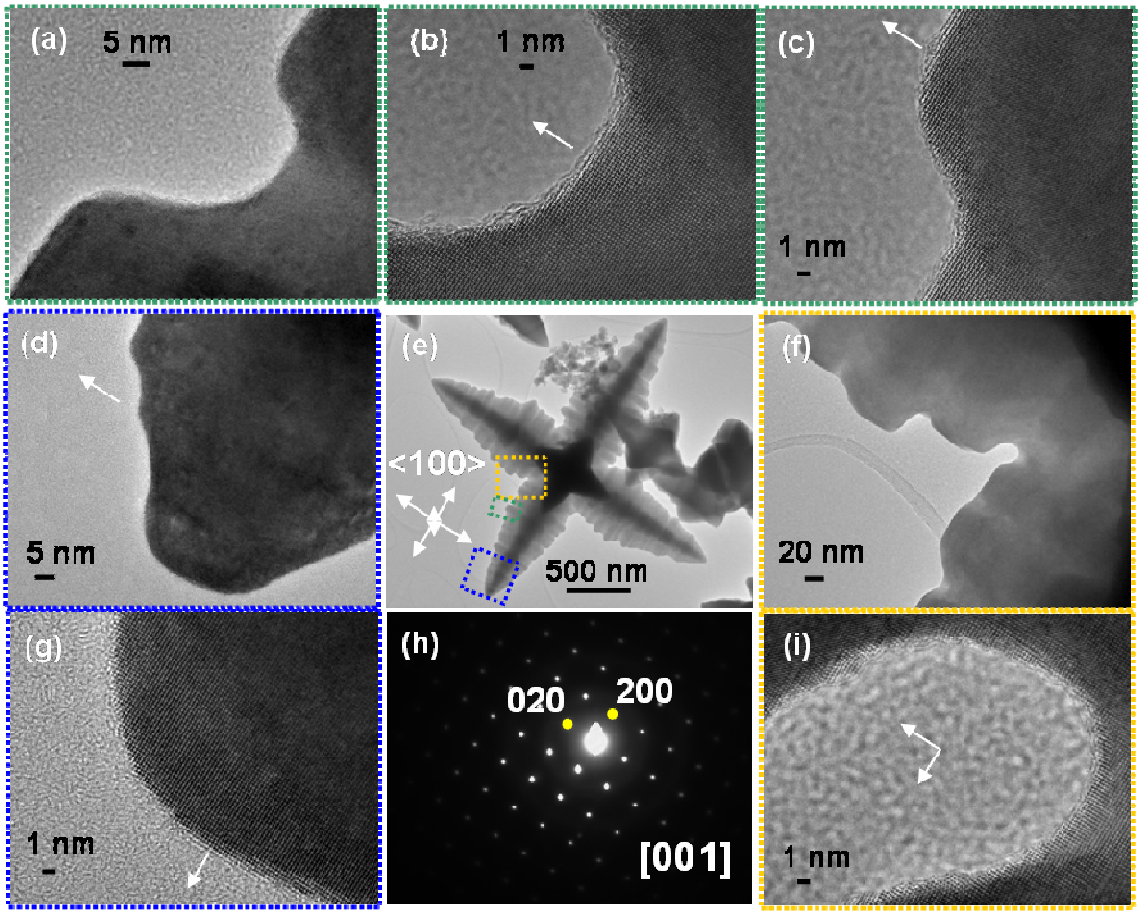


**Figure 2.** (a-g, i) TEM and HRTEM images of the highlighted areas of a microstar (e) obtained at 30 min of reaction. (h) SAED pattern of the microstar shown in (e) TEM image taken along [001] zone axis. The microstar is single-crystalline and no imperfect fusing among the constituent NPs is detected in any of the HRTEM images.

forces as those most likely responsible for the specific geometry of the 3D nano/micro crystals.

***Different stages of PbS NPs assembly and deconstruction in DES***. The respective contributions of NP SA process *vs.* the ion-by-ion growth of the NPs should be evaluated. One also needs to understand the role of the different forces governing the shape of crystals. So, we examined reaction products by collecting aliquots from the same batch at different reaction times ($t_r$). Corresponding X-ray diffraction (XRD) patterns (Figure 3) show the presence of crystalline PbS (galena) as the only product at all $t_r$ ranging from 5 min to 5 days. The peak intensities increase with $t_r$, evidencing an increase of the crystal size at longer reaction times, which matches the TEM observations (Figure 4).

Let us divide the morphological changes of the PbS structures in three periods. The first period involves the SA of PbS NPs into hyperbranched stars. The second period includes a stage of a different SA pattern followed by the third stage of deconstruction. First, we will describe the results corresponding to the initial SA period. TEM examination reveals the formation of relatively polydisperse NPs with an average diameter of 31.3 ± 10.7 nm (size histogram is in Figure S1) after 5 min of reaction (Figure 4a). They are mostly crystalline and match well the PbS-galena structure and interplanar distances (Figure 5c), although some parts without characteristic atomic lattices can be seen. The polycrystalline nature of the groups of NPs is revealed by the corresponding ring-SAED pattern (Figure 5a, b). Previous reports identified a truncated octahedral shape possessing some dipole moment (DM) as the dominant one for the nucleated PbS NPs and other NPs with rock-salt structure.[10, 28, 53]

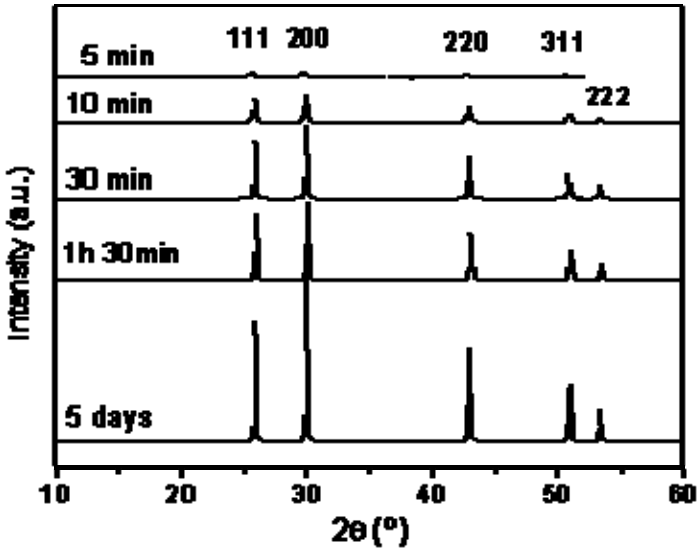


**Figure 3.** XRD patterns of the PbS (galena) products obtained at different reaction times.

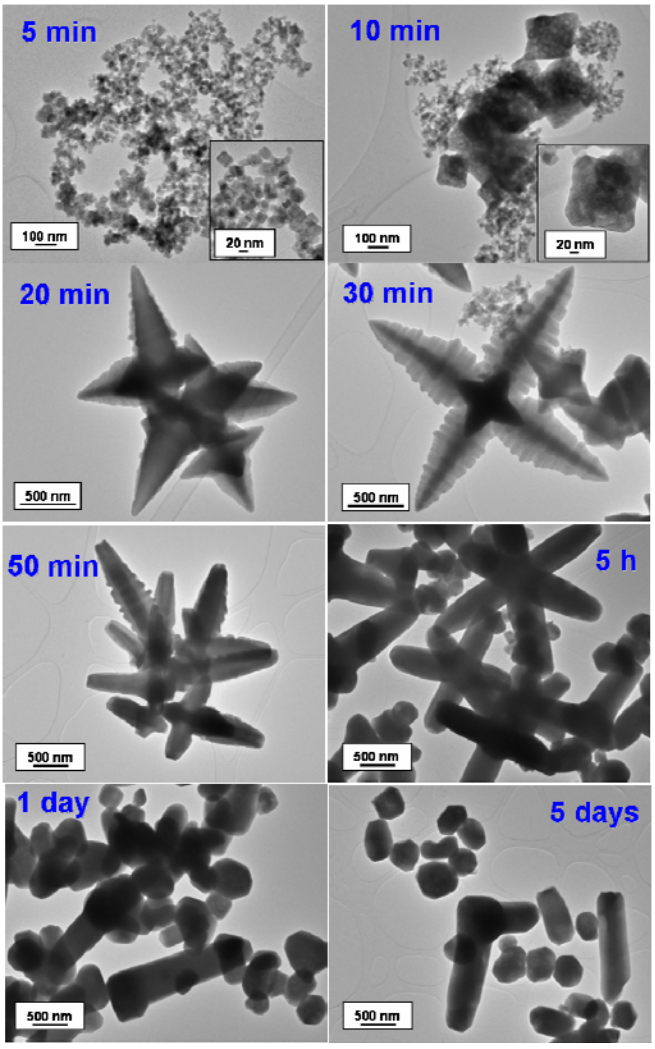


**Figure 4.** TEM images of the PbS crystals for different reaction time.

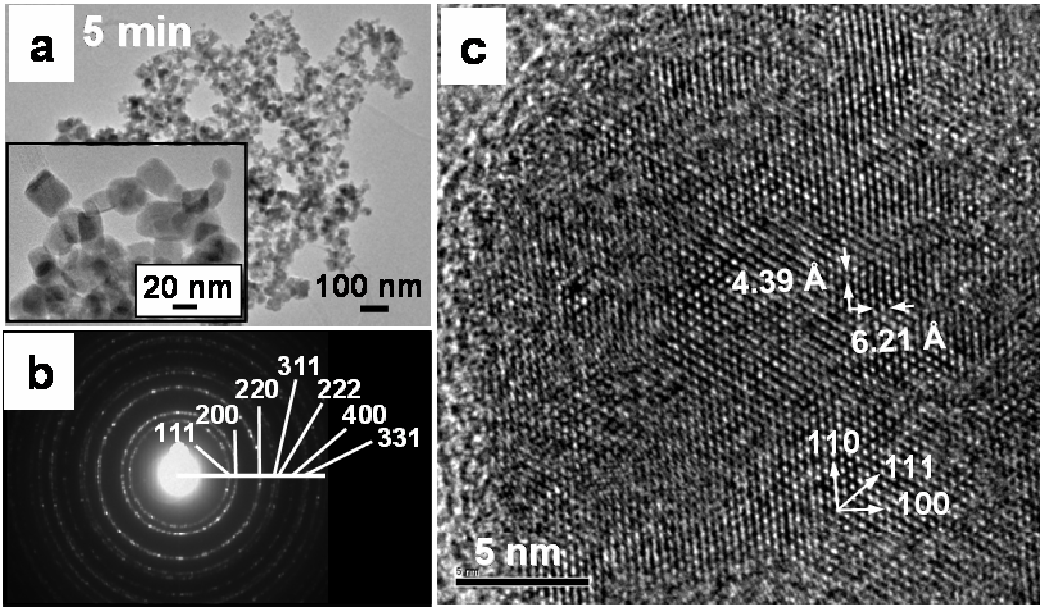


**Figure 5.** (a) TEM image of PbS NPs obtained at 5 min. Inset shows higher magnification of the NPs. (b) SAED ring pattern of the group of NPs shown in (a). (c) HRTEM characterization of a PbS NP.

The absence of geometrical perfection and uniformity does not prevent their self-organization into regular 3D structures. At $t_r$ = 10 min, NPs as well as their agglomerates (~100-500 nm in diameter) are observed (Figure 4b). SEM images (Figure 6a) reveal a familiar octahedral shape of the sub-microparticles and a rough surface stemming from imperfectly fused NPs. In spite of that, the assemblies show epitaxial match of crystal lattices at the interfaces. SAED and HRTEM (Figure S2) show a monocrystalline pattern, as well as vertexes of the octahedron orientated along the six equivalent <100> directions. The assemblies of this type can also be described as mesocrystals.[4, 5]

At $t_r$ = 20 min, the simultaneous elongation of the six vertexes of the octahedra takes place leading to 6-branched structures with diameters of ~ 250-2500 nm (Figures 4 and 6b). Notably all of them have virtually perfect symmetry and equal elongation of arms despite the heterogeneity of the growth conditions exacerbated by the broad size distribution of the constituent NPs. Each main branch is elongated along the <100> direction with incipient secondary nanobranches oriented along the four remaining <100> directions perpendicular to the main branch.

By $t_r$ = 30 min (Figures 4 and 6c), such growth fashion has led to the hierarchical, 3D hyperbranched PbS rods described in the beginning. Such superstructures are the culmination of the <100> SA period. At this point it appears that the assemblies are no longer mesocrystals, since no interfaces among NPs are detected by HRTEM (Figure 2). Thin and dynamic layer of DES acting as a capping agent seems to be displaced away from the junction faces between the building blocks.

The second period involves a switch of SA fashion which leads to the transformation of the hyperbranched PbS stars into six-arm faceted thick rods. Thus, at $t_r$ = 50 min (Figure 7a) the aesthetically pleasing 3D hyperbranched stars start to lose their regularity and harmony. It can be characterized by several observations about geometry of NP assemblies. Secondary NRs become less defined as a consequence of bridging; several NRs fuse together into a single unit. Tips of microbranches and NRs become flatter. The average thickness of the microbranches increases. Since at this point NPs are still present, although in lower number than previously, the mentioned changes can be associated with the incorporation of the NPs into the body of the branched crystals, *i.e.* a filling of empty spaces of the hyperbranched stars with remaining building blocks takes place.

As a result, at $t_r$ = 5 h, 6-branched thick microrods retaining the pseudoisotropic vector-balanced geometry are observed. Both TEM (Figure 4) and SEM (Figure 7b) images

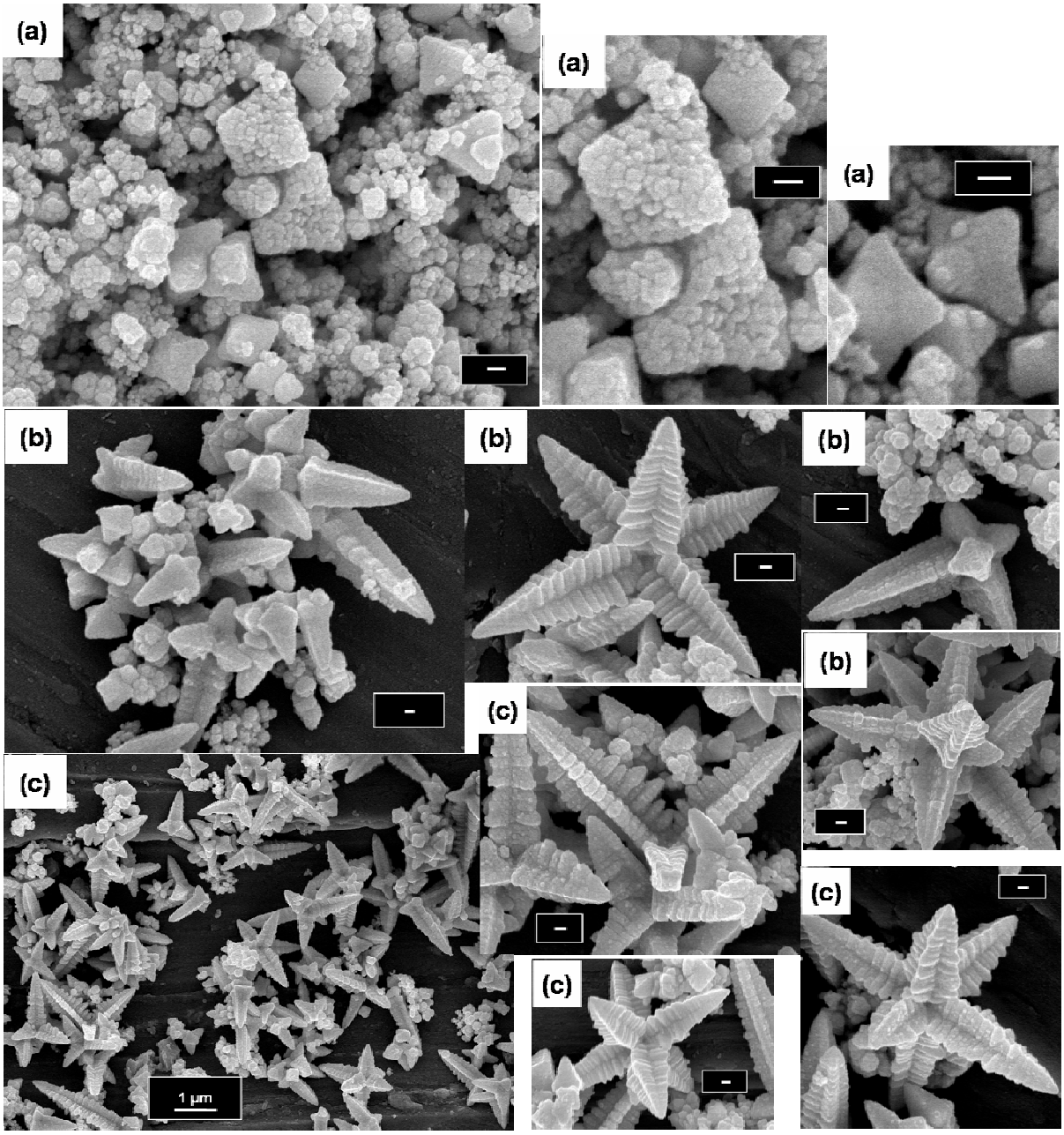


**Figure 6.** SEM images of the evolution of the PbS products at (a) $t_r$ = 10 min; (b) $t_r$ = 20 min and (c) $t_r$ = 30 min. All the scale bars correspond to 100 nm, except if otherwise indicated.

indicate that the width of the rods in the new structures matches well the end-to-end distance of the cross-section depicted by the nanobranches of the hyperbranched structures, *i.e.* such widths are sub-micron-sized. At this stage it seems that all the NPs serving as the building blocks of the assembly have been consumed.

The third period consists in the deconstruction of the six-arm faceted rods into smaller particles. Apart from some broken microbranches detected from $t_r$ = 50 min, which could be associated with mechanical washing off, from $t_r$ = 5 h cavities of *ca.* 100-150 nm of size were observed at the <100> surfaces, including the tips of the rods (arrows in Figure 7, Figure 4). The cavities in the micro-sized faces correspond to the initial point of deconstruction, which progresses generating shorter pieces of rods and faceted sub-microparticles (~170-700 nm). They are the result of the deconstruction of the microrods, since diameters and widths, respectively, match. The products of the deconstruction also exhibit holes in their surface, as can be detected in the images.

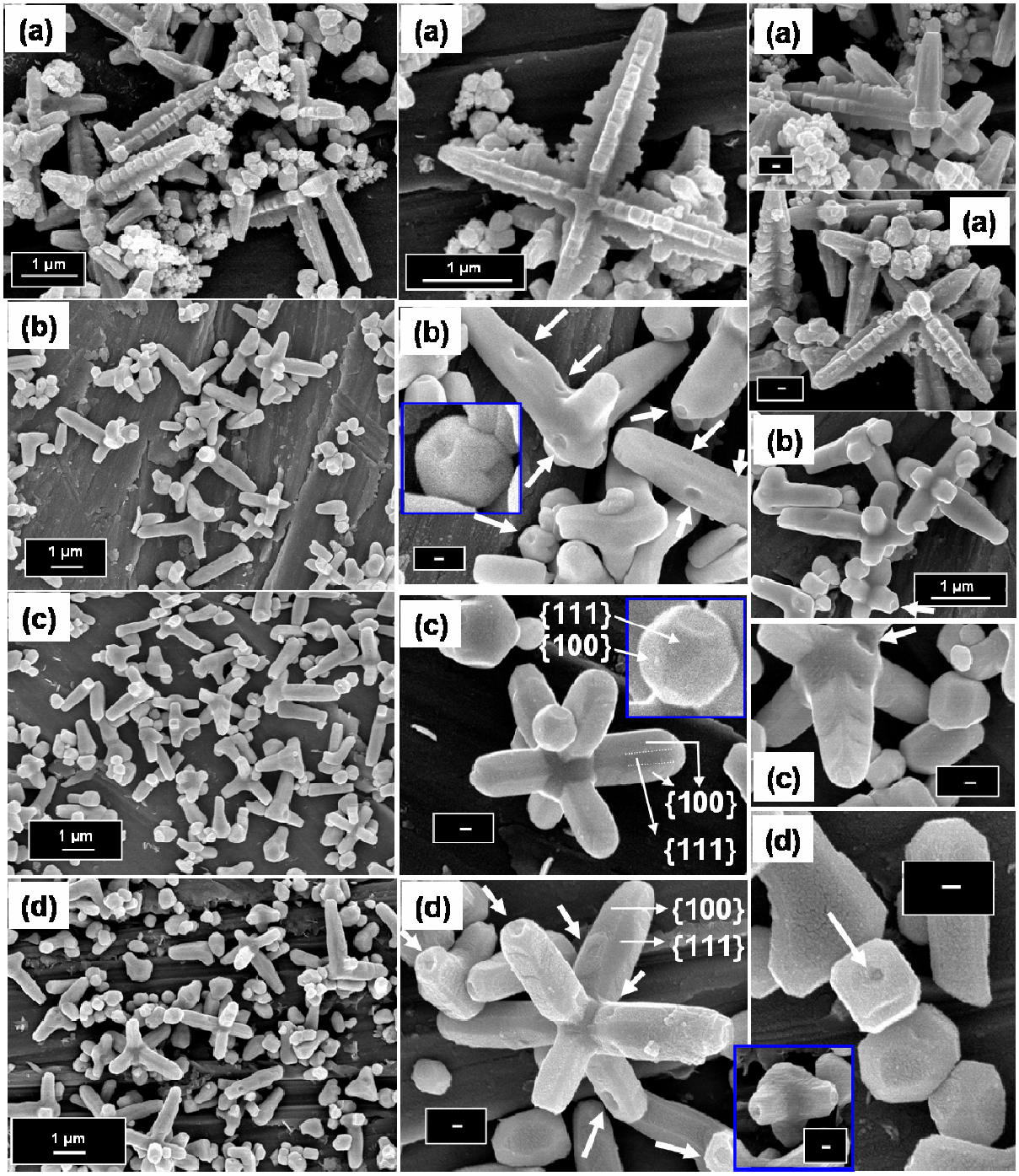


**Figure 7.** SEM images of the evolution of the PbS products at (a) $t_r$ = 50 min; (b) = $t_r$ = 5 h; (c) 1 day and (d) 5 days. Arrows point to the cavities in the {100} crystal faces. Designation of the different crystal faces is indicated. All the scale bars correspond to 100 nm, except if otherwise indicated.

Further evolution of the SA superstructures leads to the increase of several-hundred nm faceted particles and broken rods. Such features can be observed after 1 day and even in greater numbers after 5 days of the reaction (Figures 4 and 7c,d). This period of the reaction can be characterized by the switch from the dominance of long-range attraction to long-range repulsion.

Longer reaction time up to 14 days leads to etching and transformation of the well-defined faces into rough surfaces (Figure S3).

## DISCUSSION

***Why do PbS NPs form hyperbranched microscale assemblies?*** Experimental observation of 3D hyperbranched structures of PbS has probably the most extensive background information[15-25] in the framework of this study although the transition from individual NPs to such structures is still quite murky. The previous studies on PbS and other semiconductors with cubic rock salt crystal lattice indicate that seeds are nucleated at early stages of reaction with tetradecahedron or truncated octahedron shapes. The difference of relative growth rates of the six {100} faces and the eight {111} faces[10, 28, 53] of the seeds are considered to be responsible for the final geometries at the nanoscale.[16, 26-28] The faster growth of {111} faces results in their elimination and subsequent formation of cubes with six faces, while if the {100} faces grow faster, the resulting morphologies are eight-faced octahedra. If the latter growth is much faster than that of the {111} faces and longer growth times are allowed, 6-branched star-shape crystalline NPs are formed due to the progressive growth along the six {100} faces or vertexes of the octahedra.[10, 28]

These descriptive findings about the growth of small semiconductor NPs could be extrapolated to the assembly of microscale superstructures taking into account that i) the building blocks are NPs instead of ions, ii) there is dominance of long-range attraction involving a high number of NPs and iii) NPs' geometry is isotropic enough to allow them to densely pack in an isotropic fashion within the micro-sized assembly.

Multiple experimental data from this and other studies[4, 5] provide evidence that the building blocks of microstructures are crystalline NPs. Herein, NPs formed in the initial stages of the reaction ($t_r$ = 5 min) could self-assemble into octahedral mesocrystals ($t_r$ = 10 min) because of a faster growth along the <100> directions compared to the <111> ones and further growth would result in six-branched microrods. However, the appearance of secondary NRs within each microrod cannot be understood within this phenomenological description of their formation. Such a growth would lead to the uniform widening perpendicular to ach flat {100} face instead of the formation of semi-independent {100}-tiped-NRs separated among them by shorter and narrower crystalline parts. One also needs to point out that DES employed as solvent of the reaction probably plays the role of a dynamic capping agent that comes on and off the NP surface, analogously to cetyltrimethylammonium bromide (CTAB)[15-17] and primary amines[17-20, 22-24] typically used for this material, whose electrostatic interaction with polar {111} faces favors the growth of the apolar {100} vertexes. However, again, the observed geometries of the PbS crystals cannot be explained only by the retarded growth of stabilized {111} faces, which would lead to diverse array of anisotropic structures.

There is probably a different mechanism governing the final geometries. It should be thermodynamic rather than kinetic in nature because the hyperbranched morphology is found not only in DES but in other solvents and for quite different growth conditions.[15-25] The common feature shared by all the levels of hierarchy in the resulting hyperbranched rods is the octahedral motif. This probably holds the clue to the understanding of forces sculpting the topology of SA systems from NPs. Since PbS NPs in DES are quite "sticky" due to the tendency of epitaxial attachment in the high concentrated solution, they probably tend to interact in large numbers and do not come apart when the close contact is made, so the particles form large agglomerates held by close-range forces. Their collective orientation should be governed by long-range interactions with the characteristic length comparable to the physical size of NPs, *i.e.* 20-30 nm. Possible long-range forces include charge-charge and dipole-dipole interactions from intrinsic dipolar moments (DM) of the NPs.[10, 54-56] Dipolar attraction is the most plausible force that can govern such assemblies because NPs have the same charge and charge-charge interactions are repulsive. Attraction of NP dipoles has already been implicated in some SA processes.[10, 54-56] The largest probability and magnitude of DM in PbS NPs is predicted to be along the <100> axis.[10] Importantly, the origin of DM in NPs with hexagonal crystal lattice is the polarity of their crystalline lattice.[57] Similarly, semiconductor NPs with cubic structure, such as CdS, CdTe, ZnSe, PbSe and PbS, also

display a strong DM,[10, 54-56] which is ascribed to imperfections of the geometries, *i.e.* truncation of the apexes, vacancies, *etc.*, resulting in a non-compensated arrangement of polar {111} faces, which is ultimately responsible for the distribution of electric charge within the NP. So, when multiple dipolar NPs undergo epitaxial attachment either with the head-to-tail orientation of dipoles typical of 1D structures[8, 10, 11] or even without an easily recognizable short-distance order –such as that described before for other 3D assemblies–,[14] it results in the progressive growth of the DM of the superstructure proportional to the number of NPs assembled (note that a DM can induce/flip the DMs of the neighbour NPs). Consequently, the polarization, Coulombic repulsions and, thus, the global energy increases. We suggest that the behavior of SA systems of NPs is largely determined by minimization of this energy.

For assembly of ZnO NPs in chains, the increased DM limits the length of the chains when particles are assembled with head-to-tail orientation of DMs.[11] The relatively short length of the observed chains corresponds to the balance between the negative Gibbs free energy from assembly of the NPs and positive Gibbs free energy from increased polarization. However, for PbS there is an additional possibility to balance the growing dipoles. Thermodynamic stabilization of the growing structures from NPs can originate from mutual cancelation of the oppositely aimed vectors of dipoles arranged in an antiparallel fashion as was recently observed for ZnO pyramids[11] or CdTe tetrahedrons–in 2D sheets.[13, 14] In the latter cases, this becomes possible at the nanoscale, *i.e.* involving single NPs' dipoles, because of the relative weaker long range attractive forces. For these dimensions, only a single couple tail-to-tail orientation is electrostatically allowed. The use of directional surfactants and the geometries of the building blocks further hamper a 3D dense packing of NPs, reducing the dimensionality of the resultant nano-sized solids to 1D[8, 10, 11] or 2D.[13] However, in the case of PbS SA systems, due to the truncated cubic geometry of the basic structural block, a dense 3D packing of NPs is allowed, which is further prompted by the high concentration of NPs within the medium. The resulting sub-micro and eventual micro-sized solids are large enough for allowing a more complex level of organization involving many antiparallel dipole vectors. Thus, the stabilization of the complex superstructures can occur by balancing DM in 2, 4, and even 6 orthogonal directions mutually cancelling each other. This attachment pattern is likely to sculpture a pseudo-isotropic geometry in spite of the anisotropic character of the six individual main branches. Isotropic geometry with 2, 4, or 6 dipole vectors balanced in respect to each other result in the obvious decrease of the overall energy of the system as the polarization is reduced, while the entropy of the solvent is increased. Furthermore, the six main branches are large enough to generate a secondary family of mutually balanced dipole vectors which prevent the arm from electrostatic destabilization. This pseudo-isotropic octahedral motif seems to be ubiquitous for charges at the different scales. In general, one can also make a parallel with six ligands/ions positioned equidistantly around a central atom, which is the most popular motif in metal-organic complexes and other atomic systems such as ionic crystals. From this perspective it should not be terribly surprising to find the same orthogonal motif in nanoscale assemblies. Such electrostatic balance is ultimately responsible for the octahedral symmetry of the PbS microstars within each of the five levels of hierarchy.

Obviously, such a hierarchical pattern is allowed only when the building blocks are NPs and the final contructions are micro-scaled. For ion-to-ion growth, the resulting nanoobjects present also the characteristic octahedral motif, although the small dimensions do not allow the generation of the secondary family of branching.[10, 16, 26-28]

***Why do the switch of assembly pattern and deconstruction occur?*** The sequence of assembly-deconstruction stages is summarized in Figure 8 together with the temperatures and reaction times. The change in assembly pattern occurs at *ca* $t_r$ = 50 min: the NPs remaining in the medium are no longer incorporated along the length (<100> directions) of the nano and microrods, but along the <111> directions. SAED indicates that this mode of attachment of NPs leading to widening of the rays of the microstars also occurs epitaxially (Figure 9b).

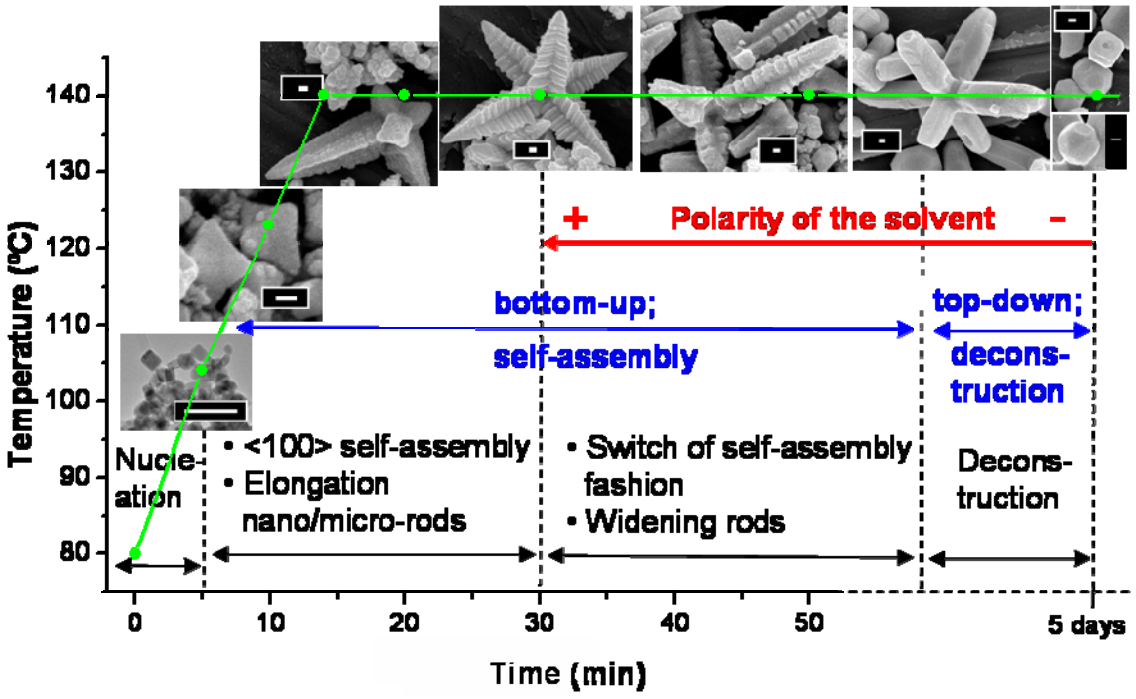


**Figure 8.** Profile of reaction along the different reaction times and temperatures (green line). TEM or SEM images of the as-obtained PbS products are shown. Scale bars, 100 nm. The different processes are indicated. DES decomposition leads to a decrease of polarity of the reaction medium from $t_r$ = 30 min. Once the nucleation of the NPs has taken place, two main processes are observed: first, a self-assembly or bottom-up event and, second, a deconstruction or top-down event occur. Within the former, firstly an elongation of the NRs and microbranches along the <100> crystallographic directions takes place and, secondly, a change of SA pattern leading to the widening of the microbranches occurs triggered by the decrease of polarity of the medium.

Since such a process involves breaking of the octahedral symmetry among the NRs, it should be less favourable than the previous SA along <100> directions and head-to-tail orientation of DMs.[8, 10, 11] Incorporation of additional charges in between orthogonal dipoles should be electrostatically less favourable than along the axes. This is reflected by the lower rate of the process (1h - 4h 30min; *i.e.* $t_r$ = 1h 30 min – 5h) as compared to the first <100> SA culminating in the hierarchical hyperbranched rods (which requires $t_r$=30 min). Despite of the slowness of the process, it still can take place, because heterogeneous attachment of NPs into microcrystals should be more favoured than homogeneous one *i.e.* than the coalescence of NPs.

A close inspection of HRTEM images (Figure 9c-e) allows the detection of a non-epitaxial interaction among the microrods's surface and crystalline NPs of dimensions < (3.5 × 6) nm, which again, strongly suggests that the elementary building blocks in the growth process are not ions, but NPs. Analysis of the images reveals a [0-11] projection of the PbS structure within the microrod, while all the NPs in the surface correspond to a PbS structure along the [001] zone axis. Thus, both PbS crystals share the (011) direction and are tilted 45 º each other. Moiré patterns characteristic of two crystals slightly overlaid at a small angle are detected. These observations might indicate that the incorporation of the NPs into the microstructures involves non-epitaxial attachment by sharing the (110) common direction followed by an *in-situ* re-attachment in the epitaxial fashion. Such a re-orientation of the NPs would be analogous to atomic-level rearrangements previously observed in NPs under the electron beam.[58]

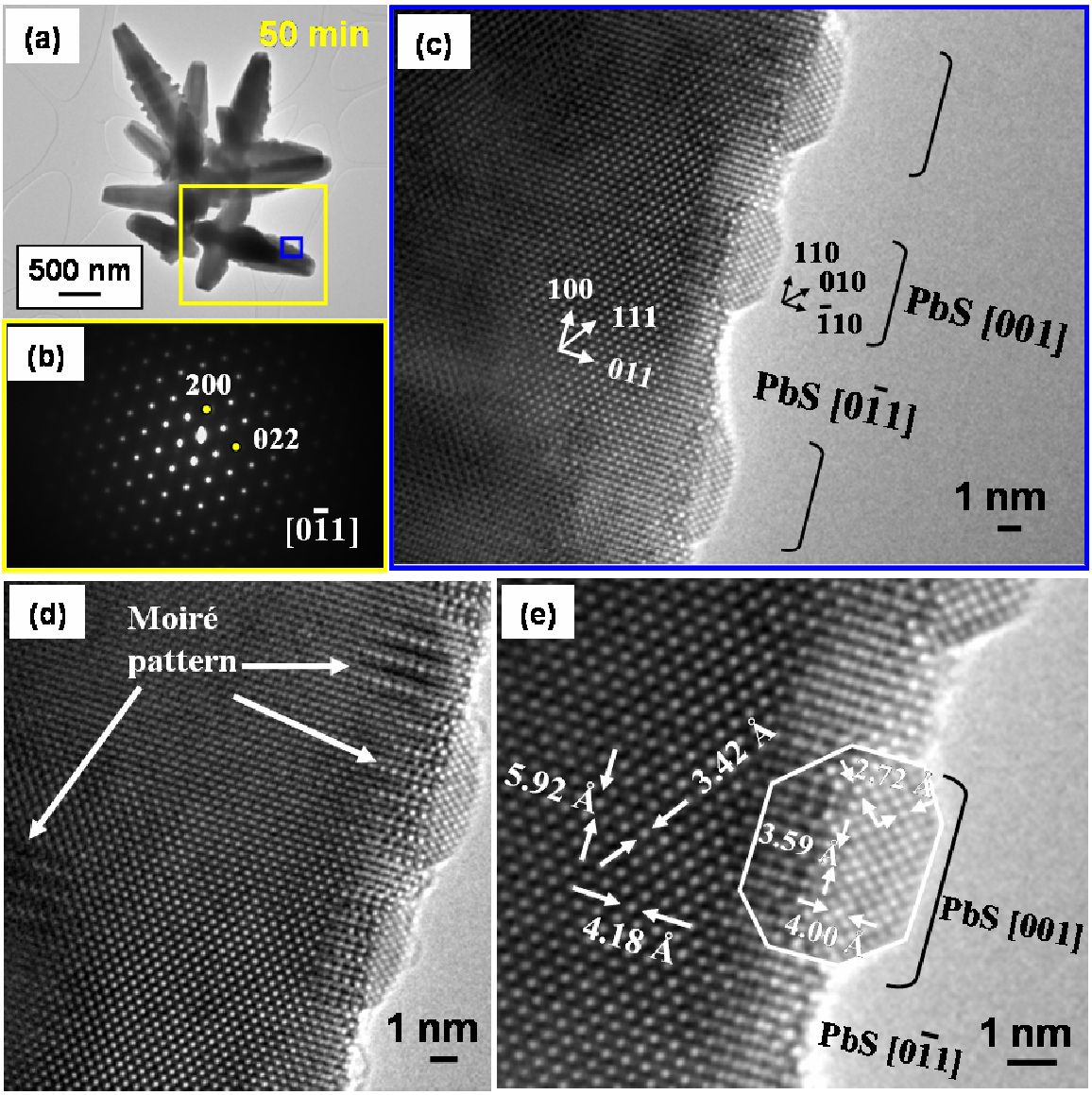


**Figure 9.** Characterization of the PbS particles obtained at $t_r$ = 50 min. (a) TEM image. (b) SAED pattern along the [0-11] zone axis of the particle highlighted in (a). (c) HRTEM image of an area within the highlighted part in (a). (d, e) HRTEM images indicating Moiré patterns and the atomic interplanar distances.

Changes on the composition and polarity of the medium upon heating are the most probable reasons for the switch of the SA process. Regarding the former, it is known that urea/choline chloride DES present the feature of being unstable upon heating;[44] specifically, urea has been observed to decompose in DES at ~200 ºC.[59] Its decomposition, which takes place at ~90 ºC normally and at higher temperature in the DES because of its strong interaction with choline chloride through hydrogen bonding, is favoured by water according to the following equations:[60, 61]

$NH_2CONH_2$ (urea) → $NH_4^+$ $NCO^-$ → $NH_3$ ↑ + HNCO (isocyanic acid) [1]
$NH_3 + H_2O$ → $NH_4^+$ $OH^-$; [2]
$NH_4^+$ $OH^-$ + $NH_2CONH_2$ → 3 $NH_3$ ↑+ $CO_2$ ↑ [3]
$HNCO + H_2O$ → $NH_3$ ↑ + $CO_2$ ↑ [4]
which can be condensed in the following general equation:
$NH_2CONH_2 + H_2O$ → 2 $NH_3$ ↑ + $CO_2$ ↑ [5]

The course of the DES/water solvent decomposition was followed by $^1$H NMR (Figure S4 and Table S1; see detailed discussion in the Supporting Information). Both molar ratios of the components and thermal treatment were identical to those employed for the

synthesis of the PbS crystals. The $^1$H NMR spectra confirm that the main change associated with the thermal treatment of DES/water mixture corresponds to urea decomposition in good accordance to Eq. 1-5 and rules out alternative pathways such as choline chloride decomposition[62] and urea oligomerization,[61] which, in turn, further supports the absence of long-chain organic molecules on the surface of the PbS particles, which is important for the potential technologies. Besides, the spectra evidences that the decomposition is noticeable at $t_r$ > 30 min, indicating that this is a turning point in the composition of the medium. Complementary, the gradual decomposition of urea is detected by the white salts collected in the condenser of the reaction system. They are well visible at $t_r$ = 24 h and their amount continuously increases along with the reaction time. At $t_r$ = 14 days, the corresponding XRD pattern corresponds at least to ammonium hydrogen carbonate ($NH_4HCO_3$) as well as ammonium hydrogen carbonate amide ($NH_4HCO_3 \cdot NH_4CO_2NH_2$) (Figure S5), in good accordance with Eq. 1-5.

Decomposition of urea must lead to change of polarity of the medium, and therefore, must affect dipole-dipole, charge-charge, and charge-dipole interactions in SA structures. Specifically, the partial disappearance of hydrogen bonding and the evaporation of salts should lead to a polarity decrease. The support of this important point is revealed by dielectric spectroscopy measurements of the [DES/water] solvent at different decomposition times. As can be seen in Figure 10, during the initial stage between $t_r$ = 0 and 10 min, the permittivity increases. In spite of this initial divergence, which might be ascribed to the early evaporation of water which does not properly reflux in the initial minutes out of equilibrium, there is a clear trend from $t_r \geq$ 10 min, coinciding with the nucleation and initial SA of NPs and water recovery by refluxing. From $t_r$ = 10 to 30 min, the permittivity is kept constant, as corresponds to a medium which undergoes negligible changes, as previously tested by $^1$H NMR. However, during $t_r$ = 30 min –24 h, there is a noticeable gradual decrease of both the real and imaginary parts of the permittivity, which can be related to a decrease of polarity, over the entire range of frequencies.

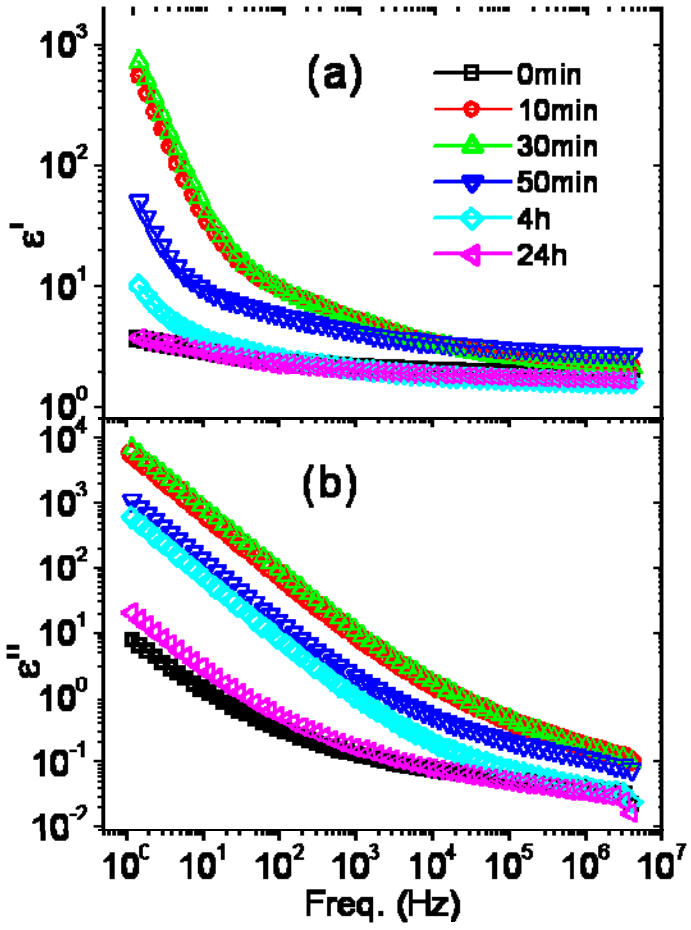


**Figure 10** . Dielectric spectroscopy measurements of the time-dependent decomposition of the DES/water solvent. (a) Real part of the permittivity *versus* the frequency of the applied electric field. (b) Imaginary part of the permittivity *versus* the frequency

As dipolar and electrostatic interactions are sensitive to the dielectric constant of the medium,[13, 54, 55] this change of the medium will switch the SA pattern. Reduction of dielectric constants results in increase of both electrostatic repulsion and attraction similarly to what had been observed before by variation of the solvent composition.[63] As in the previous case, the reduction of the

polarity of the medium results in the decomposition of the SA structures because of drastic increase of electrostatic repulsion superior to the attraction.

Note that decomposition of DES will also change its ability to cap/stabilize PbS NPs. In turn this may also contribute to change the value and orientation of DM.[55, 63] Besides retaining its orientation along the <100> axes, a dipole can flip its direction along the <110>, <111> directions or cease to exist at all.[10] In the case of dipole flipping, it will result in decrease of attraction compared to head-to-tail oriented dipoles responsible for the formation of the individual NRs, while in the case of DM becoming zero, the electrostatic repulsion will have even greater effect on the morphology of the SA structures.

In our case, the SA fashion along the <100> directions takes place from $t_r$ > 5 min until $t_r$ = 30 min, which corresponds to the stage in which the polarity of the medium is maximum and it undergoes negligible changes, as discussed above. It culminates in the formation of hierarchical branched nano/micro structures (Figure 8). The SA switch detected from $t_r$ > 30 min, related to the incorporation of the remaining NPs within the nanobranches, matches well the noticeable decomposition of urea and subsequent decrease of polarity of the medium, indicating the close connection between both events. By $t_r$ = 5 h, all the NPs have been consumed, leading to six-arm faceted microrods. (Figures 4, 7c,d, 8).

At this point, the faceted six-branched microrods start undergoing a process of deconstruction (Figures 4, 7c, d). Besides simple mechanical breakage of the microscale structures,[19, 20, 24] cavities or holes are formed at the {100} faces, including the four at the sides and also the tips of the rods. The formation of such cavities seems rather characteristic for PbS,[17, 21-23, 25, 30] and can be attributed to the points of breakage off the branches on each side of the rod at the crystalline interfaces, where both stress and accumulation of charges is the greatest. Concomitantly, four new {111} faces are developed at the expense of disappearance of some {100} ones. Face reconstruction can proceed both via NPs and ionic exchange, which are difficult to distinguish at the moment. These changes become more evident for $t_r$ = 5 days. Complementary TEM images (Figure 11a, b, e) show thinning of the {100} tips of the rods (marked with arrows) as well. HRTEM and Fourier Transform pattern (FT) (Figure 11d, c) of the eroded tips match that of PbS crystal lattice. Finally, the complete erosion of the rods through the cavities in combination with a surface reconstruction process leads to their rupture into faceted particles whose sizes (several hundred nm) correspond to the width of the (sub)-microrods. Frequently, they exhibit the projection of truncated octahedral shape oriented along [110],[53] and confirm the development of {111} faces at the cost of reduction of {100} surface area (Figure 11f, i). SAED pattern (Figure 11h) verifies the monocrystalline nature of the particles. Their shapes correspond to various types of tetradecahedron and related geometries with truncations of vertexes between octahedra and cubes. It is curious that some of the resulting NPs at the end of the deconstruction possess the same type of morphology (truncated octahedron with both {100} and {111} faces), although with a different size, than the assigned one to the PbS seeds nucleated at early stages of the reaction.

Deconstruction process is due to the greater stability by forming even more isotropic shapes than balanced dipole vectors,[64] and is triggered by greatly increased repulsive electrostatic interactions from electrical charges and quite likely from repulsive DM due to dipole flipping. Destruction of the anisotropic microrods in this case would be analogous to the previously reported disassembly in chains of ZnO NPs,[11] which were ascribed to the reduction of DM as they grew removing the truncation, as well as the decease of assembly of CdTe NPs[63] upon decrease of the polarity of the medium. Note, however, that the deconstruction herein is more surprising, since it involves the breaking-off of a continuous microcrystal rather than the previous disassembly/non-assembly of discrete NPs. After the switch of SA pattern leading to the loss of octahedral symmetries at the NRs scale, the self-similar motif of spatially balanced DMs within each main branch disappear. Consequently, and helped by the further decrease of the polarity of the medium (Figure 10), repulsive forces

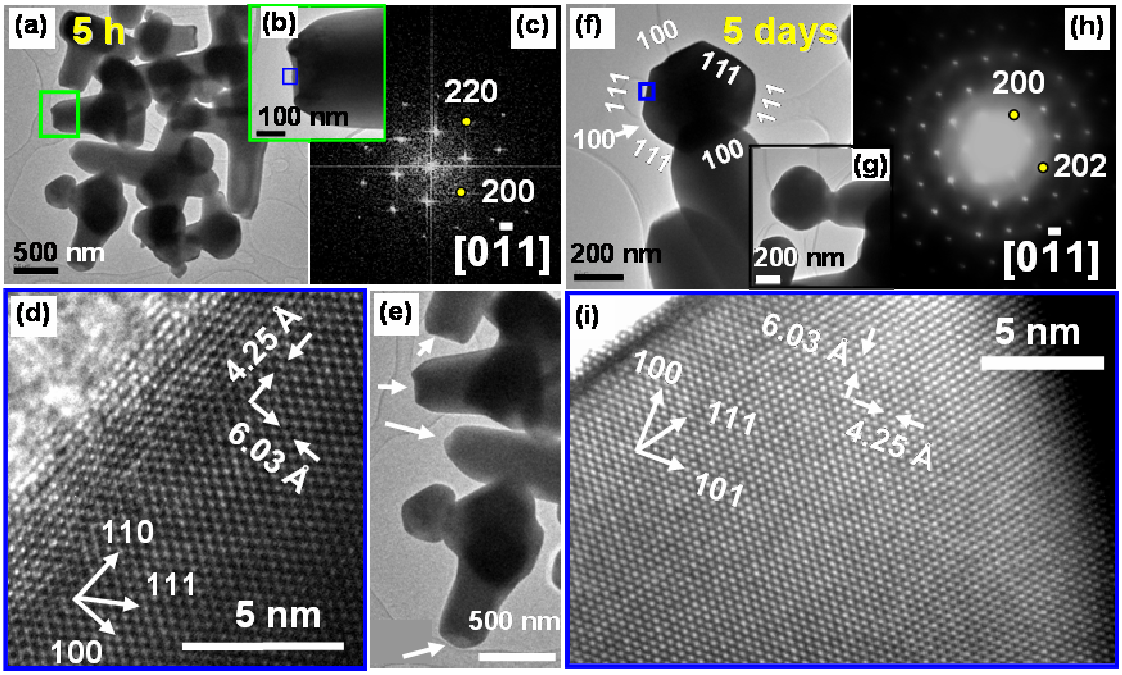


**Figure 11.** Characterization of PbS products obtained at 5 h (a-e) and 5 days (f-i) of reaction. (a) TEM overview of particles at $t_r$ = 5 h. (b) Higher magnification of the area marked in (a). (c) Fourier Transform pattern of the (d) HRTEM image of the area squared in (b). (e) Higher detail of the particles; the arrows mark the thinner, eroded tips of the rods. (f, g) TEM images of the particles undergoing deconstruction at $t_r$ = 5 days. (h) SAED pattern of the particle shown in (f) along the [0-11] zone axis. (i) HRTEM image of the area squared in (f).

within each microbranch lead to their deconstruction. The octahedral arrangements of microbranches are not stable under these circumstances. The activation energy for the breakage of the crystal lattice and conversion of anisotropic nanostructures to more energy efficient isotropic organization, might be depended on the energy of reorganization of ions on NPs interfaces by surface diffusion, which is quite low for PbS.[65, 66] The support for this point can be found in similar deconstruction of PbS rods observed under the electron beam.[67] The principle of spatially balanced dipoles proposed herein is also in consonance with previously reported 3D microstructures such as eight-arm dendrites[17, 21-23] in which the kinetic control of anisotropic patterns[52] works in combination with the thermodynamic balancing of dipoles pairs.[64]

## CONCLUSIONS

Several stages of assembly and deconstruction phenomena of PbS nano/micro particles in DES have been observed. The major thrust of this study was gaining better understanding of the mechanisms behind the assembly of PbS NPs leading to complex geometries of the resulting products. Although further work is still needed to reach greater clarity of all the stages, the following conclusions can be made.

1) PbS NPs self-organize into octahedra mesocrystals and later into 3D hyperbranched, hierarchical PbS nano/micro-crystals as the result of their preferential assembly along the six equivalent <100> directions. Octahedral symmetries characterize every level of hierarchy. The tendency to balance in space end-to-tail dipole-dipole pairs along six orthogonal directions of the three axis of a Cartesian system governs the geometry of the SA superstructures at every level of hierarchy.

2) Decrease of polarity of the medium upon urea decomposition results in the change of SA pattern. At this stage, the remaining NPs are incorporated between the nanoscale branches rather than along their length. The process is slow and frustrated by the temporal loss of balanced spatial orientation of dipoles at the nanoscale although later regained in six-

arm faceted rods with both {100} and {111} faces. It might be realized in two steps: non-epitaxial interaction followed by epitaxial re-organization.

3) Deconstruction of the six-arm microrods into individual submicro-rods and particles. The transition is governed by further decrease in solvent polarity, related increase of repulsive interactions, and reduction of energy for more isotropic structures. Deconstruction leads to particles geometrically similar to those in the first stages of the assembly with more ideal possibly apolar structure.

**Supporting Information Available** : NPs size histogram, TEM, HRTEM, SEM, XRD, results. $^{1}$H NMR spectra and discussion. Analysis of the influence of experimental variables in the resulting products. This material is available free of charge via the Internet at http://pubs.acs.org.

## ACKNOWLEDGEMTS

This research was supported by NSF DMR-9871177 and DMR-0315633 grants. A.Q.-F. acknowledges Spanish MEC for financial support through a FPU PhD fellowship and internships at UM; SPEE is also acknowledged. EMAL (UM) and Luis Bru (UCM) microscopy centres are acknowledged for facilities.

## References:

1. Grzybowski, B. A.; Wilmer, C. E.; Kim, J.; Browne, K. P.; Bishop, K. J. M., Self-assembly: From crystals to cells. *Soft Matter* **2009,** 5, (6), 1110-1128.
2. Nie, Z.; Petukhova, A.; Kumacheva, E., Properties and emerging applications of self-assembled structures made from inorganic nanoparticles. *Nature Nanotechnology* **2010,** 5, (1), 15-25.
3. Choi, C. L.; Alivisatos, A. P., From artificial atoms to nanocrystal molecules: Preparation and properties of more complex nanostructures. In *Annual Review of Physical Chemistry*, 2010; Vol. 61, pp 369-389.
4. Cölfen, H.; Antonietti, M., Mesocrystals: Inorganic superstructures made by highly parallel crystallization and controlled alignment. *Angewandte Chemie - International Edition* **2005,** 44, (35), 5576-5591.
5. Song, R. Q.; Cölfen, H., Mesocrystals - Ordered nanoparticle superstructures. *Advanced Materials* **2010,** 22, (12), 1301-1330.
6. Daniel, M. C.; Astruc, D., Gold Nanoparticles: Assembly, Supramolecular Chemistry, Quantum-Size-Related Properties, and Applications Toward Biology, Catalysis, and Nanotechnology. *Chemical Reviews* **2004,** 104, (1), 293-346.
7. Shevchenko, E. V.; Talapin, D. V.; Kotov, N. A.; O'Brien, S.; Murray, C. B., Structural diversity in binary nanoparticle superlattices. *Nature* **2006,** 439, (7072), 55-59.
8. Tang, Z.; Kotov, N. A.; Giersig, M., Spontaneous organization of single CdTe nanoparticles into luminescent nanowires. *Science* **2002,** 297, (5579), 237-240.
9. O'Sullivan, C.; Gunning, R. D.; Sanyal, A.; Barrett, C. A.; Geaney, H.; Laffir, F. R.; Ahmed, S.; Ryan, K. M., Spontaneous room temperature elongation of CdS and Ag<sub>2</sub>S nanorods via oriented attachment. *Journal of the American Chemical Society* **2009,** 131, (34), 12250-12257.
10. Cho, K. S.; Talapin, D. V.; Gaschler, W.; Murray, C. B., Designing PbSe nanowires and nanorings through oriented attachment of nanoparticles. *Journal of the American Chemical Society* **2005,** 127, (19), 7140-7147.
11. Yang, M.; Sun, K.; Kotov, N. A., Formation and assembly-disassembly processes of ZnO hexagonal pyramids driven by dipolar and excluded volume interactions. *Journal of the American Chemical Society* 132, (6), 1860-1872.
12. Tang, Z.; Wang, Y.; Shanbhag, S.; Giersig, M.; Kotov, N. A., Spontaneous transformation of CdTe nanoparticles into angled Te nanocrystals: From particles and rods to checkmarks, X-marks, and other unusual shapes. *Journal of the American Chemical Society* **2006,** 128, (20), 6730-6736.
13. Tang, Z.; Zhang, Z.; Wang, Y.; Glotzer, S. C.; Kotov, N. A., Self-assembly of CdTe nanocrystals into free-floating sheets. *Science* **2006,** 314, (5797), 274-278.
14. Srivastava, S.; Santos, A.; Critchley, K.; Kim, K. S.; Podsiadlo, P.; Sun, K.; Lee, J.; Xu, C.; Lilly, G. D.; Glotzer, S. C.; Kotov, N. A., Light-controlled self-assembly of semiconductor nanoparticles into twisted ribbons. *Science* 327, (5971), 1355-1359.
15. Wang, N.; Cao, X.; Guo, L.; Yang, S.; Wu, Z., Facile synthesis of PbS truncated octahedron crystals with high symmetry and their large-scale assembly into regular patterns by a simple solution route. *ACS Nano* **2008,** 2, (2), 184-190.

16. Zhou, G.; LÃ¼, M.; Xiu, Z.; Wang, S.; Zhang, H.; Zhou, Y.; Wang, S., Controlled synthesis of high-quality PbS star-shaped dendrites, multipods, truncated nanocubes, and nanocubes and their shape evolution process. *Journal of Physical Chemistry B* **2006,** 110, (13), 6543-6548.
17. Ding, B.; Shi, M.; Chen, F.; Zhou, R.; Deng, M.; Wang, M.; Chen, H., Shape-controlled syntheses of PbS submicro-/nano-crystals via hydrothermal method. *Journal of Crystal Growth* **2009,** 311, (6), 1533-1538.
18. Bakshi, M. S.; Thakur, P.; Sachar, S.; Kaur, G.; Banipal, T. S.; Possmayer, F.; Petersen, N. O., Aqueous phase surfactant selective shape controlled synthesis of lead sulfide nanocrystals. *Journal of Physical Chemistry C* **2007,** 111, (49), 18087-18098.
19. Shao, S.; Zhang, G.; Zhou, H.; Sun, P.; Yuan, Z.; Li, B.; Ding, D.; Chen, T., Morphological evolution of PbS crystals under the control of l-lysine at different pH values: The ionization effect of the amino acid. *Solid State Sciences* **2007,** 9, (8), 725-731.
20. Wang, D.; Yu, D.; Shao, M.; Liu, X.; Yu, W.; Qian, Y., Dendritic growth of PbS crystals with different morphologies. *Journal of Crystal Growth* **2003,** 257, (3-4), 384-389.
21. Ma, Y.; Qi, L.; Ma, J.; Cheng, H., Hierarchical, star-shaped PbS crystals formed by a simple solution route. *Crystal Growth and Design* **2004,** 4, (2), 351-354.
22. Zhang, W.; Yang, Q.; Xu, L.; Yu, W.; Qian, Y., Growth of PbS crystals from nanocubes to eight-horn-shaped dendrites through a complex synthetic route. *Materials Letters* **2005,** 59, (27), 3383-3388.
23. Zhu, J.; Duan, W.; Sheng, Y., Uniform PbS hopper (skeletal) crystals grown by a solution approach. *Journal of Crystal Growth* **2009,** 311, (2), 355-357.
24. Xiang, J.; Cao, H.; Wu, Q.; Zhang, S.; Zhang, X., L-cysteine-assisted self-assembly of complex PbS structures. *Crystal Growth and Design* **2008,** 8, (11), 3935-3940.
25. Ni, Y.; Liu, H.; Wang, F.; Liang, Y.; Hong, J.; Ma, X.; Xu, Z., Shape controllable preparation of PbS crystals by a simple aqueous phase route. *Crystal Growth and Design* **2004,** 4, (4), 759-764.
26. Zhao, N.; Qi, L., Low-temperature synthesis of star-shaped PbS nanocrystals in aqueous solutions of mixed cationic/anionic surfactants. *Advanced Materials* **2006,** 18, (3), 359-362.
27. Zhao, Z.; Zhang, K.; Zhang, J.; Yang, K.; He, C.; Dong, F.; Yang, B., Synthesis of size and shape controlled PbS nanocrystals and their self-assembly. *Colloids and Surfaces A: Physicochemical and Engineering Aspects* **2010,** 355, (1-3), 114-120.
28. Lee, S. M.; Jun, Y. W.; Cho, S. N.; Cheon, J., Single-crystalline star-shaped nanocrystals and their evolution: Programming the geometry of nano-building blocks. *Journal of the American Chemical Society* **2002,** 124, (38), 11244-11245.
29. Zhang, X. H.; Jia, C.; Chen, Y. Q.; Su, Y.; Zhou, H. Y., A mixed solvothermal route to synthesis of dice-like PbS. *Journal of the Chinese Chemical Society* **2008,** 55, (6), 1221-1224.
30. Wise, F. W., Lead salt quantum dots: The limit of strong quantum confinement. *Accounts of Chemical Research* **2000,** 33, (11), 773-780.
31. Luque, A.; Martí, A.; Nozik, A. J., Solar cells based on quantum dots: Multiple exciton generation and intermediate bands. *MRS Bulletin* **2007,** 32, (3), 236-241.
32. Ellingson, R. J.; Beard, M. C.; Johnson, J. C.; Yu, P.; Micic, O. I.; Nozik, A. J.; Shabaev, A.; Efros, A. L., Highly efficient multiple exciton generation in colloidal PbSe and PbS quantum dots. *Nano Letters* **2005,** 5, (5), 865-871.
33. Schaller, R. D.; Sykora, M.; Pietryga, J. M.; Klimov, V. I., Seven excitons at a cost of one: Redefining the limits for conversion efficiency of photons into charge carriers. *Nano Letters* **2006,** 6, (3), 424-429.
34. Nair, G.; Geyer, S. M.; Chang, L. Y.; Bawendi, M. G., Carrier multiplication yields in PbS and PbSe nanocrystals measured by transient photoluminescence. *Physical Review B - Condensed Matter and Materials Physics* **2008,** 78, (12).
35. Pijpers, J. J. H.; Ulbricht, R.; Tielrooij, K. J.; Osherov, A.; Golan, Y.; Delerue, C.; Allan, G.; Bonn, M., Assessment of carrier-multiplication efficiency in bulk PbSe and PbS. *Nature Physics* **2009,** 5, (11), 811-814.
36. Beard, M. C.; Midgett, A. G.; Hanna, M. C.; Luther, J. M.; Hughes, B. K.; Nozik, A. J., Comparing Multiple Exciton Generation in Quantum Dots To Impact Ionization in Bulk Semiconductors: Implications for Enhancement of Solar Energy Conversion. *Nano Letters* **2010,** 10, (8), 3019-3027.
37. Thielsch, R.; BÃ¶hme, T.; Reiche, R.; SchlÃ¤fer, D.; Bauer, H. D.; BÃ¶ttcher, H., Quantum-size effects of PbS nanocrystallites in evaporated composite films. *Nanostructured Materials* **1998,** 10, (2-8), 131-149.
38. Huynh, W. U.; Dittmer, J. J.; Alivisatos, A. P., Hybrid nanorod-polymer solar cells. *Science* **2002,** 295, (5564), 2425-2427.
39. Law, M.; Greene, L. E.; Johnson, J. C.; Saykally, R.; Yang, P., Nanowire dye-sensitized solar cells. *Nature Materials* **2005,** 4, (6), 455-459.
40. Gur, I.; Fromer, N. A.; Chen, C. P.; Kanaras, A. G.; Alivisatos, A. P., Hybrid solar cells with prescribed nanoscale morphologies based on hyperbranched semiconductor nanocrystals. *Nano Letters* **2007,** 7, (2), 409-414.
41. Greenham, N. C.; Peng, X.; Alivisatos, A. P., Charge separation and transport in conjugated-polymer/semiconductor-nanocrystal composites studied by photoluminescence quenching and photoconductivity. *Physical Review B - Condensed Matter and Materials Physics* **1996,** 54, (24), 17628-17637.

42. Zhang, S.; Cyr, P. W.; McDonald, S. A.; Konstantatos, G.; Sargent, E. H., Enhanced infrared photovoltaic efficiency in PbS nanocrystal/semiconducting polymer composites: 600-fold increase in maximum power output via control of the ligand barrier. *Applied Physics Letters* **2005,** 87, (23), 1-3.
43. Abbott, A. P.; Capper, G.; Davies, D. L.; Rasheed, R. K.; Tambyrajah, V., Novel solvent properties of choline chloride/urea mixtures. *Chemical Communications* **2003,** 9, (1), 70-71.
44. Morris, R. E., Ionothermal synthesis - Ionic liquids as functional solvents in the preparation of crystalline materials. *Chemical Communications* **2009**, (21), 2990-2998.
45. Cooper, E. R.; Andrews, C. D.; Wheatley, P. S.; Webb, P. B.; Wormald, P.; Morris, R. E., Ionic liquids and eutectic mixtures as solvent and template in synthesis of zeolite analogues. *Nature* **2004,** 430, (7003), 1012-1016.
46. Antonietti, M.; Kuang, D.; Smarsly, B.; Zhou, Y., Ionic liquids for the convenient synthesis of functional nanoparticles and other inorganic nanostructures. *Angewandte Chemie - International Edition* **2004,** 43, (38), 4988-4992.
47. Zhang, J.; Wu, T.; Chen, S.; Feng, P.; Bu, X., Versatile structure-directing roles of deep-eutectic solvents and their implication in the generation of porosity and open metal sites for gas storage. *Angewandte Chemie - International Edition* **2009,** 48, (19), 3486-3490.
48. Guloy, A. M.; Ramlau, R.; Tang, Z.; Schnelle, W.; Baitinger, M.; Grin, Y., A guest-free germanium clathrate. *Nature* **2006,** 443, (7109), 320-323.
49. Liao, H. G.; Jiang, Y. X.; Zhou, Z. Y.; Chen, S. P.; Sun, S. G., Shape-controlled synthesis of gold nanoparticles in deep eutectic solvents for studies of structure-functionality relationships in electrocatalysis. *Angewandte Chemie - International Edition* **2008,** 47, (47), 9100-9103.
50. Machol, J. L.; Wise, F. W.; Patel, R. C.; Tanner, D. B., Vibronic quantum beats in PbS microcrystallites. *Physical Review B* **1993,** 48, (4), 2819-2822.
51. Critchley, K.; Khanal, B. P.; Górzny, M. L.; Vigderman, L.; Evans, S. D.; Zubarev, E. R.; Kotov, N. A., Near-bulk conductivity of gold nanowires as nanoscale interconnects and the role of atomically smooth interface. *Advanced Materials* **2010,** 22, (21), 2338-2342.
52. Jun, Y. W.; Lee, J. H.; Choi, J. S.; Cheon, J., Symmetry-controlled colloidal nanocrystals: Nonhydrolytic chemical synthesis and shape determining parameters. *Journal of Physical Chemistry B* **2005,** 109, (31), 14795-14806.
53. Wang, Z. L., Transmission electron microscopy of shape-controlled nanocrystals and their assemblies. *Journal of Physical Chemistry B* **2000,** 104, (6), 1153-1175.
54. Shim, M.; Guyot-Sionnest, P., Permanent dipole moment and charges in colloidal semiconductor quantum dots. *Journal of Chemical Physics* **1999,** 111, (15), 6955-6964.
55. Shanbhag, S.; Kotov, N. A., On the origin of a permanent dipole moment in nanocrystals with a cubic crystal lattice: Effects of truncation, stabilizers, and medium for CdS tetrahedral homologues. *Journal of Physical Chemistry B* **2006,** 110, (25), 12211-12217.
56. Sinyagin, A.; Belov, A.; Kotov, N., Monte Carlo simulation of linear aggregate formation from CdTe nanoparticles. *Modelling and Simulation in Materials Science and Engineering* **2005,** 13, (3), 389-399.
57. Blanton, S. A.; Leheny, R. L.; Hines, M. A.; Guyot-Sionnest, P., Dielectric dispersion measurements of CdSe nanocrystal colloids: Observation of a permanent dipole moment. *Phys. Rev. Lett.* **1997,** 79, (5), 865-868.
58. Smith, D. J.; Petford-Long, A. K.; Wallenberg, L. R.; Bovin, J. O., Dynamic atomic-level rearrangements in small gold particles. *Science* **1986,** 233, (4766), 872-875.
59. Parnham, E. R.; Drylie, E. A.; Wheatley, P. S.; Slawin, A. M. Z.; Morris, R. E., Ionothermal materials synthesis using unstable deep-eutectic solvents as template-delivery agents. *Angewandte Chemie - International Edition* **2006,** 45, (30), 4962-4966.
60. Podsiadlo, S., Stages of the synthesis of indium nitride with the use of urea. *Thermochimica Acta* **1995,** 256, (2), 375-380.
61. Querejeta-Fernández, A. P., M.; Varela, A.; del Monte, F.; García-Hernández, M.; González-Calbet, J.M., Urea-melt Assited Synthesis of Ni/NiO Nanoparticles Exhibiting Structural Disorder and Exchange Bias. *submitted 2010*.
62. Haerens, K.; Matthijs, E.; Binnemans, K.; Van Der Bruggen, B., Electrochemical decomposition of choline chloride based ionic liquid analogues. *Green Chemistry* **2009,** 11, (9), 1357-1365.
63. Lilly, G. D.; Lee, J.; Sun, K.; Tang, Z.; Kim, K. S.; Kotov, N. A., Media effect on CdTe nanowire growth: Mechanism of self-assembly, ostwald ripening, and control of NW geometry. *Journal of Physical Chemistry C* **2008,** 112, (2), 370-377.
64. Note that isotropic shapes optimize the volume/surface a high ratio, which favours both thermodynamic (solid-solid interfaces are more stable than solid-liquid ones) and entropic (desorption of solvent molecules from the surface) aspects.
65. Watson, E. B.; Cherniak, D. J.; Frank, E. A., Retention of biosignatures and mass-independent fractionations in pyrite: Self-diffusion of sulfur. *Geochim. Cosmochim. Acta* **2009,** 73, (16), 4792-4802.
66. Seltzer, M. S.; Wagner, J. B., Diffusion of Lead in Lead Sulphide at 700 Degrees C. *Journal of Physics and Chemistry of Solids* **1963,** 24, (12), 1525-&.

67. Warner, J. H., Self-assembly of ligand-free PbS nanocrystals into nanorods and their nanosculpturing by electron-beam irradiation. *Advanced Materials* **2008,** 20, (4), 784-787.

# Supporting Information

## Assembly and Deconstruction of Hierarchical PbS Nano/Micro Crystals and Vectorial Balance of Dipolar Branches

Ana Querejeta-Fernández,[#‡] Paul A. Podsiadlo,[§] Hengxi Yang,[⊥] Yunlong Zhou,[#] Peter F. Green,[¶] Francisco del Monte,[&] Aurea Varela,[‡] Marina Parras,[‡] Jose M. González-Calbet[‡] and Nicholas A. Kotov[#¶†*]

[#]Chemical Engineering Department, University of Michigan, Ann Arbor, MI, 48109, USA; [‡]Departamento de Química Inorgánica I, Facultad de Ciencias Químicas, Universidad Complutense de Madrid, 28040 Madrid, Spain; [§]Center for Nanoscale Materials, Argonne National Laboratory, Argonne, IL 60439, USA; [⊥]Physics Department, University of Michigan, Ann Arbor, MI 48109, USA; [&]Instituto de Ciencia de Materiales de Madrid, CSIC, Campus de Cantoblanco, 28049 Madrid, Spain; [¶]Material Science and Engineering Department, University of Michigan, Ann Arbor MI, 48109, USA; [†]Biomedical Engineering Department, University of Michigan, Ann Arbor MI, 48109, USA

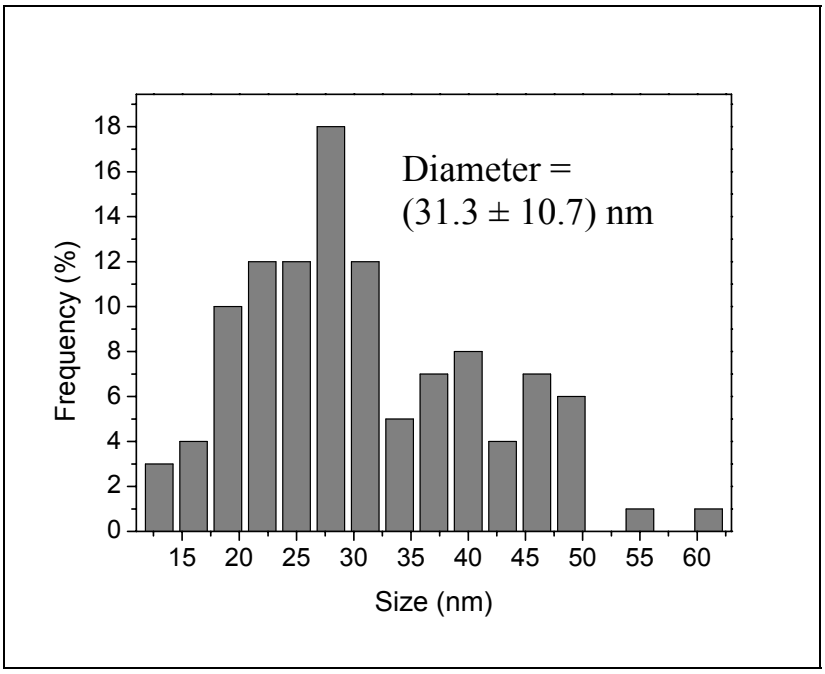


**Figure S1**. Size histogram of PbS NPs obtained at 5 min of reaction. Sizes were measured as the longest dimension of particles in TEM images.

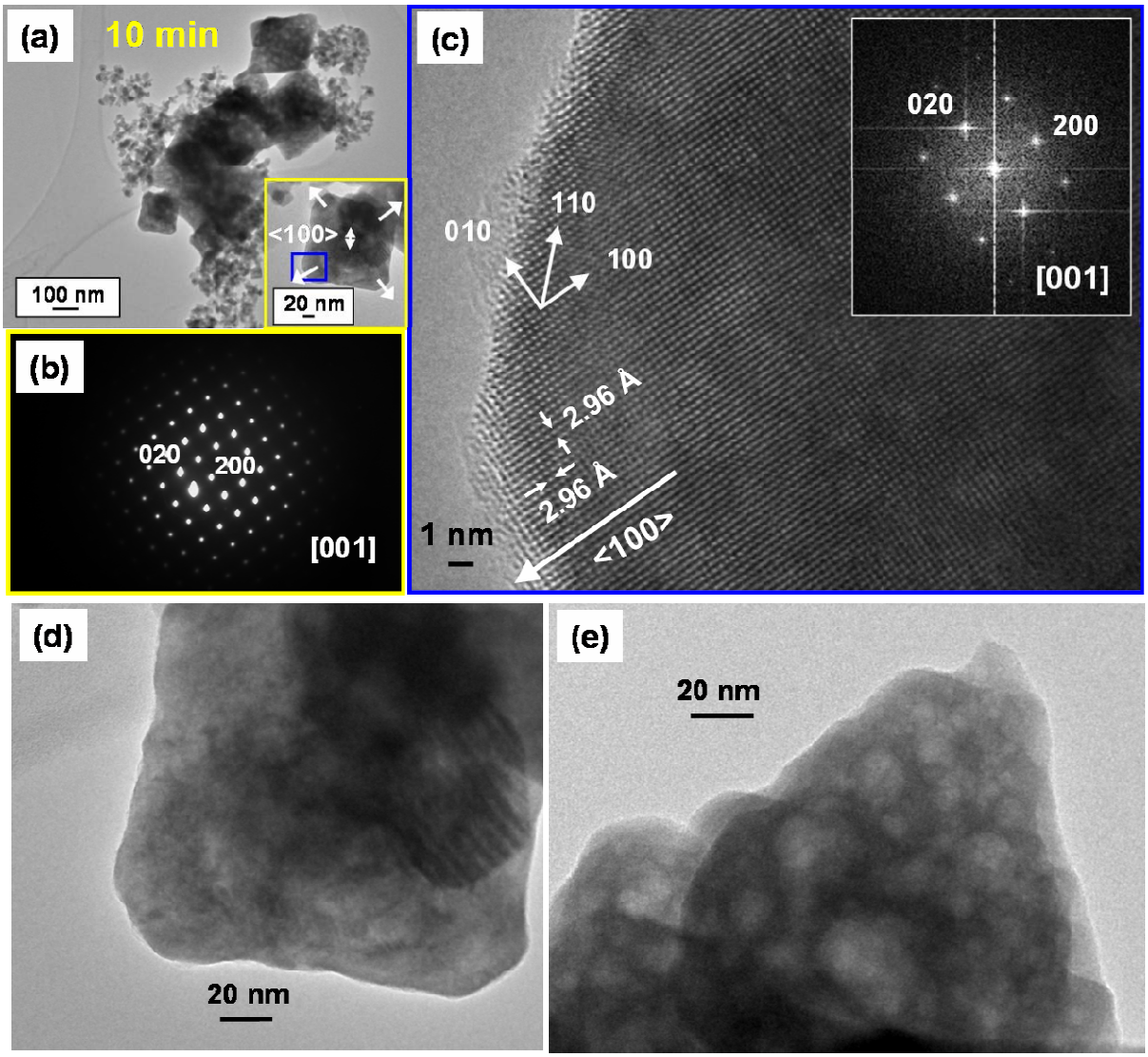


**Figure S2** . Characterization of the PbS product obtained at 10 min of reaction. (a) TEM image. Inset shows greater magnification of a sub-micron particle with an octahedral shape. (b) SAED pattern of the particle in inset of image (a). (c) HRTEM image and Fourier Transform (inset) of the squared area from the inset in (a). (d,e) TEM images evidencing the imperfect fusing among nano-building-blocks within octahedral mesocrystals. The non-smooth surfaces are evident.

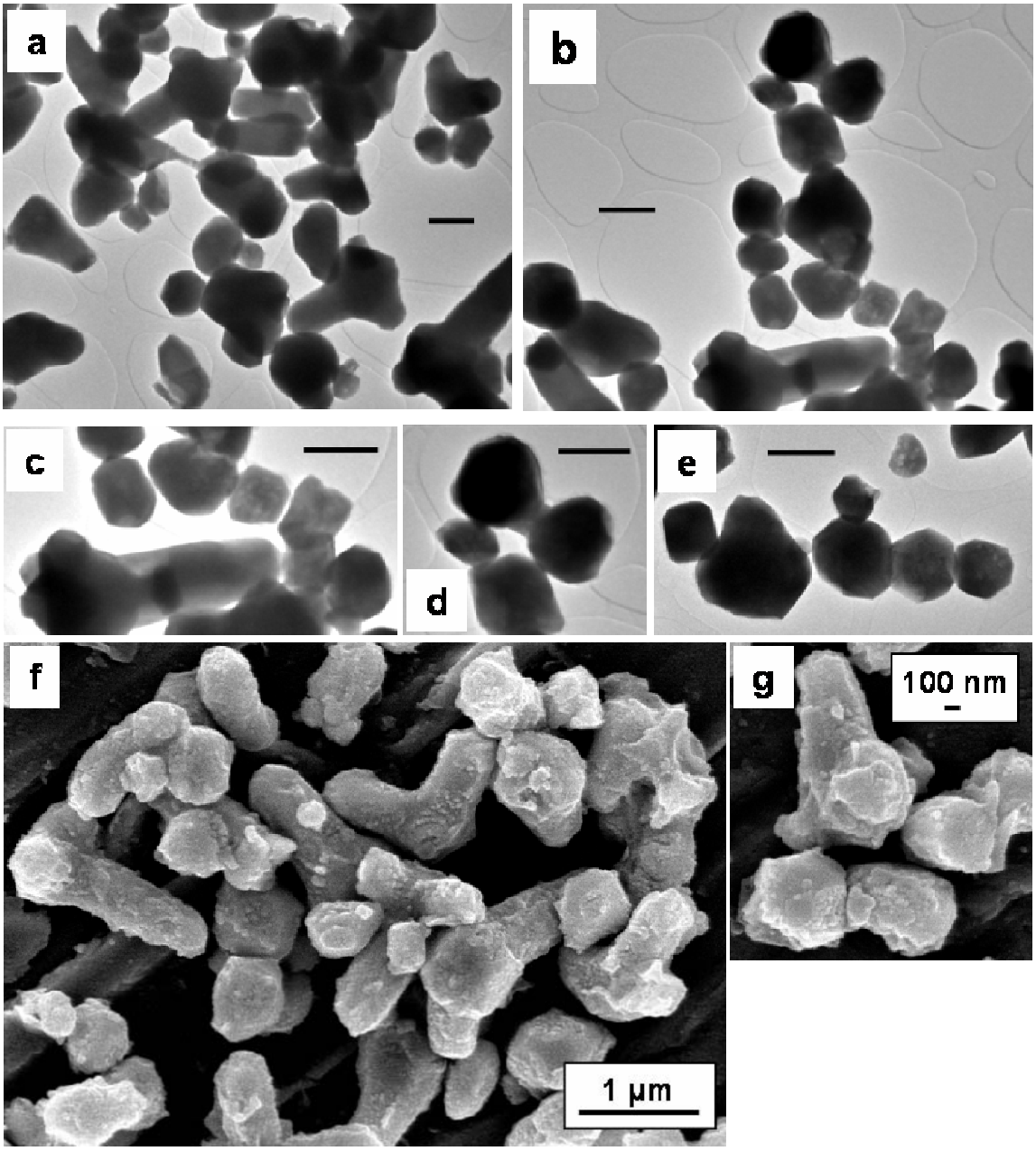


**Figure S3.** (a-e) TEM and (f, g) SEM images of PbS product obtained at 14 days of reaction. All the scale bars in TEM images correspond to 500 nm.

$^{1}$H NMR data

The DES/water solvent decomposition was followed by $^{1}$H NMR (Figure S4 and Table S1). At $t_r$ = 0 min, the spectrum is in good agreement with the characteristic signals of protons from 2urea:1choline chloride eutectic composition (8H urea : 9H choline methyls).[1, 2] However, the analysis of the area of the signals at $t_r$ = 10 min, indicates a slight decrease of the urea/choline chloride ratio (7.8H urea : 9H choline methyls), which is maintained until $t_r$ = 30 min. During this stage, the urea decomposition is slowly initiated. Afterwards, the urea:choline chloride ratio keeps remarkably decreasing (7.6, 7.4 and 5.7H urea : 9H choline methyls at $t_r$ = 50min, 4 and 24 h, respectively), evidencing the gradual urea decomposition. As a result of such decomposition, $NH_4OH$ is formed according to ec. 1-5. As this is the only proton-based stable compound that can be generated from the urea/water decomposition, its ammonium protons must be responsible for the extra peak at 4.62 ppm detected from the onset of the urea decomposition (*i.e.* $t_r$ = 10 min). During $t_r$ = 10-30 min, when urea decomposition is slowly initiated, the signal of $NH_4OH$ is constant (6.2H), while at $t_r$ > 30 min it considerably decreases (5.9, 5.4 and 2.7H at $t_r$ = 4 and 24 h, respectively). In spite of the continuous urea decomposition, which should lead to the increase of $NH_4OH$ formation, the $NH_4OH$ decrease from $t_r$ > 30 min is due to its evaporation, as revealed by XRD analysis of the white salts collected in the condenser of the reaction system (Figure S5), which indicates the formation of ammonium hydrogen carbonate ($NH_4HCO_3$) and ammonium hydrogen carbonate amide ($NH_4HCO_3 \cdot NH_4CO_2NH_2$), as mentioned in the main text (note that $NH_3$ and $CO_2$ gases form $NH_4HCO_3$ in the presence of water).

In regard to the chemical shift of the $^{1}$H NMR signals, it is not significantly shifted in respect to the initial [DES/water] solvent in any case, indicating strong supramolecular hydrogen bonding between the remaining urea and choline chloride, similar to the interactions present in the primitive mixture. In other words, the choline chloride/urea DES substantial integrity is not affected by the partial urea decomposition but it is its composition, and thus the corresponding melting temperature, which is shifted along the curve of the binary phase diagram from the initial eutective point. For instance, analysis of the data corresponding to $t_r$ = 24 h (Table S1) reveals a urea:choline chloride molar ratio close to 1.5:1, which as compared to the 2:1 initial one, indicates the transition from the 66 to the 60 % urea molar ratio, which in turn would translate into an increase of the melting point from 12 to *ca.* 32 ºC for the case of pure DES.[1] Note that, in spite of the mentioned reported melting point, the aliquot at $t_r$ = 24 h is liquid at room temperature due to the presence of some water with the urea/choline chloride mixture. Thus, melting points of the evolving

mixture can be only compared qualitatively with the tabulated ones. Confirmation of the increase of the melting point of the solvent at longer reaction times is based on the aliquot taken at $t_r$ = 3 days, which is solid at room temperature. Similarly, a visual inspection indicates an increase of viscosity at longer reaction times, which is also in agreement with the corresponding increase of the melting point.

Overall, it is demonstrated that gradual urea decomposition takes place in the DES/water solvent along with the reaction time and this leads to change of the physico-chemical properties, such as melting temperature, viscosity, polarity, *etc.*

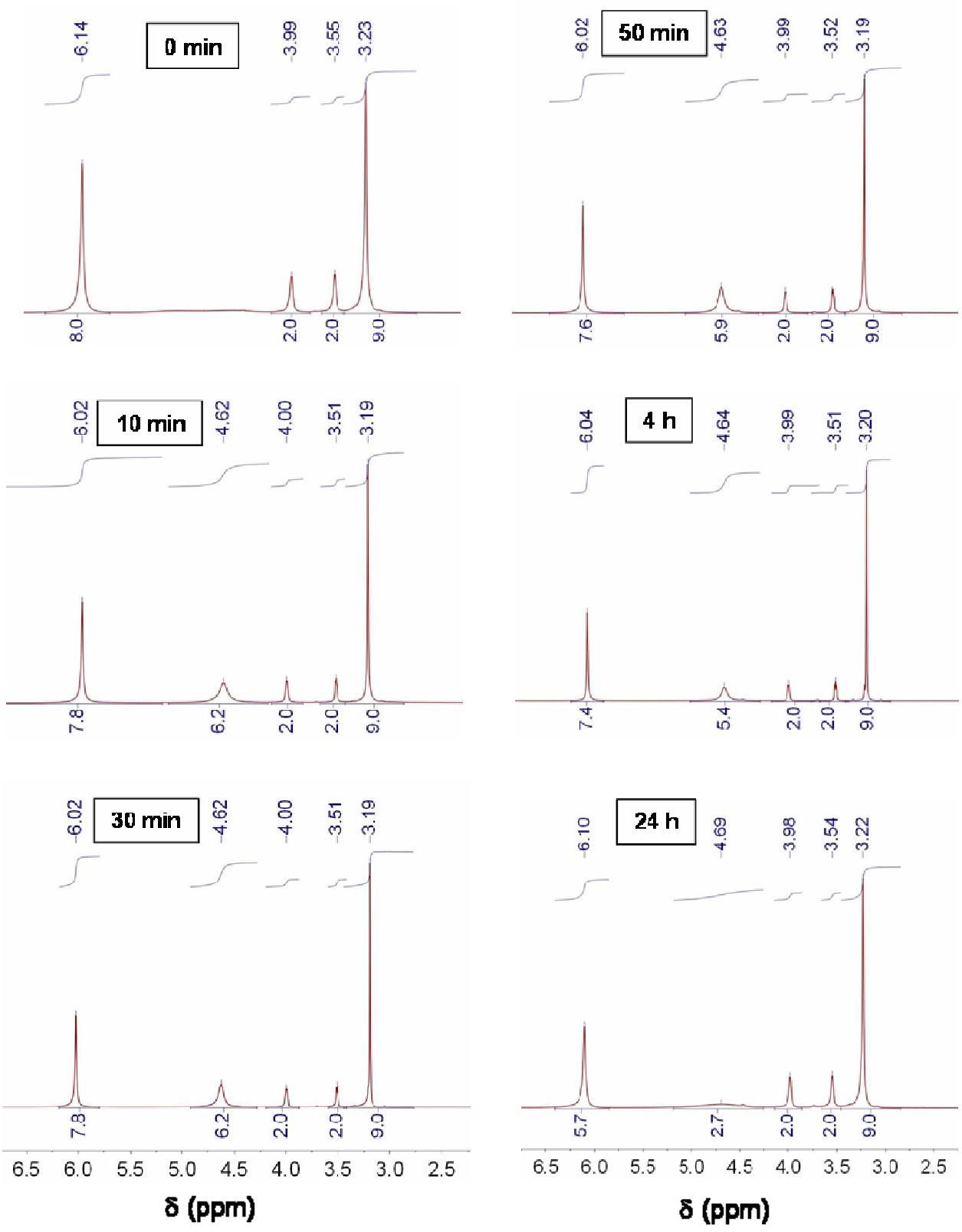


**Figure S4.** $^{1}H$ NMR ($T_{amb}$) evaluation of the time-dependent decomposition of the DES/water solvent. The peak positions and their integrals are indicated on top and bottom, respectively.

**Table S1** . $^{1}$H NMR Spectroscopy Data Details (integrated area, δ (ppm)) of the Solvent [2:1 Urea:Choline Chloride DES + water] at Different Decomposition Times.

| | (2×) urea | water | (1×) choline | | | | decomposition product |
|---|---|---|---|---|---|---|---|
| time | (-N<u>H</u>$_2$)$_2$ | <u>H</u>$_2$O[a] | O<u>H</u>[a] | β-C<u>H</u>$_2$ | α-C<u>H</u>$_2$ | (-C<u>H</u>$_3$)$_3$ | (N<u>H</u>$_4$O<u>H</u>[a]) |
| 0 min | 8H, 6.14 | - | - | 2H, 3.99 | 2H, 3.55 | 9H, 3.23 | - |
| 10 min | 7.8H, 6.02 | - | - | 2H, 4.00 | 2H, 3.51 | 9H, 3.19 | 6.2H, 4.62 |
| 30 min | 7.8H, 6.02 | - | - | 2H, 4.00 | 2H, 3.51 | 9H, 3.19 | 6.2H, 4.62 |
| 50 min | 7.6H, 6.02 | - | - | 2H, 3.99 | 2H, 3.52 | 9H, 3.19 | 5.9H, 4.63 |
| 4 h | 7.4H, 6.04 | - | - | 2H, 3.99 | 2H, 3.51 | 9H, 3.20 | 5.4H, 4.64 |
| 24 h | 5.7H, 6.10 | - | - | 2H, 3.98 | 2H, 3.54 | 9H, 3.22 | 2.7H, 4.69 |

[a] Not peaks of labile protons from $OH^-$ were detected. For the 0 min sample, two broad and very weak signals at 4.59 and 5.19 ppm could correspond to the protons from water and OH(choline), respectively.[2]

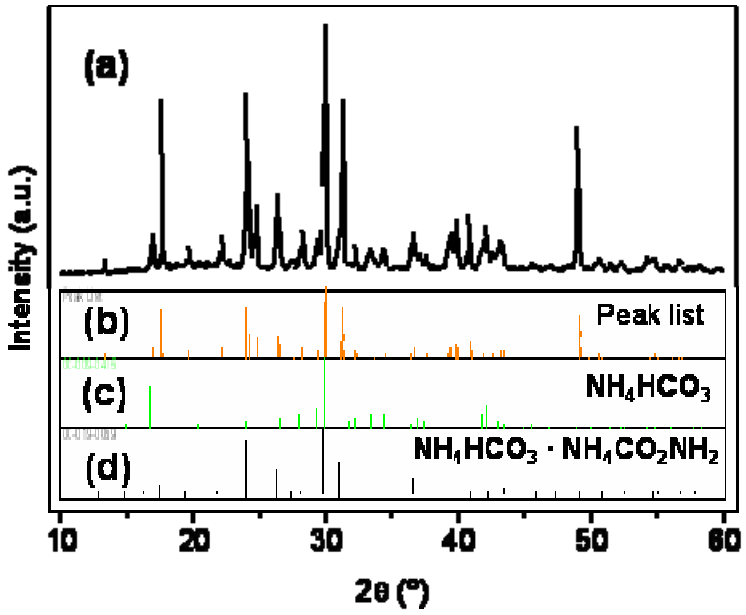


**Figure S5.** (a) XRD pattern of the white salts collected in the condenser at $t_r$ = 14 days. (b) Corresponding peak list. (c, d) XRD patterns of ammonium hydrogen carbonate ($NH_4HCO_3$, JCPDS 00-009-0415) and ammonium hydrogen carbonate amide ($NH_4HCO_3 \cdot NH_4CO_2NH_2$; JCPDS 00-019-0059), respectively.

Influence of the experimental variables in the resulting products

Influence of the temperature. Since DES decomposition ultimately determines the change of SA pattern, it is very desirable to check different reaction temperatures and heating protocols in order to explore the different possibilities of SA and resulting structures. Thus, apart from the typical temperature ($T_{injection}$ = 80 ºC, $T_{reaction}$ = 140 ºC), the reaction was carried out at two additional temperatures while keeping the rest of the parameters constant and equal to the standard protocol detailed in the Experimental Section. Figure S6 shows the TEM images of the products obtained for $T_{injection}$ = $T_{reaction}$ = 140 ºC at 30 min (Figure S6a) and for $T_{injection}$ = $T_{reaction}$ = 80 ºC at 20 min (Figure S6binset) and 1 h (Figure S6b). None of them leads to hyperbranched rods. The former leads to NPs and few six-armed rods and nascent rods whose size is ca. ≤ 500 nm. No octahedral assemblies were detected either. The high $T_{inj, react}$ in this case must lead to a fast and early decomposition of the DES, not allowing the high polarity much needed for the SA of the nucleated NPs along the <100> directions and vectorially balanced in pairs. This result corroborates the need of a highly polar medium for the SA fashion resulting in hyperbranched structures. Regarding $T_{inj, react}$ = 80 ºC, such a temperature is not enough for producing any anisotropic structure driven by DMs. Instead, the low $T_{inj, react}$ may produce a slower nucleation, leading to larger particles, and negligible DMs, leading to a random aggregation into irregular, large particles.

Influence of the content of water. The content of water also plays a crucial role in the organized SA of PbS NPs into hierarchical structures and its presence is essential for providing the DES with the suitable soft-templating properties.[3] On the other hand, water content must also determine the polarity of the medium, which is a crucial parameter in the SA fashion. It is worth noting that the content of water added to the urea/choline chloride DES is small enough (DES concentration in water is 85.6 wt %) to keep the hydrogen-bonding structure exhibited by the DES in its pure state.[2] Dilution well above 86 wt % prompts the rupture of the halide–hydrogen-bond-donor supramolecular structure, yielding a regular aqueous solution of non-interacting urea and choline chloride, which lacks the special ionic-liquid–type properties exhibited by the DES in its pure state.[2]

Two additional contents of water were tested keeping the standard protocol described in the Experimental Section. If the typical synthesis was performed with 200 µl of water per 1 ml of DES (85.6 DES wt %), 66.7 (94.7 DES wt %) and 400 (74.8 DES wt %) µl of water per 1 ml of DES were also checked.

Figures S6c, d show the TEM images of the reaction with 66.7 µl of water per 1 ml of DES (94.7 DES wt %) at 30 min and 1 h 30 min of reaction, respectively. NPs are the predominant product at 30 min; also, some bigger particles (≤ 500 nm) with a very slight rod-like and branched structure are present. Longer times of reaction failed in the anisotropic assembly of the NPs, leading to random aggregates. These results indicate that, even in the region of DES/water composition which keeps the characteristics typical of ILs,[2] very small differences in water content are critical for the shapes of the as-prepared crystals, which is in consonance with previous reports.[3]

Regarding to 400 µl of water per 1 ml of DES (74.8 DES wt %), the higher content of water in this case leads to an uncontrolled growth of the particles, so at 30 min of reaction large particles and their aggregates (> 500 nm of size) with tips and some NPs are obtained (Figure S6e) and at 1 h 30 min the products remain more or less unchanged (Figure S6f). This composition of the medium could correspond to mere aqueous solution of DES, which lacks the special properties of ILs responsible for the nucleation and stabilization of NPs at the early stages of reaction.

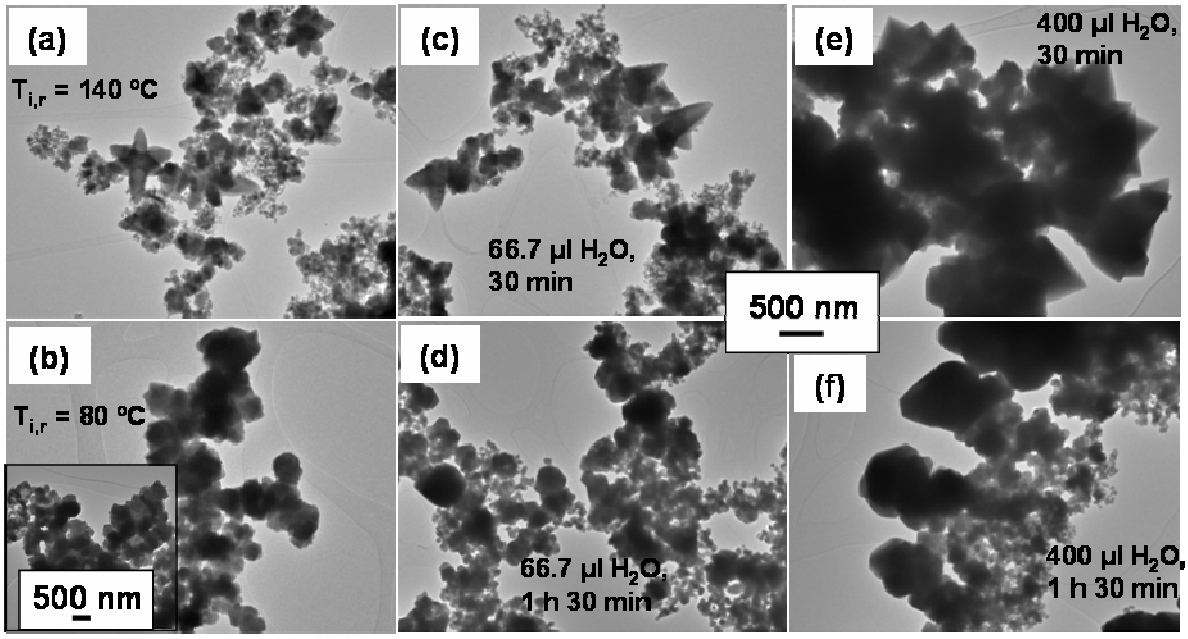


**Figure S6.** TEM analysis of the influence of experimental parameters on the final products. (a, b) Influence of temperature: (a) $T_{inj} = T_{react}$ = 140 ºC, $t_r$ = 30 min, (b) $T_{inj} = T_{react}$ = 80 ºC, $t_r$ = 1 h and (inset) 20 min. (c-f) Influence of water content: (c, d) 66.7 µl of water per 1 ml of DES at (c) 30 min and (d) 1 h 30 min. (e, f) 200 µl of water per 1 ml of DES at (e) 30 min and (f) 1 h 30 min.

**References:**

1. Abbott, A. P.; Capper, G.; Davies, D. L.; Rasheed, R. K.; Tambyrajah, V., Novel solvent properties of choline chloride/urea mixtures. *Chemical Communications* **2003,** 9, (1), 70-71.
2. Gutiérrez, M. C.; Ferrer, M. L.; Mateo, C. R.; Monte, F. D., Freeze-drying of aqueous solutions of deep eutectic solvents: A suitable approach to deep eutectic suspensions of self-assembled structures. *Langmuir* **2009,** 25, (10), 5509-5515.
3. Liao, H. G.; Jiang, Y. X.; Zhou, Z. Y.; Chen, S. P.; Sun, S. G., Shape-controlled synthesis of gold nanoparticles in deep eutectic solvents for studies of structure-functionality relationships in electrocatalysis. *Angewandte Chemie - International Edition* **2008,** 47, (47), 9100-9103.

# CHAPTER 3.2

## Urea/Choline Chloride Deep Eutectic Solvent for the Synthesis of Nanooxides

In view of the advantageous properties of urea/choline chloride DES a synthetic medium of PbS NPs, the suitability of such a solvent for the preparation of nanooxides was evaluated. Thus, this chapter reports the synthesis of nanosized iron oxides ($Fe_3O_4$/γ-$Fe_2O_3$ and α-$Fe_2O_3$; ~ 15 nm) and manganese oxides ($Mn_3O_4$; ~ 8-60 nm) NPs. Additionally, the preparation of nanoporous $Mn_2O_3$ (~ 10-60 nm) was obtained through the thermal decomposition of $MnCO_3$ synthesized via DES. These preliminary results point towards the synthesis via urea/choline chloride DES as a general strategy for the preparation of a wide range of compositions with remarkable features such as SA and textural properties.

.

# Urea/Choline Chloride Deep Eutectic Solvent for the Synthesis of Nanooxides

## 1. Introduction

Since the first paper reporting on that urea and choline chloride, among other hydrogen bond donors and ammonium quaternary salts, produce deep eutectics that are liquid at ambient temperature and have unusual solvent properties,[1] the use of deep eutectic solvent (DES) as synthetic media has emerged as an easy and inexpensive alternative to conventional ionic liquids (ILs).[2] However, while endeavours have been made towards the synthesis of hybrid organic/inorganic materials,[3-6] inorganic materials prepared in DESs are restricted to semiconductors (PbS nanoparticles and hyperbranched structures[7] and low-density germanium frameworks[8]) and gold sub-micron stars.[9] Neither the synthesis of other compositions such as oxides nor the formation of nanocrystals in DESs have been extensively exploited. Herein, we report the synthesis of nanosized iron oxides ($Fe_3O_4$/$\gamma$-$Fe_2O_3$ and $\alpha$-$Fe_2O_3$) and manganese oxides ($Mn_2O_3$ and $Mn_3O_4$) in urea/choline chloride DES. As-prepared powders were characterized by means of X-Ray diffraction (XRD) and transmission electron microscopy (TEM).

## 2. Experimental Section

Urea (ultra, Sigma), choline chloride (≥ 97 %, Fluka), iron (II) acetylacetonate (99.95 %, Aldrich), iron (III) acetylacetonate (≥ 99.9 %, Aldrich), iron (II) acetate (99.995 %, Aldrich), iron (0) pentacarbonyl (Aldrich), manganese (III) acetylacetonate (Aldrich), potassium permanganate (99+%, Aldrich) and hexadecyltrimethylammonium bromide (CTAB) (≥ 99.9 %, Sigma) were used as-received. DES was prepared by mixing the components urea and choline chloride in the molar ratio 2:1, as corresponds to the eutectic point, and heating to 80 ºC in a furnace until a homogeneous, viscous liquid was formed. The synthesis was performed as follows. The metallic precursor was added to a mixture of DES and water (amounts detailed in Tables 1-3) in a flask, which was then introduced into an oil bath and connected to a condenser. Reaction temperatures and times are detailed in Tables 1-3. After cooling down to room

temperature, the resulting products were purified by dissolution in water followed by dialysis, centrifugation and drying in an oven at a temperature ≤ 80 ºC.

Nanoporous $Mn_2O_3$ was obtained by thermal decomposition of $MnCO_3$ synthesized in DES. The as-prepared carbonate powder was put into a porcelain crucible, which was introduced into a furnace and thermally treated at 600 ºC during 3 h.

Characterization of the as-prepared powders was done by X-Ray diffraction (XRD) and transmission electron microscopy (TEM).

## 3. Results and discussion

### 3.1. Synthesis of iron oxides: $Fe_3O_4$/γ-$Fe_2O_3$ and α-$Fe_2O_3$

Experiments # 1-3 of Table 1 list the conditions for the reactions employing iron (II) acetylacetonate ($Fe(acac)_2$) precursor. The suitable ratio –let us call it "standard ratio"– DES : $H_2O$ : Fe was experimentally found to be 2 ml : 0.4 ml : 1.6 mmol for the reaction carried out at 135 ºC; therefore such parameters were kept constant while varying the reaction time from 1 to 70 h (# 1-3). XRD patterns of the three products (Figure 1) are monophasic and are compatible with two iron oxides with spinel structure and ferromagnetic behaviour: magnetite ($Fe_3O_4$) (JCPDS 01-075-1609) and maghemite (γ-$Fe_2O_3$) (JCPDS 01-089-5892). Maghemite is the Fe(II)-deficient magnetite and distinguishing both XRD patterns is not obvious and remains a task of further work. Scherrer size calculated from XRD data is approximately similar (19, 15 and 17 nm) within experimental error for samples # 1-3. Complementary TEM characterization (Figure 2) reveals similar features for the three samples: NPs of size ~15 nm randomly grouped. The TEM images also seem to suggest that the clusters of NPs might possess porosity and high superficial area. Overall, $Fe(acac)_2$ is a suitable precursor for the synthesis of pure magnetite or maghemite NPs which nucleate in early stages of the reaction (1 h) and are stable within the reaction media for longer times (70 h).

**Table 1.** Detailed reaction conditions for the synthesis in urea/choline chloride DES employing iron (II) acetylacetonate and iron pentacarbonyl precursors. XRD results are included.

| # | Precursor | Ratio DES : $H_2O$ : Fe (ml : ml : mmol) | T (ºC) | t (h) | XRD result (Scherrer size, nm) |
|---|---|---|---|---|---|
| 1 | $Fe(acac)_2$ | 2 : 0.4 : 1.6 | 135 | 1 | $Fe_3O_4$ or $\gamma$-$Fe_2O_3$ (19) |
| 2 | | | | 14 | " (15) |
| 3 | | | | 70 | " (17) |
| 4 | $Fe(CO)_5$ | 2 : 0.4 : 1.6 | 105 | 1.5 | Non crystalline |
| 5 | | | 185 | 1.5 | $Fe_3O_4$ or $\gamma$-$Fe_2O_3$ (15) |
| 6 | | 2 : 1.0 : 1.6 | 135 | 1 | $Fe_3O_4$ or $\gamma$-$Fe_2O_3$ (low crystallinity) + indeterminate compound |
| 7 | | 2 : 0.2 : 0.1 | 135 | 21 | $\alpha$-$Fe_2O_3$ (15) |

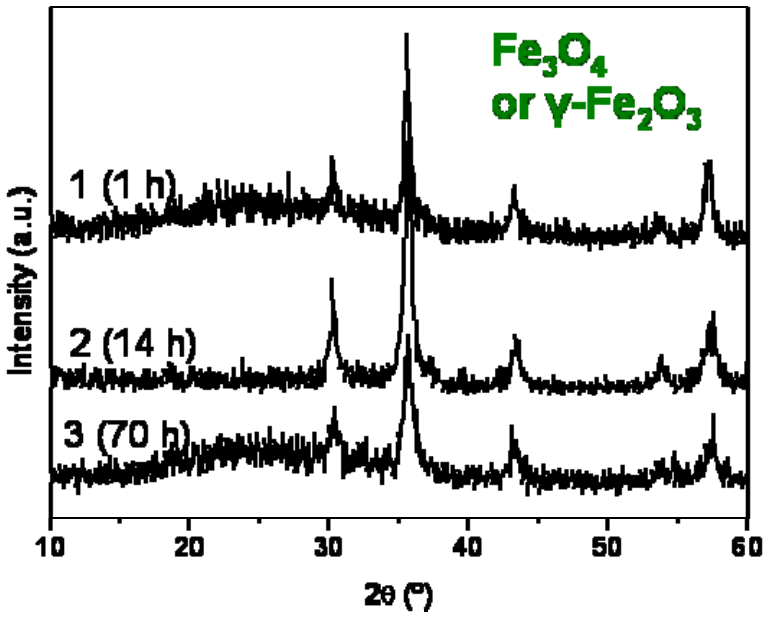


**Figure 1.** XRD patterns of samples # 1-3 of Table 1. All of them are compatible with $Fe_3O_4$ (magnetite) and $\gamma$-$Fe_2O_3$ (maghemite) iron oxides.

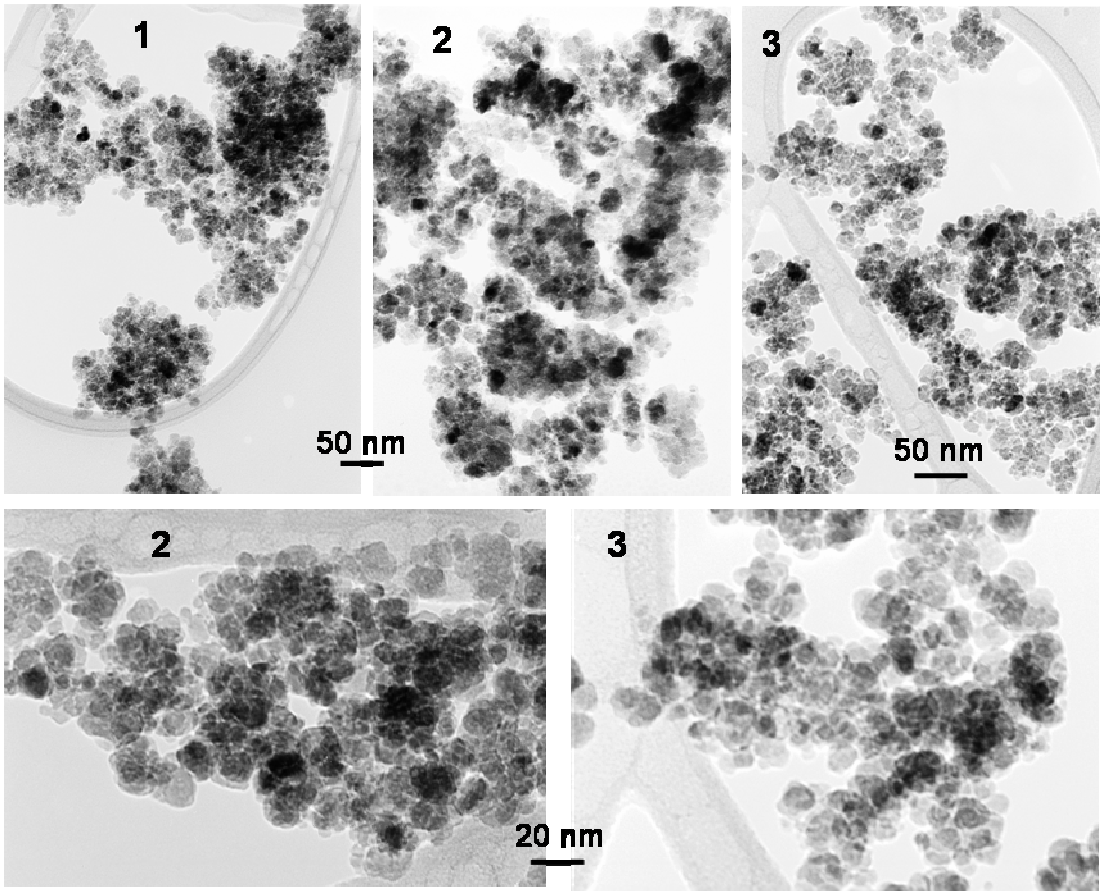


**Figure 2.** TEM images of samples # 1-3 of Table 1.

The next set of experiments (# 4-7) listed in Table 1 were carried out using iron pentacarbonyl as iron precursor. Reactions performed with the "standard" DES : $H_2O$ : Fe ratio showed that a temperature of 105 ºC (# 4) was not high enough for producing the crystallization of any product, whereas the reaction performed at 185 ºC (# 5) yielded magnetite or maghemite with Scherrer particle size of 15 nm (Figure 3), which is in good accordance with ~18 nm-sized NPs measured in the corresponding TEM images (Figure 4, (5)). In order to check the influence of the water content on the as-products, experiment # 6 (Table 1) was conducted with a 2.5 times higher water quantity than the "standard" one and a temperature of 135 ºC during 1 h. XRD characterization (Figure 3) reveals a non-pure product consisting of magnetite or maghemite and compound(s) whose nature remain unclear. Complementary TEM characterization (Figure 4, (6)) reveals the coexistence of NPs (~ 15 nm sized) and elongated crystals and both types of products may correspond to the different phases detected by XRD. These results illustrate the important role of water amount for the formation of the desired product. In this sense, we aimed to explore the suitability of the

route for the preparation of other iron oxides such as α-$Fe_2O_3$ (hematite), which has the same composition than maghemite but a different structure –corundum–. Experiment # 7 (Table 1) was carried out with a lower (half) water content than the "standard" one and (16 times) lower Fe amount, while maintaining the reaction temperature at 135 ºC during 21 h. The as-product is pure hematite (JCPDS 01-089-0596) with a particle size of 15 nm, as detected by XRD characterization (Figure 3), which is in good accordance with the analysis of the corresponding TEM image revealing NPs of sizes ~ 15 nm (Figure 4, (7)).

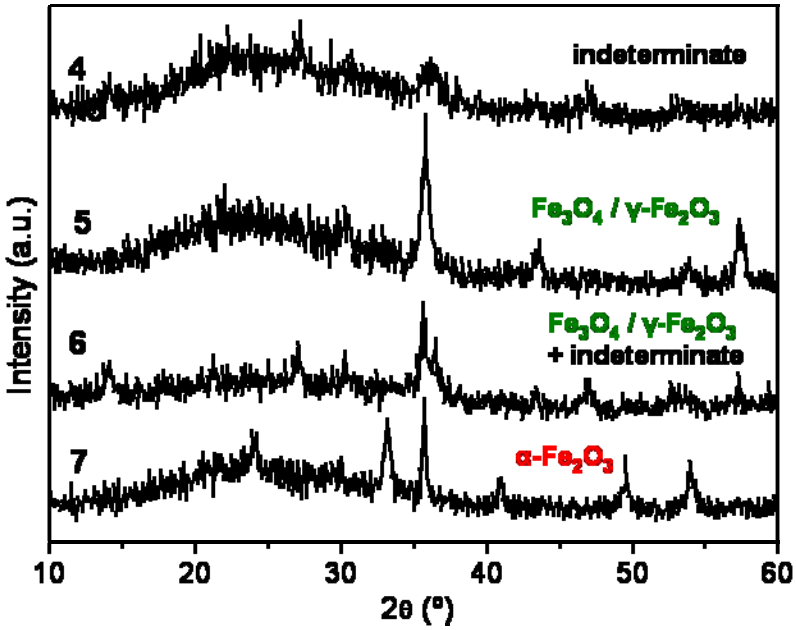


**Figure 3.** XRD patterns of samples # 4-7 of Table 1. The products associated with each pattern are indicated.

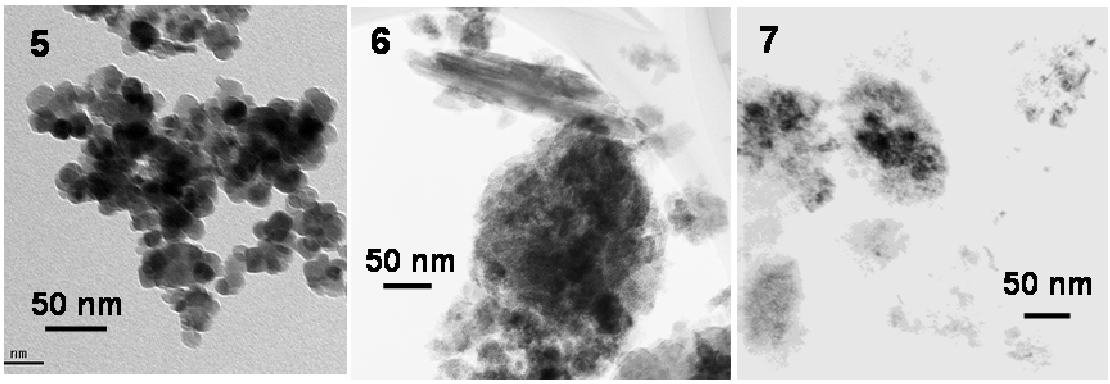


**Figure 4.** TEM images of samples # 5-7 of Table 1.

Table 2 summarizes the experiments performed using other iron precursors which did not lead to the formation of pure iron oxides. Thus, experiments # 8 and 9 were carried out starting from iron acetate ($Fe(ac)_2$) with the "standard" reaction mixture ratios at 135 ºC during 1 and 70 h, respectively. In both cases, mixtures of magnetite/maghemite and hematite were obtained and the ratio of hematite to maghemite increased at longer reaction times. When the same reaction was performed without water, no crystalline product at all was obtained at 3 h of reaction, while hematite phase of very low crystallinity was obtained at 67 h. Last, when the reaction was performed with iron (III) acetylacetonate ($Fe(acac)_3$) with the "standard" reaction mixture ratios at 135 ºC during 1 h, an indeterminate product was obtained.

**Table 2.** Detailed reaction conditions for the synthesis in urea/choline chloride DES using iron (II) acetate and iron (III) acetylacetonate as iron precursors. XRD results are included.

| # | Precursor | Ratio DES : $H_2O$ : Fe (ml : ml : mmol) | T (ºC) | t (h) | XRD result (Scherrer size, nm) |
|---|---|---|---|---|---|
| 8 | $Fe(ac)_2$ | 2 : 0.4 : 1.6 | 135 | 1 | $Fe_3O_4$ or $\gamma$-$Fe_2O_3$ + $\alpha$-$Fe_2O_3$ |
| 9 | | | | 70 | $\alpha$-$Fe_2O_3$ + $Fe_3O_4$ or $\gamma$-$Fe_2O_3$ |
| 10 | $Fe(ac)_2$ | 2 : 0.0 : 1.6 | 130 | 3 | Non crystallline |
| 11 | | | 140 | 67 | $\alpha$-$Fe_2O_3$ (low intensity) |
| 12 | $Fe(acac)_3$ | 2 : 0.4 : 1.6 | 135 | 1 | indeterminate |

### 3.2. Synthesis of manganese oxides: $Mn_3O_4$ and $Mn_2O_3$

Table 3 collects the experiments involving manganese precursors. In all of them but in the last one, the "standard" ratios for the reaction mixture and temperatures of 135 ºC were employed. First, manganese acetylacetonate ($Mn(acac)_3$) was used as the precursor and reactions during 1 and 17 h (experiments # 1 and 2) were carried out. Corresponding XRD patterns are identical in both cases: they show $MnCO_3$ products (rhodochrosite, JCPDS 01-085-1109) with Scherrer particle sizes of 29 nm (Figure 5 (a)). TEM characterization (Figure 6 (a)) also reveals the same features for the two $MnCO_3$ products obtained at different reaction times: a continuous solid without a particular size or shape which is finely divided, presenting voids of size ~1-2 nm.

**Table 3.** Detailed reaction conditions for the synthesis in urea/choline chloride employing manganese precursors. XRD results are included.

| # | **Precursor** | **Ratio DES : $H_2O$ : Mn (ml : ml : mmol)** | **T (ºC)** | **t (h)** | **XRD result (Scherrer size, nm)** |
|---|---|---|---|---|---|
| 1 | $Mn(acac)_3$ | 2 : 0.4 : 1.6 | 135 | 1 | $MnCO_3$ (29) |
| 2 | | | | 17 | $MnCO_3$ (29) |
| Product # 2 treated at 600 ºC, 3 h | | | | | **$Mn_2O_3$** (25) |
| 3 | $KMnO_4$ | 2 : 0.4 : 1.6 | 135 | 1 | **$Mn_3O_4$** (18) |
| 4 | | | | 3 | **$Mn_3O_4$** (18) |
| 5 | $KMnO_4$ + CTAB (0.15 mmol) | 2 : 0.4 : 0.1 | 135 | 1 | **$Mn_3O_4$** (29) |

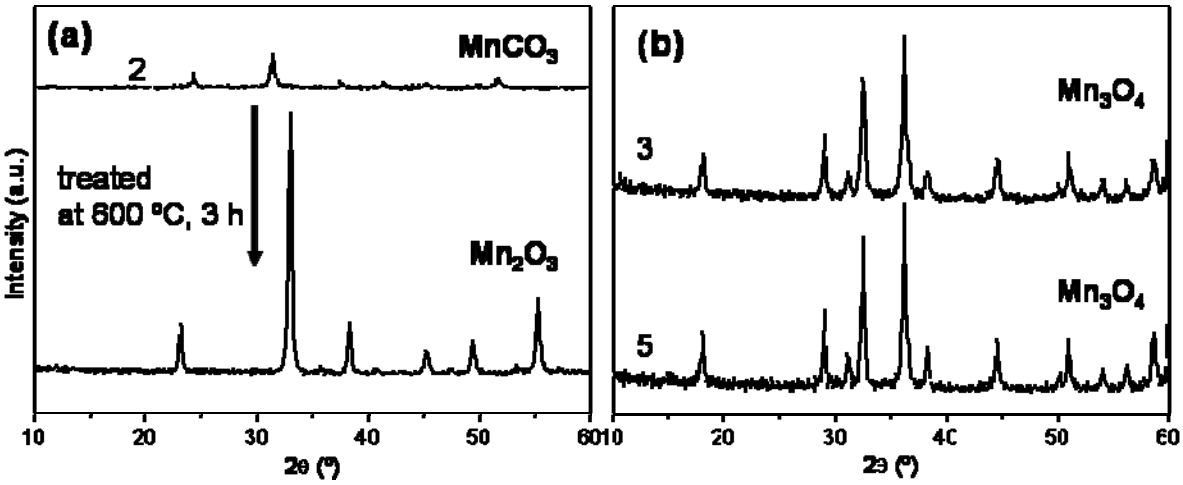


**Figure 5.** XRD patterns of (a) samples # 2 and "#2 treated at 600 ºC, 3 h", and (b) samples # 3 and 5 of Table 3. The product associated with each pattern is indicated.

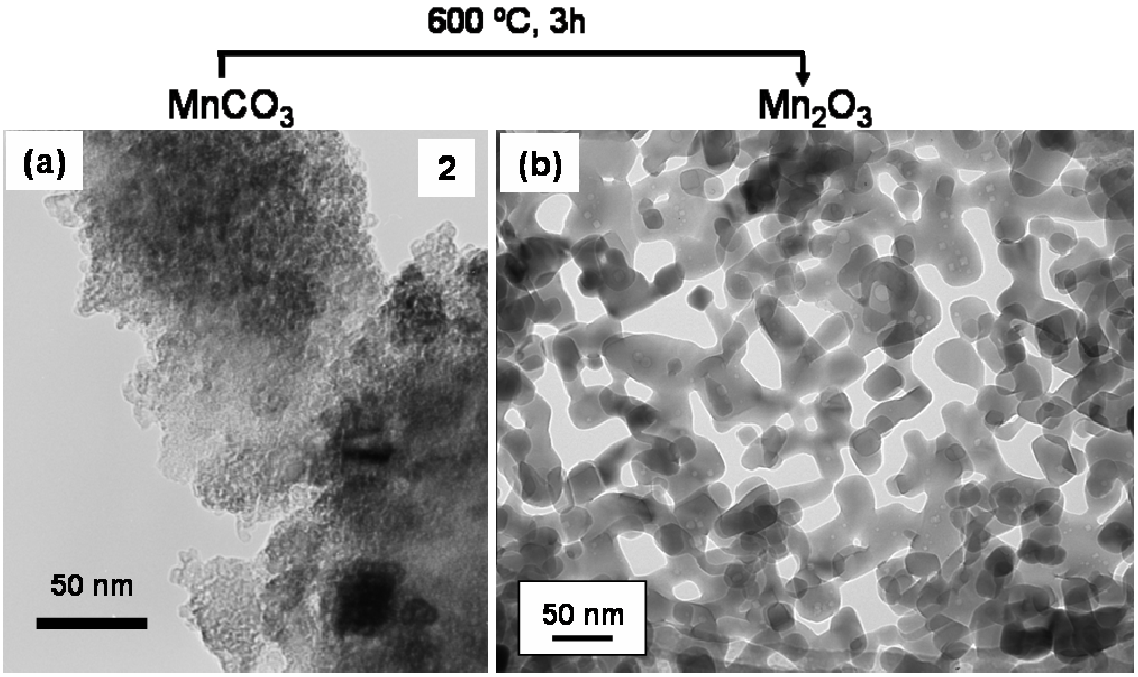


**Figure 6.** TEM images of (a) sample # 2 of Table 3, corresponding to a $MnCO_3$ phase, and (b) the $Mn_2O_3$ phase obtained after thermal treatment at 600 ºC during 3 h of sample # 2.

Interestingly, it is known that $MnCO_3$ decomposes between 350 and 540 ºC yielding nanoporous $Mn_2O_3$ as a result of gas ($CO_2$) release.[10] Therefore, we used the $MnCO_3$ obtained in experiment # 2 as a precursor for the formation of nanostructured $Mn_2O_3$. Thermal treatment was performed at 600 ºC during 3 h. XRD characterization of the product (Figure 5 (a)) confirms the formation of pure $Mn_2O_3$ (bixbyite, JCPDS 01-071-0636), whereas TEM imaging (Figure 6 (b)) verifies its nanostructured morphology, consisting of a continuous net of NPs (~ 10-60 nm) enclosing nanopores (10-60 nm).

The following manganese precursor tested was manganese permanganate and the reaction was performed at 1 and 3 h (experiments # 3 and 4, Table 3). In both cases, pure $Mn_3O_4$ (hausmannite, JCPDS 01-080-0382) was obtained, as detected by XRD (Figure 5 (b)). TEM analysis (Figure 7 (3)) reveals NPs of size ~ 60 nm with a rough surface and inhomogeneous contrasts as well as smaller NPs *ca.* 8 nm. It is suggested that the larger NPs consist of aggregated smaller ones, although further analysis by high resolution TEM (HRTEM) would be required to confirm the microstructure.

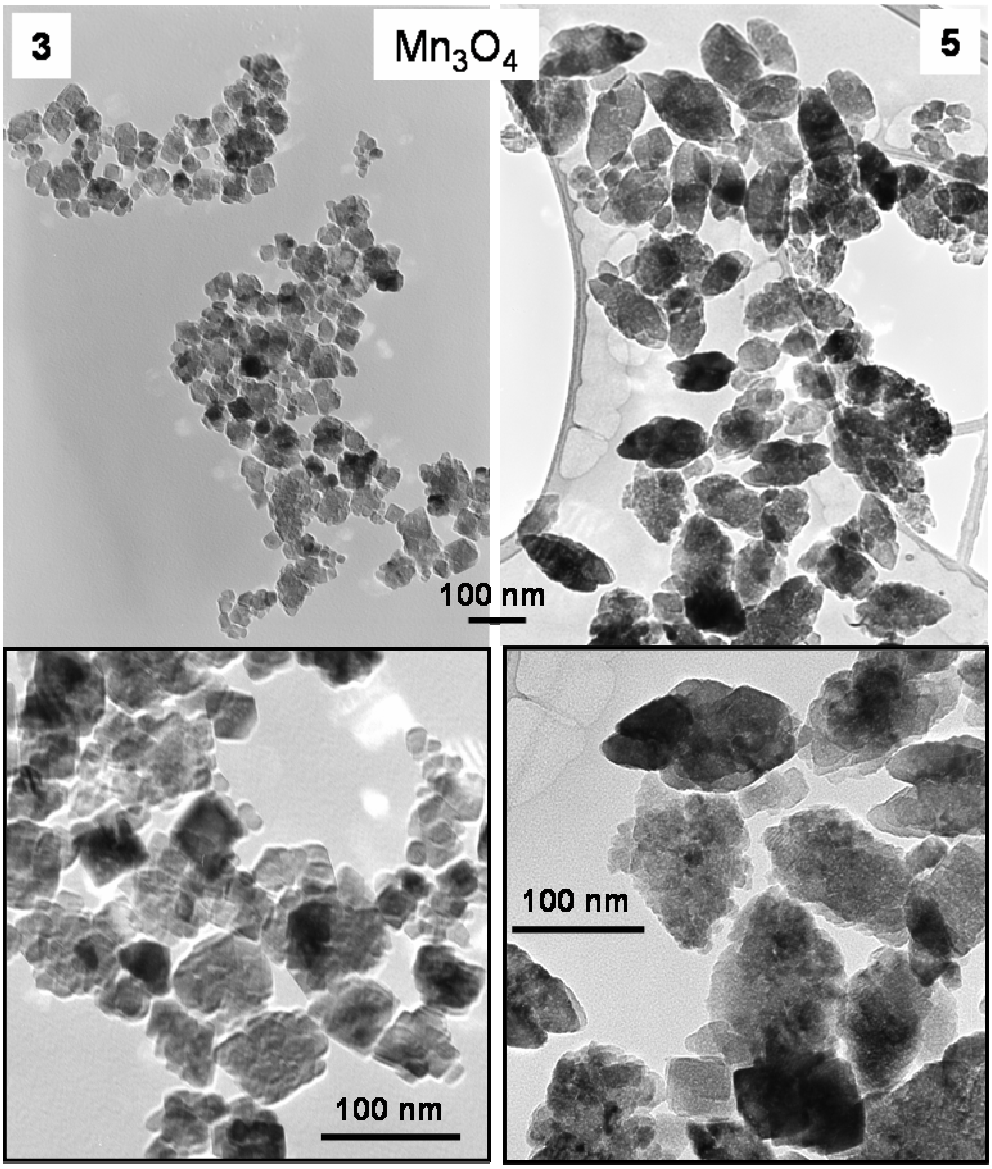


**Figure 7.** TEM images of samples # 3-5 of Table 3. Second row shows greater magnification of the images displayed in the first row.

Finally, experiment # 5 (Table 3) includes the addition of the cationic surfactant CTAB to the DES : $H_2O$ : Mn reaction mixture in the ratio 2 : 0.4 : 0.1. Given that the quantity of CTAB to be used is limited by its low solubility in the reaction media, small CTAB amounts (*e.g.* 0.15 mmol) were used and, in consonance, the manganese precursor amount was decreased as compared to previous experiments. Thus, as there is a lack of a couple of reactions with and without CTAB under equal quantities of the reaction mixture, the influence of the surfactant in the as-prepared NPs cannot be extracted for the moment. However, the experiment serves to test the compatibility of the synthetic route with the use of surfactants. The XRD pattern (Figure 5 (b), (5)) of the as-prepared product corresponds to $Mn_3O_4$ (Scherrer particle size of 29 nm),

similarly to the reactions carried out without CTAB. The shape and size of the NPs was evaluated by means of TEM (Figure 7, (5)) , which reveals that, in general, the NPs have a rice-like morphology and a diameter of ~ 140 nm. In addition, they present a peculiar very rough texture; it seems that they consist of smaller NPs. In this sense, a self-organization mechanism might be involved in the oriented aggregation of the smaller NPs into the rice-like particles. Although further work is needed to i) check the hypothesis of NP's self-organization and ii) study the influence of the surfactants on the resulting NPs, it has been demonstrated that the size and shape of the NPs can be controlled by means of the reaction conditions, including the use of surfactants.

## 4. Conclusions

It has been demonstrated that the urea/choline chloride DES synthesis is a general pathway for the preparation of a number of binary oxides. In the case of iron oxides, both magnetite ($Fe_3O_4$)/maghemite ($\gamma$-$Fe_2O_3$) and hematite ($\alpha$-$Fe_2O_3$) NPs (~ 15 nm) could be obtained as a function of the reaction conditions. In regard to manganese oxides, $Mn_3O_4$ NPs (~ 8-60 nm) could be directly obtained, while the preparation of nanoporous $Mn_2O_3$ (~ 10-60 nm) required the thermal decomposition of $MnCO_3$ prepared through the urea/choline chloride route. In addition, it has been shown that the route is compatible with the presence of surfactants, which serve as a further tool to have control over the features of the as-prepared NPs. Specifically, CTAB might play the role of guiding the self-assembly of $Mn_3O_4$ NPs of ~ 8 nm into rice-like NPs of ~ 140 nm. Further work is needed to better characterize the products as well as to gain understanding of the role of the different experimental variables on the features of the resulting nanomaterials.

## References:

1. Abbott, A. P.; Capper, G.; Davies, D. L.; Rasheed, R. K.; Tambyrajah, V., Novel solvent properties of choline chloride/urea mixtures. *Chemical Communications* **2003,** 9, (1), 70-71.
2. Morris, R. E., Ionothermal synthesis - Ionic liquids as functional solvents in the preparation of crystalline materials. *Chemical Communications* **2009**, (21), 2990-2998.
3. Cooper, E. R.; Andrews, C. D.; Wheatley, P. S.; Webb, P. B.; Wormald, P.; Morris, R. E., Ionic liquids and eutectic mixtures as solvent and template in synthesis of zeolite analogues. *Nature* **2004,** 430, (7003), 1012-1016.
4. Parnham, E. R.; Drylie, E. A.; Wheatley, P. S.; Slawin, A. M. Z.; Morris, R. E., Ionothermal materials synthesis using unstable deep-eutectic solvents as template-delivery agents. *Angewandte Chemie - International Edition* **2006,** 45, (30), 4962-4966.

5. Drylie, E. A.; Wragg, D. S.; Parnham, E. R.; Wheatley, P. S.; Slawin, A. M. Z.; Warren, J. E.; Morris, R. E., Ionothermal synthesis of unusual choline-templated cobalt aluminophosphates. *Angewandte Chemie - International Edition* **2007,** 46, (41), 7839-7843.
6. Zhang, J.; Wu, T.; Chen, S.; Feng, P.; Bu, X., Versatile structure-directing roles of deep-eutectic solvents and their implication in the generation of porosity and open metal sites for gas storage. *Angewandte Chemie - International Edition* **2009,** 48, (19), 3486-3490.
7. *Chapter 3.1 of the present thesis*.
8. Guloy, A. M.; Ramlau, R.; Tang, Z.; Schnelle, W.; Baitinger, M.; Grin, Y., A guest-free germanium clathrate. *Nature* **2006,** 443, (7109), 320-323.
9. Liao, H. G.; Jiang, Y. X.; Zhou, Z. Y.; Chen, S. P.; Sun, S. G., Shape-controlled synthesis of gold nanoparticles in deep eutectic solvents for studies of structure-functionality relationships in electrocatalysis. *Angewandte Chemie - International Edition* **2008,** 47, (47), 9100-9103.
10. Yang, L. X.; Zhu, Y. J.; Tong, H.; Wang, W. W., Submicrocubes and highly oriented assemblies of $MnCO_3$ synthesized by ultrasound agitation method and their thermal transformation to nanoporous $Mn_2O_3$. *Ultrasonics Sonochemistry* **2007,** 14, (2), 259-265.

# GENERAL DISCUSSION

# GENERAL DISCUSSION

## Hydrothermal Synthesis of $BaMnO_3$ Nanoparticles

In the hydrothermal synthesis of $BaMnO_3$ NPs, a couple of parameters have been shown to exert the main influence in the shape and size of the $BaMnO_3$ crystals. Anisotropic and isotropic shapes are determined by the reactor filling volume (70% and 48-53%, respectively), whereas a high KOH concentration is crucial for the stabilization of NPs.

The achievement of $BaMnO_3$ NPs (~20 nm) under ultra-high KOH concentrations (20 M) can be interpreted on the basis of the concept of "burst nucleation" proposed by LaMer and Dinegar in 1951,[1] whose basic principles are currently adopted for the theoretical description of the synthesis of uniform colloidal particles. Basically, a burst homogeneous nucleation can lead to the separation of nucleation and growth events and the subsequent equal growth histories for the NPs is the key to attain narrow size distributions.

The LaMer-Dinegar plot (Figure 1) illustrates that in order to induce a homogeneous nucleation, a high energy barrier must be surpassed because the system changes from the homogeneous phase to the heterogeneous phase, which is both thermodynamically and entropically disfavoured. Thus, in stage I the concentration of "monomer", which is the minimum subunit of bulk crystal, constantly increases with time and precipitation does not occur even under supersaturated conditions (S>1), because the energy barrier for spontaneous homogeneous nucleation is extremely high. In stage II, nucleation occurs because the degree of supersaturation is high enough. Since the rate of monomer consumption resulting from the nucleation exceeds the rate of monomer

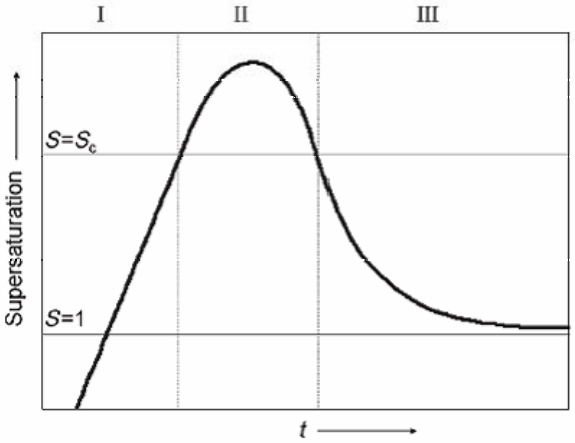


**Figure 1.** LaMer-Dinegar plot: Change of degree of supersaturation as a function of time. Reproduction of ref. 2.

supply, the monomer concentration decreases until it reaches the level at which nucleation does not occur. From this point (stage III) only growth (by means of heterogeneous nucleation) of the particles takes place as long as the solution is supersaturated.

In our hydrothermal system, the high KOH concentration may contribute to the high supersaturation conditions needed for a burst nucleation. Thus, the solid-liquid initial mixture (note that a KOH concentration of 20 M prevents the alkali solid from a complete dissolution) would become a very concentrated, viscous liquid upon heating and the subsequent activation energy and decreased solubility of the target material would result in a homogeneous nucleation. Besides, the rapid heating process (note that the autoclave is introduced into the preheated oven) should further contribute to minimize thermal gradients within the system and, eventually, to achieve a burst nucleation in which many equally-sized nuclei are simultaneously formed. In turn, such event should lead to a decrease of the "monomer" (ions, molecular precursors…) concentration, which would stops further nucleation while maintaining the supersaturation regime necessary for the growth (or heterogeneous nucleation) of the pre-formed nuclei.

It is worth mentioning that the role of KOH in the nucleation stage might not only be related to the achievement of a high supersaturation condition, but it also may be involved as a chemical reagent providing the target oxide with the oxygen atoms. This way, metallic hydroxides molecules and extended sol-gel compounds build up through condensation reactions might be initially formed. This kind of sol-gel compound would be the "monomer", whose high concentration eventually leads to a homogeneous nucleation within a viscous medium.

The second stage of the reaction is the growth and the earlier growth mechanism is the ion-to-ion or "monomer" attachment to the pre-formed crystalline nuclei. During such a process, the size distribution is narrowed regardless of the initial size distribution of the nuclei.[2] This is due to the fact that smaller particles growth faster than larger ones because the latter demand a larger amount of monomers to create a new layer. In other words, as the number of monomers diffused onto the surface of a particle increases in proportion to the square of its radius, whereas the volume increases in proportion to the

third power of its radius, the growth rate of a particle is decreased as the radius increases. This diffusion-controlled growth self-regulates the size distribution during the first growth stages as long as no additional nucleation occurs. It is called the "focusing" effect.

In our case, it is expected that a "focusing" effect contributes to decrease the size distribution of the particles initially nucleated in a vessel where thermal gradients may exist at short times. Besides, the walls of the Teflon vessel may facilitate the heterogeneous nucleation of crystals, further contributing to the heterogeneity of the initial nuclei, whose size distribution would be narrowed by the "focusing" effect.

However, a "defocusing" effect of the particle size distribution competes with the "focusing" effect.[2, 3] The "defocusing" effect or Ostwald ripening growth[4] involves that smaller particles are harder to growth because they are more easily dissolved due to their higher chemical potential. Thus, smaller particles under a critical radius dissolve and larger particles grow by receiving the monomers from the former. This is a reaction-controlled growth which is thought to operate when the supersaturation is low, *i.e.* at later stages of reaction, and that broadens the particle size distribution.

If Ostwald ripening growth was taking place under our hydrothermal reaction, shorter times should minimize it. Although a careful statistical study would be required to ascertain solid conclusions, an inspection to our results (see experiments # 13 and 14 of Table 1, Chapter 1.1) seems to suggest that average TEM-based particle size is slightly smaller at 4 h (6-37 nm, average is 18.0 nm) as compared to 24 h of reaction (12-41 nm, average is 25.6 nm), indicating that some Ostwald ripening occurs between 4 and 24 h of reaction, although the small size change shows that NPs are already quite stabilized at 4 h of reaction.

Actually, the fact that no significant NP evolution takes place up to 24 h indicates that the reaction medium is quite suitable for the stabilization of the as-prepared NPs, which are prevented from two additional growth mechanisms: aggregation followed by sintering and SA. In this sense, the key aspect hampering such growth mechanism could be the high ionic strength of the medium rich in KOH. Anions and/or cations of the alkali mineralizer may adsorb to the surface of the NPs, accounting thus for the

electrostatic repulsion among them. Otherwise, NPs would either aggregate or self-assemble pulled by Van der Waal forces, universal attractive forces of electrical origin, to gain both thermodynamics (replacing unstable solid-liquid interfaces by stable solid-solid ones) and entropy (desorbing molecules of solvent from the surface).

Therefore, experimentally we found the hydrothermal conditions for the formation and stabilization of NPs, for stopping their long-range attraction through a short-range repulsion. Such conditions, mainly medium reactor filling volumes (48-53 %) and high KOH concentrations (14-20 M), translate into a compendium of the physico-chemical parameters of water ultimately responsible for the isolation of NPs. In this sense, as it is known that the density, viscosity, dielectric constant, ionic product, etc. of water dramatically change under hydrothermal conditions, where water is heated above its boiling point thanks to the autogeneous pressure, it is expected that a different pysico-chemical system can be created through variations of the temperature and pressure of water, this is, through different reactor filling volumes. Thus, we experimentally found that high (70 %) reactor filling volumes lead to the SA of NPs into NRs due to their lower electrostatic stabilization. Although the accurate conditions for the isolation of homogeneous NRs were not found, this encounter sets the preliminary steps for the control over the SA and shape of hydrothermally prepared $BaMnO_3$ NPs and NRs.

Interestingly, mesocrystals were detected as intermediate structures between unoriented NPs and single crystals. Within the mesocrystal, the NPs are mutually oriented but not perfectly fused, due to the balance between long-range attractive and short-range repulsive forces, according to the Deryagin-Landau-Verwey-Overbeek (DLVO) theory.[5, 6] The highly concentrated and viscous reaction medium may slow down the diffusion of building units toward the growing surface. Furthermore, the layer of viscous solvent in between NPs within an ensemble may be hardly stripped off, preventing NPs from fusing together while allowing their rotation and orientation into the same crystallographic direction. Actually, many mesocrystals formation, including mesocrystals in biomineralization, takes place in viscous media such as gels, polymers, etc.[7], which suggests that such a characteristic may be a requisite for the detection of metastable mesocrystals.

A further comment regarding the synthesis of $BaMnO_3$ NPs is related to the issues of purity of products and segregation of two distinct metallic oxide phases. Although the carbonate formation in alkali medium is a persistent problem, we experimentally found that a mere variation of the protocol for mixing the precursors is responsible for the formation or not of $BaCO_3$ together with $BaMnO_3$ (results not shown).

Overall, both the hydrothermal conditions and the high KOH concentration play a leading role in altering the physico-chemical parameters of water. Figures are illustrative of the dramatic effect of hydrothermal conditions on the water characteristics.[8] For instance, at 150-200 kbar and 1000 ºC its density is 1.7-1.9 $g \cdot cm^{-3}$ (nearly double than at standard conditions) and it is completely dissociated into $H_3O^+$ and $OH^-$, behaving like a molten salt, isoelectronic with $NH_4F$ or NaOH.[9] Hence, there is a close scenario between hydrothermal and molten salt situations. Although our experimental conditions are far from those temperature and pressure conditions, the mentioned example clearly illustrates a tendency towards a "molten-salt behaviour" – *i.e.* towards an ionic solvent rather than a molecular one– of water under hydrothermal conditions. If such an extreme scenario is further carried towards a more ionic solvent through the addition of high quantities of KOH mineralizer, our hydrothermal system certainly should keep a strong resemblance to that of a molten salt medium where no "free" water clusteres exist. This observation encouraged us to explore the $BaMnO_3$ synthesis in the limit of the alkali-assisted hydrothermal synthesis: *i.e.* using an alkali molten medium.

**Hydroxides Eutectic Route for the Synthesis of Nanooxides**

In the search of a suitable alkali molten medium, we found that an optimum one could be a mixture of NaOH and KOH in its eutectic composition, whose melting temperature (165 ºC) is much lower than those of the separate components (323 and 360 ºC, respectively). Both the high ionic strength and the mild reaction temperature are fulfilled requisites for the synthesis of NPs, which indeed had been previously reported.[10, 11] In spite of the fact that we did not succeed in reproducing the results reported by Hu *et al.* because of the formation of the $BaCO_3$ impurity together with the

target $BaMnO_3$, even when performing the reaction under a nitrogen atmosphere to avoid fixing of atmospheric $CO_2$ as $CO_3^{2-}$, a comparison between this method and the alkali-assisted hydrothermal method is worth. First, note that the as-obtained rods in the eutectic molten method do not seem to have the same appearance in all the experiments: for the reaction performed under air for 98 h (sample # 2, Figure 4, chapter 1.2), compact rods with a smooth surface are obtained, while when a nitrogen atmosphere is used during 72 h of reaction (sample # 5, Figure 6, chapter 1.2), the rods seem to be constituted by spherical NPs, revealing a SA formation mechanism.[12] The detection of a SA property matches with the high-reactor-filling-volume-alkali-assisted hydrothermal synthesis, which yields NRs constructed through the SA of elongated NPs. Thus, both synthetic media –hydrothermal and molten hydroxides– lead to precipitation of NPs in a first stage of burst nucleation and "monomer-nuclei" growth, followed by prompting their SA into anisotropic mesocrystals. This indicates the shared features of both solvents, among which polarity and viscosity may be determinant factors. Actually, revisions of the literature suggest that the lubricant properties of viscous media with polarity contrasts (amphiphilicity) should, first, be responsible for the strong interaction between the fluid and the NP's surface and, second, allow the NPs within an ensemble to mutually orientate while hampering them from fusing.[7, 13] An encouraging example is the formation of anisotropic mesocrystals quite similar to our images obtained by the hydrolysis of Ce (IV) salts into viscous sulphuric acid solutions.[14] In our case, given the clearer detection of mesocrystals through the hydrothermal conditions as compared to molten hydroxides method, the former route would possess better lubricant properties stemming from the higher polarity contrasts in the mixed molecular/ionic system.

The extension of the route for the preparation of NiO showed that, in this case, NPs were also stabilized, although the determination of the existence or not of the SA phenomenon would require further characterization. For this material, whose bulk has the rock-salt crystalline structure, the most relevant feature is the control over octahedral shapes, whose formation probably is intimately related to the high ionic character of the medium, which would allow the preferential growth of non-polar crystal phases, as already discussed.

In conclusion, the hydroxides deep eutectic molten medium is suitable for the dissolution of precursors[15] and crystallization of binary (NiO) and ternary ($BaMnO_3$)

nanooxides, although in the case of manganites, formation of contaminant $BaCO_3$ could not be avoided. An appealing control over the shape and SA features of the as-prepared NPs is disclosed for this method of synthesis. A remarkable feature of the as-prepared NPs is their ligand-free surface.

As compared to previously reported synthetic routes based on melted salts, such as carbonates,[16] NaCl[17] or eutectic mixtures of nitrates, which only lead to the formation of NPs if suitable ligands are used,[18-20] the hydroxides eutectic medium does not require the use of stabilizers to protect the NPs from aggregation. Among the causes for this dual self-stabilizing and solvent characters, not only the high ionic content must play a role because this feature is similar to other salts, but also the low melting temperature (and, thus, low reaction temperature) –165 ºC–, much inferior to those of NaCl –820 ºC– or eutectic mixtures of nitrates –550 ºC–, must play a leading role in the formation of non-aggregated NPs. Therefore, both requirements –high ionic character and low melting temperature– must be fulfilled by molten salts synthetic media in order to prepare ligand-free NPs. Furthermore, high viscosities and polarity contrasts of the fluids might be related to the stabilization of mesocrystals.

**Urea-melt Assisted Route for the Synthesis of Nanooxides**

On the track of new melted media for the synthesis of NCs, urea was selected as a potential candidate according to its shared attributes with the media mentioned above: i) alkaline character in the presence of water,[21] ii) low melting temperature (133 ºC) and iii) as an organic melted fluid, high viscosity and lubricant properties were expected. However, neither the precipitation of the nickel, cobalt, iron and manganese oxides nor the formation of their respective metallic compounds was realized up to 16 h of thermal treatment at 150 ºC, but instead the precursor metallic cations were stabilized within the respective colourful fluids undergoing oligomerization. The low reactivity of the metallic cations is attributed to the lack of ionic character of the medium and attempts to improve it by introducing KOH, NaOH or KOH/NaOH eutectic mixture in the reaction system failed in the precipitation of the oxides (results not shown). On the other hand,

the inert melted fluid as regards its redox activity, did not yield either the reduction of the transition metals.

In spite of the lack of suitability of melted urea to precipitate NPs, the resulting system was found to be advantageous for calcination routes.[22] This way, the metallic cation-oligomer formed upon the first step of thermal treatment at 150 ºC can be combusted at 400 ºC, yielding the corresponding metallic oxides. Interestingly, the case of nickel (chapter 2.1) evidences reduction and oxidation steps for the formation of the NPs: a reduction of the metallic cations paralleled to the oxidation of the organic matrix[23] yielding loosely-aggregated metallic NPs, is followed by the outer oxidation of the matrix-(almost)-free NPs under the air atmosphere within the furnace. Thus, for the cations relatively difficult to be reduced and easily oxidized, such as those corresponding to iron, cobalt and manganese, either a complete preliminar reduction does not take place and/or the second step of oxidation from the surface penetrates until the very core of the NCs, yielding the oxide monophase (α-$Fe_2O_3$ and γ-$Fe_2O_3$, $Co_3O_4$, $Mn_3O_4$ and $Mn_2O_3$) (chapter 2.2). However, as it is widely known, metallic nickel is more difficult to oxidize,[24, 25] so the self-combustion of the organics prompts the formation of $Ni^0$ NPs, whose progressive oxidation from the surface inwards can be quenched, depicting a $Ni_{core}NiO_{shell}$ microstructure of the NPs. The thickness of the passivating layer can be controlled by means of the oxidation time after removal of the organic matrix and this translates in a two-fold manipulation through the urea amount and calcination time.

Assets associated to this route as compared to other organic matrix calcination pathways[26-30] are its simplicity as well as the improved size distribution and lower aggregation of the as-prepared NPs. While the quenching nature of the synthetic method has allowed the achievement of a NiO nanostructured material with a degree of interesting imperfection manifested both as structural disorder and tiny Ni nuclei, liquid routes are desirable for the size-, shape- and SA-controlled mild preparation of nanomaterials. In this sense, we aimed to improve the synthetic capability of melted urea keeping two hints in mind: i) high ionic character and ii) mild melting temperature.

## Urea/Choline Chloride DES Route for the Synthesis of NCs

In the framework of eutectic molten salts and melted urea medium, a logic hybrid is a mixture of a salt and urea to enhance the ionic character of the latter. Indeed, mixtures of choline chloride ((2-Hydroxyethyl)trimethylammonium chloride, $T_m$ = 302 ºC) and urea ($H_2NCONH_2$, $T_m$ = 133 ºC) have been reported to exhibit a deep eutectic ($T_m$ = 12 ºC) as well as exceptional solvent properties.[31]

The strong depression of the freezing point of urea/choline chloride, in particular, or "hydrogen bond donors/ammonium quaternary salts", in general, relative to the individual components stems from the charge delocalization between the hydrogen atoms of the donor and the anion of the salt through hydrogen bonding,[31] as well as to the large size and conformational flexibility of the ions involved.[32] The resulting DESs have the typical properties of ILs: high polarity, high ionic conductivity, low vapour pressure, low interface tensions, high degree of supramolecular organization, high viscosity, etc.,[33-36] with the advantage of being easily prepared at low cost. In addition, while most of the ILs have a very wide liquidus range owing to the combination of thermal stability and non-volatility, urea/choline chloride DES is thermally unstable,[37] which can be an advantageous feature for the cation-templating of the as-prepared structures[38] and for the self-evolving polarity of the medium, eventually influencing the NPs' SA fashion (chapter 3.1). Given the optimized properties of classical ILs for the synthesis of inorganic NPs,[35, 37] we considered highly desirable to explore the synthetic capability of DESs.

The successful preparation of PbS NPs (chapter 3.1) and nanooxides ($Fe_3O_4$/γ-$Fe_2O_3$, α-$Fe_2O_3$, $Mn_3O_4$) (chapter 3.2) in urea/choline chloride reported herein further reinforces the similarities between ILs and DESs. Analogously to previously reported mesoporous nanooxides prepared in ILs,[39, 40] the DES-obtained nanooxides seem to shelter porosity: γ-$Fe_2O_3$ NPs group together (~15 nm) with non-defined shapes and $Mn_3O_4$ NPs cluster together into rice-grain-like morphologies of diameters ~140 nm, pointing out towards a possible cooperative behaviour of the NPs. Porous $MnCO_3$ was also obtained and it has shown to be a suitable precursor for the formation of nanostructured $Mn_2O_3$ (~10-60 nm) through thermal treatment at 600 ºC. The case of

PbS synthesis in DES is especially interesting. The DM-driven hierarchical self-organization of PbS NPs into star-like structures with both nano and microlevels of hierarchy is an important step for both practical technologies and fundamental understanding of diverse SA patterns. Particularly, the instability of the ensembles upon DES decomposition leading to deconstruction opens some preliminary steps towards the dynamic behaviour of mesocrystals.

## Ionic Fluids: Connections Between Alkaline Hydrothermal Route, Eutectic Molten Hydroxides, DESs and ILs

At this point it is worth to analyse the similarities of the distinct reaction media designed in this thesis. Except for the melted urea fluid (chapter 2), which did not yield the precipitation of any crystal, the rest of the solvents are low temperature liquid salts and, thus, they contain predominantly ions. That is the key for their multifold role, comprising solvent, reactant and stabilizer abilities.

Actually, there is a substantial difference between ionic solutions and low temperature ionic fluids –including both inorganic and organic molten salts–, even considering that small amounts of water are normally required in ionic liquids for synthetic purposes. While ionic solutions are essentially molecular solvents, where each of the ions from the salt –such as NaOH– is surrounded by a "sea" of molecules from the solvent –like water–, ionic liquids are basically made of ions, so the isolated units are the water molecules, which strongly interact with the surrounding ions into an organized pattern; hence water does not behave as such and shows a decreased reactivity. The higher water content, the larger would be the molecular clusters up to a situation in which the properties of water emerge.

Traditional liquid routes for the synthesis of NPs[41] make use of molecular liquids such as water or organic solvents, requiring thus the presence of organic ligands to stabilize the NCs. However, ionic fluids offer the advantage of being "all-in-one" systems, simultaneously behaving as solvents and stabilizers (and sometimes reactants) due to their highly organized and charged structure. Regarding the first step of

precipitation of NCs, it is attained through a burst nucleation, which for molecular solvents has been traditionally explained on the basis of high supersaturations, following the LaMer-Dinegar model. Ionic fluids have been also shown to possess optimal properties for burst nucleations.

The ability for the nucleation and stabilization of inorganic NPs exhibited by both inorganic and organic low temperature molten systems employed in this thesis must arise from their shared physico-chemical properties. Aside from their ionic character, the requisite of being fluid at low temperature is crucial, hence traditional inorganic molten salts are not called ILs. However, those inorganic molten salts, such as the NaOH/KOH eutectic mixture, which are fluid under or around ca. 100 ºC, could be included in the modern term "ionic liquids", given their synthetic capability and to the similar characteristics with organic ILs. Such characteristics are the following.[33, 34, 36, 37, 40, 42]

First, the high polarity is the basis for the solvent and reactivity properties. Metallic salts are completely dissociated in the polar liquid and the separation of charges is crucial for the Coulombic-mediated reactivity.

Second, low interface tensions (measured for organic ILs[35, 42]) in combination with high precursors concentrations lead to high nucleation rates, which generates very small particles. Interface tension is the property of a liquid that allows it to resist an external force; therefore low surface tensions translate into "adaptability" to many species. Thus, when a high degree of supersaturation exists, many equally-sized nuclei precipitate creating a high solid-liquid interfacial area. Obviously, the surface energy of the NPs is lowered by the strong surface interacting solvent and that minimizes Ostwald ripening, further contributing to narrow particle size distributions.

Third, solvent self-structuration can lead to the stabilization of NPs as well as to their SA property. The self-structuration is the result of polarity contrasts as well as hydrogen bonding and other types of electrostatic interactions. In turn, this can lead to the extraordinary lubricant properties because the NPs' surface is strongly protected by the part of liquid of similar polarity whereas the dissimilar polarity part is aligned perpendicular to the surface, so the solvated NPs, although attracted by Van der Waal

forces, feel a short-range repulsion which hampers their perfect fusion and allows their re-arrangement into the same crystallographic direction. Thus, the stabilization of mesocrystals is achieved.

Interestingly, one of the main novelties associated to the synthesis of inorganic NPs in ionic liquids in comparison to traditional liquid solvents is the trend towards the three-dimensional (3D) SA behaviour of the NPs, directly related to the self-structuration and lubricant properties. It is worth to comparatively analyse the distinct methods reported in this thesis and elsewhere in regard to the SA phenomenon.

The two extreme schemes are the inorganic salts, such as the NaOH/KOH eutectic mixture, and the organic salts (known as ILs), whose organic component is frequently the cation. Generally, it is attributed a complete dissociation and short-range order to inorganic salts, whereas ILs (such as the standard imidazolium tetrafluoroborate derivatives) exhibit an incomplete dissociation, charge delocalization (hydrogen bonds, etc.) and contrasts of polarity (polar ions and apolar organic parts) leading to order at larger range.[35, 42] Thus, it is commonly assumed that organic ILs present better lubricant properties and higher viscosity than molten salts,[42] which are supposed to be requisites for the stabilization of mesocrystals.[7] However, for the materials studied, many "traditional" ILs have been reported to stabilize spongelike nanostructures, which cannot be considered mesocrystals due to a lack of mutual crystallographic order within the ensemble.[39, 40] Perhaps an excessive stabilization prevents the NP-IL system from the "fluidity" required for the re-orientation of the NPs. Molten hydroxides (chapter 1.2), on the other hand, have shown a low ability to stabilize $BaMnO_3$ mesocrystals because the oriented NPs rapidly collapse into monocrystals, revealing a too weak stabilization of the NPs. Thus, both extreme systems do not seem the most suitable ones for the controlled formation of "crystals of nanocrystals". Nevertheless, variations of those two limit schemes have led to better results.

The capability of molten hydroxides to hamper the perfect fusion of NPs while allowing their orientation has been shown to be improved by the addition of water in combination with performing the reaction under hydrothermal conditions (chapter 1.1). The detection of $BaMnO_3$ mesocrystals in this case might be due to the more structured liquid with some polarity contrasts stemming from the water dipoles/ions system; also

water might catalyze the condensation reactions needed to form the required bonds in the target oxide. Analogously, it is known that the properties of organic ILs and of the as-synthesized materials are also very sensitive to small differences in the water content, being the presence of small water amount vital for the successful preparation of inorganic nanostructured materials.[34, 37, 42, 43]

In between the inorganic and the organic solvents, urea/choline chloride DES occupies a place.[31] The components have short organic chains leading to less predominant apolar part as compared to "traditional" ILs.[44] Such organic part corresponds to the urea and the cation from the salt, while the chloride anion represents the inorganic part. In a somewhat resemblance to urea, which was the first organic molecule synthesized from inorganic starting materials without the use of living organisms,[45] urea/choline chloride DES bridges the two formal disciplines (inorganic and organic) of low temperature ionic fluids. Furthermore, in addition to ions, it also contains neutral molecules (urea). In this sense, DESs possess features of both ionic liquids and molecular solvents. It is in this frontier field of intermediate molecular/ionic and inorganic/organic properties where we experimentally found the interesting DM-driven SA phenomenon for PbS NPs as well as the detection of octahedral mesocrystals. Interestingly, a reverse phenomenon, related to the deconstruction of anisotropic structures, which are broken down into isotropic NPs, occurred within such a medium for PbS material. The complex ligand and lubricant properties of urea/choline chloride DES as well as its polarity evolution during reaction as a consequence of decomposition upon heating makes it an appealing candidate for future studies in the field of NP's assemblies.

It is worth mentioning that mixtures of urea and nickel nitrate hexahydrate (chapter 2.1) in the lowest urea : Ni ratio tested (0.2 g urea : 1 mmol $Ni^{2+}$) were observed to spontaneously melt at room temperature, indicating the existence of an eutectic point in the phase diagram of the components. This is in consonance with the previously reported high capability of anions to decrease the melting point of hydrogen bond donors such urea.[46] Although the system did not lead to the crystallization of either NiO or Ni NPs, this DES might need to be considered for the synthesis of alternative inorganic NPs, like for instance those corresponding to metals with a higher tendency towards reduction.

Overall, although the nomenclature employed in the literature conveys the idea that the term "deep eutectic solvent" exclusively refers to organic salts merely because such a word was first employed for synthetic organic molecules/salt mixtures (like urea/choline chloride), NaOH/KOH eutectic mixture, although inorganic, is actually a low-temperature DES. Even more hybrid organic/inorganic DESs –such as urea/nickel nitrate mixtures– are also possible. In general, the term "ionic liquid", traditionally used for salts with an organic ion –*e.g.* imidazolium tetrafluoroborate derivatives–, probably could be extended to all low temperature molten salts, as recently suggested in the book *"Molten Salts and Ionic Liquids. Never the Twain?"*.[42] Just different strokes in the same canvas. The only condition that synthetic solvents composed entirely of ions should fulfil in order to be considered ionic liquids is to be fluid below *ca.* 100 ºC. Further understanding of ionic liquids, all of them, as synthetic media of NCs and "crystals of NCs" is very much desired. In this field, mixtures among ILs would enrich the already wealthy diversity of potential ILs for the great flexibility in the synthesis and cooperative behaviour of NPs.

## Relation Between the Features and Properties of the As-Prepared Nanostructured Functional Materials

In this thesis we have manipulated diverse characteristics of the as-prepared nanostructured functional materials, demonstrating a high versatility in the handling of the corresponding physico-chemical properties. First, the small size of $BaMnO_3$ NPs (chapter 1.1) has seemed to be responsible for the FM component accompanying the predominant AFM common behaviour of this material. In turn, this could be due to the non-stoichiometry of the $BaMnO_3$ NPs, as demonstrated for other NPs,[47] which would translate into uncompensated surface spins responsible for the FM contributions. Therefore, this would be an example of size-defects connection.

Not so visible but not less important, the defective crystallinity exhibited by the Ni/NiO NPs (chapter 2.1) exemplifies the transcendental implications of defects in the magnetic phenomenology. The higher the FM Ni / AFM NiO interfacial area, which would equal to think of the higher presence of imperfect crystallinity, the larger shifts of

the magnetic hysteresis loops have been observed. In the case where FM $Ni_{cores}$ were embedded within the AFM $NiO_{shells}$ the effects have been described as exchange bias interactions, whereas in the cases where the potential $Ni_{cores}$ were too small to be detected by the available techniques, the enhanced loop shifts could not be described as an exchange bias effect according to the current conventionalisms. In the latter, either if $Ni_{nuclei}$ remained within the NiO NPs or just disordered NiO NPs existed, both cases could belong to a common situation in which the non-periodicity of an AFM crystal would lead to the magnetic loop's shifts. A unique magnetic behaviour could be described.

Shape, size, non-stoichiometry and SA are intimately connected in the cooperative behaviour of PbS NPs in decomposing urea/choline chloride DES. The truncated octahedral shape of the initially nucleated NPs would be responsible for the existence of both polar and apolar {100} crystal faces and the random distribution of $Pb^{2+}$ and $S^{2-}$ faces,[46] which contain only one type of ion, would render the NPs with a neat DM eventually responsible for the SA behaviour. Complementary, the small particle size could translate into non-stoichiometric NPs and the non-equivalent number of cations and anions would lead to a neat charge. The growing crystal would exhibit a scaled DM and the combination of both attractive and repulsive forces would sculpture the hyperbranched morphology. Octahedral symmetries govern all the levels of hierarchy. Reversely, once the octahedral symmetry had been lost at some levels of hierarchy, the preponderance of the repulsive Coulombic forces within the microcrystals would have led to the deconstruction phenomenon. It is curious the fact that the primitive PbS NPs and the final deconstructed ones have the same truncated octahedral morphology despite possessing different sizes and mechanism of formation (bottom-up and top-down, respectively).

In summary, the present thesis contributes from different perspectives to the nanochemistry discipline, comprising both varied synthetic strategies and the manipulation of the surface, size, shape, defect and SA important attributes of the NPs.

# BIBLIOGRAPHY


1. Reiss, H., The growth of uniform colloidal dispersions. *The Journal of Chemical Physics* **1951,** 19, (4), 482-487.
2. Park, J.; Joo, J.; Soon, G. K.; Jang, Y.; Hyeon, T., Synthesis of monodisperse spherical nanocrystals. *Angewandte Chemie - International Edition* **2007,** 46, (25), 4630-4660.
3. Talapin, D. V.; Rogach, A. L.; Haase, M.; Weller, H., Evolution of an ensemble of nanoparticles in a colloidal solution: Theoretical study. *Journal of Physical Chemistry B* **2001,** 105, (49), 12278-12285.
4. Ostwald, W. Z., *Phys. Chem.* **1901,** 37, 385.
5. Deryagin, B. L., L., *Acta Phys. Chem. URSS* **1941,** 14, 633-662.
6. Verwey, E. J. W. O., J. T. G. , *Theory of the stability of lyophobic colloids*. Elsevier: Amsterdam, **1948**.
7. Song, R. Q.; Cölfen, H., Mesocrystals - Ordered nanoparticle superstructures. *Advanced Materials* **2010,** 22, (12), 1301-1330.
8. Rabenau, A., Role of hydrothermal synthesis in preparative chemistry. *Angewandte Chemie - International Edition in English* **1985,** 24, (12), 1026-1040.
9. Hamann, S. D., Properties of electrolyte solutions at high pressures and temperatures. *Physics and Chemistry of the Earth* **1981,** 13-14, (C), 89-111.
10. Hu, C. G.; Liu, H.; Lao, C. S.; Zhang, L. Y.; Davidovic, D.; Wang, Z. L., Size-manipulable synthesis of single-crystalline $BaMnO_3$ and $BaT_{0.5}Mn_{0.5}O_3$ nanorods/nanowires. *Journal of Physical Chemistry B* **2006,** 110, (29), 14050-14054.
11. Liu, H.; Hu, C.; Wang, Z. L., Composite-hydroxide-mediated approach for the synthesis of nanostructures of complex functional-oxides. *Nano Letters* **2006,** 6, (7), 1535-1540.
12. It cannot be concluded whether the mentioned differences in the resulting nanorods are ascribed to the different atmosphere (under nitrogen bubbling some water may be removed, leading to changes in the property of the medium) or to the reaction time (longer reaction times would lead to the disappearance of the mesocrystals by fusing together the building units into the anisotropic ensembles).
13. Cölfen, H.; Antonietti, M., Mesocrystals: Inorganic superstructures made by highly parallel crystallization and controlled alignment. *Angewandte Chemie - International Edition* **2005,** 44, (35), 5576-5591.
14. Hsu, W. P.; Rönnquist, L.; Matijević, E., Preparation and properties of monodispersed colloidal particles of lanthanide compounds. 2. Cerium(IV). *Langmuir* **1988,** 4, (1), 31-37.
15. A visual inspection of the melted medium revealed a homogeneous, turquoise-blue liquid.
16. Kojima, T.; Nomura, K.; Miyazaki, Y.; Tanimoto, K., Synthesis of various $LaMO_3$ perovskites in molten carbonates. *Journal of the American Ceramic Society* **2006,** 89, (12), 3610-3616.
17. Battisha, I. K.; Speghini, A.; Polizzi, S.; Agnoli, F.; Bettinelli, M., Molten chloride synthesis, structural characterisation and luminescence spectroscopy of ultrafine $Eu^{3+}$-doped $BaTiO_3$ and $SrTiO_3$. *Materials Letters* **2002,** 57, (1), 183-187.
18. Mao, Y.; Banerjee, S.; Wong, S. S., Large-Scale Synthesis of Single-Crystalline Perovskite Nanostructures. *Journal of the American Chemical Society* **2003,** 125, (51), 15718-15719.
19. Mao, Y.; Wong, S. S., Composition and shape control of crystalline $Ca_{1-x}Sr_xTiO_3$ perovskite nanoparticles. *Advanced Materials* **2005,** 17, (18), 2194-2199.
20. Tian, Y.; Chen, D.; Jiao, X., $La_{1-x}Sr_xMnO_3$ (x = 0, 0.3, 0.5, 0.7) nanoparticles nearly freestanding in water: Preparation and magnetic properties. *Chemistry of Materials* **2006,** 18, (26), 6088-6090.
21. Note the hydration water of metallic salts.
22. Failed attempts to eliminate the organic matrix (at different stages of oligomerization and decomposition, from biurea to cyanuric acid) through oxidation by treating the samples with a plasma ozone in a commercial ozonizer were realized.
23. The combustion of an organic compund involves its oxidation to yield $CO_2$ and $H_2O$.
24. The reduction potentials of $Ni^{2+}$ ($E^0$ = -0.257 V), $Co^{2+}$ ($E^0$=-0.28 V), $Fe^{2+}$ ($E^0$ = -0.447 V) and $Mn^{2+}$ ($E^0$ = -1.18 V) indicate the following capability for the oxidation of the metallic elements: $Mn^0 > Fe^0 > Co^0 > Ni^0$.
25. Cushing, B. L.; Kolesnichenko, V. L.; O'Connor, C. J., Recent advances in the liquid-phase syntheses of inorganic nanoparticles. *Chemical Reviews* **2004,** 104, (9), 3893-3946.
26. Li, Y.; Cai, M.; Rogers, J.; Xu, Y.; Shen, W., Glycerol-mediated synthesis of Ni and Ni/NiO core-shell nanoparticles. *Materials Letters* **2006,** 60, (6), 750-753.

27. Li, Q.; Wang, L. S.; Hu, B. Y.; Yang, C.; Zhou, L.; Zhang, L., Preparation and characterization of NiO nanoparticles through calcination of malate gel. *Materials Letters* **2007,** 61, (8-9), 1615-1618.
28. Carnes, C. L.; Stipp, J.; Klabunde, K. J.; Bonevich, J., Synthesis, characterization, and adsorption studies of nanocrystalline copper oxide and nickel oxide. *Langmuir* **2002,** 18, (4), 1352-1359.
29. Boskovic, S. B.; Matovic, B. Z.; Vlajic, M. D.; Kristic, V. D., Modified glycine nitrate procedure (MGNP) for the synthesis of SOFC nanopowders. *Ceramics International* **2007,** 33, (1), 89-93.
30. Armelao, L.; Bandoli, G.; Barreca, D.; Bettinelli, M.; Bottaro, G.; Caneschi, A., Synthesis and characterization of nanophasic $LaCoO_3$ powders. *Surface and Interface Analysis* **2002,** 34, (1), 112-115.
31. Abbott, A. P.; Capper, G.; Davies, D. L.; Rasheed, R. K.; Tambyrajah, V., Novel solvent properties of choline chloride/urea mixtures. *Chemical Communications* **2003,** 9, (1), 70-71.
32. Krossing, I.; Slattery, J. M.; Daguenet, C.; Dyson, P. J.; Oleinikova, A.; WeingÃ¤rtner, H., Why are ionic liquids liquid? A simple explanation based on lattice and solvation energies. *Journal of the American Chemical Society* **2006,** 128, (41), 13427-13434.
33. Wilkes, J. S., A short history of ionic liquids - From molten salts to neoteric solvents. *Green Chemistry* **2002,** 4, (2), 73-80.
34. Seddon, K. R.; Stark, A.; Torres, M. J., Influence of chloride, water, and organic solvents on the physical properties of ionic liquids. *Pure and Applied Chemistry* **2000,** 72, (12), 2275-2287.
35. Antonietti, M.; Kuang, D.; Smarsly, B.; Zhou, Y., Ionic liquids for the convenient synthesis of functional nanoparticles and other inorganic nanostructures. *Angewandte Chemie - International Edition* **2004,** 43, (38), 4988-4992.
36. Bonhote, P.; Dias, A. P.; Papageorgiou, N.; Kalyanasundaram, K.; Grätzel, M., Hydrophobic, Highly Conductive Ambient-Temperature Molten Salts. *Inorganic Chemistry* **1996,** 35, (5), 1168-1178.
37. Morris, R. E., Ionothermal synthesis - Ionic liquids as functional solvents in the preparation of crystalline materials. *Chemical Communications* **2009**, (21), 2990-2998.
38. Cooper, E. R.; Andrews, C. D.; Wheatley, P. S.; Webb, P. B.; Wormald, P.; Morris, R. E., Ionic liquids and eutectic mixtures as solvent and template in synthesis of zeolite analogues. *Nature* **2004,** 430, (7003), 1012-1016.
39. Zhou, Y.; Antonietti, M., Synthesis of Very Small $TiO_2$ Nanocrystals in a Room-Temperature Ionic Liquid and Their Self-Assembly toward Mesoporous Spherical Aggregates. *Journal of the American Chemical Society* **2003,** 125, (49), 14960-14961.
40. Zhou, Y.; Schattka, J. H.; Antonietti, M., Room-temperature ionic liquids as template to monolithic mesoporous silica with wormlike pores via a sol-gel nanocasting technique. *Nano Letters* **2004,** 4, (3), 477-481.
41. See a review about liquid routes for the synthesis of NPs in the Introduction section of this thesis.
42. Gaune-Escard, M. and Seddon, K. R., *Molten Salts and Ionic Iiquids. Never the Twain?* Wiley: **2010**.
43. Liao, H. G.; Jiang, Y. X.; Zhou, Z. Y.; Chen, S. P.; Sun, S. G., Shape-controlled synthesis of gold nanoparticles in deep eutectic solvents for studies of structure-functionality relationships in electrocatalysis. *Angewandte Chemie - International Edition* **2008,** 47, (47), 9100-9103.
44. Analogously to “traditional” ILs, small amounts of water are crucial for synthetic purposes.
45. Indeed, urea was obtained by reaction of cyanate and ammonium ions. The discoverer was the German chemist Friedrich Wöhler in 1828 and the results debunked vitalism, the theory that the chemicals of the living organisms are fundamentally different from inanimate matter.
46. For experiments realized in solutions, adducts of urea and anions with a fixed stoichiometry were detected: W. G. McGavock, J. M. Bryant and W. W. Wendlandt, *Science*, 1956, 123, 897; P. S. Gentile and L. H. Talley, *J. Am. Chem. Soc*., **1957**, 79, 4296. In the absence of water, mixtures of urea and anions show a drastically reduced melting point as a result of the decrease of the lattice energy by means of supramolecular anions extended through all the system: M. Gambino and J. P. Bros, *Thermochim. Acta*, **1988**, 127, 223; M. Gambino, P. Gaune, M. Nabavian, M. Gaune-Escard and J. P. Bros, *Thermochim. Acta*, **1987**, 111, 37.
47. Morris-Cohen, A. J.; Frederick, M. T.; Lilly, G. D.; McArthur, E. A.; Weiss, E. A., Organic surfactant-controlled composition of the surfaces of CdSe quantum dots. *Journal of Physical Chemistry Letters* **2010,** 1, (7), 1078-1081.

# CONCLUSIONS / CONCLUSIONES

# CONCLUSIONS

**1.** Hydrothermal alkali route is a suitable pathway for the synthesis of non-agglomerated, ligand-free $BaMnO_3$ NPs.

- Tailoring of the features of the as-prepared products can be accessed through the reaction conditions:
  - The reactor filling volume influences the particle shape: 70 and ~ 50 % filling volumes lead to microrods and NPs, respectively.
  - For filling volumes of 70 %, epitaxial SA of NPs occurs. It leads to mesocrystals with rod shape and, eventually, to microrods.
  - For filling volumes of ~ 50 %, the higher the KOH concentration, the smaller the particle sizes. This trend finds a limit in 20 M, for which average particle sizes of 20 nm (with an interval of 8-40 nm) are obtained.
  - Metallic salts concentrations and reaction temperature and time exert a minor influence on the as-prepared products within the ranges explored. Suitable values of these parameters are 50 mM, 200 ºC and 24 h, respectively.
- Magnetic characterization reveals shifts of the hysteresis cycles. This difference in respect to the AFM bulk material is ascribed to FM contributions from uncompensated surface spins.

**2.** Hydroxides eutectic route is suitable for the synthesis of ligand-free NiO nanooctahedra of diameter ~ 100-265 nm. However, it fails in the preparation of pure $BaMnO_3$ and other manganites of alkaline earth metals under the explored conditions.

**3.** Urea-melt assisted route is a convenient strategy for the facile synthesis of ligand-free Ni/NiO NPs upon calcination of the organic matrix. The fraction of NiO shell surrounding Ni cores can be controlled as a function of urea content and calcination time: lower urea contents and longer calcination times lead to thicker NiO shells.

Three regimes (A, B and C), corresponding to 0.2, 2 and 20 g urea, respectively, and 1 mmol of $Ni^{2+}$ salt, were thoroughly analysed. While XPS demonstrates the presence of a NiO shell in all the samples, Ni cores are detected in B and C samples by

XRD and magnetic characterization. In the case of A samples, there is no evidence of Ni, although both the formation mechanism and the magnetic properties are compatible with the existence of Ni nuclei. This work points towards the incapability of XRD technique to detect defects or tiny inclusions of a crystalline phase embedded within another one, which actually has transcendental implications in the physico-chemical properties.

The defective crystallinity of the NPs, which is due to the two-fold reason of high FM/AFM interface area as well as quenching of the NCs undergoing oxygen diffusion, has important repercussions in the magnetic phenomenology, characterized by large coercitivities and vertical and horizontal loop's shifts.

**4.** The urea-melt assisted route can be successfully extended to the preparation of pure, ligand-free $Co_3O_4$ (~ 20 nm) and $Mn_3O_4$ (~ 40 nm) NPs.

**5.** Urea/choline chloride DES is suitable for the synthesis of PbS NPs of ~ 30 nm of size. Furthermore, subsequent assembly and deconstruction phenomena of the crystals take place under the reaction conditions. These processes are ascribed to electrostatic forces which are varied together with the evolution of the solvent upon decomposition. Several stages were detected:

- PbS NPs self-organize into octahedral mesocrystals and later into 3D hierarchical, hyperbranched PbS crystals as the result of their preferential assembly along the six equivalent <100> directions. The tendency to balance in space end-to-tail dipole-dipole pairs along six orthogonal directions of a Cartesian system governs the octahedral geometries at every level of hierarchy.
- SA modality switches to the incorporation of the remaining NPs into the body of the hierarchical nano/microcrystals yielding six-arm faceted rods. The change of SA is associated with the decrease of polarity of the DES upon decomposition.
- Deconstruction of the six-arm rods into sub-microparticles. The transition is governed by further decrease of solvent polarity and greater thermodynamic preference to most isotropic geometries.

**6.** Urea/choline chloride DES is a suitable solvent for the preparation of γ-$Fe_2O_3$ (~ 15 nm), α-$Fe_2O_3$ (~ 15 nm) and $Mn_3O_4$ (porous, rice-grain 140 nm) NPs.

# CONCLUSIONES

**1.** La ruta hidrotermal alcalina es un método adecuado para la síntesis de NPs de $BaMnO_3$ sin ligandos y no aglomeradas.

- Las características de los productos pueden ser controladas mediante las condiciones de reacción:
  - El porcentaje de llenado del reactor influye en la forma de las partículas: porcentajes de llenado del 70 y del ~ 50 % conducen a *microrods* y NPs, respectivamente.
  - Para porcentajes de llenado del 70 %, el AE epitaxial de las NPs conduce a mesocristales con forma de *rod* y, finalmente, a *microrods*.
  - Para porcentajes de llenado del ~ 50 %, a mayor concentración de KOH, menor tamaño de partícula. Esta tendencia se mantiene hasta el límite de 20 M, para el cual se obtienen partículas con tamaño medio de 20 nm (comprendidas en el intervalo de 8-40 nm).
  - Las concentraciones de sales metálicas y la temperatura y tiempos de reacción, dentro de los rangos explorados, ejercen una influencia leve en los productos. 50 mM, 200 ºC y 24 h, respectivamente, son valores adecuados de estos parámetros.
- La caracterización magnética revela desplazamientos de los ciclos de histéresis. Esta diferencia respecto al correspondiente material masivo AFM se atribuye a las contribuciones FM de espines superficiales descompensados.

**2.** La ruta del eutéctico de hidróxidos es adecuada para la síntesis de nanooctaedros de NiO sin ligandos y con diámetros de ~ 100-265 nm. Sin embargo, bajo las condiciones exploradas, fracasa en la preparación de $BaMnO_3$ puro y de otras manganitas de metales alcalinotérreos.

**3.** La ruta asistida por fundido de urea es una estrategia conveniente para la síntesis sencilla de NPs de Ni/NiO sin ligandos e involucra la calcinación de la matriz orgánica. Puede controlarse la fracción de la cáscara de NiO que envuelve los núcleos de Ni en función del contenido de urea y del tiempo de calcinación: contenidos bajos de urea y tiempos largos de calcinación conducen a cáscaras de NiO gruesas.

Se analizaron rigurosamente tres regímenes (A, B y C) correspondientes a 0.2, 2 y 20 g de urea, respectivamente, y 1 mmol de sal de $Ni^{2+}$. Mientras que el XPS demuestra la presencia de una cáscara de NiO en todas las muestras, los núcleos de Ni en las muestras B y C son detectados mediante DRX y caracterización magnética. En el caso de las muestras A, no hay evidencia de Ni, aunque tanto el mecanismo de formación como las propiedades magnéticas son compatibles con la existencia de pequeños núcleos de Ni. Este trabajo apunta hacia la incapacidad de la técnica de DRX para detectar defectos o inclusiones diminutas de una fase cristalina embebida en otra, hecho que tiene implicaciones transcendentales en las propiedades fisico-químicas.

La cristalinidad defectuosa de las NPs, la cual se debe a la doble causa de una alta interfase FM/AFM así como al enfriamiento brusco de los NCs que sufren difusión de oxígeno, tiene importantes repercusiones en la fenomenología magnética, caracterizada por grandes coercitividades y desplazamientos verticales y horizontales de los ciclos.

**4.** La ruta asistida por fundido de urea puede extenderse con éxito a la preparación de NPs de $Co_3O_4$ (~ 20 nm) y $Mn_3O_4$ (~ 40 nm) sin ligandos.

**5.** El DES urea/cloruro de colina es adecuado para la síntesis de NPs de PbS de ~ 30 nm de tamaño. Además, bajo el medio de reacción tienen lugar fenómenos de ensamblaje y deconstrucción de los cristales. Estos procesos se atribuyen a fuerzas electrostáticas, las cuales varían junto con la evolución del disolvente, que se descompone durante la reacción. Se detectaron varias etapas:

- Las NPs de PbS se auto-organizan en mesocristales octaédricos y después en cristales de PbS super-ramificados y jerárquicos como resultado de su ensamblaje preferencial a lo largo de las seis direcciones equivalentes <100>. Las geometrías octaédricas en cada nivel de jerarquía están gobernadas por el balance de parejas de dipolos a lo largo de las seis direcciones perpendiculares de un sistema de ejes Cartsiano.
- La modalidad de AE cambia hacia la incorporación de las NPs restantes en el cuerpo de los nano/microcristales jerárquicos, produciendo *rods* facetados de seis ramas. El cambio de AE se asocia con la disminución de polaridad del DES durante su descomposición.

- La deconstrucción de los *rods* de seis ramas en sub-micropartículas. La transición está gobernada por la continua disminución de la polaridad del disolvente y por la preferencia termodinámica por geometrías más isotrópicas.

**6.** El DES urea/cloruro de colina es un disolvente adecuado para la preparación de NPs de $\gamma$-$Fe_2O_3$ (~ 15 nm), $\alpha$-$Fe_2O_3$ (~ 15 nm) y $Mn_3O_4$ (poroso, con forma de grano de arroz, 140 nm).

# APPENDIX A / ANEXO A
# GENERAL ASPECTS OF INORGANIC NANOPARTICLES / ASPECTOS GENERALES DE LAS NANOPARTÍCULAS INORGÁNICAS

# APPENDIX A
## General Aspects of Inorganic Nanoparticles

The terms *nanoparticles* (NPs), *nanocrystals* (NCs), *nanoclusters* and *colloids* are frequently arbitrarily interchanged in the literature. Nevertheless, some nuances difference those notations. *Nanocluster* refers to the nanometer scale particles with well-defined number and positions of the constituent atoms. Such a term was incorporated to the nanoscience discipline from the traditional metallic clusters present in metalorganic compounds (those molecules containing organic ligands attached to metal atoms). The metallic cluster is formed by a group of a low number of metallic atoms (active sites of enzymes are a convenient example of metallic clusters). With the advent of nanoscience, the preparation of increasingly larger metalorganic compounds, in the borderline between single molecules and cutouts of solid-state lattices, led to the new term nanocluster, which involves a much larger number of atoms than molecules but much shorter than bulk matter. Thus, nanoclusters consist of a reduced and well-determined number of atoms corresponding to a specific number of layers, which involves that only magic numbers of atoms can be contained within a nanocluster.[1-5] On the contrary, the term *nanocrystal* refers to a crystalline particle in the nanometer regime and does not necessarily involve an understanding of the precise positions of the atoms, giving rise to a particle size distribution.[6] Nanocrystals are larger than nanoclusters, possessing an identifiable interior, structurally identical to the corresponding bulk solid, with a substantial fraction of the total number of atoms on the surface.[7, 8] *Nanoparticle* just denotes a size in the nanometer range, comprising the previous definitions of nanoclusters and nanocrystals as well as amorphous nano-objects or those with an undetermined crystal structure.[9] Last, the word *colloid* comes from the pioneer chemical liquid-based routes for the preparation of nanoparticles.[10] A *colloid* is a suspension in which the dispersed phase is so small (1-1000 nm) than gravitational forces are negligible and interactions are dominated by short-range forces, such as van der Waals attraction and surface charges. If the dispersed particles are solid and the medium is liquid, the colloidal suspension is called a *sol*. If the particles are dispersed in a gas, it is an *aerosol* (which in turn may be called a *fog* if the particles are liquid and *smoke* if they are solid); an *emulsion* is a suspension of liquid droplets in another liquid. A *gel* is the result of the further polymerization of a sol into a continuous

solid skeleton enclosing a continuous liquid phase, both of which posses colloidal dimensions. A *xerogel* is a gel dried under normal conditions, with a notable reduction in volume, and an *aerogel* is a gel dried under supercritical conditions, with little shrinkage. All of those types of colloids have been used to prepare nanostructured[11] and ceramic materials.[12] So the term *colloids* is connected with chemical pathways and with a dispersant medium, as opposite to the term *nanoparticles*, which does not involve a fluid medium as dispersant of the nanosized particles. Also, *colloids* encompasses a broader particle size, from 1 to 1000 nm, being more typical the colloids between 100 and 1000 nm, whereas *nanoparticles* is more focused on sizes from 1 to 100 nm.[13]

The properties of solid matter are determined by the "infinite" 3D arrangement of its building units, which can be single ions in the ionic crystals typical of solid-state compounds, single atoms (like covalently bonded carbon atoms in diamond), covalently organized units (such as "$SiO_2$" in quartz) or individual molecules in a molecular lattice (like $S_8$ in sulphur crystals or organic molecules –such as proteins– in organic crystals). On the contrary, individual molecules place finite atoms in discrete locations and no repetition through the space is maintained. Between these two limits –the 3D long-range order and the punctual order– nanostructures find their realm. Specifically, inorganic NCs are intermediate entities between solid-state compounds and metalorganic molecules. Thus, the study of inorganic NCs requires of concepts from solid state chemistry/physics and other disciplines related to the study of molecules, surfaces, *etc.* In other words, in spite of the fact that inorganic NCs can be regarded as fragments of bulk inorganic crystals, a net of interconnected concepts strongly distinguishes nanostructures from bulk materials.[14] Such concepts are surface, size, shape, self-assembly and defects and are described as follows:

**1. Surface**

Compared to bulk solid-state matter, inorganic NPs are governed by a much larger area/volume ratio and, thus, by disorder. Figure 1 collects the surface area and total volume of a group of cubes formed by subsequent division of a cube of 1 cm of length into cubes with edges 1 nm in length. While the sum of the volumes remains constant, the number of total surface area increases strikingly. The surface area of the $10^{21}$ nanocubes, 6000 $m^2$, is close to the area of a football field (*ca.* 7000 $m^2$). By the same token, Figure 2 shows how the surface/volume ratio of a spherical NP increases with

decreasing diameter. As can be seen, a NP with a diameter of 5 nm possesses approximately half of their atoms at the surface. So, all the characteristics related to the surface which are ignored for bulk materials in traditional solid state science, cannot be neglected in the case of NPs.

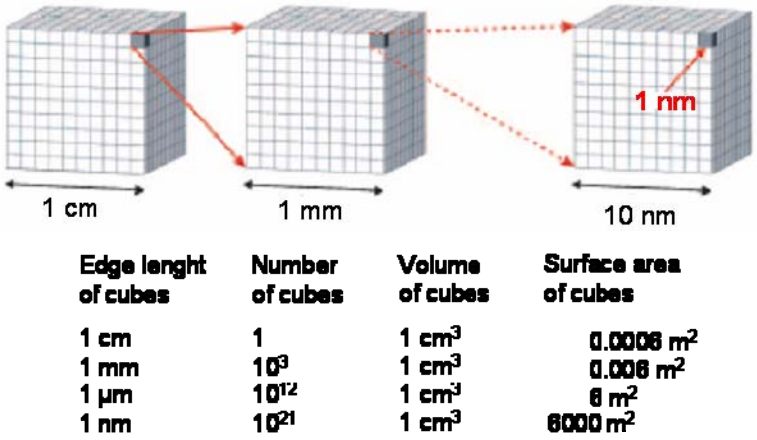


**Figure 1.** Surface area of NPs. Modified reproduction of ref. [15].

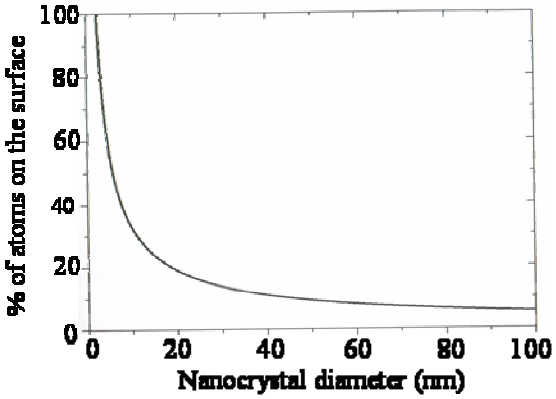


**Figure 2.** Approximate percentage of surface atoms as a function of nanocrystal size, assuming a spherical morphology and a PbS lattice. Modified reproduction of ref. [1].

Firstly, atoms at the surface usually possess dangling bonds, *i.e.* unshared valence electrons, and often bear a partial electric charge, rendering the NP with an extra, destabilizing surface energy:

$$\gamma = n_{db} \times (\Phi/2) \quad (1)$$

where $\gamma$ is the surface energy, $n_{db}$ is the surface density of dangling bonds and $\Phi$ is the energy of the bond. Thus, the surface energy increases with the density of dangling bonds. As a consequence, different crystal faces exposing different densities or types of atoms, possess distinct surface energies. This has important implications in shape-

controlled crystal growth[16, 17] and in the catalytic properties of different geometries of the crystals.[18, 19]

Such extra energy is accommodated through a series of mechanisms like surface reconstruction, which leads to different positions and bonding of the superficial atoms from those in the bulk. Specifically, a compression of the atomic structure several atomic layers beneath the surface or even the stabilization of a different structure than the typical for the bulk can occur.[20, 21] Also, in alloy nanomaterials, the stable solid solution found in the bulk is replaced by the separation of phases –core-shell NPs– where the component with the lowest surface energy segregates as an outer shell.[22-24]

For the same reasons, NPs, which are metastable, respond to the environment, tending to undergo a series of dynamic phenomena to gain stability:

- Adsorption of impurities. This involves a high chemical reactivity of NPs and is an important attribute in areas such as catalysis, fuel cells, batteries and chemical sensing.[25]

- Passivation, *i.e.* the spontaneous reaction with molecules from the atmosphere leading to a protective outer layer of a different composition than the core. When this is an issue leading to undesired oxidation, coating of NPs with a stable protective outer layer such as silica is a required step.[26] On the other hand, spontaneous passivation can be an advantageous feature for the facile achievement of "metallic core/metallic oxide shell" NPs, which is highly desired in the case of ferromagnetic (FM) and antiferromagnetic (AFM) components due to the interesting magnetic phenomenology called exchange bias (EB) exhibited by the interaction of such components at the nanoscale.[27-29] Chapter 2.1 of the present thesis tackles the phenomena of passivation in nickel NPs and the EB effects exhibited by the resulting $Ni_{core}$-$NiO_{shell}$ NPs.

- Functionalization, *i.e.* reaction with species from a liquid medium. It takes place through both covalent bonds and electrostatic interactions. For instance, positively charged surfaces can be stabilized with a high concentration of

hydroxyl groups ($OH^-$) from a base of Brönsted. This is discussed in chapter 1 of this thesis.

An intentional functionalization is a key requirement in the preparation of NPs in liquid media. It can enable a multi-fold target:

- The synthesis of NPs, *i.e.* their stabilization. Without functionalization, NPs would coagulate within the reaction medium to replace the unstable solid-liquid interfaces by stable solid-solid ones. The more epitaxial character, *i.e*. match of the atomic lattices, has the solid-solid interface, the more stabilization is gained. Apart from this thermodynamic aspect, entropic factors related to the desorption of solvent molecules from the surface of the NPs, also favor the aggregation and sintering of NPs into single microcrystals in the absence of functionalization.[30]
- Manipulation of the NPs in media of different polarity.
- Manipulation of the properties of the inorganic core.[31]
- Biocompatibility and specificity. Functionalization allows the engineering of nanobiosensors,[32-34] the magnetic separation and recovery of target molecules,[35-37] the magnetic resonance imaging (MRI)[38] and magneto-thermal cancer therapy.[39]
- Self-assembly of NPs into multifunctional materials showing interesting properties resulting from i) combination of nano and micro-scales of hierarchy, ii) the integration of different functionalities, iii) the enhancement of a property and iv) new properties arising from the interaction of the excitons, magnetic moments and plasmons of the (semiconductor, magnetic and metal) components.[40-43] Functionalization is a key aspect for tuning of the SA pattern (*e.g.* end-by-end or side-by-side SA of nanorods –NRs–).[44, 45]

Overall the surface plays a leading role in NP's behavior. Further concepts which are not independent among them but whose ensemble characterizes NPs and distinguish them from bulk materials are the following:

**2. Size**

It is the most direct parameter defining NPs. The main special properties of NPs distinguishing them from bulk materials are connected in a first approximation with size effects. Such particular properties can be divided into three groups:[15]

1) Surface-dependent particle properties. These are properties which in principle the bulk material also displays, but which only become dominant in NPs due to the high surface-to-volume ratio. Representative examples are the drastic increase of the chemical reactivity of NPs as compared to the bulk counterpart, which has important implications for catalysis.[25] Also, the melting temperature is very reduced (up to ~ 40%) for NPs.[46-48]A further example is the surface electron conductivity of oxide NPs, such as the $TiO_2$ NPs exploited in dye-sensitized solar cells.[49] Analogously, oxide NPs are currently a major attraction for lithium ion batteries, fuel cells and supercapacitors due to the faster diffusion resulting in increased charging and discharging speeds.[50]

2) Size-dependent particle properties. These are new properties displayed by the NPs as compared to the bulk counterparts not related to the electronic structure. Superparamagnetism is exhibited by those NPs whose bulk displays ferromagnetism; this is the case of nickel, iron or cobalt. Ferromagnetism is characterized by Weiss domains of size 10-50 nm within which the magnetic moments associated with unpaired electron spins are oriented in the same direction (Figure 3). When an external magnetic field is applied all the domains are oriented in the same direction, along the magnetic field, resulting in a neat remnant magnetization of the material after removing the applied field. However, if the size of the particle is small enough, each NP will be a single domain. In this case, thermal energy becomes comparable to the magnetic anisotropy energy of the particle, so the magnetization fluctuates and the particle acts as a giant spin, the "superparamagnet".[51] Ferroelectric materials follow similar rules substituting magnetic by electric phenomena.

3) Size-dependent quantum effects. These are new properties displayed by the NPs which stem from the change of the electronic structure of the material as its size

4)

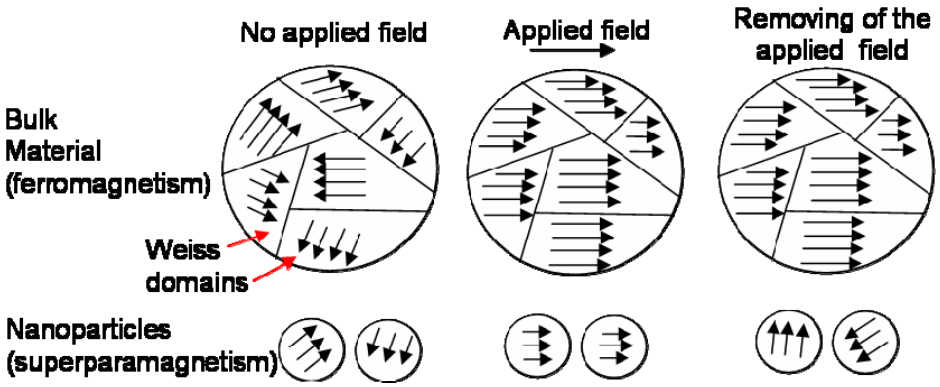


**Figure 3.** Depiction of the ferromagnetism and superparamagnetism exhibited by the same material in its bulk and nanosized forms, respectively.

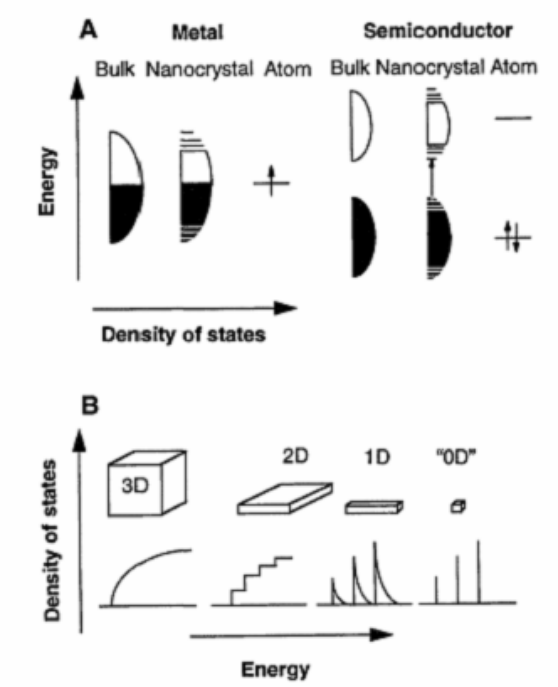


**Figure 4.** (A) Schematic illustration of the density of states in metal and semiconductor materials. (B) Density of states in one band of a semiconductor as a function of dimension. Reproduced from ref. [52].

is reduced down to the nanoscale. Optical and electronic properties are thus affected and the two most prominent examples are the plasmon resonance of noble metals and the exciton of semiconductor quantum dots (QDs).[52, 53] Plasmon resonance, *i.e.* the frequency at which the conduction electrons can collectively oscillate, determines the color of noble metals. On the other hand, Figure 4 illustrates the density of states in metal and semiconductor bulk, NPs

and atoms. As the size is reduced, the band gap between the valence and conduction bands increases, *i.e.* metals can become semiconductors or insulators. In the case of semiconductors, the color is determined by the energy required to create an exciton (a hole-electron pair); *i.e.* by the band gap energy. Since the band gap increases when the size is reduced, a blue-shift of the color is observed as the size of the NPs is decreased. Besides, the continuous electronic bands typical of the bulk start to be split, *i.e.* they acquire discrete values of energy. These phenomenon is due to the fact that the so called *exciton Bohr radius*, which is the distance –typically between 2 and 20 nm– at which excited electrons are moved away from their parent atom within the semiconductor crystal lattice, becomes comparable or smaller than the crystal size, so the excitons find a reduced space, leading to an increase of the band gap energy and of the density of the charge carriers (electrons and holes) at the NP surface. The charge carriers behave like "the particle in the box" typical of quantum mechanics.

In general, it can be stated that new size-dependent phenomena emerge when the length of the physical property becomes comparable to a characteristic length of the object showing it or being affected by it. In the case of magnetism, such a length is represented by the Weiss domains size, while in the case of QDs, the dimension under consideration is the exciton Bohr radius. Given that many physical phenomena have natural length scales between 1 and 100 nm, NPs frequently exhibit novel size-dependent phenomena. The relevance of such size-dependent effects lies in the fact that the properties of the material can be finely tuned as a function of the particle size (rather than the traditional compositional-mediated control over the properties).

The influence of size on the magnetic properties is discussed in chapter 1.1, in regard to the magnetic characteristics of $BaMnO_3$ NPs, and in chapter 2.1, where the EB magnitude is studied as a function of the size of the Ni core in $Ni_{core}$-$NiO_{shell}$ NPs.

**3. Shape**

There are several ways in which shape determines the characteristics of NPs, as exemplified by the following binomials:

Shape-size connection. On one hand, shape is the result of different relative sizes along different directions. For example, NRs and nanowires (NWs) have a 1D shape because they have two different sizes: length and diameter, measured as the aspect ratio (the ratio between the former and the latter). NRs have a shorter aspect ratio than NWs.[53, 54]

Shape-surface connection. In addition, shape conditions the crystallographic faces at the surface and, thus, the density of dangling bonds responsible for the catalytic activity.[18, 55, 56]

Shape-self-assembly connection. On the other hand, shape also determines the properties of the nanostructured material because of their mutual recognition through different SA patterns. The other way round also operates here: given a macroscopic shape, it is possible to infer a related shape for the building-blocks forming part of the lower levels within the hierarchical structure.[57]

The shape property is tackled in chapter 1.1 of this thesis in regard to the stabilization of $BaMnO_3$ rods and NPs. Likewise, chapter 1.3 reports the formation of NiO nanooctahedra. Both chapters deal with reaction media rich in strong bases such as KOH and NaOH, where the high ionic character may play a role in guiding the morphology of the NPs. On the other hand, the 1D SA of $BaMnO_3$ NPs into nanorods is discussed in chapter 1.1, whereas the 3D SA of PbS NPs into hierarchical hyperbranched structures is reported in chapter 3.1. In the latter case, the relation between the shape of the nanosized building-blocks and the shape of the final microcrystal is discussed.

In summary, shape, intimately inter-related to size, surface and self-assembly, is a further variable in order to gain control and degrees of functionality of nanomaterials.

**4. Self-assembly**

Self-assembly is the autonomous organization of discrete components into patterns or structures without human intervention.[58] It is a ubiquitous process in nature, from the molecular level to the planetary scale. NCs also exhibit such an inherent collective organization, behaving as “artificial atoms” which are autonomously combined into complex structures, in the same way that atoms are ordered in molecules or in covalent

and ionic solids. Actually, SA is being found to govern crystallization mechanisms traditionally attributed to ion-to-ion attachment. This is especially true for biomineralization processes, where mesocrystals, in which the NCs can be identified because a lack of perfect fusion among them, are frequently detected as intermediates stages of the single crystal formation.[59-62]

Self-assembly is governed by the balance of attractive forces (such as hydrogen bonding, electrostatic attraction and dipole-induced dipole interactions) and repulsive forces (such as steric forces and electrostatic repulsion). It is an important direction towards the design of advanced materials. First, SA enables the facile synthesis of complex morphologies (1D,[63] 2D[64] or 3D[65]) which can take advantage of both the nano and micro dimensions for the great benefit of both. Second, simple combinations of different types of materials are realized, taking advantage of the exciton-plasmon and plasmon-plasmon interactions[66] as platforms for biodetection,[67] energy-conversion, nanoscale thermometers,[68] and "plasmon rulers".[69] Architectures such as symmetric pairs of NPs[67, 69] and satellite-like grouping of NPs[68] (*i.e.* "colloidal molecules") are autonomously constructed. Third, SA opens the path to the crystallization of distinct NPs into multinary 3D networks ("colloidal crystals"), with properties resulting from the collective behavior of the (electronic, magnetic, optical) components.[41, 70-80]

The SA spontaneously occurring for ligand-stabilized NPs in liquid media can be further manipulated through diverse strategies,[41, 81] such as the use of templates,[82-87] SA at interfaces (such as the Langmuir-Blodgett technique[88]), assisted SA under the action of electric[89, 90] or magnetic[91, 92] fields and layered assemblies of NPs through the layer-by-layer technique.[93]

Last, although up-to-date the SA has mainly focused on the so-called static SA, which involves systems that are at global or local equilibrium and do not dissipate energy, futuristic sights are put towards the dynamic SA, that one only occurring if the system is dissipating energy and defining life.[40, 58]

In this thesis, the detection of mesocrystals is reported in chapters 1.1 and 3.1, dealing with the SA of $BaMnO_3$ and PbS NPs, respectively.

## 5. Defects

Defects in NCs, as in any crystal, break the periodicity and symmetry in which the atoms are positioned. The classical classification from solid-state chemistry divides the types of defects according to their dimensionality:

- 0D or point deffects: vacancies (a missing atom), interstitials (an extra atom in the lattice), misplaced atoms and impurities (different atom).
- 1D: dislocations (a misplaced line of atoms).
- 2D: stacking faults (a misplaced or missing plane of atoms), twin planes and grain boundaries (interfaces between various crystalline grains)
- 3D: inclusions (clusters of foreign atoms within the parent lattice).

Since the surface of a crystal can indeed be regarded as a defect, nanostructures show a substantial contribution of defects due to their high surface and their influence extends to the whole particle. Paradoxically, point defects within the inner part of the NP resembling the bulk are very rare, since they tend to be segregated to the surface where they can reduce the high surface energy. Multitude of properties benefit from the "surface" defect, such as thermoelectricity,[94] from the segregation of point defect to the surface, such as annealing of radiation damage,[95] and from the mutual interaction of defects, such as the ultrahigh strength and ductility in nanotwinned metals.[96]

Similarly, another effect that the high surface area of nanomaterials has on defects is the stoichiometry. Given the two-fold reason that the NCs can be terminated in their surfaces by crystalline planes containing only one type of atoms and that the atoms on the surface account for a substantial percentage of all the atoms, non-stoichiometry is specially remarkable for nanomaterials (*i.e.* $Pb_{1.15}S_{0.85}$ is more likely to happen than the $Pb_1S_1$ stoichiometry). This has repercussions in the intrinsic dipolar moment (DM) of the NPs and thus in the SA fashion (*i.e.* due to the different electronegativity of cations and anions in PbS, the distribution of cation or anion-faces, which are polar, is ultimately responsible for rendering the NCs with a DM which prompts their SA).[97, 98]

The existence of defects on local parts of a nanostructure can have a dominoes-like collective effect at their microscale, leading to the formation of fascinating

geometries. For instance, dislocations with screw components can propagate anisotropically forming nanowire pine trees.[99] Also, light-induced photocorrosion of individual NPs assembled into ribbons has been demonstrated to induce their helicity.[100]

Therefore, defects constitute a further degree of freedom to tailor the properties of nanostructured materials. There is plenty of room for perfecting imperfection (and perfecting imperfection will generate a myriad of possibilities).

This property is discussed in chapter 2.1 in regard to the role of structural disorder of a nanostructured NiO matrix on the magnetic phenomenology. In addition, in chapter 3.1 it is discussed the role of non-stoichiometry of PbS NPs in their DM and SA. Chapter 1.1 reports the role of non-stiochiometry of $BaMnO_3$ NPs on their magnetic properties.

# ANEXO A

## Aspectos Generales de las Nanopartículas Inorgánicas

Los términos *nanopartículas* (NPs), *nanocristales* (NCs), *nanoclusters* y *coloides* son con frecuencia intercambiados de forma aleatoria en la literatura. Sin embargo, existen ciertos matices que diferencian estas notaciones. *Nanocluster* se refiere a las partículas en la escala nanométrica con un número y posiciones bien definidos de los átomos constituyentes. Este término se incorporó a la disciplina de la nanociencia desde los clusters metálicos presentes en los tradicionales compuestos metalorgánicos (aquellas moléculas que contienen *ligandos* orgánicos unidos a átomos metálicos). Un cluster metálico está formado por un grupo de unos pocos átomos metálicos (los sitios activos de las enzimas son un ejemplo de clusters metálicos). Con el advenimiento de la nanociencia, la preparación de compuestos metalorgánicos cada vez mayores, en la frontera entre moléculas y trozos de redes de estado sólido, condujo al nuevo término nanocluster, el cual implica un número de átomos mucho mayor que el de las moléculas pero mucho menor que el de la materia masiva. Así, los nanoclusters están formados por un número reducido y bien definido de átomos que corresponden a un número específico de capas, lo cual conlleva que sólo ciertos números mágicos de átomos pueden estar contenidos en un nanocluster.[1-5] Por el contrario, el término *nanocristal* se refiere a las partículas cristalinas en el régimen nanométrico y no implica necesariamente el conocimiento de las posiciones precisas de los átomos, dando lugar a una distribución del tamaño de partícula.[6] Los nanocristales son más grandes que los nanoclusters y poseen un interior estructuralmente idéntico al sólido masivo correspondiente, con una fracción sustancial del número total de átomos en la superficie.[7,8] *Nanopartícula* denota simplemente un tamaño en el régimen nanométrico, con lo que comprende las definiciones previas de nanoclusters y nanocristales, así como nanoobjetos amorfos o aquellos con una estructura cristalina indeterminada.[9] Por último, la palabra *coloide* proviene de las rutas líquidas de carácter químico pioneras en la preparación de nanopartículas.[10] Un coloide es una suspensión en la cual la fase dispersada es tan pequeña (1-1000 nm) que las fuerzas gravitacionales son despreciables y las interacciones están dominadas por fuerzas a corto alcance, como las de van der Waals o las cargas superficiales. Si las partículas dispersadas son un sólido y el medio es un líquido, la suspensión coloidal se dice que es un *sol*. Si las partículas se

encuentran dispersas en un gas, es un *aerosol* (el cual, a su vez, se llama *niebla* si las partículas son líquidas y *humo* si las partículas son sólidas); una emulsión es una suspensión de gotas de un líquido en otro líquido. Un *gel* es el resultado de la polimerización de un sol formando un esqueleto sólido y continuo que atrapa una fase líquida continua, ambas con dimensiones coloidales. Un *xerogel* es un gel secado bajo condiciones normales, que conllevan una reducción notable del volumen, y un *aerogel* es un gel secado bajo condiciones supercríticas, lo que conlleva poco encogimiento. Todos estos tipos de coloides han sido usados para preparar materiales nanoestructurados[11] y cerámicos.[12] Luego el término *coloides* está conectado con rutas químicas y con un medio dispersante, al contrario que el término *nanopartículas*, el cual no conlleva un medio fluido como dispersante de las partículas nanométricas. Asimismo, la palabra *coloides* abarca un rango más amplio de tamaños de partícula, entre 1 y 1000 nm, siendo más típicos los coloides entre 100 y 1000 nm, mientras que el término *nanopartículas* está más enfocado a los tamaños comprendidos entre 1 y 100 nm.[13]

Las propiedades de la materia sólida vienen determinadas por la disposición 3D "infinita" de las unidades constructoras, las cuales pueden ser iones en los cristales iónicos típicos de los compuestos de estado sólido, átomos (como los átomos de carbono covalentemente enlazados en el diamante), unidades covalentemente organizadas (como el "$SiO_2$" en el cuarzo) o moléculas individuales en una red molecular (como el $S_8$ en los cristales de azufre o las moléculas orgánicas –como las proteínas– en cristales orgánicos). Por el contrario, las moléculas individuales posicionan átomos finitos en posiciones discretas y no se mantiene una repetición a lo largo del espacio. Entre estos dos límites –el orden 3D a largo alcance y el orden puntual– reside el reino de las nanoestructuras. En concreto, los NCs inorgánicos son entidades intermedias entre los compuestos de estado sólido y moléculas metalorgánicas. Así, el estudio de los NCs inorgánicos demanda conceptos de la química/física del estado sólido y de otras disciplinas relacionadas con el estudio de moléculas, superficies, *etc.* En otras palabras, a pesar de que los NCs inorgánicos pueden ser considerados como fragmentos de cristales inorgánicos masivos, existe un entramado de conceptos interconectados que distinguen claramente las nanoestructuras de los materiales masivos.[14] Estos conceptos son la superficie, el tamaño, la forma, el auto-ensamblado y los defectos y se describen a continuación:

## 1. Superficie

En comparación con la materia de estado sólido masiva, las NPs inorgánicas se encuentran gobernadas por una relación área/volumen mucho mayor y, por tanto, por desorden. La Figura 1 indica el área superficial y el volumen total de un grupo de cubos formados al dividir sucesivamente un cubo de 1 cm de arista en cubos con aristas de 1 nm. Mientras que la suma de los volúmenes de todos los cubos permanece constante, el área superficial total aumenta de forma espectacular. Así, el área de los $10^{21}$ nanocubos es 6000 $m^2$, superficie cercana al área de un campo de fútbol (*ca.* 7000 $m^2$). Del mismo modo, la Figura 3 muestra cómo aumenta la relación superficie/volumen de una NP esférica al disminuir su diámetro. Como puede observarse, una NP con un diámetro de 5 nm posee aproximadamente la mitad de sus átomos en la superficie. Por consiguiente, todas las características relacionadas con la superficie, las cuales son ignoradas para materiales masivos en la ciencia de estado sólido tradicional, no pueden ser despreciadas en el caso de las NPs.

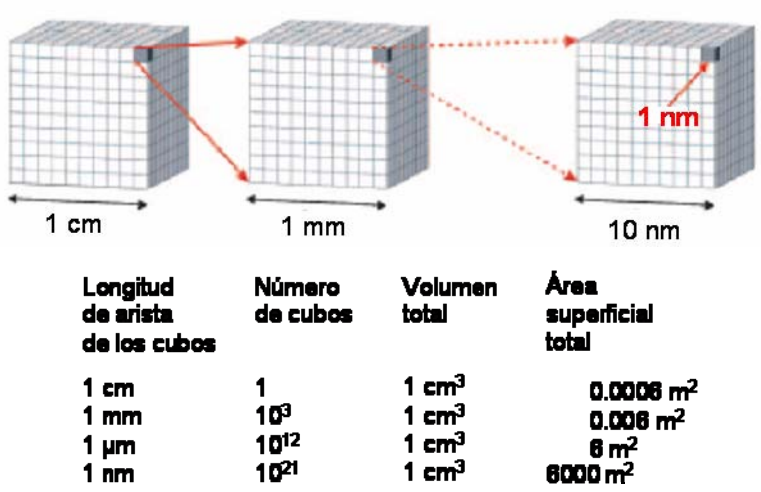


**Figura 1**. Área superficial de NPs. Reproducción modificada de la ref.[15].

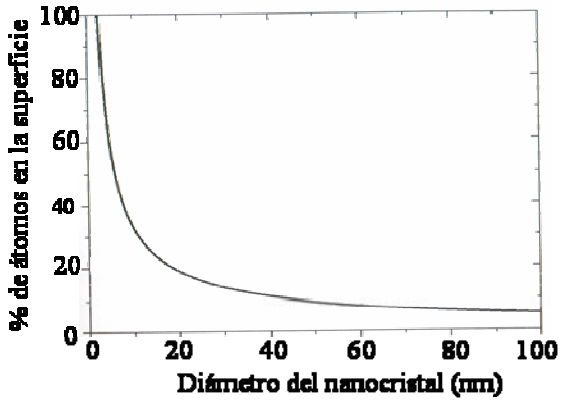


**Figura 3.** Porcentaje aproximado de átomos superficiales en función del tamaño del nanocristal, considerando una morfología esférica y una red PbS. Reproducción modificada de la ref. [1].

En primer lugar, los átomos superficiales por lo general poseen enlaces "no satisfechos", es decir, electrones de valencia sin compartir, y con frecuencia soportan una carga eléctrica parcial, proporcionándole a la NP una energía superficial extra y desestabilizadora:

$$\gamma = n_{db} \times (\Phi/2) \quad (1)$$

donde $\gamma$ es le energía superficial, $n_{db}$ es la densidad superficial de enlaces "no satisfechos" y $\Phi$ es la energía de cada enlace. Por tanto, la energía superficial aumenta al aumentar la densidad de enlaces "no satisfechos". Como consecuencia, diferentes caras cristalinas con diferentes densidades o tipos de átomos poseen distintas energías superficiales. Esto tiene importantes implicaciones en el crecimiento de cristales con morfología controlada[16,17] y en las propiedades catalíticas de distintas geometrías cristalinas.[18,19]

Dicha energía superficial es acomodada a través de una serie de mecanismos entre los que destaca la reconstrucción superficial, la cual conduce a posiciones y enlaces de los átomos superficiales distintos que las encontrados en el interior. En concreto, puede darse una compresión de la estructura atómica varias capas por debajo de la superficie e incluso puede estabilizarse una estructura distinta de la del material masivo.[20,21] De igual modo, las aleaciones encontradas en materiales masivos son con frecuencia reemplazadas en los nanomateriales por una separación de fases –NPs núcleo-cáscara–, donde el componente con la menor energía superficial es segregado como una capa externa.[22-24]

Por las mismas razones, las NPs, que son metaestables, responden al medio que las rodea, de manera que tienden a sufrir una serie de fenómenos dinámicos para ganar estabilidad:

- Adsorción de impurezas. Esto conlleva el que las NPs tengan una alta reactividad química y es una importante cualidad en áreas como la catálisis, las pilas de combustible, las baterías y los sensores químicos.[25]

- Pasivación, es decir, la reacción espontánea con moléculas de la atmósfera, conducente a una capa protectora externa de distinta composición que el interior. En ocasiones esto conduce a una oxidación indeseada, lo que se puede solucionar protegiendo las NPs con una capa externa, como por ejemplo la sílice.[26] Por otro lado, se puede sacar ventaja de la pasivación espontánea para preparar de manera sencilla NPs "núcleo metálico/cáscara de óxido metálico", lo cual es muy deseable en el caso de componentes ferro (FM) y antiferromagnéticos (AFM) debido a la interesante fenomenología magnética llamada exchange bias (EB) típica de la interacción de dichos componentes a la nanoescala.[27-29] El capítulo 2.1 de la presente tesis aborda los fenómenos de pasivación en NPs de níquel y de los efectos de EB mostrados por las NPs $Ni_{núcleo}$-$NiO_{cáscara}$ resultantes.

- La funcionalización, es decir, la reacción con especies de un medio líquido. Puede tener lugar mediante enlaces covalentes o interacciones electrostáticas. Por ejemplo, las superficies cargadas positivamente pueden ser estabilizadas con una alta concentración de grupos hidroxilo ($OH^-$) de una base de Brönsted. Este aspecto se discute en el capítulo 1 de esta tesis.

  Para la preparación de NPs en medio líquido se requiere una funcionalización, la cual puede desempeñar varios papeles:

  - La síntesis de NPs en sí misma; es decir, su estabilización. Sin funcionalización, las NPs coagularían en el medio de reacción reemplazando las interfases inestables sólido-líquido por las más estables sólido-sólido. Cuanto más epitaxial sea la interfase sólido-sólido, es decir, cuanto mejor encajen las redes atómicas, más estabilización se gana. Aparte de este factor termodinámico, existen aspectos entrópicos, relacionados con la desorción de moléculas de disolvente de la superficie de las NPs, que también favorecen en la ausencia de funcionalización la agregación y el sinterizado de las NPs dando como resultado microcristales.[30]
  - La manipulación de NPs en medios de distinta polaridad.
  - La manipulación de las propiedades de los núcleos inorgánicos.[31]

- La biocompatibilidad y especificidad. La funcionalización permite la fabricación de nanobiosensores,[32-34] la separación magnética de moléculas objetivo,[35-37] la imagen por resonancia magnética (MRI)[38] y la terapia magneto-térmica contra el cáncer.[39]
- El auto-ensamblado (AE) de NPs en materiales multifuncionales que muestran interesantes propiedades que resultan de i) la combinación de nano y microescalas de jerarquía, ii) la integración de distintas funcionalidades, iii) el aumento de una propiedad y iv) nuevas propiedades resultantes de la interacción de los excitones, los momentos magnéticos y los plasmones de los componentes semiconductores, magnéticos y metálicos.[40-43] La funcionalización es un aspecto fundamental para la modificación del patrón de AE (por ejemplo, el AE de *nanorods* –NRs– en forma de cola-cola o lado-lado).[44,45]

En resumen, la superficie juega un papel destacado en el comportamiento de las NPs. A continuación se describen el resto de conceptos que no son independientes entre sí pero cuyo ensamblado caracteriza las NPs y las distingue de los materiales masivos:

## 2. Tamaño

Es el parámetro más inmediato a la hora de definir las NPs. Las propiedades especiales de las NPs que las hace distintas de los materiales masivos están relacionadas en una primera aproximación con efectos de tamaño. Dichas propiedades peculiares pueden dividirse en tres grupos:[15]

1) Propiedades dependientes de la superficie. Éstas son propiedades que en principio el material masivo también presenta, pero que sólo se hacen dominantes en el caso de las NPs debido a la alta relación superficie/volumen. Un ejemplo representativo es el drástico aumento de la reactividad química de las NPs en comparación con su análogo masivo, lo cual tiene importantes repercusiones en catálisis.[25] Además, la temperatura de fusión se reduce mucho (hasta un ~ 40%) en las NPs.[46-48] Un ejemplo adicional es la conductividad eléctrica superficial de los nanoóxidos tales como las NPs de $TiO_2$ empleadas en células solares sensibilizadas con un tinte.[49] Análogamente, los nanoóxidos

constituyen en la actualidad una atracción muy importante para las baterías de litio, pilas de combustible y supercondensadores debido a la rápida difusión que se traduce en velocidades mayores de carga y descarga.[50]

2) Propiedades dependientes del tamaño. Éstas son nuevas propiedades de las NPs que no exhiben sus análogos masivos y que no están relacionadas de la estructura electrónica. El superparamagnetismo lo muestran aquellas NPs cuyo análogo masivo exhibe ferromagnetismo; es el caso del níquel, el hierro o el cobalto. El ferromagnetismo se caracteriza por dominios de Weiss de tamaño 10-50 nm en el que los momentos magnéticos asociados a espines de electrones desapareados se orientan en la misma dirección (Figura 3). Cuando se aplica un campo magnético externo todos los dominios se orientan en la misma dirección, a lo largo del campo magnético, dando como resultado una magnetización neta remanente del material tras la retirada del campo. Sin embargo, si el tamaño de partícula es suficientemente pequeño, cada NP será un dominio. Entonces, la energía térmica es comparable a la energía de anisotropía magnética de la partícula, de manera que la magnetización fluctúa y la partícula actúa como un espín gigante, el "superparamagneto".[51] Los materiales ferroeléctricos siguen reglas similares con fenomenología eléctrica en lugar de magnética.

3) Efectos cuánticos dependientes del tamaño. Estas son nuevas propiedades de las NPs provenientes del cambio de estructura electrónica del material al reducir su tamaño de partícula hasta la nanoescala. Las propiedades ópticas y electrónicas se ven así afectadas y los dos ejemplos más destacados son la resonancia del plasmón de los metales nobles y el excitón de los *quantum dots* (QDs) de materiales semiconductores.[52,53] La resonancia del plasmón, es decir, la frecuencia a la que los electrones de conducción pueden oscilar colectivamente, determina el color de los metales nobles. Por otro lado, la Figura 4 ilustra la densidad de estados de metales y semiconductores en sus formas material masivo, NPs y atómos. A medida que se reduce el amaño de partícula, aumenta el *band gap* entre las bandas de valencia y de conducción, es decir, los metales pueden mostrar un comportamiento semiconductor o incluso aislante. En el caso de los semiconductores, el color viene determinado por la energía requerida para crear un excitón (un par hueco-electrón); es decir por la energía del *band gap*.

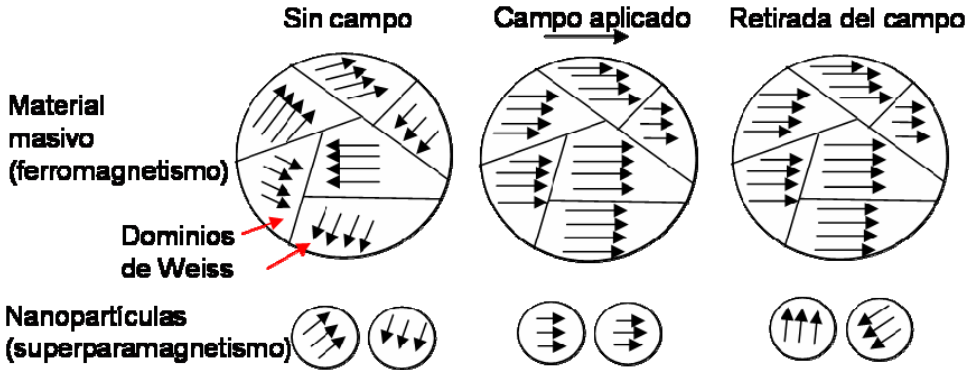


**Figura 3.** Representación de los fenómenos de ferromagnetismo y superparamagnetismo mostrados por el mismo material en sus formas masiva y nanoparticulada, respectivamente.

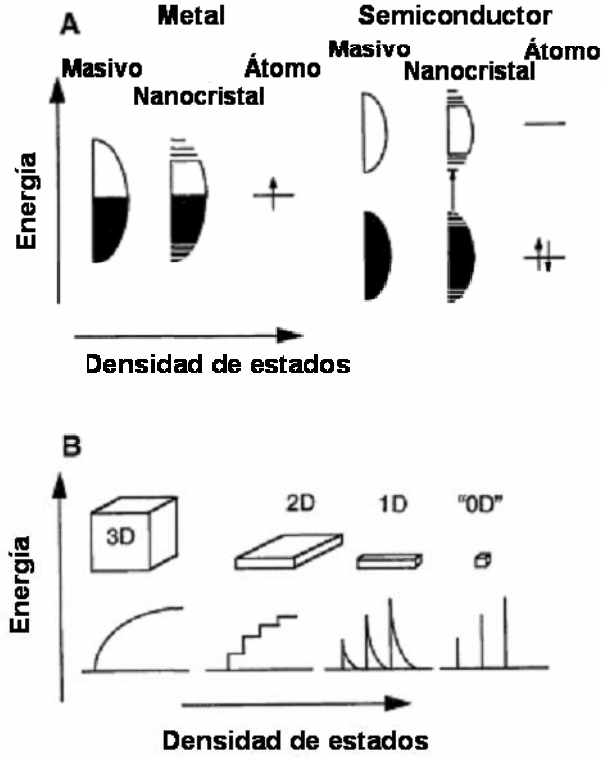


**Figura 4.** (A) Ilustración esquemática de la densidad de estados en materiales metálicos y semiconductores. (B) Densidad de estados en una banda de materiales metálicos y semiconductores en función de su dimensionalidad. Reproducción modificada de la ref. [52].

Puesto que éste aumenta al disminuir el tamaño, se observa un desplazamiento del color hacia el azul al disminuir el tamaño de las NPs. Además, las t bandas electrónicas continuas típicas del material masivo comienzan a desdoblarse, es

decir, adquieren valores discretos de energía. Este fenómeno es debido al hecho de que el llamado *radio del excitón de Bohr*, el cual es la distancia –típicamente de entre 2 y 20 nm– a la que se desplazan los electrones excitados desde su átomo paterno dentro de la red cristalina, se vuelve comparable o menor que el tamaño del cristal, de manera que los excitones encuentran un espacio reducido para ubicarse, lo que conduce a un aumento de la energía del *band gap* y a un aumento de la densidad de portadores de carga (electrones y huecos) en la superficie de la NP. Los portadores de carga se comportan como "la partícula en la caja" típica de la mecánica cuántica.

En general, puede afirmarse que emergen nuevos fenómenos dependientes del tamaño cuando la longitud de la propiedad física se vuelve comparable a la longitud física del objeto que la muestra o que se ve afectado por ella. En el caso del magnetismo, la longitud de la propiedad física viene dada por el tamaño de los dominios de Weiss, mientras que en el caso de los QDs por el radio del excitón de Bohr. Dado que éstos y muchos otros fenómenos físicos poseen longitudes naturales de entre 1 y 100 nm, las NPs exhiben con frecuencia nuevos fenómenos dependientes del tamaño. La relevancia de estos efectos reside en el hecho de que se puede controlar con precisión las propiedades del material en función del tamaño de partícula (en lugar del tradicional control de las propiedades mediante la composición).

La influencia del tamaño en las propiedades magnéticas se discute en el capítulo 1.1, que trata las propiedades magnéticas de NPs de $BaMnO_3$, y en el capítulo 2.1, donde la magnitud de EB se estudia en función del tamaño del núcleo de Ni de NPs $Ni_{núcleo}$-$NiO_{cáscara}$.

**3. Forma**

Existen varias maneras en las cuales la forma determina las características de las NPs, como se ejemplifica en los siguientes binomios:

Conexión forma-tamaño. Por un lado, la forma es el resultado de los distintos tamaños relativos a lo largo de las distintas dimensiones. Por ejemplo, los NRs y los nanohilos (NWs) tienen una forma 1D porque poseen dos distintas distancias: la longitud y el

diámetro, lo que se mide con la relación de aspecto (el cociente entre la longitud y el diámetro). Los NRs tienen una relación de aspecto menor que los NWs.[53,54]

Conexión forma-superficie. Además, la forma condiciona las caras cristalográficas en la superficie y, por tanto, la densidad de enlaces "no satisfechos" responsables de la actividad catalítica.[18,55,56]

Conexión forma-autoensamblado. Por otro lado, la forma también determina las propiedades del material nanoestructurado debido al reconocimiento mutuo a través de distintos patrones de AE. Y *viceversa*: dado una forma macroscópica, es posible inferir una estructura relacionada para los bloques constituyentes de los niveles más bajos de la estructura jerárquica.[57]

La propiedad de la forma se aborda en el capítulo 1.1 de esta tesis en relación a la estabilización de *rods* y NPs de $BaMnO_3$. Asimismo, el capítulo 1.3 describe la formación de nanooctaedros de NiO. Ambos capítulos tratan de medios de reacción ricos en bases fuertes como el KOH y el NaOH, cuyos altos caracteres iónicos podrían ser responsables de la morfología de las NPs. Por otro lado, el AE 1D de NPs de $BaMnO_3$ en *nanorods* se discute en el capítulo 1.1, mientras que el capítulo 3.1 describe el AE 3D de NPs de PbS en estructuras super-ramificadas y jerárquicas. En este último caso, se discute la relación entre las formas de los nanounidades constituyentes y la de los microcristales finales.

En resumen, la forma, íntimamente interrelacionada con el tamaño, la superficie y el autoensamblado, es una variable más a la hora de ganar control y grados de funcionalidad de los nanomateriales.

## 4. Auto-ensamblado

El auto-ensamblado es la organización autónoma de componentes discretos en patrones o estructuras sin la intervención humana.[58] Se trata de un proceso ubicuo en la naturaleza, desde el nivel molecular a la escala planetaria. Los NCs también muestran esa organización colectiva inherente, comportándose como "átomos artificiales" que se combinan autónomamente en estructuras complejas, de la misma manera que los átomos se ordenan en moléculas o en sólidos iónicos y covalentes. De hecho, se ha visto

que el AE gobierna mecanismos de cristalización que tradicionalmente se atribuían al acoplamiento ión a ión. Esto es especialmente cierto para los procesos de biomineralización, donde frecuentemente se detectan mesocristales, que carecen de una fusión perfecta entre NPs, como intermedios de la formación de monocristales.[59-62]

El auto-ensamblado viene gobernado por el balance de fuerzas atractivas (como los enlaces de hidrógeno, las atracciones electrostáticas y las interacciones dipolo-dipolo inducido) y fuerzas repulsivas (como las fuerzas de repulsión estéricas y electrostáticas). Constituye una dirección importante en el diseño de materiales avanzados. En primer lugar, el AE posibilita la síntesis sencilla de morfologías complejas (1D,[63] 2D[64] y 3D[65]), que pueden beneficiarse de las dimensiones nano y micro. En segundo lugar, puede utilizarse para realizar combinaciones simples de distintos tipos de materiales, haciendo uso de las interacciones excitón-plasmón y plasmón-plasmón[66] como plataformas para la biodetección,[67] la conversión de energía, nanotermómetros,[68] y "reglas plasmónicas".[69] Construye de forma autónoma arquitecturas como parejas de NPs[67,69] y agrupaciones de NPs en forma de satélites[68] (*i.e.* "moléculas coloidales"). En tercer lugar, el AE abre el camino a la cristalización de distintas NPs en redes 3D ("cristales coloidales"), con propiedades que resultan del comportamiento colectivo de los componentes eléctricos, magnéticos y ópticos.[41,70-80]

Aunque el AE ocurre de manera espontánea entre las NPs estabilizadas con *ligandos* en medios líquidos, puede manipularse adicionalmente por medio de diversas estrategias,[41,81] tales como el empleo de plantillas,[82-87] el AE en las interfases (como la técnica de Langmuir-Blodgett[88]), el AE asistido bajo la acción de campos eléctricos[89,90] o magnéticos[91,92] y los ensamblajes de NPs en capas por medio de la técnica capa-por-capa.[93]

Por último, aunque hasta la fecha el AE se ha enfocado principalmente hacia el denominado AE estático, el cual considera sistemas que están en equilibrio global o local y no disipan energía, ideas más futuristas contemplan el AE dinámico, aquel que ocurre únicamente si el sistema disipa energía y, por tanto, que define la vida.[40,58]

En esta tesis, en los capítulos 1.1 y 3.1 se recoge la detección de mesocristales durante los procesos de AE de NPs $BaMnO_3$ y PbS, respectivamente.

## 5. Defectos

Los defectos en NCs, como en cualquier otro cristal, rompen la periodicidad y la simetría en la que están emplazados los átomos. La clasificación clásica de la química del estado sólido divide los tipos de defectos de acuerdo a su dimensionalidad:

- Defectos puntuales o 0D: vacantes (la ausencia de un átomo), intersticiales (un átomo extra en la red), átomos descolocados e impurezas (átomos intrusos).
- 1D: dislocaciones (una línea de átomos fuera de lugar).
- 2D: faltas de apilamiento (un plano de átomos descolocado), maclas y fronteras de grano (interfases entre varios granos cristalinos).
- 3D: inclusiones (agrupaciones de átomos intrusos dentro de la red).

Puesto que la superficie de un cristal puede considerarse un defecto, las nanoestructuras muestran una contribución sustancial de defectos debido a su gran área superficial, cuya influencia se extiende a toda la partícula. Paradójicamente, los defectos puntuales en la parte interna de la NP raramente se dan, ya que tienden a ser segregados a la superficie, donde pueden reducir su alta energía. Multitud de propiedades se benefician del defecto de la superficie, como la termoelectricidad,[94] de la segregación de defectos puntuales a la superficie, como el alivio del daño de la radiación,[95] y de la interacción mutua entre defectos, como la dureza ultra-alta y la ductilidad de metales nanomaclados.[96]

Alternativamente, la alta superficie de los nanomateriales puede representar un defecto cuando afecta a la estequiometría. Puesto que los NCs pueden poseer superficies constituidas por planos cristalinos que contengan un solo tipo de átomos y puesto que los átomos en la superficie corresponden a un alto porcentaje del total, la no estequiometría es un efecto destacable en los nanomateriales (*i.e.* es más probable encontrar la estequiometría $Pb_{1.15}S_{0.85}$ que la $Pb_1S_1$). Esto tiene repercusiones en el momento bipolar (MD) de las NPs y, por tanto, en su forma de AE (*i.e.* debido a las diferencias de electronegatividad de los cationes y los aniones del PbS, la distribución de caras polares constituidas exclusivamente por cationes o por aniones es en última instancia responsable de dotar a las NCs con un MD, el cual induce su AE).[97,98]

La existencia de defectos en partes específicas de una nanoestructura puede desencadenar un efecto dominó que se transmita a la microescala y que conduzca a la formación de geometrías fascinantes. Por ejemplo, las dislocaciones con componentes "de tornillo" se pueden propagar anisotrópicamente formando NWs con forma "de pino".[99] Además, se ha demostrado que la fotocorrosión de NPs ensambladas en forma de lazos induce su retorcimiento dando lugar a hélices.[100]

Por consiguiente, los defectos constituyen un grado más de libertad a la hora de modificar las propiedades de los materiales nanoestructurados. Hay un montón de posibilidades para perfeccionar la imperfección (y *viceversa*: el perfeccionar la imperfección generará una multitud de posibilidades).

Esta propiedad se discute en el capítulo 2.1 en relación al papel del desorden estructural de una matriz nanoestructurada de NiO en la correspondiente fenomenología magnética. Además, en el capítulo 3.1 se discute el papel de la no estequiometría de NPs de PbS en su MD y AE. El capítulo 1.1 comenta el papel de la no estequiometría de NPs de $BaMnO_3$ en sus propiedades magnéticas.

# VII. Anexo A

# BIBLIOGRAPHY APPENDIX A / BIBLIOGRAFÍA ANEXO A


1. Schmid, G.; Pfeil, R.; Bo ese, R.; Bandermann, F.; Meyer, S.; Calis, G. H. M.; Vand ervelden, W. A., $Au_{55}[P(C_6h_5)_3]_{12}Cl_6$ - a Gold Cluster of an Exceptional Size. *Chem. Ber.-Recl.* **1981,** 114, (11), 3634-3642.
2. Günter, S.; Bernd, M.; Jan-Olle, M., $Pt_{309}Phen_{36}O_{30} \pm 10$, a Four-Shell Platinum Cluster. *Angewandte Chemie International Edition in English* **1989,** 28, (6), 778-780.
3. Simon, U.; SchÃ¶n, G.; Schmid, G., The application of $Au_{55}$ clusters as quantum dots. *Angewandte Chemie (International Edition in English)* **1993,** 32, (2), 250-254.
4. Schön, G.; Si mon, U., A fascinating n ew field in co lloid scien ce: small lig and-stabilized m etal clusters a nd possible a pplication i n m icroelectronics - Part I: State of the a rt. *Colloid & Polymer Science* **1995,** 273, (2), 101-117.
5. Schmid, G., Larg e clusters and colloids. Metals in the embry onic state. *Chemical Reviews* **1992,** 92, (8), 1709-1727.
6. Schmid, G.; Chi, L. F., Metal clusters and colloids. *Advanced Materials* **1998,** 10, (7), 515-526.
7. Weller, H., C olloidal sem iconductor Q-p articles: Ch emistry in th e tran sition region between so lid state and molecules. *Angewandte Chemie (International Edition in English)* **1993,** 32, (1), 41-53.
8. Schmid, G.; BÃ¤umle, M.; Geerkens, M.; Heim, I.; Osemann, C.; Sawitowski, T., Current and future applications of nanoclusters. *Chemical Society Reviews* **1999,** 28, (3), 179-185.
9. Ozin, G. A. and Arsenault, A. C., *Nanochemistry*. RSC Publishing: **2005**; p 266.
10. Graham, T. H., *Philos. Trans. R. Soc. London* **1861,** 151, 183-196.
11. Fendler, J. H.; Meldrum, F. C., The colloid chemical approach to nanostructured materials. *Advanced Materials* **1995,** 7, (7), 607-632.
12. Brinker, C. Jeffrey and Scherer, G. W., *Sol-gel Science*. Academic Press, INC.: **1990**.
13. Cademartiri, L. and Ozin, G.A., *Concepts of Nanochemistry*. Wiley-VCH: **2009**; p 21.
14. Cademartiri, L. and Ozin, G.A., *Concepts of Nanochemistry*. Wiley-VCH: **2009**.
15. Goesmann, H .; Fel dmann, C ., Nan oparticulate funct ional m aterials. *Angewandte Chemie - International Edition* **2010,** 49, (8), 1362-1395.
16. Manna, L.; Milliron, D. J.; Meisel, A.; Sch er, E. C.; Alivisatos, A. P., Controlled growth of tetrapod-branched inorganic nanocrystals. *Nature Materials* **2003,** 2, (6), 382-385.
17. Jun, Y. W.; Lee, J. H.; C hoi, J. S.; C heon, J., Sy mmetry-controlled colloidal n anocrystals: Nonhydrolytic chemical synthesis and shape determining parameters. *Journal of Physical Chemistry B* **2005,** 109, (31), 14795-14806.
18. Liao, H. G.; Jiang, Y. X .; Zhou, Z. Y.; Chen, S. P.; Sun, S. G. , Shape-controlled synthesis of g old nanoparticles in d eep eu tectic so lvents for st udies of stru cture-functionality relatio nships in electrocatalysis. *Angewandte Chemie - International Edition* **2008,** 47, (47), 9100-9103.
19. Liu, M.; Piao, L.; Lu, W.; Ju, S.; Z hao, L. ; Zhou, C.; Li, H.; Wang, W., Flow er-like $TiO_2$ nanostructures with e xposed {001} facets: Facile synthesi s and enha nced photocatalysis. *Nanoscale* **2010,** 2, (7), 1115-1117.
20. Iijima, S., Helical microtubules of graphitic carbon. *Nature* **1991,** 354, (6348), 56-58.
21. Frey, M. H.; Payne, D. A., Gr ain-size effect on st ructure a nd phase t ransformations f or barium titanate. *Physical Review B - Condensed Matter and Materials Physics* **1996,** 54, (5), 3158-3168.
22. Lozano-Perez, S.; de C astro Bernal, V .; Nicholls, R. J., Achieving sub-nanometre particle mapping with energy-filtered TEM. *Ultramicroscopy* **2009,** 109, (10), 1217-1228.
23. Shibata, T.; B unker, B. A.; Zhang, Z.; Meisel, D.; Vardeman, C. F.; Gezelter, J. D., Size-dependent spontaneous alloying of Au-Ag nanoparticles. *Journal of the American Chemical Society* **2002,** 124, (40), 11989-11996.
24. Eccles, J. W. L.; Bangert, U.; Bromfield, M.; C hristian, P.; Ha rvey, A. J., D o nanomaterials fo rm truly homogeneous alloys? *Journal of Applied Physics* **2010,** 107, (10).
25. Bell, A. T., The impact of nanoscience on heterogeneous catalysis. *Science* **2003,** 299, (5613), 1688-1691.
26. Alejandro-Arellano, M.; Ung, T.; Blanco, Á.; Mulvaney, P.; Liz-Marzán, L. M., Silica-coated metals and semiconductors. Stabilization and nanostructuring. *Pure and Applied Chemistry* **2000,** 72, (1-2), 257-267.
27. Peng, D. L.; Sumiyama, K .; H ihara, T.; Y amamuro, S.; K onno, T. J., Magn etic pr operties of monodispersed C o/CoO cl usters. *Physical Review B - Condensed Matter and Materials Physics* **2000,** 61, (4), 3103-3109.

28. Salazar-Alvarez, G.; Sort, J .; SuriÃ±ach, S.; BarÃ³ , M. D.; NoguÃ©s, J., Sy nthesis and size-dependent exchange bias in inverted core-shell MnO|$Mn_3O_4$ nanoparticles. *Journal of the American Chemical Society* **2007,** 129, (29), 9102-9108.
29. Nogués, J.; Sort, J.; Langlais, V.; Skumryev, V.; Suriñach, S.; Muñoz, J. S.; Baró, M. D., Exchange bias in nanostructures. *Physics Reports* **2005,** 422, (3), 65-117.
30. Templeton, A. C.; Wuelfing, W. P.; M urray, R. W., Monolayer-protected clust er m olecules. *Accounts of Chemical Research* **2000,** 33, (1), 27-36.
31. Garcia, M. A.; Merino, J. M.; Pinel, E. F.; Quesada, A.; De La Venta, J.; González, M. L. R.; Castro, G. R.; Crespo , P.; Llop is, J.; González-Calbet, J. M .; Hernando, A ., M agnetic p roperties of Z nO nanoparticles. *Nano Letters* **2007,** 7, (6), 1489-1494.
32. Cui, Y.; Wei, Q.; Park , H.; Lieber, C . M., Na nowire n anosensors for h ighly sensitiv e and selectiv e detection of biological and chemical species. *Science* **2001,** 293, (5533), 1289-1292.
33. Wang, W. U.; Chen, C.; Lin, K. H.; Fang, Y.; Lieber, C. M., Label-free detection of small-molecule-protein interactions by using nan owire n anosensors. *Proceedings of the National Academy of Sciences of the United States of America* **2005,** 102, (9), 3208-3212.
34. Kneipp, K.; Wang, Y.; Kneip p, H.; Perelman , L. T. ; Itzkan, I.; Dasari, R. R.; Feld, M. S., Single molecule detection using surface-enhanced Raman scattering (SERS). *Physical Review Letters* **1997,** 78, (9), 1667-1670.
35. Lee, I. S.; Lee , N.; Pa rk, J.; Kim, B. H.; Yi, Y. W.; Kim , T.; Kim , T. K.; Lee, I. H.; Paik , S. R.; Hyeon, T., Ni/NiO co re/shell nanoparticles fo r selectiv e binding an d m agnetic separation of histidine-tagged proteins. *Journal of the American Chemical Society* **2006,** 128, (33), 10658-10659.
36. Lee, K. B.; Park, S.; Mirkin, C. A., Multicom ponent magnetic nanorods for biom olecular separations. *Angewandte Chemie - International Edition* **2004,** 43, (23), 3048-3050.
37. Bao, J.; C hen, W.; Li u, T.; Zh u, Y.; Jin, P.; Wang, L.; Liu, J.; Wei, Y.; Li, Y., Bifu nctional Au-Fe3O4 nanoparticles for protein separation. *ACS nano* **2007,** 1, (4), 293-298.
38. McCarthy, J. R.; Kelly, K. A.; Su n, E. Y.; Weissleder, R., Targ eted delivery of m ultifunctional magnetic nanoparticles. *Nanomedicine* **2007,** 2, (2), 153-167.
39. Hede, S.; Huilgol, N., " Nano": The new nemesis of cancer . *Journal of Cancer Research and Therapeutics* **2006,** 2, (4), 186-195.
40. Grzybowski, B . A.; Wilmer, C. E.; Kim , J.; Brow ne, K. P .; Bishop, K. J. M., Self-assembly: From crystals to cells. *Soft Matter* **2009,** 5, (6), 1110-1128.
41. Nie, Z.; Pet ukhova, A.; Kumacheva, E ., Properties and e merging app lications of self-assem bled structures made from inorganic nanoparticles. *Nature Nanotechnology* **2010,** 5, (1), 15-25.
42. Choi, C. L.; Aliv isatos, A. P., Fro m art ificial ato ms to na nocrystal m olecules: Pr eparation an d properties of more complex nanostructures. In *Annual Review of Physical Chemistry*, 2010; Vol. 61, pp 369-389.
43. Costi, R .; Sa unders, A . E .; Banin, U ., C olloidal hy brid nanostructures: A new t ype of f unctional materials. *Angewandte Chemie - International Edition* **2010,** 49, (29), 4878-4897.
44. Nie, Z.; Fava, D.; Kumacheva, E.; Zou , S.; Walker, G. C.; Ru binstein, M., Self-assem bly o f metal-polymer analogues of amphiphilic triblock copolymers. *Nature Materials* **2007,** 6, (8), 609-614.
45. Park, H. S.; Agarwal, A.; Kotov, N. A.; Lavrentovich, O. D., Controllable side-by-side and end-to-end as sembly of Au nanorods by l yotropic chr omonic m aterials. *Langmuir* **2008,** 24 , (24), 1 3833-13837.
46. Buffat, P.; Borel, J. P ., Size effect on the melting temperature of gold particles. *Physical Review A* **1976,** 13, (6), 2287-2298.
47. Schmidt, M.; Kusche, R.; Von Issendorff, B.; Haberland, H., Irregular variations in the melting point of size-selected atomic clusters. *Nature* **1998,** 393, (6682), 238-240.
48. Goldstein, A. N.; Echer, C. M.; Alivisatos, A. P., Melting in sem iconductor n anocrystals. *Science* **1992,** 256, (5062), 1425-1427.
49. Grätzel, M., The magic world of nanocrystals, from batteries to solar cells. *Current Applied Physics* **2006,** 6, (SUPPL. 1).
50. Aricò, A. S.; Bruce, P.; Scrosati, B.; Tarascon, J. M .; Van Schalkwijk, W., Nanostructured materials for advanced energy conversion and storage devices. *Nature Materials* **2005,** 4, (5), 366-377.
51. Liz-Marzán, L. M. a. G. M. E., *Low-Dimensional Systems: Theory, Preparation, and Some Applications*. **2003**; Vol. Kluwer Academic Publishers, p 173-192.
52. Alivisatos, A . P., Semiconductor cl usters, na nocrystals, an d q uantum d ots. *Science* **1996,** 27 1, (5251), 933-937.
53. Rodríguez-Lorenzo, L.; Ál varez-Puebla, R. A.; De Aba jo, F. J. G.; Liz-Marzán, L. M., Surface enhanced R aman scat tering usi ng st ar-shaped gold col loidal nan oparticles. *Journal of Physical Chemistry C* **2010,** 114, (16), 7336-7340.

54. Huang, X.; El-Sayed, I. H.; Qian, W.; El-Sayed, M. A., Cancer cell imaging and photothermal therapy in the near-infrared region by using gold nanorods. *Journal of the American Chemical Society* **2006,** 128, (6), 2115-2120.
55. Narayanan, R.; El-Sayed, M. A., Shape-dependent catalytic activity of platinum nanoparticles in colloidal solution. *Nano Letters* **2004,** 4, (7), 1343-1348.
56. Sanles-Sobrido, M.; Correa-Duarte, A.; Carregal-Romero, S.; Rodríguez-González, B.; Álvarez-Puebla, R. A.; Hervás, P.; Liz-Marzán, L. M., Highly catalytic single-crystal dendritic Pt nanostructures supported on carbon nanotubes. *Chemistry of Materials* **2009,** 21, (8), 1531-1535.
57. Phillips, F. C., *Introducción a la cristalografía*. Paraninfo: Madrid, 1978; p 53.
58. Whitesides, G. M.; Grzybowski, B., Self-assembly at all scales. *Science* **2002,** 295, (5564), 2418-2421.
59. Cölfen, H.; Antonietti, M., Mesocrystals: Inorganic superstructures made by highly parallel crystallization and controlled alignment. *Angewandte Chemie - International Edition* **2005,** 44, (35), 5576-5591.
60. Cölfen, H.; Mann, S., Higher-order organization by mesoscale self-assembly and transformation of hybrid nanostructures. *Angewandte Chemie - International Edition* **2003,** 42, (21), 2350-2365.
61. Niederberger, M.; Cölfen, H., Oriented attachment and mesocrystals: Non-classical crystallization mechanisms based on nanoparticle assembly. *Physical Chemistry Chemical Physics* **2006,** 8, (28), 3271-3287.
62. Song, R. Q.; Cölfen, H., Mesociystals - Ordered nanoparticle superstructures. *Advanced Materials* **2010,** 22, (12), 1301-1330.
63. Tang, Z.; Kotov, N. A.; Giersig, M., Spontaneous organization of single CdTe nanoparticles into luminescent nanowires. *Science* **2002,** 297, (5579), 237-240.
64. Tang, Z.; Zhang, Z.; Wang, Y.; Glotzer, S. C.; Kotov, N. A., Self-assembly of CdTe nanocrystals into free-floating sheets. *Science* **2006,** 314, (5797), 274-278.
65. Zhang, Z.; Sun, H.; Shao, X.; Li, D.; Yu, H.; Han, M., Three-dimensionally oriented aggregation of a few hundred nanoparticles into monocrystalline architectures. *Advanced Materials* **2005,** 17, (1), 42-47.
66. Sebba, D. S.; Mock, J. J.; Smith, D. R.; LaBean, T. H.; Lazaridis, A. A., Reconfigurable core-satellite nanoassemblies as molecularly-driven plasmonic switches. *Nano Letters* **2008,** 8, (7), 1803-1808.
67. Lee, J.; Hernandez, P.; Lee, J.; Govorov, A. O.; Kotov, N. A., Exciton-plasmon interactions in molecular spring assemblies of nanowires and wavelength-based protein detection. *Nature Materials* **2007,** 6, (4), 291-295.
68. Lee, J.; Govorov, A. O.; Kotov, N. A., Nanoparticle assemblies with molecular springs: A nanoscale thermometer. *Angewandte Chemie - International Edition* **2005,** 44, (45), 7439-7442.
69. Sönnichsen, C.; Reinhard, B. M.; Liphardt, J.; Alivisatos, A. P., A molecular ruler based on plasmon coupling of single gold and silver nanoparticles. *Nature Biotechnology* **2005,** 23, (6), 741-745.
70. Shevchenko, E. V.; Talapin, D. V.; Kotov, N. A.; O'Brien, S.; Murray, C. B., Structural diversity in binary nanoparticle superlattices. *Nature* **2006,** 439, (7072), 55-59.
71. Rogach, A. L.; Talapin, D. V.; Shevchenko, E. V.; Kornowski, A.; Haase, M.; Weller, H., Organization of matter on different size scales: Monodisperse nanocrystals and their superstructures. *Advanced Functional Materials* **2002,** 12, (10), 653-664.
72. Redl, F. X.; Cho, K. S.; Murray, C. B.; O'Brien, S., Three-dimensional binary superlattices of magnetic nanocrystals and semiconductor quantum dots. *Nature* **2003,** 423, (6943), 968-971.
73. Leunissen, M. E.; Christova, C. G.; Hynninen, A. P.; Royall, C. P.; Campbell, A. I.; Imhof, A.; Dijkstra, M.; Van Roij, R.; Van Blaaderen, A., Ionic colloidal crystals of oppositely charged particles. *Nature* **2005,** 437, (7056), 235-240.
74. Shevchenko, E. V.; Talapin, D. V.; O'Brien, S.; Murray, C. B., Polymorphism in $AB_{13}$ nanoparticle superlattices: An example of semiconductor-metal metamaterials. *Journal of the American Chemical Society* **2005,** 127, (24), 8741-8747.
75. Kalsin, A. M.; Fialkowski, M.; Paszewski, M.; Smoukov, S. K.; Bishop, K. J. M.; Grzybowski, B. A., Electrostatic self-assembly of binary nanoparticle crystals with a diamond-like lattice. *Science* **2006,** 312, (5772), 420-424.
76. Shevchenko, E. V.; Talapin, D. V.; Murray, C. B.; O'Brien, S., Structural characterization of self-assembled multifunctional binary nanoparticle superlattices. *Journal of the American Chemical Society* **2006,** 128, (11), 3620-3637.
77. Shevchenko, E. V.; Kortright, J. B.; Talapin, D. V.; Aloni, S.; Alivisatos, A. P., Quasi-ternary nanoparticle superlattices through nanoparticle design. *Advanced Materials* **2007,** 19, (23), 4183-4188.

78. Talapin, D. V.; Shevchenko, E. V.; Bodnarchuk, M. I.; Ye, X.; Chen, J.; Murray, C. B., Quasicrystalline order in self-assembled binary nanoparticle superlattices. *Nature* **2009,** 461, (7266), 964-967.
79. Evers, W. H.; Friedrich, H.; Filion, L.; Dijkstra, M.; Vanmaekelbergh, D., Observation of a ternary nanocrystal superlattice and its structural characterization by electron tomography. *Angewandte Chemie - International Edition* **2009,** 48, (51), 9655-9657.
80. Podsiadlo, P.; Krylova, G.; Lee, B.; Critchley, K.; Gosztola, D. J.; Talapin, D. V.; Ashby, P. D.; Shevchenko, E. V., The role of order, nanocrystal size, and capping ligands in the collective mechanical response of three-dimensional nanocrystal solids. *Journal of the American Chemical Society* **2010,** 132, (26), 8953-8960.
81. Grzelczak, M.; Vermant, J.; Furst, E. M.; Liz-Marzán, L. M., Directed Self-Assembly of Nanoparticles. *ACS Nano* **2010,** 4, (7), 3591-3605.
82. Correa-Duarte, M. A.; Pérez-Juste, J.; Sánchez-Iglesias, A.; Giersig, M.; Liz-Marzán, L. M., Aligning Au nanorods by using carbon nanotubes as templates. *Angewandte Chemie - International Edition* **2005,** 44, (28), 4375-4378.
83. Dujardin, E.; Peet, C.; Stubbs, G.; Culver, J. N.; Mann, S., Organization of metallic nanoparticles using tobacco mosaic virus templates. *Nano Letters* **2003,** 3, (3), 413-417.
84. Aldaye, F. A.; Palmer, A. L.; Sleiman, H. F., Assembling materials with DNA as the guide. *Science* **2008,** 321, (5897), 1795-1799.
85. Warner, M. G.; Hutchison, J. E., Linear assemblies of nanoparticles electrostatically organized on DNA scaffolds. *Nature Materials* **2003,** 2, (4), 272-277.
86. Yin, Y.; Lu, Y.; Gates, B.; Xia, Y., Template-assisted self-assembly: A practical route to complex aggregates of monodispersed colloids with well-defined sizes, shapes, and structures. *Journal of the American Chemical Society* **2001,** 123, (36), 8718-8729.
87. Gutiérrez, M. C.; Ferrer, M. L.; Del Monte, F., Ice-templated materials: Sophisticated structures exhibiting enhanced functionalities obtained after unidirectional freezing and ice-segregation-induced self-assembly. *Chemistry of Materials* **2008,** 20, (3), 634-648.
88. Tao, A. R.; Huang, J.; Yang, P., Langmuir-Blodgettry of nanocrystals and nanowires. *Accounts of Chemical Research* **2008,** 41, (12), 1662-1673.
89. Hermanson, K. D.; Lumsdon, S. O.; Williams, J. P.; Kaler, E. W.; Velev, O. D., Dielectrophoretic assembly of electrically functional microwires from nanoparticle suspensions. *Science* **2001,** 294, (5544), 1082-1086.
90. Ryan, K. M.; Mastroianni, A.; Stancil, K. A.; Liu, H.; Alivisatos, A. P., Electric-field-assisted assembly of perpendicularly oriented nanorod superlattices. *Nano Letters* **2006,** 6, (7), 1479-1482.
91. Sheparovych, R.; Sahoo, Y.; Motornov, M.; Wang, S.; Luo, H.; Prasad, P. N.; Sokolov, I.; Minko, S., Polyelectrolyte stabilized nanowires from $Fe_3O_4$ nanoparticles via magnetic field induced self-assembly. *Chemistry of Materials* **2006,** 18, (3), 591-593.
92. Lalatonne, Y.; Richardi, J.; Pileni, M. P., Van der Waals versus dipolar forces controlling mesoscopic organizations of magnetic nanocrystals. *Nature Materials* **2004,** 3, (2), 121-125.
93. Kotov, N. A., *Nanoparticle Assemblies and Superstructures*. CRC Press, Taylor & Francis Group: **2006**.
94. Dresselhaus, M. S.; Chen, G.; Tang, M. Y.; Yang, R.; Lee, H.; Wang, D.; Ren, Z.; Fleurial, J. P.; Gogna, P., New directions for low-dimensional thermoelectric materials. *Advanced Materials* **2007,** 19, (8), 1043-1053.
95. Bai, X. M.; Voter, A. F.; Hoagland, R. G.; Nastasi, M.; Uberuaga, B. P., Efficient annealing of radiation damage near grain boundaries via interstitial emission. *Science* **2010,** 327, (5973), 1631-1634.
96. Wu, Z. X.; Zhang, Y. W.; Srolovitz, D. J., Dislocation-twin interaction mechanisms for ultrahigh strength and ductility in nanotwinned metals. *Acta Materialia* **2009,** 57, (15), 4508-4518.
97. Cho, K. S.; Talapin, D. V.; Gaschler, W.; Murray, C. B., Designing PbSe nanowires and nanorings through oriented attachment of nanoparticles. *Journal of the American Chemical Society* **2005,** 127, (19), 7140-7147.
98. Shanbhag, S.; Kotov, N. A., On the origin of a permanent dipole moment in nanocrystals with a cubic crystal lattice: Effects of truncation, stabilizers, and medium for CdS tetrahedral homologues. *Journal of Physical Chemistry B* **2006,** 110, (25), 12211-12217.
99. Lau, Y. K. A.; Chernak, D. J.; Bierman, M. J.; Jin, S., Formation of PbS nanowire pine trees driven by screw dislocations. *Journal of the American Chemical Society* **2009,** 131, (45), 16461-16471.
100. Srivastava, S.; Santos, A.; Critchley, K.; Kim, K. S.; Podsiadlo, P.; Sun, K.; Lee, J.; Xu, C.; Lilly, G. D.; Glotzer, S. C.; Kotov, N. A., Light-controlled self-assembly of semiconductor nanoparticles into twisted ribbons. *Science* **2010,** 327, (5971), 1355-1359.

# APPENDIX B / ANEXO B
# GENERAL STRATEGIES FOR THE PREPARATION OF NANOSTRUCTURED INORGANIC FUNCTIONAL MATERIALS / ESTRATEGIAS GENERALES PARA LA PREPARACIÓN DE MATERIALES FUNCIONALES INORGÁNICOS NANOESTRUCTURADOS

# APPENDIX B
# General Strategies for the Preparation of Nanostructured Functional Materials

The key step for achieving a nanostructured functional material is its preparation, which involves the conversion of primitive raw components into useful nanostructured solids displaying certain features which allows the functionality. Actually, synthesis allows the creation of new materials which are not found in nature, possessing thus a huge potential for discovery, for making possible the impossible, for realizing the unreal. Synthesis methods for NPs are generally grouped into two main categories: top-down and bottom-up. In a bottom-up procedure individual atoms/molecules react to build a nanosized entity; *i.e.* the construction is realized from the smallest components, as if a puzzle or a house were built up from the building units or bricks and glue, respectively. On the contrary, top-down approach starts from the bulk material and a controlled destruction sculptures it into a nanostructured pattern. Usually bottom-up strategies are associated with chemical synthesis,[1-3] while top-down are addressed from physical processing techniques, like lithography, laser ablation, arc-discharge, vapor deposition, pulsed-laser deposition, mechanical milling, *etc.*[4] While top-down approaches access nanostructured materials with high quality in terms of crystallinity, monodispersity, 3D patterning…, they are neither cost- nor time-effective, and exhibit a shortage of flexibility for the tailoring of the features (composition, surface, size, shape, defects, SA) of nanostructured materials.

In the present thesis, the topic of nanostructured functional materials is tackled from a chemistry perspective, from bottom-up synthetic pathways. This section overviews the state of the art of the existing chemical approaches for the synthesis of nanostructured materials.

Given that NPs are metastable, they tend to aggregate and sinter under the reaction conditions, so the main endeavor when designing a chemical synthetic pathway is focused on strategies preventing NPs from aggregation. The general prospect is to protect the NP's surface with a foreign agent. According to the aggregation state of the protecting agent or the medium containing it, chemical strategies for the synthesis of

NPs can be divided in two main blocks: a) solid-matrix methods and b) liquid-phase routes. In all the cases, the use of mild temperatures of reaction is desired to minimize gaining thermodynamics; *i.e.* to minimize the aggregation.

**a) Solid-matrix methods**

Solid matrices act as a physical barrier preventing NPs from uncontrolled aggregation. Inorganic ones such as silica (in its mesoporous or xerogel forms),[5-8] mesoporous carbon[9] or carbon nanotubes[10, 11] offer hard confined spaces or nanoreactors formed by their voids/porosity, making it possible to avoid the uncontrolled growth of the target material from the solution containing the building ions. In general, inorganic solid matrices act as hard- or exo-templates. The term "template" connotes a 1:1 correspondence between the shape of the matrix playing the role of template and the void remaining after template removal.[12, 13] This is the case of the mentioned examples, where the organized voids/porosity leads to the exact replication of the void organization into the inorganic final product. This way, the connectivity of the templating solid is eventually responsible for the connectivity of the final product: a solid consisting of two continuous solid and pore phases leads to the same but inverted architecture in the final inorganic product, whereas a solid with non-connected pores/voids leads to inorganic NPs, although some aggregation of the NPs occurs after the template removal.[12] The removal of the hard-template is typically undertaken through calcination for carbons and carbon nanotubes and through dissolution with sodium hydroxide for silica.

Nevertheless, solid-matrix methods are not restricted to inorganic matrices. Organic ones can shelter inorganic precursors which are crystallized to NCs within confined spaces. The mixing of the metallic reactants and the organics is normally realized in liquid media to ensure a molecular-level mixing, avoiding diffusion barrier typical of solid state synthesis.[14] Usually, the matrix is not involved only physically, but also chemically.[15] In this sense, polymer-like extended molecules are formed through covalent bonding between the metal and the oxygen atoms from the organics. A final step of calcination is required to i) crystallize the NPs within the confined spaces of the polymeric matrix and/or ii) eliminate the matrix by self-combustion isolating thus the NPs. Calcination temperatures typically range between 250-900 ºC, which is a

stumbling block because it leads to the lack of control over particle size, size distribution, shape, aggregation, SA, defects and composition. In this sense, binary metal nanooxides, *i.e.* those containing one type of metal atom, are frequently the only NPs which can be obtained because high temperatures favor the segregation of phases. Besides, impurity phases such as alkaline earth carbonates are prone to contaminate the desired product. Control over the features of the NPs is mainly limited to variations of calcination temperature. A common feature of the as-prepared NPs, which can be pros or cons depending on the application, is their ligand-free surface. As opposite to many inorganic solid matrices, organic hard ones less frequently belong to the notion "template" due to the lack of defined voids that can be replicated into a NC's shape.

One of the most widely employed organic-solid-matrix method is the sol-gel.[16] Briefly, metal alkoxides, such as tetraethyl orthosilicate –TEOS–, $Si(OC_2H_5)_4$, are hydrolyzed by water forming metal-hydroxyl bonds (Eq. 1) and, subsequently, partially hydrolyzed molecules are condensed forming metal-O-metal bonds and releasing molecules of alcohol or water (Eq. 2). This process of polymerization continues building larger molecules, yielding first a sol and finally a gel. Aging and annealing of the solid result in the inorganic nanostructured material ($SiO_2$ in the example).

$$Si(OR)_4 + H_2O \rightarrow HO\text{-}Si(OR)_3 + ROH \quad (1)$$

$$(OR)_3Si\text{-}OH + OH\text{-}Si(OR)_3 \rightarrow (OR)_3Si\text{-}O\text{-}Si(OR)_3 + H_2O \quad (2)$$

Alternatively, other gels containing the desired metal can be prepared from compounds different from alcoxides. In general, (poly)-alcohol and (poly)-carboxylic acid moieties are suitable for the preparation of metalorganic gels via chelating of the metal (formation of several oxygen-metal bonds). Subsequent condensation and combustion reactions lead to the nanostructured metallic oxides.[17] Those types of routes are collectively referred as the Pechini method.[18] For example, metallic hydroxide gels can be prepared from the metallic chlorides/nitrates and sodium hydroxide in water or ethanol medium. Annealing at 250-600 ºC leads to the metallic oxide NPs.[19, 20] Citric acid,[21] ethylenediaminetetraacetic acid (EDTA)[22] and polyvinyl alcohol (PVA)[23] are well-known chelating agents for Pechini type synthesis. Further examples are glycerol ($CH_2OH\text{-}CHOH\text{-}CH_2OH$)[24], malic acid ($HO_2C\text{-}CH_2\text{-}CHOH\text{-}CO_2H$)[25] and oxalic acid ($HO_2C\text{-}CO_2H$)[26], whose mixtures with metallic nitrates/acetates result in the

corresponding gels which upon calcination at 400-450 ºC yields the corresponding binary metallic oxide NPs. Glycine ($NH_2$-$CH_2$-COOH) has been used for the synthesis of multinary oxide nanostructured powders with perovskite structure and different compositions.[27, 28] Cellulose has also allowed the successful preparation of perovskite-type nanooxides through calcination at 400-800 ºC.[29]

Although widely applied for the synthesis of nano-sized oxides, organic-matrix calcination methods have been extended to nitrides,[30-34] oxynitrides[35] and carbides.[34] In this sense, the use of urea ($H_2N$-CO-$NH_2$) as a source of nitrogen and carbon combined with the suitable atmosphere to avoid oxidation is the general strategy.

In chapter 2 of this thesis, the use of a polymeric organic matrix formed by thermal treatment of urea is described for the synthesis of NiO, $Ni_{core}$-$NiO_{shell}$ and other binary oxide NPs such as $Co_3O_4$ and $Mn_3O_4$.

**b) Liquid-phase routes**

Liquid phase routes offer the advantage of enabling the use of milder temperatures of reaction as well as a broad range of synthetic strategies to have control over the features of the as-prepared nanostructured materials. The crystallization of a solid in a homogeneous liquid medium is governed by two fundamental stages: nucleation and growth.[36] The nucleation is driven by supersaturation –higher concentration than the corresponding to the saturation point–[37] and leads to small embryonic nuclei which are thought to be metal clusters with magic numbers.[38] Both thermodynamic (involving the formation of more stable solid-solid interfaces) and entropic (involving the desorption of solvent molecules from the solid surface) factors point towards the growth of the nuclei. The four most typical growth mechanisms are: ion-to-ion attachment, NC's SA (which involves a collective organization), aggregation and sintering (aggregation involves a random agglomeration of NPs and sintering is the collapse of pores driven by surface energy) and Ostwald ripening or coarsening, which is associated with the enlargement of larger crystals at the expense of smaller unstable ones, which are dissolved and incorporated back into the more stable, larger NCs. For attaining monodispersed NCs, two crucial requisites must be fulfilled: i) separation of nucleation and growth and ii) growth prohibition.

The first requirement –separation of nucleation and growth– can be achieved by means of a burst nucleation according to the LaMer-Dinegar plot.[39] In turn, this is attainable through a high sudden supersaturation in order that many equally-sized nuclei are generated at once. If such monodisperse nuclei are allowed to grow from the incorporation of the precursor with neither further nucleation, on one hand, or NCs SA/Ostwald ripening growth mechanisms, on the other, then monodisperse NCs are stabilized in solution. Experimentally, the burst nucleation can be achieved via high precursors concentration, rapid heating rates in heating-up methods,[40] hot-injection of the reactants,[41, 42] changes of pH, chemical reactions (such as reduction of metals), *etc.* Alternatively, nucleation and growth can be physically separated by means of the use of preformed seeds. In this sense, the seed-mediated growth method[43-45] consists in the slow addition of precursor to the solution containing the preformed nuclei, which leads to the selective precipitation of the material on the surface of the existing nuclei instead of the formation of additional nuclei through homogeneous nucleation. The preference of the heterogeneous over the homogeneous nucleation is driven by the lower demand of energy from the former and it can be employed either for the production of homogeneous particles[43, 44] or heterogeneous ones,[46, 47] such as symmetric core-shell structures,[45] nonsymmetric dimmers[48, 49] and NP-nanorod heterostructures.[50, 51]

As concerns the prohibition of growth (via NCs SA and aggregation-sintering, chiefly, and Ostwald ripening, secondly), it is feasible by means of two main strategies of surface stabilization: a) electrostatic and b) steric repulsion. Regarding the former, if the NC's surfaces are coated with adsorbed cations or anions, the repulsive Coulombic forces between positively and negatively charges, respectively, hamper the aggregation/assembly of the nano-sized crystals. Experimentally, this can be performed by means of high alkaline solutions (*i.e.* use of strong Brönsted bases, such as NaOH or KOH) or via surface functionalization with charged molecules such as amines, which can be protonated under acidic conditions. The second type of surface stabilization deals with the steric repulsion of ligand-stabilized NCs and is related to van der Waals repulsive forces.[52] Ligands or capping agents are organic molecules which can be attached to the NP's surface either through covalent bonds with the suitable functional group or through electrostatic interaction. Figure 1 shows a schematic illustration of the chemical strategies mentioned above for the synthesis of NPs.

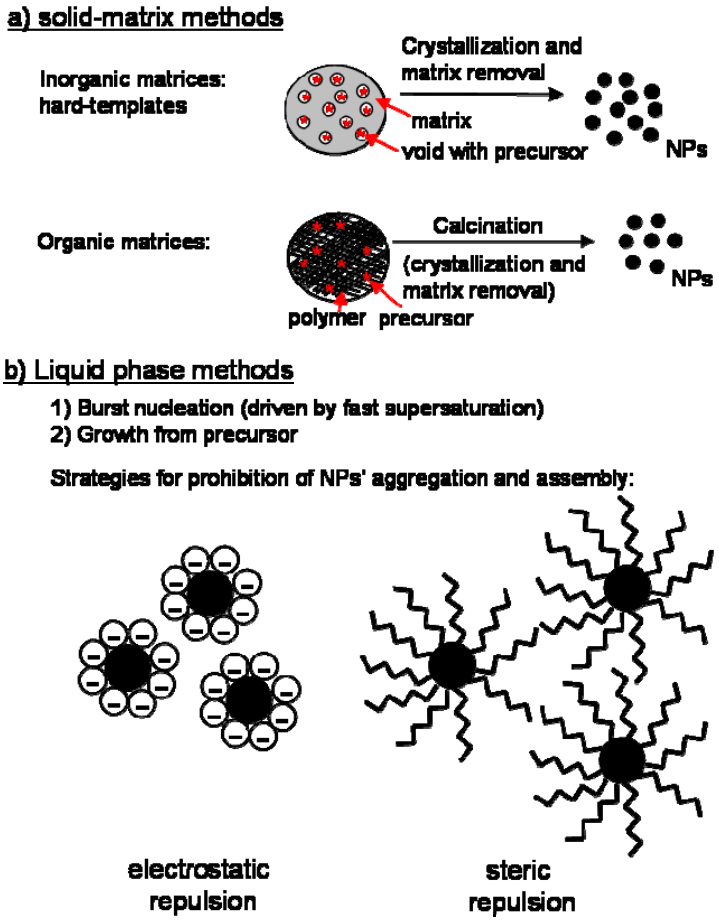


**Figure 1.** Schematic illustration of the chemical strategies for the synthesis of nanoparticles.

According to the type of precursor and synthetic strategy, liquid-based methods for the preparation of NCs can be grouped into two classical groups: 1) decomposition of metalorganic precursors in hot-boiling-point solvents and 2) reduction of metallic salts. In both cases, a suitable surface functionalization is needed. In the first type of methods, typical capping agents are carboxylic acids (oleic acid –OLEA–), amines (hexadecylamine –HDA–, oleylamine – OA–, *etc.*) and alkylphosphines (tributylphosphine –TBP–, trioctylphosphine –TOP–, trioctylphosphine oxide –TOPO–, *etc.*). Such long-hydrocarbon-chain capping agents form covalent bonds with metals leading to metalorganic non-polar precursors whose thermolysis either via heating-up or hot- injection in hot-boiling-point organic solvents (such as oleic acid, octyl ether, hexadecane, trioctylamine, *etc.*, $T_{reaction}$ is ca. 300 ºC) leads to the successful preparation of monodisperse NCs with a multitude of compositions. From metals,[53, 54] metal oxides,[55] metal sulfides[56] to multinary (including quaternary)[57, 58] and hybrid[47] nano-sized compounds, this route provides a versatile access, which even has proven to be ultra-large-scale[40]. Particle size can be finely tuned by variation of the reaction

conditions. A variant of the method is the decomposition of organometallic compounds, such as metal carbonyls.[59] However, these frequently act as mere precursors for the formation of metalorganic intermediates, which are the ones undergoing thermolysis and leading to the formation of the NCs.[55, 60]

As concerns the reduction of metallic salts, this mild route (temperatures are normally < 100 ºC) is typically employed for the size-selective and shape-controlled preparation of noble and transition metals.[18, 61-64] The suitable reducing agent is determined by the negative reduction potential of the metal. In this sense, transition metal cations such as $Ni^{2+}$, $Co^{2+}$ and $Fe^{2+}$ require of a strong reducing agent such as sodium borohydride ($NaBH_4$), sodium hypophosphite ($NaH_2PO_2$) or hydrazine ($NH_2NH_2$). On the contrary, noble metal cations such as $Ag^{+}$ and $Au^{3+}$ are normally more easily reduced, so milder reducing agents such as sodium citrate, ascorbic acid, formamide or N, N-dimethylformamide (DMF) are suitable. Besides, alcohols possess the ability to act concomitantly as reducing agents and solvents. In this sense, single alcohols such as ethanol can be problematic regarding particle aggregation, so polyalcohols such as ethylene glycol, 1,2-propanediol or 1,5-pentanediol are preferred due to their additional ability to act as bidentate chelating agents for the effective stabilization effect.[65, 66] The reducing ability in all the cases can be enhanced by means of the use of elevated pH (*i.e.* strong base).[66] Alternatively, electrochemical reductions can be employed.[67] All of these types of routes can be carried out both in aqueous and in organic solvents of moderate boiling point (the mentioned alcohols, HDA, toluene, dioctyl ether, tetrahydrofurane –THF–, etc.). Stabilizers are needed; the reducing agents can act in turn as capping agents and so do solvents. Additional stabilizers are based on thiol moieties (like dodecanethiol and mercaptosuccinic acid), due to the high tendency of sulphur to form coordinate covalent bonds with transition metals.

A further type of route is the synthesis of NPs within the nanoreactors formed by reverse micelles; *i.e.* the synthesis in microemulsions.[68-71] When a surfactant (amphiphilic organic molecule with both hydrophobic and hydrophilic groups) or certain polymers are added to a biphasic polar/apolar solvent (such as water/oil), its molecules spontaneously self-organize into structures such as micelles or vesicles. Specifically, reverse micelles expose their hydrophilic heads towards the micelle core, where the polar solvent is sequestered, whereas the hydrophobic tails extend away from

the centre facing the surrounding apolar solvent. Thus, if the metallic precursor is dissolved in the polar phase, the crystallization can be carried out in the confined nano-sized core of the micelle, being the size and shape of the resultant NCs the replica of such a space. It is said, then, that micelles act as soft-templating agents. Typical positively- and negatively-charged and nonionic surfactants are, respectively, cetyltrimethylammonium bromide (CTAB), sodium dodecyl sulphate (SDS) and sodium bis(2-ethylhexyl)sulfosuccinate (AOT); and Pluronics (which are triblock copolymers), polyvinylpyrrolidone (PVP) and Igepal. Such surfactants are also used as capping agents in the single-phase liquid synthesis mentioned above. An alternative solvent for the synthesis in microemulsions is the supercritical $CO_2$.[72, 73] Compositions accessible through microemulsions method range from metals, to metal oxides and metal sulfides.[18] In general, only binary compounds can be obtained, although ternary compositions have also been achieved through the use of bimetallic precursors.[71]

Apart from the well-established liquid-based routes described above (*i.e.* decomposition of metalorganic precursors in hot-boiling point organic solvents, reduction of salts in aqueous or organic media and microemulsion routes), a couple of recent advances have broaden the range of liquid-based synthetic strategies. These are the "benzyl alcohol route" and synthesis in ionic liquids (ILs).

In regard to the "benzyl alcohol route", also known as "organic nonaqueous route", it really comprises a range of nonaqueous, surfactant-free routes developed originally in benzyl alcohol,[74, 75] but extended to related solvents like ketones and benzylamine.[76, 77] Such solvents exhibit the ability of simultaneously acting as reactant, providing both the oxygen for the formation of metal oxide NPs and the reducing characteristic typical of alcohols, as well as stabilizers, constituting a surfactant-free synthetic medium. Although it shares some common features with the thermal decomposition of metalorganic precursors, it requires a simpler reaction system (just the metal precursor and the solvent) where no intermediate metalorganic precursor needs to be formed/isolated. Similarly, it resembles the polyol (or polyalcohol) method, with the differences that no extra stabilizers/reducing agents are needed and no water is present at all. The distinct organic reactions implicated (several mechanisms) have been postulated and deal with sol-gel chemistry with the particularity that no water is involved, which drastically decreases the reaction rates as compared to aqueous sol-gel

reactions and leads to robust procedures for the crystallization within the liquid media of a broad range of binary and also ternary metal oxides displaying several size, shape and SA behaviour, although a rational design and tailoring has not been achieved.

Ionic liquids are organic salts that are fluid at or near room temperature. Focus of much attention from varied fields,[78] ILs offer outstanding properties as a medium for the synthesis of NPs.[79-81] Because of their ionic nature, they possess a high polarity which translates into the attribute of being efficient solvents for precursors as well as triggers of reactions via separation of charges. Besides, their low surface tension leads to high nucleation rates and, as a consequence, to small particles. Complementarily, their intrinsic self-organization at the molecular level allows a two-fold electronic and steric stabilization, depressing the tendency for particle growth. As highly structured liquids, they can act as soft-templates for directing the structure of inorganic and hybrid organic/inorganic materials.[82] Overall, they are a complete system for the synthesis of NPs, simultaneously acting as solvents, reactants and stabilizers. Within this realm, deep eutectic solvents (DES),[83] a type of IL made up of liquid mixtures of organic compounds with a deep eutective point in their phase diagram, offer the advantage of being easily prepared at low cost.[81] In chapter 3 of this thesis, the use of a urea/choline chloride DES is described for the synthesis of PbS NPs and nanooxides such as γ-$Fe_2O_3$, α-$Fe_2O_3$, $Mn_3O_4$ and $Mn_2O_3$.

---

In regard to the type of energy transmission aiming to precipitate the product by means of a sudden supersaturation, several paths exist, which can be interchangeably applied to the above types of chemical synthesis. Apart from the conventional convective heating by means of a heating plate or electric mantle, alternative valuable methods are solvothermal treatment, sonication and microwave irradiation. Solvothermal[84] ("hydrothermal" if the solvent is water) synthesis takes place in sealed recipients called autoclaves, where the reaction mixture is heated above its boiling temperature so that an autogenous pressure is generated. Under solvothermal conditions all the physico-chemical parameters of the solvent (such as density, ionic product, viscosity, dielectric constant, *etc.*) dramatically change, accessing crystallization reactions that would not occur under conventional conditions. The incorporation of the

basic principles for the synthesis of NPs to solvothermal methods allows the successful preparation of nanostructured materials.[85] In this sense, solvothermal reactions employing high-boiling point solvents and long-chain organic capping agents have succeeded for instance in the preparation of nano-sized oxides[86] via decomposition of metalorganic precursors, while the hydrothermal reaction in the presence of surfactants and reducing agents has allowed for instance the synthesis of nanometer-sized metallic hollow spheres[87] via a micelle system. In particular, "organic nonaqueous routes" are originally associated to an autoclave performance.[76] A further recent application of autoclaves is the synthesis of NPs in ILs, which has been named ionothermal synthesis.[81] In the present thesis, chapter 1.1 tackles the high-alkali-mediated hydrothermal synthesis of $BaMnO_3$ NPs.

The sonication applied to chemical reactions, *i.e.* sonochemistry,[88] makes use of ultrasounds[89] to create acoustic cavitation, which is the formation, growth and implosive collapse of bubbles in a liquid. As a consequence of these phenomena, both intense local heatings and high pressures of extremely short lifetimes are produced. Figures are illustrative of the radical conditions of the hot spots developed: temperatures of 5000 ºC, pressures of about 500 atmospheres and heating and cooling rates greater than $10^9$ K/s. Sonochemistry has been successfully applied to the synthesis of NPs,[90, 91] as well as to their chemical transformations such as doping.[92]

Microwave irradiation[93] provides very efficient and local heating, offering thus great advantage for large-scale reactions where thermal gradients are prone to happen under conventional heating methods. Additionally, it has been shown to enhance the reaction rates for inorganic materials,[94] allowing the short-time preparation of high-quality inorganic NCs.[95, 96] Special mention should be given to the microwave synthesis in ILs because their high dielectric constant allows an efficient radiation-mediated energy absorption ultimately responsible for the crystallization of the inorganic NPs stabilized from aggregation by the IL.[97, 98] Interestingly, ILs can be used as aids for microwave heating of nonpolar solvents above their boiling point,[99] which can enable reactions that would not occur otherwise. On the other hand, microwave irradiation has found great deal of interest in the preparation of NPs via the "organic nonaqueous route".[100, 101]

Last, it is worth mentioning that "simple" sources of energy have been discovered as new means of shaping the matter. This is the case of visible light, which have recently been shown to induce the twisting of ribbons of NPs.[102]

---

Finally, an overview of the biosynthesis of inorganic NPs is tackled, the purpose being not only to illustrate the creativity and versatility of nature to design synthetic pathways that can inspire the mankind' ingenuity for the preparation of novel materials not found in nature, but also and within the scope of this Appendix, to clarify some concepts used until now, such as "hard-" and "soft-templating" as well as hierarchy and bottom-up and top-down approaches. Really, biosynthesis is the chemical synthesis performed either by alive organisms or making use of them and, consequently, learning from the organic/inorganic compounds used by alive organisms to have control over the size, shape and hierarchy features is very desirable in the area of the chemical synthesis of nanomaterials. The so-called biotemplating[103] makes use of biological materials with a multitude of morphologically sophisticated hollow nanostructures for their transcription into the target material. It really encompasses both inorganic/organic compositions and hard-/soft- nature of the templates.[104] From the inorganic side, silica motifs from butterfly wings[105] and diatoms[106] have been replicated into oxide and metallic hierarchical nanostructures. This strategy is thus similar to the so-called hard-template technique since it offers a hard, outer scaffold as a transcriptional motif (nanostructured silica plays the same role in its mesoporous and biomaterial forms). Organic biotemplates, on the other side, include (micro)organisms, such as bacteria,[107] viruses,[108] fungi[109] and yeasts[32] and also a wide range of SA architectures derived from various types of biomacromolecules, including lipids,[110] peptides[111]/proteins,[112] DNA[113] and enzymes.[114] This realm of biomacromolecules-based morphologies can be comprised into the soft-templating methods of synthesis. What defines the "template" concept, both in its hard- and soft- variants, is the exact (inverted) transcription of the template's morphology into the nanostructured material's shape, being the latter ultimately determined by the empty spaces of the template. What distinguishes "hard-" from "soft-" templates is the type of architectural frame: continuous and a rigid solid for hard-templates and disrupted, single-molecule-based for soft-templates. Alternatively, they are named exo- and endotemplates, in analogy to the terms exo- and endoskeleton

from biology.[12] The key asset of all of the biotemplates is the structurally complex morphologies attainable, including the co-existence of various levels of hierarchy from the nano- to the macroscales, which is crucial for advanced functionalities through the integration and synergism of distinct levels of hierarchy performing different functions. In this sense, biotemplates are not only used for the direct synthesis of nano-sized materials, but also for the SA of prefabricated NPs into nano/microstructures.[115-119] Regarding the use of templates for assembly purposes, it is worth noting the existence of alternatives to transcriptional templates, such as ice-segregation induced self-assembly (ISISA),[120] in which aqueous colloidal dispersions, for instance, are first frozen, prompting the expulsion of the NPs into the boundaries of adjacent ice crystals, and later defrosted by freeze-drying, leading to microporous channels made up of matter enclosing empty areas where ice crystals originally resided. Last, while the task of a soft-biotemplate is the controlled guiding of the crystallization of NPs, *i.e.* they offer a bottom-up synthesis, the "bio-world" also employs the inverse approach, the top-down synthesis, in which microorganisms act as "bio-milling" agents downsizing the particle diameter from ~150-200 nm into < 10 nm NPs.[121, 122]

# ANEXO B

## Estrategias Generales para la Preparación de Materiales Funcionales Inorgánicos Nanoestructurados

El paso clave para que exista un material funcional nanoestructurado es sintetizarlo, lo cual implica la conversión de componentes primitivos en sólidos nanostructurados útiles con características que permitan su funcionalidad. De hecho, la síntesis posibilita la creación de nuevos materiales que no existen en la naturaleza, poseyendo así un potencial enorme para el descubrimiento, para hacer posible lo imposible, para realizar lo irreal. Los métodos de síntesis de NPs pueden agruparse en dos categorías principales: "de arriba a abajo" y "de abajo a arriba". En los procedimientos "de abajo a arriba" reaccionan átomos/moléculas individuales dando lugar a una entidad nanométrica; *i.e.* la construcción tiene lugar a partir de los componentes más pequeños, como si se construyera un puzzle o una casa a partir de las piezas o de los ladrillos y el pegamento, respectivamente. Por el contrario, los procedimientos "de arriba a abajo" parten del material masivo y mediante una destrucción controlada se esculpe el patrón nanoestructurado. Generalmente las estrategias "de abajo a arriba" se encuentran asociadas a síntesis químicas,[1-3] mientras que las "de arriba a abajo" se abordan mediante el uso de técnicas físicas, como la litografía, la ablación láser, el arco eléctrico, la deposición de vapor, la deposición por láser, la molienda mecánica, *etc.*[4] A pesar de que las aproximaciones "de arriba a abajo" dan acceso a materiales nanoestructurados con una alta calidad en términos de cristalinidad, baja disparidad de tamaños, colocación 3D…, ni son eficientes en cuanto a tiempo/costes ni disponen de flexibilidad para modificar las características (composición, superficie, tamaño, forma, defectos, AE) de los materiales nanoestructurados.

En esta tesis, el tema de los materiales funcionales nanoestructurados es abordado desde una perspectiva química, desde rutas sintéticas "de abajo a arriba". Esta sección repasa el estado del arte de las aproximaciones químicas actuales para la síntesis de materiales nanoestructurados.

Puesto que las NPs son metaestables, tienden a agregarse y a sinterizar bajo las condiciones de reacción, de manera que el principal esfuerzo a la hora de diseñar nuevas rutas de síntesis químicas debe ir dirigido hacia la búsqueda de estrategias que impidan la agregación de las NPs. La idea general consiste en proteger la superficie de las NPs con un agente externo. En función del estado de agregación del agente estabilizador o del medio que lo contiene, las estrategias químicas para la síntesis de NPs pueden dividirse en dos grupos principales: a) los métodos de matriz sólida y b) las rutas en fase líquida. En todos los casos es deseable el uso de bajas temperaturas de reacción para minimizar el ganar termodinámica, es decir, para minimizar la agregación.

**a) Métodos de matriz sólida**

Las matrices sólidas actúan como barreras físicas que impiden la agregación incontrolada de NPs. Las inorgánicas como la sílice (en sus formas mesoporosa o xerogel),[5-8] el carbón mesoporoso[9] o los nanotubos de carbono[10-11] ofrecen huecos/porosidad que actúan como nanoreactores impidiendo el crecimiento incontrolado del material objetivo a partir de la disolución de precursores. En general, las matrices sólidas inorgánicas actúan como plantillas duras o exoplantillas. El término "plantilla" connota una correspondencia 1:1 entre la forma de la matriz que actúa como plantilla y el hueco que queda tras su eliminación.[12,13] Este es el caso de los ejemplos mencionados, en los que la organización de la porosidad/huecos es replicada de forma exacta en el producto inorgánico final. De este modo, la conectividad del sólido plantilla es responsable en última instancia de la conectividad del producto final: un sólido que consta que dos fases continuas sólida y hueca conduce a la arquitectura invertida en el producto inorgánico final, mientras que un sólido con huecos/poros sin conexión conduce a NPs inorgánicas, aunque algo de agregación puede tener lugar tras la eliminación de la plantilla.[12] La eliminación de la plantilla dura se lleva a cabo típicamente por medio de calcinación para los carbones y nanotubos de carbono y mediante disolución con hidróxido sódico en el caso de la sílice.

Sin embargo, los métodos de matriz sólida no están restringidos a las matrices inorgánicas. Las orgánicas pueden albergar en su interior precursores inorgánicos que cristalizan en NCs dentro de espacios confinados. La mezcla de reactivos metálicos y orgánicos se realiza normalmente en medios líquidos para asegurar un entremezclado a

nivel molecular, evitando la barrera de difusión típica de la síntesis en estado sólido.[14] Normalmente, la matriz no está involucrada sólo físicamente, sino también químicamente.[15] Así, se forman polímeros mediante enlaces covalentes entre el metal y los átomos de oxígeno de la materia orgánica. Se requiere un paso final de calcinación para i) cristalizar las NPs en el interior de los espacios confinados de la matriz polimérica y/o ii) eliminar la matriz mediante auto-combustión, aislando así las NPs. Las temperaturas de calcinación típicas están comprendidas entre los 250 y 900 ºC, lo que es un problema, ya que conduce a la pérdida de control del tamaño, distribución de tamaños, forma, agregación, AE, defectos y composición. En este sentido, con frecuencia sólo se pueden obtener nanoóxidos metálicos binarios, es decir, aquellos que contienen sólo un tipo de átomo metálico, ya que las altas temperaturas favorecen la segregación de fases. Además, las fases impurezas, como carbonatos alcalinotérreos, tienden a contaminar el producto deseado. El control de las características de las NPs se limita a variaciones de la temperatura de calcinación. Una característica común de las NPs resultantes, que puede ser una ventaja o un inconveniente dependiendo de la aplicación, es su superficie sin *ligandos*. Al contrario que muchas matrices sólidas inorgánicas, las orgánicas raramente pertenecen a la noción "plantilla" debido a la falta de huecos definidos que puedan ser replicados en forma de NCs.

Uno de los métodos de matriz sólida orgánica más ampliamente empleados es el sol-gel.[16] Brevemente, la hidrólisis de alcóxidos metálicos, como el ortosilicato tetraetílico –TEOS–, $Si(OC_2H_5)_4$, genera enlaces metal-hidroxilo (Ec. 1) y, a continuación, las moléculas parcialmente hidrolizadas condensan formando enlaces metal-O-metal y liberando moléculas de alcohol o agua (Ec. 2). Este proceso de polimerización prosigue dando lugar a moléculas de mayor tamaño cada vez, que primero forman un sol y finalmente un gel. Mediante el envejecido y la calcinación del sólido resultante se aísla el material inorgánico nanoestructurado final ($SiO_2$ en el ejemplo).

$$Si(OR)_4 + H_2O \rightarrow HO\text{-}Si(OR)_3 + ROH \quad (1)$$

$$(OR)_3Si\text{-}OH + OH\text{-}Si(OR)_3 \rightarrow (OR)_3Si\text{-}O\text{-}Si(OR)_3 + H_2O \quad (2)$$

Alternativamente, se pueden preparar geles que contengan el metal deseado a partir de compuestos distintos de los alcóxidos. En general, las funcionalidades (poli)-

alcohol y (poli)-ácido carboxílico son adecuadas para la preparación de geles metalorgánicos por medio del efecto quelante del metal (formación de varios enlaces oxígeno-metal). Las posteriores reacciones de condensación y combustión conducen a los óxidos metálicos nanoestructurados.[17] Estos tipos de rutas se conocen colectivamente con el nombre de método de Pechini.[18] Por ejemplo, se pueden preparar geles hidroxílicos metálicos a partir de los correspondientes cloruros/nitratos metálicos e hidróxido sódico en agua o etanol. Los nanoóxidos metálicos se obtienen tras calcinación a 250-600 ºC.[19,20] Algunos agentes quelantes ampliamente empleados en síntesis tipo Pechini son el ácido cítrico, el ácido etilendiaminotetraacético (EDTA)[22] y el alcohol polivinílico (PVA).[23] El glicerol ($CH_2OH$-$CHOH$-$CH_2OH$),[24] el ácido málico ($HO_2C$-$CH_2$-$CHOH$-$CO_2H$)[25] y el ácido oxálico ($HO_2C$-$CO_2H$)[26] son otros ejemplos. Sus mezclas con nitratos/acetatos metálicos forman los geles correspondientes, cuya calcinación a 400-450 ºC genera los correspondientes nanoóxidos metálicos binarios. Se ha empleado la glicina ($NH_2$-$CH_2$-$COOH$) para la síntesis de óxidos multinarios nanoestructurados con estructura perovskita y distintas composiciones.[27,28] La celulosa también ha sido empleada para la preparación de nanoóxidos tipo perovskita mediante calcinación entre 400 y 800ºC.[29]

Aunque ampliamente utilizados para la síntesis de nanoóxidos, los métodos de calcinación de matriz orgánica se han extendido para la preparación de nitruros,[30-34] oxinitruros[35] y carburos.[34] En este sentido, la estrategia general se basa en el uso de urea ($H_2N$-$CO$-$NH_2$) como fuente de nitrógeno y carbono en combinación con la atmósfera adecuada para evitar la oxidación.

En el capítulo 2 de esta tesis se describe el uso de una matriz orgánica polimérica obtenida mediante el tratamiento térmico de la urea para la síntesis de NiO, $Ni_{núcleo}$-$NiO_{cáscara}$ y otros nanoóxidos metálicos como el $Co_3O_4$ y el $Mn_3O_4$.

**b) Rutas en fase líquida**

Las rutas en fase líquida ofrecen la ventaja de permitir el uso de temperaturas de reacción suaves y de un amplio rango de estrategias sintéticas para controlar las características de los materiales nanoestructurados. La cristalización de un sólido en un medio líquido homogéneo se encuentra gobernada por dos etapas fundamentales: la

nucleación y el crecimiento.[36] La nucleación es causada por la sobresaturación –una concentración más alta que la correspondiente al punto de saturación–[37] y conduce a pequeños núcleos embrionarios que se piensa que son clusters metálicos con números mágicos.[38] El crecimiento de los núcleos es impulsado por factores tanto termodinámicos (que implican la formación de interfases más estables sólido-sólido) como entrópicos (relacionados con la desorción de moléculas del disolvente de la superficie del sólido). Los cuatro mecanismos de crecimiento típicos son: la unión ión a ión, el AE de NCs (que conlleva una organización colectiva), la agregación y sinterizado (la agregación es la aglomeración al azar de NPs y el sinterizado es el subsiguiente colapso de los poros impulsado por la disminución de la energía superficial) y "la maduración de Ostwald" o engrosamiento, el cual consiste en el crecimiento de los cristales más grandes a expensas de la desaparición de los más pequeños, que son inestables y se disuelven para incorporarse en forma de iones a los NCs estables de mayor tamaño. Para obtener NCs con una distribución estrecha de tamaños de partícula se deben dar dos requisitos: i) la separación de la nucleación y el crecimiento y ii) la prohibición del crecimiento.

El primer requisito –la separación de la nucleación y el crecimiento– puede alcanzarse por medio de una nucleación súbita, de acuerdo al diagrama de LaMer-Dinegar.[39] A su vez, esto se consigue mediante una alta sobresaturación repentina que haga que se generen de una vez muchos núcleos del mismo tamaño. Si dichos núcleos crecen mediante la incorporación del precursor y no se dan ni una nucleación adicional ni los mecanismos de crecimiento por AE/"maduración de Ostwald", entonces se logra la estabilización de NCs con una estrecha distribución de tamaños. Experimentalmente, la nucleación súbita se consigue mediante el uso de una alta concentración de precursores, velocidades rápidas de calentamiento en los métodos "de calentamiento progresivo",[40] una inyección en caliente de los reactivos,[41,42] cambios de pH, reacciones químicas (como reducción de metales), *etc.* Alternativamente, la nucleación y el crecimiento pueden separarse físicamente mediante el uso de semillas. Así, el método del crecimiento con semillas[43-45] consiste en la lenta adición de precursores a la disolución que contiene los núcleos preexistentes o semillas, lo cual conduce a la precipitación selectiva del material en la superficie de las semillas en lugar de a la formación de núcleos adicionales mediante la nucleación homogénea. La preferencia de la nucleación heterogénea sobre la homogénea se debe a la menor demanda de energía

por parte de la primera y puede emplearse para la producción de partículas de composición homogénea[43,44] o heterogénea,[46,47] como las estructuras núcleo-cáscara simétricas,[45] los dímeros no simétricos[48,49] y las heteroestructuras NP-nanorod.[50,51]

En lo que concierne a la prohibición del crecimiento (vía AE de NCs y agregación-sinterizado, principalmente, y "maduración de Ostwald", secundariamente), esto es factible por medio de dos estrategias principales de estabilización superficial: repulsión a) electrostática y b) estérica. Respecto a la primera, si las superficies de los NCs están recubiertas con cationes o aniones adsorbidos, las fuerzas Culómbicas de repulsión entre cargas positivas y negativas, respectivamente, impide la agregación/ensamblaje de los NCs. Experimentalmente, esto puede llevarse a cabo haciendo uso de disoluciones altamente alcalinas (*i.e.* mediante el uso de bases de Brönsted, como el NaOH o el KOH) o mediante la funcionalización superficial con moléculas cargadas como las aminas, que se pueden protonar bajo las condiciones ácidas. El segundo tipo de estabilización superficial consiste en la repulsión estérica de NCs estabilizadas con *ligandos* y está relacionada con fuerzas repulsivas de van der Waals.[52] Los *ligandos* son moléculas orgánicas que se unen a la superficie de las NPs mediante enlaces covalentes entre grupos funcionales o mediante interacciones electrostáticas. La Figura 1 muestra una representación esquemática de las estrategias químicas mencionadas para la síntesis de NPs.

De acuerdo al tipo de precursor y estrategia sintética, los métodos en fase líquida para la preparación de NCs pueden agruparse en dos grupos clásicos: 1) descomposición de precursores metalorgánicos en disolventes de alto punto de ebullición y 2) reducción de sales metálicas. En ambos casos, se necesita una funcionalización superficial adecuada. Para el primer tipo de métodos, algunos *ligandos* típicos son ácidos carboxílicos (ácido oleico –OLEA–), aminas (hexadecilamina –HDA–, oleilamina –OA–, *etc.*) y alquilfosfinas (tributilfosfina –TBP–, trioctilfosfina –TOP–, óxido de trioctilfosfina –TOPO–, *etc.*). Estos *ligandos* de cadena hidrocarbonada larga se enlazan covalentemente a los metales, formando precursores metalorgánicos no polares cuya termólisis en disolventes orgánicos (como el ácido oleico, el éter octílico, el hexadecano, la trioctilamina, *etc.*, la $T_{reacción}$ es *ca.* 300 ºC) por medio de métodos de calentamiento progresivo o inyección en caliente conduce a la preparación de NCs de

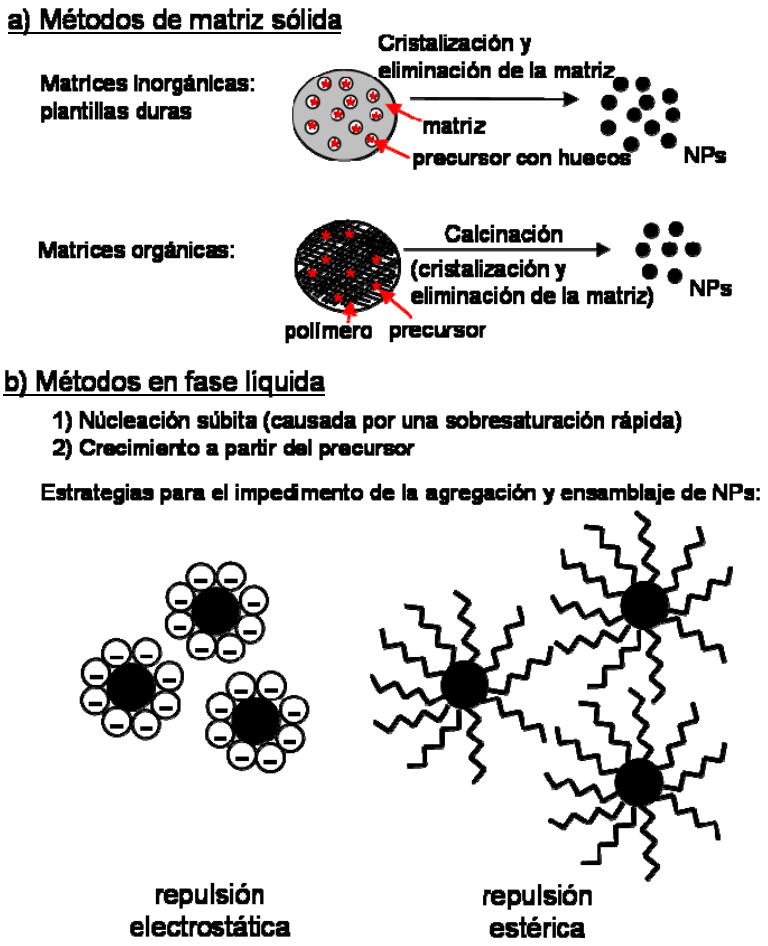


**Figura 1.** Ilustración esquemática de las estrategias químicas para la síntesis de nanopartículas.

tamaños homogéneos con una multitud de composiciones. Esta versátil ruta da acceso a metales,[53,54] óxidos metálicos,[55] sulfuros metálicos,[56] así como a composiciones multinarias (incluyendo cuaternarias)[57,58] e híbridas.[47] Ha sido utilizada incluso a la gran escala.[40] El tamaño de partícula puede ser controlado con precisión mediante la variación de las condiciones de reacción. Una variante del método es la descomposición de compuestos organometálicos (como los carbonilos metálicos).[59] Sin embargo, éstos actúan normalmente como meros precursores para la formación de intermedios metalorgánicos, que son los que sufren la termólisis que conduce a la formación de NCs.[55,60]

En lo que respecta a la reducción de sales metálicas, esta ruta suave (las temperaturas son normalmente < 100 ºC) se emplea típicamente para la síntesis de NPs de metales nobles y de transición con tamaño y forma controladas.[18,61-64] El agente reductor a emplear viene determinado por el potencial de reducción del metal. En este

sentido, los cationes metálicos como el $Ni^{2+}$, el $Co^{2+}$ y el $Fe^{2+}$ requieren de un agente reductor fuerte como el borohidruro sódico ($NaBH_4$), el hipofosfito sódico ($NaH_2PO_2$) o la hidracina ($NH_2NH_2$). Por el contrario, los cationes de metales nobles como el $Ag^+$ y el $Au^{3+}$ se reducen más fácilmente, así que los agentes reductores pueden ser más suaves, como el citrato sódico, el ácido ascórbico, la formamida o la N, N-dimetilformamida (DMF). Además, los alcoholes poseen la habilidad de actuar simultáneamente como agentes reductores y disolventes. En este sentido, los monoalcoholes, como el etanol, pueden generar problemas de agregación de las partículas, así es que se prefieren polialcoholes como el etilenglicol, el 1,2-propanediol o el 1,5-pentanediol debido a su habilidad adicional de actuar como agentes quelantes bidentados, que estabiliza las NPs.[65,66] En todos los casos, el carácter reductor puede aumentarse haciendo uso de altos pH (*i.e.* bases fuertes).[66] De forma alternativa, se pueden emplear reducciones electroquímicas.[67] Todos estos tipos de rutas pueden ser llevadas a cabo tanto en disolución acuosa como en disolventes orgánicos de punto de ebullición moderado (los alcoholes mencionados, el HDA, el tolueno, el éter octílico, el tetrahidrofurano –THF-, *etc.*). El uso de agentes estabilizadores es necesario; los agentes reductores y el mismo disolvente pueden actuar a su vez como agentes estabilizadores. Otros agentes estabilizadores son los tioles (como el dodecanetiol y el ácido mercaptosuccínico) debido a la alta tendencia del azufre a enlazarse covalentemente a metales de transición.

Otro tipo de ruta es la síntesis de NPs en los nanoreactores formados por micelas inversas; *i.e.* la síntesis en microemulsiones.[68-71] Cuando sobre un disolvente bifásico polar/apolar (como el agua/aceite) se adiciona un surfactante (molécula orgánica anfifílica con grupos hidrofóbicos e hidrofílicos) o ciertos polímeros, estas moléculas se auto-organizan espontáneamente en estructuras como las micelas o las vesículas. En concreto, las micelas inversas exponen sus cabezas hidrofílicas hacia el centro de la micela, donde el disolvente polar se encuentra secuestrado, mientras que las colas hidrofóbicas se extienden radialmente desde el centro hacia el exterior hidrofóbico. Así, si el precursor metálico se disuelve en la fase polar, la cristalización es llevada a cabo en los nanonúcleos confinados del centro de la micela, de manera que el tamaño y forma de los NCs finales es una réplica de dicho espacio. Se dice entonces que las micelas son agentes de plantilla suave. Algunos surfactantes típicos cargados positiva y negativamente son, respectivamente, el bromuro de cetiltrimetilamonio (CTAB), el

dodecilsulfato sódico (SDS) y el sulfosuccinato bis(2-etilhexil) sódico (AOT); y los Pluronics (que son copolímeros tribloque), la polivinilpirrolidona (PVP) y el Igepal. Estos surfactantes también pueden ser usados como agentes estabilizadores en las síntesis en un medio líquido monofásico, como los citados anteriormente. Un disolvente alternativo para la síntesis en microemulsiones es el $CO_2$ supercrítico.[72,73] Las composiciones accesibles por medio del método de las microemulsiones van desde los metales, hasta los óxidos metálicos y sulfuros metálicos.[18] En general, sólo se pueden obtener compuestos binarios, aunque también se han obtenido composiciones ternarias mediante el uso de precursores bimetálicos.[71]

Aparte de las rutas líquidas descritas anteriormente (es decir, la descomposición de precursores metalorgánicos en disolventes orgánicos de alto punto de ebullición, la reducción de sales en medios acuosos u orgánicos y las rutas con microemulsiones), existen un par de avances más recientes que han ampliado el rango de estrategias sintéticas en líquidos. Éstas son la "ruta del alcohol bencílico" y la síntesis en líquidos iónicos (LIs).

Respecto a la "ruta del alcohol bencílico", también conocida como "ruta orgánica no acuosa", en realidad abarca una serie de rutas no acuosas libres de surfactantes desarrolladas originalmente para el alcohol bencílico,[74,75] pero que pueden ser extendidas a disolventes relacionados, como las cetonas y la bencilamina.[76,77] Dichos disolventes muestran la habilidad de actuar simultáneamente como reactivo, proporcionando tanto los átomos de oxígeno para la formación de nanoóxidos como el carácter reductor típico de los alcoholes, así como de agentes estabilizadores, constituyendo por sí mismos un medio sintético sin surfactantes. Aunque comparte ciertas características con la descomposición térmica de precursores metalorgánicos, requiere un sistema de reacción más sencillo (simplemente el precursor metálico y el disolvente), donde no se necesita formar/aislar un intermedio metalorgánico. De igual forma, se parece al método del polialcohol, con la diferencia de que no se necesitan agentes extras estabilizadores/reductores y de que no hay agua. Se han postulado varios mecanismos de reacción, que están relacionados con la química sol-gel con la particularidad de la ausencia de agua, lo cual disminuye drásticamente las velocidades de reacción en comparación a las reacciones sol-gel acuosas, conduciendo a procedimientos muy reproducibles para la cristalización en medio líquido de un amplio

rango de óxidos metálicos binarios y ternarios que muestran distintos rasgos de tamaño, forma y AE, aunque no se ha logrado el control racional de éstos.

Los líquidos iónicos son sales orgánicas fluidas a temperatura cercana a la ambiente. Foco de mucha atención desde campos diversos,[78] los LIs ofrecen propiedades sobresalientes como medio para la síntesis de NPs.[79-81] Gracias a su naturaleza iónica, poseen una alta polaridad, la cual se traduce en que son disolventes muy eficientes para los precursores y en que disparan la reactividad por medio de la separación de cargas. Además, su baja tensión superficial conduce a altas velocidades de nucleación y, como consecuencia, a partículas de pequeño tamaño. De forma complementaria, su intrínseca auto-organización a la escala molecular permite la estabilización electrostática y estérica, disminuyendo la tendencia hacia el crecimiento de partícula. Como líquidos altamente estructurados, pueden actuar como plantillas blandas dirigiendo la estructura de materiales inorgánicos e híbridos orgánicos/inorgánicos.[82] En conjunto, son un sistema muy completo para la síntesis de NPs, actuando simultáneamente como disolventes, reactivos y agentes estabilizadores. En este terreno, los disolventes con eutéctico profundo (DES),[83] un tipo de LI formado por la mezcla de compuestos orgánicos con un punto eutéctico profundo en su diagrama de fases, ofrecen la ventaja de poder ser preparados fácilmente a bajo coste.[81] En el capítulo 3 de esta tesis, se describe el uso del DES urea/cloruro de colina para la síntesis de NPs de PbS y de los nanoóxidos $\gamma$-$Fe_2O_3$, $\alpha$-$Fe_2O_3$, $Mn_3O_4$ y $Mn_2O_3$.

---

En relación al tipo de transmisión de energía que promueva la precipitación del producto por medio de una sobresaturación súbita, existen varias vías, las cuales pueden ser aplicadas a cada uno de los tipos de síntesis química descritos anteriormente. Además del convencional calentamiento por convección por medio de una placa calefactora o una manta eléctrica, existen otros métodos alternativos como el tratamiento solvotermal, la sonicación y la irradiación por microondas. La síntesis solvotermal[84] ("hidrotermal" si el disolvente es agua) se lleva a cabo en recipientes cerrados llamados autoclaves, donde la mezcla de reacción es calentada por encima de su temperatura de ebullición, de manera que se auto-genera presión. Bajo las condiciones hidrotermales, todos los parámetros físico-químicos del disolvente (como la densidad, el producto iónico, la viscosidad, la constante dieléctrica, *etc.*) cambian de

manera drástica, posibilitando reacciones de cristalización que no ocurrirían bajo condiciones convencionales. La incorporación de los principios básicos de la síntesis de NPs a los métodos solvotermales permite la preparación de materiales nanoestructurados.[85] Así, las reacciones solvotermales que hacen uso de disolventes de alto punto de ebullición y de agentes estabilizadores orgánicos de cadena larga han dado frutos, por ejemplo, en la preparación de nanoóxidos[86] mediante la descomposición de precursores metalorgánicos, mientras que las reacciones hidrotermales en presencia de surfactantes y agentes reductores han permitido, por ejemplo, la síntesis de nanoesferas huecas metálicas[87] por medio de la formación de un sistema micelar. De forma particular, "las rutas orgánicas no acuosas" son llevadas a cabo en autoclaves.[76] Otra aplicación reciente de los autoclaves es la síntesis de NPs en LIs, lo que se ha dado en llamar síntesis ionotermal.[81] En la presente tesis, el capítulo 1.1 aborda la síntesis hidrotermal alcalina de NPs de $BaMnO_3$.

La sonicación aplicada a las reacciones químicas, *i.e.* la sonoquímica,[88] emplea ultrasonidos[89] para crear el fenómeno de cavitación acústica, que consiste en la formación, crecimiento y colapso explosivo de burbujas en un líquido. Como consecuencia de este fenómeno se producen calentamientos locales muy intensos y altas presiones de tiempos de vida extremadamente cortos. Las cifras son ilustrativas de las radicales condiciones desarrolladas en los puntos calientes: temperaturas de 5000 ºC, presiones de 500 atmósferas y velocidades de calentamiento y enfriamiento superiores a $10^9$ K/s. La sonoquímica ha sido aplicada con éxido a la síntesis de NPs,[90,91] así como a sus transformaciones químicas, como el dopaje.[92]

La irradiación por microondas[93] constituye un método de calentamiento local muy eficiente, ofreciendo así grandes ventajas para las reacciones a gran escala, donde tienden a darse gradientes térmicos bajo condiciones convencionales de calentamiento. Además, se ha visto que aumenta las velocidades de reacción de los materiales inorgánicos,[94] permitiendo la rápida preparación de NCs inorgánicos de alta calidad.[95,96] La síntesis en LIs asistida por microondas merece una especial atención, ya que la alta constante dieléctrica de estos líquidos favorece una absorción de energía muy eficiente vía radiación, lo que es responsable en última instancia de la cristalización de NPs inorgánicas.[97,98] Curiosamente, los LIs pueden usarse como ayudantes para el calentamiento por microondas de disolventes no polares por encima de su punto de

ebullición,[99] lo que puede producir reacciones que no se darían de otra manera. Por otro lado, la irradiación por microondas ha encontrado un gran interés en la preparación de NPs via la "ruta orgánica no acuosa".[100,101]

Por último, se debe mencionar que se ha descubierto que fuentes "simples" de energía pueden modificar la forma de la materia. Este es el caso de la luz visible, que recientemente se ha visto que induce el retorcimiento de lazos de NPs.[102]

---

Finalmente, se darán unas ideas generales de la biosíntesis de NPs inorgánicas. El propósito es doble. Por un lado, es ilustrativo de la creatividad y versatilidad de la naturaleza para diseñar vías sintéticas que puedan servir de inspiración a los humanos a la hora de investigar nuevas rutas de preparación de materiales que no existen en la naturaleza. Por otro lado, y dentro de la temática de este Anexo, servirá para clarificar algunos conceptos mencionados hasta ahora, como plantillas duras y blandas así como el concepto de jerarquía y de rutas "de abajo a arriba" y "de arriba abajo". En realidad, la biosíntesis es la síntesis química, o bien llevada a cabo por organismos vivos, o bien haciendo uso de los mismos, y, como consecuencia, el aprender de los compuestos orgánicos/inorgánicos usados por los organismos vivos para dirigir las características de tamaño, forma y jerarquía es muy deseable en el área de la síntesis química de nanomateriales. Las así llamadas bioplantillas[103] son materiales biológicos con una multitud de nanoestructuras huecas de sofisticadas morfologías que se transcriben en el material objetivo. En realidad comprende composiciones inorgánicas y orgánicas y plantillas duras y blandas.[104] Del lado inorgánico, se han replicado los motivos de sílice de las alas de las mariposas[105] y diatomeas[106] en nanoestructuras jerárquicas de metales y óxidos. Esta estrategia es similar a la así llamada técnica de plantillas duras, ya que ofrece un soporte duro con huecos que se transcriben (la sílice nanoestructurada juega el mismo papel en sus formas mesoporosa y biomaterial). Respecto a las bioplantillas orgánicas, incluyen (micro)organismos como las bacterias,[107] los virus,[108] los hongos[109] y las levaduras[32] y también un amplio rango de arquitecturas AE derivadas de varios tipos de biomacromoléculas, incluyendo los lípidos,[110] los péptidos[111]/proteínas,[112] ADN[113] y enzimas.[114] Este terreno de morfologías basadas en biomacromoléculas puede ser encuadrado en los métodos de plantilla blanda. Lo que define al concepto

"plantilla", tanto en sus variantes dura y blanda, es la transcripción invertida de la morfología de la plantilla en la forma del material nanoestructurado, viniendo ésta determinada por los espacios huecos de la plantilla. Lo que distingue a las plantillas duras de las blandas es el tipo de armazón arquitectónico: un sólido continuo y rígido para las duras e interrumpido, basado en moléculas, para las blandas. Se denominan también exo y endoplantillas, en analogía a los términos exo y endoesqueleto usados en biología.[12] La ventaja fundamental de todos los tipos de bioplantillas es la complejidad estructural de morfologías que están al alcance, incluyendo la coexistencia de varios niveles de jerarquía, desde la nano hasta la macroescala, lo que es clave a la hora de conseguir funcionalidades avanzadas mediante la integración y sinergia de distintos niveles de jerarquía que desempeñan distintas funciones. En este sentido, las bioplantillas no sólo son usadas en la síntesis directa de NPs, sino también en el AE de NPs en nano/microestructuras.[115-119] Respecto al uso de plantillas para propósitos de ensamblaje, se debe remarcar que existen alternativas a las plantillas transcripcionales, como por ejemplo el auto-ensamblado inducido por segregación de hielo (ISISA).[120] En este caso se congela una dispersión, por ejemplo coloidal, lo que provoca la expulsión de las NPs hacia los bordes de los cristales de hielo, para posteriormente descongelarla mediante liofilizado, lo que conduce a canales microporosos cuyas paredes son las NPs mientras que las zonas huecas son los lugares donde residieron los cristales de hielo. Por último, mientras que la función de una bioplantilla blanda es guiar la cristalización de NPs, *i.e.* ofrecen una ruta "de abajo a arriba", el "biomundo" emplea también la ruta contraria, la síntesis "de arriba a abajo", en el cual los microorganismos actúan como agentes de "biomolienda", disminuyendo el tamaño de partícula desde los ~150-200 nm hasta < 10 nm.[121,122]

# VII. Anexo B

# BIBLIOGRAPHY APPENDIX B / BIBLIOGRAFÍA ANEXO B


1. Caruso, F., *Colloids and Colloid Assemblies*. Wiley-VCH: **2004**.
2. Klabunde, K. J., *Nanoscale Materials in Chemistry*. John Wiley & Sons, Inc.: **2001**.
3. Rao, C. N. R.; Müller, A and Cheetham, A. K. (Eds.), *Nanomaterials Chemistry*. Wiley-VCH: **2007**.
4. Edelstein, A. S. and Cammarata, R. C. (Eds.), *Nanomaterials: Synthesis, Properties and Applications*. Taylor & Francis Group, LLC: **1996**.
5. Tian, B.; Liu, X.; Yang, H.; Xie, S.; Yu, C.; Tu, B.; Zhao, D., General Synthesis of Ordered Crystallized Metal Oxide Nanoarrays Replicated by Microwave-Digested Mesoporous Silica. *Advanced Materials* **2003,** 15, (16), 1370-1373.
6. Valdés-Solís, T.; Marbán, G.; Fuertes, A. B., Preparation of nanosized perovskites and spinels through a silica xerogel template route. *Chemistry of Materials* **2005,** 17, (8), 1919-1922.
7. Fuertes, A. B., A general and low-cost synthetic route to high-surface area metal oxides through a silica xerogel template. *Journal of Physics and Chemistry of Solids* **2005,** 66, (5), 741-747.
8. Fuertes, A. B., Low-Cost Synthetic Route to Mesoporous Carbons with Narrow Pore Size Distributions and Tunable Porosity through Silica Xerogel Templates. *Chemistry of Materials* **2004,** 16, (3), 449-455.
9. Schwickardi, M.; Johann, T.; Schmidt, W.; Schüth, F., High-surface-area oxides obtained by an activated carbon route. *Chemistry of Materials* **2002,** 14, (9), 3913-3919.
10. Ajayan, P. M.; Stephan, O.; Redlich, P.; Colliex, C., Carbon nanotubes as removable templates for metal oxide nanocomposites and nanostructures. *Nature* **1995,** 375, (6532), 564-567.
11. Han, W.; Fan, S.; Li, Q.; Hu, Y., Synthesis of gallium nitride nanorods through a carbon nanotube-confined reaction. *Science* **1997,** 277, (5330), 1287-1289.
12. Schüth, F., Endo- and exotemplating to create high-surface-area inorganic materials. *Angewandte Chemie - International Edition* **2003,** 42, (31), 3604-3622.
13. In the literature, the term template is frequently arbitrarily employed with and without the underlaying connotation of 1:1 correspondence between the shape of the matrix playing the role of template and the void remaining after the template.
14. In traditional solid state synthesis, the limiting factor for the reaction of the precursors, mixed and grounded in solid sate, is the diffusion of the ions within a solid lattice. Only with high temperatures diffusion mechanisms are allowed, but this is incompatible with the stabilization of high surface area NCs. Overcoming of such an obstacle can be realized by the reaction of the precursors at the molecular level, which in turn is attainable through liquid-phase routes of mixing. That makes it possible the use of mild temperatures of reaction, which together with the use of a suitable surface protection for the NCs, allows the preparation of nanostructured materials.
15. The characteristic feature of a gel is not the type of bonding. Polymeric gels are covalently linked, gelatine gels are formed by entanglement of chains and particulate gels are established by van der Waals forces. The bonds may be reversible, as in the particulate system, or permanent, as in polymer systems. What defines a gel is the existence of two intergrown phases, solid and liquid, which are continuous and possess colloidal dimensions.
16. Brinker, C. Jeffrey and Scherer, G. W. *Sol-gel Science*. Academic Press, INC.: **1990**.
17. Although the self-combustion of the organic matrix (which involves its oxidation through reduction of another species) usually reduces the metallic ions to their non-oxidated state, a. l. o.
18. Cushing, B. L.; Kolesnichenko, V. L.; O'Connor, C. J., Recent advances in the liquid-phase syntheses of inorganic nanoparticles. *Chemical Reviews* **2004,** 104, (9), 3893-3946.
19. Carnes, C. L.; Stipp, J.; Klabunde, K. J.; Bonevich, J., Synthesis, characterization, and adsorption studies of nanocrystalline copper oxide and nickel oxide. *Langmuir* **2002,** 18, (4), 1352-1359.
20. Makhlouf, S. A.; Parker, F. T.; Spada, F. E.; Berkowitz, A. E., Magnetic anomalies in NiO nanoparticles. *Journal of Applied Physics* **1997,** 81, (8 PART 2B), 5561-5563.
21. Marbán, G.; Fuertes, A. B., Highly active and selective $CuO_x/CeO_2$ catalyst prepared by a single-step citrate method for preferential oxidation of carbon monoxide. *Applied Catalysis B: Environmental* **2005,** 57, (1), 43-53.
22. Xu, Y.; He, Y.; Wang, L., Synthesis of $Ba_2Ti_9O_{20}$ via ethylenediaminetetraacetic acid precursor. *Journal of Materials Research* **2001,** 16, (4), 1195-1199.
23. Zhang, L.; Xue, D., Preparation and magnetic properties of pure CoO nanoparticles. *Journal of Materials Science Letters* **2002,** 21, (24), 1931-1933.
24. Li, Y.; Cai, M.; Rogers, J.; Xu, Y.; Shen, W., Glycerol-mediated synthesis of Ni and Ni/NiO core-shell nanoparticles. *Materials Letters* **2006,** 60, (6), 750-753.

25. Li, Q.; Wang, L. S.; Hu, B. Y.; Yang, C.; Zhou, L.; Zhang, L., Preparation and characterization of NiO nanoparticles through calcination of malate gel. *Materials Letters* **2007,** 61, (8-9), 1615-1618.
26. Wang, X.; Song, J.; Gao, L.; Jin, J.; Zheng, H.; Zhang, Z., Optical and electrochemical properties of nanosized NiO via thermal decomposition of nickel oxalate nanofibres. *Nanotechnology* **2005,** 16, (1), 37-39.
27. Boskovic, S. B.; Matovic, B. Z.; Vlajic, M. D.; Kristic, V. D., Modified glycine nitrate procedure (MGNP) for the synthesis of SOFC nanopowders. *Ceramics International* **2007,** 33, (1), 89-93.
28. Armelao, L.; Bandoli, G.; Barreca, D.; Bettinelli, M.; Bottaro, G.; Caneschi, A., Synthesis and characterization of nanophasic $LaCoO_3$ powders. *Surface and Interface Analysis* **2002,** 34, (1), 112-115.
29. Shao, Z.; Xiong, G.; Ren, Y.; Cong, Y.; Yang, W., Low temperature synthesis of perovskite oxide using the adsorption properties of cellulose. *Journal of Materials Science* **2000,** 35, (22), 5639-5644.
30. Podsiadlo, S., Stages of the synthesis of indium nitride with the use of urea. *Thermochimica Acta* **1995,** 256, (2), 375-380.
31. Gomathi, A.; Sundaresan, A.; Rao, C. N. R., Nanoparticles of superconducting γ-Mo2N and δ-MoN. *Journal of Solid State Chemistry* **2007,** 180, (1), 291-295.
32. Qiu, Y.; Gao, L., Metal-Urea Complex - A Precursor to Metal Nitrides. *Journal of the American Ceramic Society* **2004,** 87, (3), 352-357.
33. Sardar, K.; Dan, M.; Schwenzer, B.; Rao, C. N. R., A simple single-source precursor route to the nanostructures of AlN, GaN and InN. *Journal of Materials Chemistry* **2005,** 15, (22), 2175-2177.
34. Giordano, C.; Erpen, C.; Yao, W.; Antonietti, M., Synthesis of Mo and W carbide and nitride nanoparticles via a simple "urea glass" route. *Nano Letters* **2008,** 8, (12), 4659-4663.
35. Gomathi, A.; Reshma, S.; Rao, C. N. R., A simple urea-based route to ternary metal oxynitride nanoparticles. *Journal of Solid State Chemistry* **2009,** 182, (1), 72-76.
36. Park, J.; Joo, J.; Soon, G. K.; Jang, Y.; Hyeon, T., Synthesis of monodisperse spherical nanocrystals. *Angewandte Chemie - International Edition* **2007,** 46, (25), 4630-4660.
37. The saturation is the point at which a solution of a substance can dissolve no more of that substance and additional amounts of it will appear as a precipitate.
38. Crystallization mechanisms remain still unclear in spite of the high volume of work devoted to its study. It is believed that there is a critical radius under which nuclei redisolve. Nucleation can be understood at the point where the nucleation rate is high enough to equilibrate or to surpass the redissolution rate of the particles.
39. Lamer, V. K.; Dinegar, R. H., Theory, production and mechanism of formation of monodispersed hydrosols. *Journal of the American Chemical Society* **1950,** 72, (11), 4847-4854.
40. Park, J.; An, K.; Hwang, Y.; Park, J. E. G.; Noh, H. J.; Kim, J. Y.; Park, J. H.; Hwang, N. M.; Hyeon, T., Ultra-large-scale syntheses of monodisperse nanocrystals. *Nature Materials* **2004,** 3, (12), 891-895.
41. Murray, C. B.; Norris, D. J.; Bawendi, M. G., Synthesis and characterization of nearly monodisperse CdE (E = S, Se, Te) semiconductor nanocrystallites. *Journal of the American Chemical Society* **1993,** 115, (19), 8706-8715.
42. Talapin, D. V.; Rogach, A. L.; Kornowski, A.; Haase, M.; Weller, H., Highly Luminescent Monodisperse CdSe and CdSe/ZnS Nanocrystals Synthesized in a Hexadecylamine-Trioctylphosphine Oxide-Trioctylphospine Mixture. *Nano Letters* **2001,** 1, (4), 207-211.
43. Brown, K. R.; Walter, D. G.; Natan, M. J., Seeding of colloidal Au nanoparticle solutions. 2. Improved control of particle size and shape. *Chemistry of Materials* **2000,** 12, (2), 306-313.
44. Jana, N. R.; Gearheart, L.; Murphy, C. J., Seeding growth for size control of 5-40 nm diameter gold nanoparticles. *Langmuir* **2001,** 17, (22), 6782-6786.
45. Yu, H.; Gibbons, P. C.; Kelton, K. F.; Buhro, W. E., Heterogeneous seeded growth: A potentially general synthesis of monodisperse metallic nanoparticles [1]. *Journal of the American Chemical Society* **2001,** 123, (37), 9198-9199.
46. Costi, R.; Saunders, A. E.; Banin, U., Colloidal hybrid nanostructures: A new type of functional materials. *Angewandte Chemie - International Edition* **2010,** 49, (29), 4878-4897.
47. Shi, W.; Zeng, H.; Sahoo, Y.; Ohulchanskyy, T. Y.; Ding, Y.; Wang, Z. L.; Swihart, M.; Prasad, P. N., A general approach to binary and ternary hybrid nanocrystals. *Nano Letters* **2006,** 6, (4), 875-881.
48. Gu, H.; Zheng, R.; Zhang, X.; Xu, B., Facile One-Pot Synthesis of Bifunctional Heterodimers of Nanoparticles: A Conjugate of Quantum Dot and Magnetic Nanoparticles. *Journal of the American Chemical Society* **2004,** 126, (18), 5664-5665.
49. Li, Y.; Zhang, Q.; Nurmikko, A. V.; Sun, S., Enhanced magnetooptical response in dumbbell-like Ag-$CoFe_2O_4$ nanoparticle pairs. *Nano Letters* **2005,** 5, (9), 1689-1692.

50. Kudera, S.; Carbone, L.; Casula, M. F.; Cingolani, R.; Falqui, A.; Snoeck, E.; Parak, W. J.; Manna, L., Selective growth of PbSe on one or both tips of colloidal semiconductor nanorods. *Nano Letters* **2005,** 5, (3), 445-449.
51. Mokari, T.; Rothenberg, E.; Popov, I.; Costi, R.; Banin, U., Selective growth of metal tips onto semiconductor quantum rods and tetrapods. *Science* **2004,** 304, (5678), 1787-1790.
52. Van der Waals forces have two components: a repulsive one at short distances which prevents the collapse of molecules, and an attractive one at longer distances between permanent dipoles, permanent dipole-induced dipole or induced dipole-induced dipole.
53. Lee, D. K.; Kang, Y. S., Synthesis of silver nanocrystallites by a new thermal decomposition method and their characterization. *ETRI Journal* **2004,** 26, (3), 252-256.
54. Kim, S. W.; Park, J.; Jang, Y.; Chung, Y.; Hwang, S.; Hyeon, T.; Kim, Y. W., Synthesis of monodisperse palladium nanoparticles. *Nano Letters* **2003,** 3, (9), 1289-1291.
55. Hyeon, T.; Su Seong, L.; Park, J.; Chung, Y.; Hyon Bin, N., Synthesis of highly crystalline and monodisperse maghemite nanocrystallites without a size-selection process. *Journal of the American Chemical Society* **2001,** 123, (51), 12798-12801.
56. Joo, J.; Na, H. B.; Yu, T.; Yu, J. H.; Kim, Y. W.; Wu, F.; Zhang, J. Z.; Hyeon, T., Generalized and facile synthesis of semiconducting metal sulfide nanocrystals. *Journal of the American Chemical Society* **2003,** 125, (36), 11100-11105.
57. Riha, S. C.; Parkinson, B. A.; Prieto, A. L., Solution-based synthesis and characterization of $Cu_2ZnSnS_4$ nanocrystals. *Journal of the American Chemical Society* **2009,** 131, (34), 12054-12055.
58. Kang, E.; Park, J.; Hwang, Y.; Kang, M.; Park, J. G.; Hyeon, T., Direct synthesis of highly crystalline and monodisperse manganese ferrite nanocrystals. *Journal of Physical Chemistry B* **2004,** 108, (37), 13932-13935.
59. Note the difference between the terms "metalorganic" and "organometallic". "Metalorganic" refers to compounds containing metals and organic ligands without a direct metal-carbon bonds. On the contrary, “organometallic” compound contain bonds between carbon and metal.[16]
60. Bönnemann, H.; Brijoux, W.; Brinkmann, R.; Matoussevitch, N.; Waldöfner, N.; Palina, N.; Modrow, H., A size-selective synthesis of air stable colloidal magnetic cobalt nanoparticles. *Inorganica Chimica Acta* **2003,** 350, 617-624.
61. Grzelczak, M.; Pérez-Juste, J.; Mulvaney, P.; Liz-Marzán, L. M., Shape control in gold nanoparticle synthesis. *Chemical Society Reviews* **2008,** 37, (9), 1783-1791.
62. Sánchez-Iglesias, A.; Pastoriza-Santos, I.; Pérez-Juste, J.; Rodríguez-González, B.; García De Abajo, F. J.; Liz-Marzán, L. M., Synthesis and optical properties of gold nanodecahedra with size control. *Advanced Materials* **2006,** 18, (19), 2529-2534.
63. Chen, D. H.; Hsieh, C. H., Synthesis of nickel nanoparticles in aqueous cationic surfactant solutions. *Journal of Materials Chemistry* **2002,** 12, (8), 2412-2415.
64. Xia, Y.; Xiong, Y.; Lim, B.; Skrabalak, S. E., Shape-controlled synthesis of metal nanocrystals: Simple chemistry meets complex physics? *Angewandte Chemie - International Edition* **2009,** 48, (1), 60-103.
65. Viau, G.; Brayner, R.; Poul, L.; Chakroune, N.; Lacaze, E.; FiÃ©vet-Vincent, F.; FiÃ©vet, F., Ruthenium nanoparticles: Size, shape, and self-assemblies. *Chemistry of Materials* **2003,** 15, (2), 486-494.
66. Wu, S. H.; Chen, D. H., Synthesis and characterization of nickel nanoparticles by hydrazine reduction in ethylene glycol. *Journal of Colloid and Interface Science* **2003,** 259, (2), 282-286.
67. Reetz, M. T.; Helbig, W., Size-Selective Synthesis of Nanostructured Transition Metal Clusters. *Journal of the American Chemical Society* **1994,** 116, (16), 7401-7402.
68. Taleb, A.; Petit, C.; Pileni, M. P., Synthesis of Highly Monodisperse Silver Nanoparticles from AOT Reverse Micelles: A Way to 2D and 3D Self-Organization. *Chemistry of Materials* **1997,** 9, (4), 950-959.
69. Chen, D. H.; Wu, S. H., Synthesis of nickel nanoparticles in water-in-oil microemulsions. *Chemistry of Materials* **2000,** 12, (5), 1354-1360.
70. Zhang, D. E.; Ni, X. M.; Zheng, H. G.; Li, Y.; Zhang, X. J.; Yang, Z. P., Synthesis of needle-like nickel nanoparticles in water-in-oil microemulsion. *Materials Letters* **2005,** 59, (16), 2011-2014.
71. O'Brien, S.; Brus, L.; Murray, C. B., Synthesis of monodisperse nanoparticles of barium titanate: Toward a generalized strategy of oxide nanoparticle synthesis. *Journal of the American Chemical Society* **2001,** 123, (48), 12085-12086.
72. Ji, M.; Chen, X.; Wai, C. M.; Fulton, J. L., Synthesizing and dispersing silver nanoparticles in a water-in- supercritical carbon dioxide microemulsion [18]. *Journal of the American Chemical Society* **1999,** 121, (11), 2631-2632.

73. Sun, Y.-P.; Rollins, H. W.; Guduru, R., Preparations of Nickel, Cobalt, and Iron Nanoparticles through the Rapid Expansion of Supercritical Fluid Solutions (RESS) and Chemical Reduction. *Chemistry of Materials* **1998,** 11, (1), 7-9.
74. Niederberger, M.; Bartl, M. H.; Stucky, G. D., Benzyl alcohol and titanium tetrachloride - A versatile reaction system for the nonaqueous and low-temperature preparation of crystalline and luminescent titania nanoparticles. *Chemistry of Materials* **2002,** 14, (10), 4364-4370.
75. Niederberger, M.; Bartl, M. H.; Stucky, G. D., Benzyl alcohol and transition metal chlorides as a versatile reaction system for the nonaqueous and low-temperature synthesis of crystalline nano-objects with controlled dimensionality. *Journal of the American Chemical Society* **2002,** 124, (46), 13642-13643.
76. Garnweitner, G.; Niederberger, M., Nonaqueous and surfactant-free synthesis routes to metal oxide nanoparticles. *Journal of the American Ceramic Society* **2006,** 89, (6), 1801-1808.
77. Niederberger, M.; Garnweitner, G., Organic reaction pathways in the nonaqueous synthesis of metal oxide nanoparticles. *Chemistry - A European Journal* **2006,** 12, (28), 7282-7302.
78. Giernoth, R., Task-specific ionic liquids. *Angewandte Chemie - International Edition* **2010,** 49, (16), 2834-2839.
79. Antonietti, M.; Kuang, D.; Smarsly, B.; Zhou, Y., Ionic liquids for the convenient synthesis of functional nanoparticles and other inorganic nanostructures. *Angewandte Chemie - International Edition* **2004,** 43, (38), 4988-4992.
80. Taubert, A.; Li, Z., Inorganic materials from ionic liquids. *Dalton Transactions* **2007**, (7), 723-727.
81. Morris, R. E., Ionothermal synthesis - Ionic liquids as functional solvents in the preparation of crystalline materials. *Chemical Communications* **2009**, (21), 2990-2998.
82. Cooper, E. R.; Andrews, C. D.; Wheatley, P. S.; Webb, P. B.; Wormald, P.; Morris, R. E., Ionic liquids and eutectic mixtures as solvent and template in synthesis of zeolite analogues. *Nature* **2004,** 430, (7003), 1012-1016.
83. Abbott, A. P.; Capper, G.; Davies, D. L.; Rasheed, R. K.; Tambyrajah, V., Novel solvent properties of choline chloride/urea mixtures. *Chemical Communications* **2003,** 9, (1), 70-71.
84. Rabenau, A., Role of hydrothermal synthesis in preparative chemistry. *Angewandte Chemie - International Edition in English* **1985,** 24, (12), 1026-1040.
85. Mao, Y.; Park, T. J.; Zhang, F.; Zhou, H.; Wong, S. S., Environmentally friendly methodologies of nanostructure synthesis. *Small* **2007,** 3, (7), 1122-1139.
86. Ghosh, M.; Biswas, K.; Sundaresan, A.; Rao, C. N. R., MnO and NiO nanoparticles: Synthesis and magnetic properties. *Journal of Materials Chemistry* **2006,** 16, (1), 106-111.
87. Liu, Q.; Liu, H.; Han, M.; Zhu, J.; Liang, Y.; Xu, Z.; Song, Y., Nanometer-sized nickel hollow spheres. *Advanced Materials* **2005,** 17, (16), 1995-1999.
88. Suslick, K. S., Sonochemistry. *Science* **1990,** 247, (4949), 1439-1445.
89. Sounds with a frequency greater than the upper limit of human hearing.
90. Mizukoshi, Y.; Okitsu, K.; Maeda, Y.; Yamamoto, T. A.; Oshima, R.; Nagata, Y., Sonochemical preparation of bimetallic nanoparticles of gold/palladium in aqueous solution. *Journal of Physical Chemistry B* **1997,** 101, (36), 7033-7037.
91. Yang, L. X.; Zhu, Y. J.; Tong, H.; Wang, W. W., Submicrocubes and highly oriented assemblies of $MnCO_3$ synthesized by ultrasound agitation method and their thermal transformation to nanoporous $Mn_2O_3$. *Ultrasonics Sonochemistry* **2007,** 14, (2), 259-265.
92. Xiong, H. M.; Shchukin, D. G.; Möhwald, H.; Xu, Y.; Xia, Y. Y., Sonochemical synthesis of highly luminescent zinc oxide nanoparticles doped with magnesium(II). *Angewandte Chemie - International Edition* **2009,** 48, (15), 2727-2731.
93. electromagnetic radiation whose wavelengths lie in the range 1 mm to 1 m, above the visible.
94. Rao, K. J.; Vaidhyanathan, B.; Ganguli, M.; Ramakrishnan, P. A., Synthesis of inorganic solids using microwaves. *Chemistry of Materials* **1999,** 11, (4), 882-895.
95. Gerbec, J. A.; Magana, D.; Washington, A.; Strouse, G. F., Microwave-enhanced reaction rates for nanoparticle synthesis. *Journal of the American Chemical Society* **2005,** 127, (45), 15791-15800.
96. Tu, W.; Liu, H., Rapid synthesis of nanoscale colloidal metal clusters by microwave irradiation. *Journal of Materials Chemistry* **2000,** 10, (9), 2207-2211.
97. Wang, W. W.; Zhu, Y. J., Shape-controlled synthesis of zinc oxide by microwave heating using an imidazolium salt. *Inorganic Chemistry Communications* **2004,** 7, (9), 1003-1005.
98. Ding, K.; Miao, Z.; Liu, Z.; Zhang, Z.; Han, B.; An, G.; Miao, S.; Xie, Y., Facile synthesis of high quality $TiO_2$ nanocrystals in ionic liquid via a microwave-assisted process. *Journal of the American Chemical Society* **2007,** 129, (20), 6362-6363.
99. Leadbeater, N. E.; Torenius, H. M., A study of the ionic liquid mediated microwave heating of organic solvents. *Journal of Organic Chemistry* **2002,** 67, (9), 3145-3148.

100. Bilecka, I.; Niederberger, M., New developments in the nonaqueous and/or non-hydrolytic sol-gel synthesis of inorganic nanoparticles. *Electrochimica Acta* **2010**.
101. Bilecka, I.; Djerdj, I.; Niederberger, M., One-minute synthesis of crystalline binary and ternary metal oxide nanoparticles. *Chemical Communications* **2008**, (7), 886-888.
102. Srivastava, S.; Santos, A.; Critchley, K.; Kim, K. S.; Podsiadlo, P.; Sun, K.; Lee, J.; Xu, C.; Lilly, G. D.; Glotzer, S. C.; Kotov, N. A., Light-controlled self-assembly of semiconductor nanoparticles into twisted ribbons. *Science* **2010,** 327, (5971), 1355-1359.
103. Sotiropoulou, S.; Sierra-Sastre, Y.; Mark, S. S.; Batt, C. A., Biotemplated nanostructured materials. *Chemistry of Materials* **2008,** 20, (3), 821-834.
104. Van Bommel, K. J. C.; Friggeri, A.; Shinkai, S., Organic templates for the generation of inorganic materials. *Angewandte Chemie - International Edition* **2003,** 42, (9), 980-999.
105. Huang, J.; Wang, X.; Wang, Z. L., Controlled replication of butterfly wings for achieving tunable photonic properties. *Nano Letters* **2006,** 6, (10), 2325-2331.
106. Payne, E. K.; Rosi, N. L.; Xue, C.; Mirkin, C. A., Sacrificial biological templates for the formation of nanostructured metallic microshells. *Angewandte Chemie - International Edition* **2005,** 44, (32), 5064-5067.
107. Zhou, H.; Fan, T.; Zhang, D.; Guo, Q.; Ogawa, H., Novel bacteria-templated sonochemical route for the in situ one-step synthesis of ZnS hollow nanostructures. *Chemistry of Materials* **2007,** 19, (9), 2144-2146.
108. Mao, C.; Solis, D. J.; Reiss, B. D.; Kottmann, S. T.; Sweeney, R. Y.; Hayhurst, A.; Georgiou, G.; Iverson, B.; Belcher, A. M., Virus-Based Toolkit for the Directed Synthesis of Magnetic and Semiconducting Nanowires. *Science* **2004,** 303, (5655), 213-217.
109. Li, Z.; Chung, S. W.; Nam, J. M.; Ginger, D. S.; Mirkin, C. A., Living templates for the hierarchical assembly of gold nanoparticles. *Angewandte Chemie - International Edition* **2003,** 42, (20), 2306-2309.
110. Lvov, Y. M.; Price, R. R.; Selinger, J. V.; Singh, A.; Spector, M. S.; Schnur, J. M., Imaging nanoscale patterns on biologically derived microstructures. *Langmuir* **2000,** 16, (14), 5932-5935.
111. Reches, M.; Gazit, E., Casting metal nanowires within discrete self-assembled peptide nanotubes. *Science* **2003,** 300, (5619), 625-627.
112. Behrens, S.; Habicht, W.; Wagner, K.; Unger, E., Assembly of nanoparticle ring structures based on protein templates. *Advanced Materials* **2006,** 18, (3), 284-289.
113. Shemer, G.; Krichevski, O.; Markovich, G.; Molotsky, T.; Lubitz, I.; Kotlyar, A. B., Chirality of silver nanoparticles synthesized on DNA. *Journal of the American Chemical Society* **2006,** 128, (34), 11006-11007.
114. Brutchey, R. L.; Yoo, E. S.; Morse, D. E., Biocatalytic synthesis of a nanostructured and crystalline bimetallic perovskite-like barium oxofluorotitanate at low temperature. *Journal of the American Chemical Society* **2006,** 128, (31), 10288-10294.
115. Correa-Duarte, M. A.; Pérez-Juste, J.; Sánchez-Iglesias, A.; Giersig, M.; Liz-Marzán, L. M., Aligning Au nanorods by using carbon nanotubes as templates. *Angewandte Chemie - International Edition* **2005,** 44, (28), 4375-4378.
116. Dujardin, E.; Peet, C.; Stubbs, G.; Culver, J. N.; Mann, S., Organization of metallic nanoparticles using tobacco mosaic virus templates. *Nano Letters* **2003,** 3, (3), 413-417.
117. Aldaye, F. A.; Palmer, A. L.; Sleiman, H. F., Assembling materials with DNA as the guide. *Science* **2008,** 321, (5897), 1795-1799.
118. Warner, M. G.; Hutchison, J. E., Linear assemblies of nanoparticles electrostatically organized on DNA scaffolds. *Nature Materials* **2003,** 2, (4), 272-277.
119. Yin, Y.; Lu, Y.; Gates, B.; Xia, Y., Template-assisted self-assembly: A practical route to complex aggregates of monodispersed colloids with well-defined sizes, shapes, and structures. *Journal of the American Chemical Society* **2001,** 123, (36), 8718-8729.
120. Gutiérrez, M. C.; Ferrer, M. L.; Del Monte, F., Ice-templated materials: Sophisticated structures exhibiting enhanced functionalities obtained after unidirectional freezing and ice-segregation-induced self-assembly. *Chemistry of Materials* **2008,** 20, (3), 634-648.
121. Mazumder, B.; Uddin, I.; Khan, S.; Ravi, V.; Selvraj, K.; Poddar, P.; Ahmad, A., Bio-milling technique for the size reduction of chemically synthesized $BiMnO_3$ nanoplates. *Journal of Materials Chemistry* **2007,** 17, (37), 3910-3914.
122. Mazumder, B.; Uddin, I.; Khan, S.; Ravi, V.; Selvraj, K.; Poddar, P.; Ahmad, A., Erratum: Bio-milling technique for the size reduction of chemically synthesized $BiMnO_3$ nanoplates (Journal of Materials Chemistry (2007) 17 (3910-3914) DOI: 10.1039/b706154d). *Journal of Materials Chemistry* **2008,** 18, (48), 5998.

123. Kotov, N. A., *Nanoparticle Assemblies and Superstructures*. CRC Press, Taylor & Francis Group: **2006**.

# ABBREVIATIONS / ABREVIATURAS

# ABBREVIATIONS

0D: zero-dimensinal
1D: mono-dimensional
2D: bi-dimensional
3D: three-dimensional
AD: (*anno Domino*); after the birth of Christ
AFM: atomic force microscopy
AFM: antiferromagnetic
AOT: (*aerosol OT*); Bis(2-ethylhexyl)sulfosucinate
BC: before Christ
*ca.*: (*circa*); approximately
CTAB: cetyltrimethylammonium bromide
DESs: deep eutectic solvents
DM: dipolar moment
DMF: N, N-dimethylformamide
DNA: deoxyribonucleic acid
EDTA: ethylenediaminetetraacetic acid
*e.g.*: (*exempli gratia*); for example
*et al.*: (*et alii*); and others
*etc.*: (*et cetera*); and other things
EX: exchanbe bias
FM: ferromagnetic
HDD: hexadecanediol
HDA: hexadecylamine
HRTEM: high resolution transmission electron microscopy
*i.e.*: (*id est*); that is, in other words
ISISA: ice-segregation induced self-assembly
ILs: ionic liquids
LEDs: light-emittin diodes
MRI: magnetic resonance imaging
NCs: nanocrystals
NPs: nanoparticles
NRs: nanorods
NWs: nanowires
DMF: N, N-dimethylformamide
OLEA: oleic acid
OA: oleylamine
PVA: polyvinyl alcohol
PVP: polyvinylpyrrolidone
QDs: quantum dots
RIR: reference intensity ratio
SA: self-assembly
SAED: selected area electron diffraction
SDS: sodium dodecyl sulphate
SEM: scanning electron microscopy
SPM: scanning probe microscopy
SQUID: superconducting quantum interference device
STM: scanning tunneling microscopy
TBP: tributylphosphine
TEM: transmission electron miscroscopy
TEOS: tetraethyl orthosilicate
TG-DTA: thermogravimetric and differential thermal analysis
THF: tetrahydrofurane
TOPO: trioctylphosphine oxide
*vs*: (*versus)*; against
XPS: X-ray photoelectron spectroscopy
XRD: X-ray diffraction

Physical units (length, volume, time,…) are abbreviated following the International System of Units.

# ABREVIATURAS

0D: cerodimensinal
1D: monodimensional
2D: bidimensional
3D: tridimensional
a.C.: antes de Cristo
ADN: ácido desoxirribonucleico
AE: autoensamblado
AFM: *(atomic force microscopy)*; microscopía de fuerza atómica
AFM: antiferromagnético
AOT: (*aerosol OT* ); sulfosuccinato bis(2-etilhexil) sódico
*ca.*: (*circa*); aproximadamente
CTAB: *(cetyltrimethylammonium bromide)*; bromuro de cetiltrimetilamonio
DES: (*deep eutectic solvent*) disolvente con eutéctico profundo
DMF: N, N-dimetilformamida
DRX: difracción de rayos X
EB: *exchange-bias*
EDTA: *(ethylenediaminetetraacetic acid)*; ácido etilendiaminotetraacético
*e.g.*: (*exempli gratia*); por ejemplo
*et al.*: (*et alii*); y otros
*etc.*: (*et cetera*); y más cosas
FM: ferromagnético
HDA: hexadecilamina
HRTEM:
*i.e.*: (*id est*); es decir
ISISA: *(ice-segregation induced self-assembly)*; auto-ensamblado inducido por segregación de hielo
LIs: líquidos iónicos
MD: momento dipolar
MRI: *(magnetic resonance imaging)*; imagen por resonancia magnética
NCs: nanocristales
NPs: nanopartículas
NRs: *nanorods*
NWs: *(nanowires)*; nanohilos
OA: oleilamina
OLEA: *(oleic acid)*, ácido oleico
PVA: *(polyvinyl alcohol)*; alcohol polivinílico
PVP: polivinilpirrolidona
QDs: *(quantum dots)*; puntos cuánticos
SDS: *(sodium dodecyl sulphate)*; dodecilsulfato sódico
SEM: *(scanning electron microscopy)*; microscopía electrónica de barrido
SPM: *(scanning probe microscopy)*; microscopía de sonda de barrido
STM: *(scanning tunneling microscopy)*; microscopía de efecto tunnel
TBP: tributilfosfina
TEM: *(transmission electron microscopy*); microscopía electrónica de transmisión
TEOS: *(tetraethyl orthosilicate)*; ortosilicato tetraetílico
THF: tetrahidrofurano
TOPO: *(trioctylphosphine oxide)*; óxido de trioctilfosfina
XPS: (*X-ray photoelectron spectroscopy*) espectroscopía de fotoelectrones de rayos X

Las abreviaturas correspondientes a las unidades físicas (longitud, volumen, tiempo,…) siguen el Sistema Internacional de Unidades.

VIII. Abreviaturas